



# Durham E-Theses

---

## *Condensate film flow on the surface of rotating cones*

Smith, Derek Beaman

### How to cite:

---

Smith, Derek Beaman (1976) *Condensate film flow on the surface of rotating cones*, Durham theses, Durham University. Available at Durham E-Theses Online: <http://etheses.dur.ac.uk/8160/>

### Use policy

---

The full-text may be used and/or reproduced, and given to third parties in any format or medium, without prior permission or charge, for personal research or study, educational, or not-for-profit purposes provided that:

- a full bibliographic reference is made to the original source
- a [link](#) is made to the metadata record in Durham E-Theses
- the full-text is not changed in any way

The full-text must not be sold in any format or medium without the formal permission of the copyright holders.

Please consult the [full Durham E-Theses policy](#) for further details.

Condensate Film Flow on the Surface of Rotating Cones

By

Derek Beauman Smith · B.Sc.

This Thesis Submitted

For

The Degree of Doctor of Philosophy

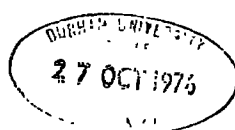
in the

University of Durham

Dept. of Engineering Science

University of Durham

Sept. 1976



## ABSTRACT

A theoretical and experimental analysis has been made of condensate flow on the outer surface of  $10^\circ$  and  $20^\circ$  included angled, truncated, rotating cones. Experiments were carried out at steam pressures of 1.5, 2, 2.5, 3, and 4 bar absolute. The rotational speed range examined was such that it was possible to follow the progress from the stage at which ridge like waves are formed to that at which drops are thrown from the crests of the ridges.

The peak film thickness was measured, employing an inculated pointer and micrometer technique, and a photographic record of the condensate surface profile was obtained. The latter record provided wavelength and ridge orientation measured with reference to the cone generator line.

A theoretical equation is developed from the Navier-Stokes equations of motion with suitable boundary conditions for predicting the behaviour of the condensate film. Given basic information: rotational speed, cone apex angle, radius, condensate film temperature difference and the physical properties of the condensate film then the wavelength, minimum film thickness and wave amplitude may be determined for a known heat flux.

The various configurations of ridge like waves, as both steam pressure and rotational speed were varied, are presented and discussed. The points at which ridge like waves form and drops begin to be thrown from these ridges are examined and a correlation made to predict these conditions. The effect of coriolis forces compared with centrifugal forces is examined to ascertain the angle which the ridge makes with the cone generator as it progresses down the surface. Correlations of Nusselt against Weber and Taylor numbers are given and discussed.

ACKNOWLEDGEMENTS

I am greatly indebted to everyone who has helped in any aspect with the work included in this thesis. Especially to Professor Russell Hoyle and Sir Derman Christopherson. The former for his assistance in developing the initial work and the latter for his valuable help and guidance during the project.

I am also extremely grateful to Mr. Albert Harker and Mr. Wilf Johnson, and Chief Technician Mr. C. Campbell for their assistance and helpful suggestions.

CONTENTS

	page no.
Abstract.	(i)
Acknowledgements.	(ii)
Contents.	(iii)
List of tables.	(vi)
List of figures.	(vii)
Symbols.	(xi)
1.0 Introduction.	1
2.0 Historical Background.	
2.1 Introduction.	4
2.2 Non-dimensional parameters.	6
2.3 Film flow on stationary surfaces.	10
2.4 Film flow during condensation.	23
2.5 Condensate flow on rotating surfaces.	
2.5.1 Condensation and heat transfer on rotating cylindrical bodies.	36
2.5.2 Condensation and heat transfer on rotating discs.	42
2.5.3 Condensation and heat transfer on rotating conical bodies.	47
2.6 Present research.	54
3.0 Theory.	
3.1 Introduction.	55
3.2 Coordinate system and equations of motion.	58
3.3 Gravitational forces and pressure terms.	65
3.4 , Development of governing equations.	65
3.5 General assumptions and boundary conditions.	67
3.6 Velocity profiles.	
3.6.1 Velocity profile in the 'X' direction.	68
3.6.2 Relative circumferential velocity, $V_{\theta}$ .	69

	page no.
3.7 Continuity equations.	73
3.8 Solution of the governing equation.	74
Formation of non-dimensional equation.	76
3.9 Parameter variation.	79
4.0 Experimental work.	
4.1 Apparatus.	84
4.2 Instrumentation.	
4.2.1 Film thickness measurement.	86
4.2.2 Installation and testing of film thickness measuring equipment.	91
4.2.3 Temperature measurement.	93
4.2.4 Pressure measurement.	99
4.2.5 Flowrate, cooling water and condensate measurement.	99
4.2.6 Photography.	100
4.2.7 Rotational speed measurement.	103
4.3 Preliminary test runs.	104
4.4 Test procedure.	105
4.5 Results.	
4.5.1 Limits of experimental results.	107
4.5.2 Measurements made from photographs.	108
4.6 Error analysis.	109
5.0 Discussion.	
5.1 Description of condensate behaviour.	113
5.1.1 Variation of speed at constant pressure.	
10° Cone.	114
20° Cone.	124

	page no.
5.1.2 Variation due to pressure changes at constant rotational speed	
10° Cone	126
20° Cone	129
5.2 Initiation speeds for ridge formation and drop departure	132
5.3 Comparison of theoretical and experimental results	141
5.3.1 Wavelength	142
5.3.1 Film thickness	150
5.4 Inertia forces and drag	160
5.5 Energy transfer	173
6.0 Conclusion	184
7.0 References	190
8.0 Appendices: A Film thickness measurement literature survey	197
B Design of conductivity film thickness measuring equipment	205
C Variation of parameter $\xi$	211
D Numerical solution of governing equations	213
E Least squares polynomial fit programme	226
F Error introduced by using $\Omega$ throughout the thesis instead of $2\Omega + \frac{g \cos \beta}{\bar{\kappa} a_x}$ .	229a
9.0 Tables	

List of tables.

	page no.
Table 1 Experimental results for $10^\circ$ cone.	230
" 2 " " " $20^\circ$ " .	231
" 3 Theoretical results for $10^\circ$ cone.	232
" 4 " " " $20^\circ$ cone.	233
" 5 Experimental parameters for $10^\circ$ cone.	234
" 6 " " " $20^\circ$ cone.	235
" 7 Experimental and theoretical ridge angles and Rossby number for the $10^\circ$ cone.	236
" 8 Experimental and theoretical ridge angles and Rossby number for the $20^\circ$ cone.	237

<u>list of figures.</u>	page no.
Figure 1	Laminar film thickness model. 53
" 2	General photograph of condensate flow at 350 r.p.m. 56
" 3	Model of surface profile. 57
" 4 (a)	Coordinate system. 57
" 4 (b)	Position vector for coordinate system. 57
" 5	Elemental segment in model surface. 73
" 6	Variation of non-dimensional half wavelength with $\Lambda$ . 80
" 7	Variation of non-dimensional film thickness with $\Lambda$ . 82
" 8	General arrangement of apparatus. 85
" 9	General arrangement of experimental body. 87
" 10	Line diagram of apparatus. 89
" 11	Point contact monitoring circuit. 94
" 12	Eccentricity of experimental body. 94
" 13	Thermo-couple orientation. 96
" 14	Temperature measuring circuit. 97
" 15	Lighting and camera positioning for $10^\circ$ and $20^\circ$ cones. 101
" 16	Photograph of lighting and camera position for the $20^\circ$ cone. 102
" 17 (a)	Condensate surface photograph, $10^\circ$ cone, stationary. 115
" 17 (b)	" " " " " , 135 r.p.m. 115
" 18 (a)	" " " " " , 200 " . 117
" 18 (b)	" " " " $20^\circ$ " , 200 " . 117
" 19 (a)	" " " " $10^\circ$ " , 250 " . 119
" 19 (b)	" " " " $20^\circ$ " , 250 " . 119
" 20 (a)	" " " " $10^\circ$ " , 300 " . 121
" 20 (b)	" " " " $20^\circ$ " 300 " . 121

	page no.
Figure 21 (a) Condensate surface photograph, $10^\circ$ cone, 350 r.p.m.	122
" 21 (b) " " " $20^\circ$ " , 350 " .	122
" 22 (a) " " " $10^\circ$ " , 400 " .	123
" 23 " " " $20^\circ$ " , 450 " .	123
" 24 (a) " " " $10^\circ$ " , 1.5 bar abs.	128
" 24 (b) " " " $20^\circ$ " , 1.5 " " .	128
" 25 (a) " " " $10^\circ$ " , 2.5 " " .	128
" 25 (b) " " " $20^\circ$ " , 2.5 " " .	128
" 26 (a) " " " $10^\circ$ " , 3.0 " " .	130
" 26 (b) " " " $20^\circ$ " , 3.0 " " .	130
" 27 (a) " " " $10^\circ$ " , 4.0 " " .	131
" 27 (b) " " " $20^\circ$ " , 4.0 " " .	131
" 28 Ridge initiation and drop formation speeds.	133
" 29 Graph of energy flux versus the ratio of acceleration in the Y direction to that in the X direction.	138
" 30 Graph of dimensional film thickness versus dimensional wavelength.	143
" 31 Graph of wavelength and film thickness versus rotational speed at a steam pressure of 2.5 bar abs.	144
" 32 Graph of wavelength versus rotational speed $10^\circ$ cone.	146
" 33 " " " " " $20^\circ$ " .	147
" 34 " " " " perpendicular acceleration, $a_y$ .	148
" 35 Graph of film thickness versus rotational speed $10^\circ$ cone.	152
" 36 Graph of film thickness versus rotational speed $20^\circ$ cone.	153

Figure 37	Graph of ratio of laminar to calculated mean film thickness versus acceleration perpendicular to generator.	156
" 38	Graph of ratio of laminar to minimum and measured peak film thickness versus acceleration in the Y direction.	158
" 39	Variation of ridge angle along cone generator, 1.5 bar.	161
" 40	" " " " " " " " ,2.0 "	162
" 41	" " " " " " " " ,2.5 "	163
" 42	" " " " " " " " ,3.0 "	164
" 43	" " " " " " " " ,4.0 "	165
" 44 (a)	Graph of mid-point ridge angle versus rotational speed, 10° cone.	166
" 44 (b)	Graph of mid-point ridge angle versus rotational speed, 20° cone.	166
" 45 (a)	Graph of theoretical ridge angle versus rotational speed, 10° cone.	167
" 45 (b)	Graph of theoretical ridge angle versus rotational speed, 20° cone.	167
" 46	Graph of Rossby number versus rotational speed.	172
" 47 (a)	Graph of temperature profile for 10° and 20° cones.	174
" 47 (b)	Graph of heat flux versus Drew reference temperature.	174
" 48	Graph of Weber number versus theoretical Nusselt number.	177
" 49 (a)	Graph of Weber number versus experimental Nusselt number, 10° cone.	178
" 49 (b)	Graph of Weber number versus experimental Nusselt number, 20° cone.	178

		page no.
Figure 50	Comparison of authors results to those obtained by other workers.	180
" 51	Graph of Taylor number versus experimental Nusselt number.	191
" 52	Nusselt number versus Taylor number for different shaped bodies.	193
" 53	Initial conductivity film thickness measuring gauge design.	206
" 54	Measuring circuit diagram.	206
" 55	Final conductivity film thickness measuring equipment.	206
" 56	Graph of potential difference versus film thickness.	208
" 57	Arrangement of traversing mechanism for conductance gauge calibration.	209A
" 58	Calibration curves for conductance measuring devices.	210

Symbols.

$A', A_0, B', B_0$	Constants of integration.	
A	Area.	$m^2$
$a_x$	Component of acceleration parallel to the cone generator line.	
$a_y$	Component of acceleration perpendicular to the cone generator line.	
C	Non-dimensional wave velocity.	
$C'$	Wave velocity.	m/s
cp	Specific heat.	kJ/kg K
$F_x, Y, \Theta$	Components of body force in X , Y , and $\Theta$ directions.	
f	Function.	
g	Acceleration due to gravity.	$m/s^2$
G	Conductivity per unit length.	mm/cm
h	Heat transfer coefficient.	$kW/m^2 K$
$h_{1,2,3}$	Scale factors in curvilinear coordinates.	
$h_{fg}$	Enthalpy of vapourisation.	kJ/kg
k	Thermal conductivity.	$kW/m K$
$L, L_0$	Dimensionless length in the X direction.	
m	Mass of vapour condensed.	
N	Speed of rotation of body.	r.p.m.
P	Steam pressure.	bar ( $10^5 N/m^2$ )
pw	Parameter for conductivity changes.	
Q	Flowrate.	$m^3/s$
q	Energy flow.	kW
R	General radial coordinate.	
$R_s$	Cone radius.	
$R_x$	Electrical resistance.	ohm

$r$	Position vector.	
$T$	Temperature.	$^{\circ}\text{C}$
$t$	Time	$\text{s}$
$U_0$	Average velocity.	$\text{m/s}$
$u$	Velocity in the $x$ direction.	"
$V$	Voltage.	$\text{v}$
$V_{X,Y,\theta}$	Velocity components in the $X$ , $Y$ , and $\theta$ directions.	
$v$	Velocity in the $y$ direction.	
$X,Y,\theta$	Cone coordinates.	
$x,y,z$	Rectangular coordinates.	

## Greek symbols.

$\alpha$	Ridge angle.	
$2\beta$	Cone angle.	
$\Delta$	Small changes in quantities.	
$\delta$	Film thickness.	$\text{mm.}$
$\epsilon$	Constant for $X$ direction increase in film thickness.	
$\lambda$	Wavelength.	$\text{m}$
$\mu$	Dynamic viscosity.	$\text{N s/m}^2$
$\nu$	Kinematic viscosity.	$\text{m}^2/\text{s}$
$\rho$	Density.	$\text{kg/m}^3$
$\sigma$	Surface tension	$\text{N/m}$
$\tau$	Shear stress.	$\text{N/m}^2$
$\tau_{\infty}$	Free stream time component.	
$\phi$	Heat flux.	$\text{kW/m}^2$
$\omega$	Angular velocity.	$\text{l/s}$

## Subscripts.

$av$	Average value.
$l$	Liquid.

max	Maximum value.
min	Minimum value.
s	Saturation value.
v	Vapour.
w	Wall.
wi	Inside wall.
wo	Outside wall.

## Superscripts

-	Indicates non-dimensional terms.
'	Indicates differentiation with respect to $\theta$ .

## Non-dimensional groups.

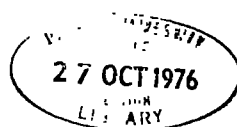
$\Lambda$	$\frac{k \Delta T \mu \sigma}{h_{fg} \rho^2 a_y^2 s_{\min} (1 + 0.375 cp \Delta T / h_{fg})}$	
$\textcircled{N}$	$\omega \sin \beta a_x s_{\min} \left( \frac{\sigma \rho}{a_y^3 \mu^2} \right)^{\frac{1}{2}}$	
$\Omega$	$\frac{\omega^2 \sin^2 \beta \sigma}{s_{\min} \rho a_y^2}$	
Re	Reynolds number	$\frac{V_{av} D \rho}{\mu}$
We	Weber number	$\frac{\omega^2 D^3 \rho}{4 \sigma}$
Ro	Rosby number	$\frac{2 V_x \omega \sin \beta}{a_x}$
Ta	Taylor number	$\left( \frac{\omega D^2 \rho}{\mu} \right)^2$
Nu	Nusselt number	$\frac{h D}{2 k}$
Pr	Prandtl number	$\frac{cp \mu}{k}$

1.0 INTRODUCTION

The work reported in this thesis is a contribution to the study of heat transfer from a rotating solid on the surface of which steam condenses where the condensate flows away under the action of gravity and centrifugal forces.

The particular case considered is that of a truncated cone rotating about a vertical axis with its apex uppermost. In this thesis, attention is directed particularly to the measurement of the thickness of a condensate film on the surface of cooled rotating cones and to study the process of condensate removal. A series of experiments using pure dry saturated steam at various pressures was observed condensing on  $10^\circ$  and  $20^\circ$  apex angled, truncated cones.

The present problem is part of a much wider field of work which has been carried out in the past to provide information required to examine the temperature distributions in rotating bodies and the associated thermal stresses. The significance of the work from the practical point of view arises from the need to study the stresses which are introduced when a steam turbine is started up from cold. The stresses and thermal gradients in land based and marine steam turbines have been predicted by Chow and Hoyle (38) and Hoyle and Mabahir (39) respectively. The effect of quick starts from cold and warm up time was studied. Careful control of the steam quality is necessary if the turbine rotor and its casing are not to be heated too quickly, so that high thermal stresses are introduced, and after a number of starts fatigue failures may occur. When the steam is admitted condensation occurs on the cold rotor and casing. The condensate layer then forms a barrier to further condensation. The thickness and distribution of this layer is of particular importance since it limits the transference of energy. After a suitable time, governed in the past by experience, the super-



heated steam is admitted and the rotor attains a temperature above the saturation temperature and condensation ceases. If information was available about the true condensation process, the warm through time could be predicted more accurately and safely, and the quickest time to bring the steam turbine up to maximum power would be calculable. In particular, in cases where steam turbines are employed in naval vessels and in standby power systems, it is often necessary to reach maximum power output in the shortest possible time.

Condensation occurs in two forms, dropwise and filmwise. Perfect dropwise, or filmwise, condensation in practice is difficult to obtain and usually there is a mixture of both. For filmwise condensation the surface must be perfectly wettable and a continuous film exists over the whole surface, whereas in the dropwise condition discrete drops are produced. Dropwise condensation occurs on surfaces even slightly contaminated with fats or oils. There is however a general cleansing action by the steam so that in cases where un-contaminated steam is supplied filmwise condensation will ultimately be the stable form.

In classical analyses of condensation the condensate layer has been assumed smooth. These analyses have produced correlations which have adequately encompassed the experimental data, but in general underestimate the energy transfer. The dynamics of the flow occurring in the condensate layer, and its resulting thickness and shape have received little study, despite their practical significance, no doubt because of the theoretical complexity of the problem, and the experimental difficulties of obtaining direct measurements of film thickness in these conditions.

In previous work the condensate flow on the surface of rotating  $10^\circ$ ,  $20^\circ$  and  $60^\circ$  apex angled cones has been shown to support several regimes of flow depending on the rotational speed. Condensate removal

at higher speeds was assisted by drops being thrown from the film of the  $10^{\circ}$  cone. The main emphasis in this thesis is on the prediction of the form of the interface between the steam and the condensate layer and the conditions under which condensate begins to be drained from the surface in the form of drops. A theoretical analysis beginning with the Navier-Stokes equations is given.

Details of the experimental work and the methods employed are given under the appropriate headings. Experimental results are used in the theoretically predicted equations to test their validity and correlations made to relate the energy transfer to the controlling forces; inertia, gravity and surface tension.

The thesis begins with a brief account of the previous work which is relevant to the subject, including the theoretical studies which have been published of the film flow and wave generation on thin films, and on condensation on stationary and rotating surfaces.

## 2.0 HISTORICAL BACKGROUND

## 2.1 Introduction

Liquid films formed by condensation or other means occur in many types of engineering equipment, especially those concerned with heat and mass transfer. They are important, for example in wetted wall and packed towers, in film evaporators, in condensers and in some water tube boilers. In a number of these applications liquid removal is continuous under the action of gravity as the draining force and in some by centrifugal or other inertial forces. In many cases, the character of the film, its thickness and uniformity, and its velocity have an important effect on the heat and mass transfer taking place in the equipment and hence on the latter's capabilities. These films normally have one surface in contact with a solid surface and the other in contact with a gas or vapour phase. In one aspect, therefore, they can be seen as an example of a two-phase system of flow.

Often the thickness of the films thus formed, including those to which this thesis refers, are quite small, measured in hundredths of a millimetre, as in other cases of thin film flow a number of distinct types of film can be distinguished. When the film thickness is very small the effect of surface tension may be of dominating importance in determining what occurs, and as a consequence travelling waves or ripples often appear on the surface of the film. These surface irregularities and discontinuities may effect the heat and mass transfer taking place.

Much work has been published concerning fluid flow, separately and including heat and mass transfer, on stationary and rotating surfaces. For the present purpose it is convenient to divide this work into three categories

- (i) that concerned with flow of fluids under the action of gravity, over stationary surfaces, in cases where condensation and

evaporation are not important. In practice this means the flow of fluids, whose temperatures are well below boiling point, on surfaces which can have varying inclinations between the vertical and horizontal planes.

- (ii) that concerned with condensation on stationary surfaces under the action of gravity, of particular interest for the present purpose is the case of condensation on the underside of a surface slightly inclined from the horizontal.
- (iii) that concerned with the flow of fluids under the action of inertial forces, particularly those produced by rotation of the surface over which the fluid flows.

In this chapter, an attempt is made to outline the development of the subject, and to refer to the most significant contributions to the literature. The key points in each contribution are discussed briefly. The aim has been to provide a guide enabling the reader to form an opinion as to whether a particular paper should be consulted on any one of the problems considered.

## 2.2 Non-Dimensional Parameters

The equations of motion and energy transfer take on their most powerful form when expressed in terms of dimensionless variables. These dimensionless variables are obtained by dividing the various quantities by the free stream values of each of the quantities. Let the quantities carrying a superscript \* be dimensionless and those carrying a subscript  $\infty$  refer to the free stream quantities. Then we may write the scheme:

$$\begin{aligned}
 t^* &= \frac{t}{t_\infty} ; & X^* &= \frac{X}{L} ; & V_i^* &= \frac{V_i}{V_\infty} ; & F_i^* &= \frac{F_i}{g_i} ; \\
 \rho^* &= \frac{\rho}{\rho_\infty} ; & P^* &= \frac{P}{P_\infty} ; & T^* &= \frac{T}{T_\infty} ; & \omega^* &= \frac{\omega}{\omega_\infty}
 \end{aligned}
 \tag{2.2.1}$$

These quantities are then substituted into the equations of motion. It is possible by rearranging the resulting equations to obtain groups of the free stream quantities which qualify the now dimensionless differentials. Certain dimensionless groups can then be recognised which allow the relative effects of the various forces acting on the fluid to be uniquely specified. It is convenient to have a set of symbols which allow for easy reference to the dimensionless groups which now appear in the non-dimensional equations of motion. For this purpose it is now customary to name certain of the dimensionless coefficients after people who realised their significance under given conditions.

In the following text those dimensionless groups which are relevant to this thesis will be discussed. For convenience it is usual to drop the subscript  $\infty$  upon these numbers on the strict understanding that actual values are always calculated for free stream conditions. The most important dimensionless groups are :-

- (i) The Reynolds number, which gives the ratio of the inertial to viscous forces and defined as

$$Re = \frac{v \rho L}{\mu} \quad 2.2.2$$

where  $L$  is some characteristic length. A high Reynolds number is associated with the situation where the viscous forces are weak in comparison with the inertial forces. The high Reynolds number ( $Re$ ) may be due to low viscosity or high free stream velocity. The larger  $Re$  the more nearly does the fluid approximate to the ideal. The viscous forces, however, act in such a way as to damp out instabilities in the flow. It has been found that laminar flow only occurs for  $Re$  less than some critical value which is a characteristic

of the particular system. For any given system  $L$  may be chosen as any suitable dimension but which particular one must be carefully explained. Thus for thin film flow a choice of  $L$  must be made from distance along the surface, diameter of the body or even the film thickness itself.

(ii) The Froude number, which gives the ratio of gravitational to inertial forces acting on the fluid, is defined as

$$Fr = \frac{V^2}{gL} \quad 2.2.3$$

This number has particular use in reference to gravity waves. Froude number modelling is only useful in the study of long gravity waves and not of short surface waves or ripples.

(iii) When a liquid has a free surface it may be necessary to include the effects of surface tension. The Weber number ( $We$ ) may be used for this purpose and is defined as the ratio of surface tension to inertial forces

$$We = \frac{\rho V^2 L}{\sigma} \quad 2.2.4$$

(iv) Another term which appears when the equations of motion are converted into one of their dimensionless forms is the Rossby number ( $Ro$ ). This term is concerned with the rotational effects and gives the ratio of the inertial to coriolis forces

$$Ro = \frac{V}{\omega L} \quad 2.2.5$$

(v) The Taylor number ( $Ta$ ) may be considered as a rotational Reynolds number squared. The Taylor number is the ratio of the magnitude of the coriolis force to that of the viscous force

$$Ta = \frac{\omega^2 L^4}{\mu^2} \rho^2 \quad 2.2.6$$

- This number plays an important role in the study of rotational systems.

(vi) The previous five non-dimensional groups are those most often used in fluid flow. For heat transfer purposes the Nusselt number is one of the most important. It is essentially the ratio of the total heat transfer to the conductive heat transfer at the fluid boundary. The Nusselt number is defined as

$$\text{Nu} = \frac{hL}{k} \quad 2.2.7$$

(vii) The Prandtl number is a characteristic of the fluid rather than the flow. It is expressed in molecular terms as the ratio of the molecular diffusivity of momentum to molecular diffusivity of energy

$$\text{Pr} = \frac{\mu c_p}{k} \quad \text{or} \quad \frac{\nu}{\alpha} \quad 2.2.8$$

where  $\alpha$  is the thermal diffusivity.

The method of obtaining the dimensionless groups was by expressing the equations of motion in non-dimensional variables. Once these groups had been established the one relevant to any particular situation may be derived without the explicit use of differential equations by employing the method of dimensions in the form proposed by Lord Rayleigh. The method is based on the requirement that any equation describing a physical situation must be dimensionally homogeneous throughout. Any relationships suggested by dimensional analysis must be checked experimentally.

Another very convenient and general method of isolating the dimensionless groups relevant to any particular complex physical situation is the so called Pi theorem of Vaschy and Buckingham. The use of both

the method of dimensions and the Pi theorem are covered thoroughly in most fluid text books.

### 2.3 Film flow on stationary surfaces

One of the first investigators of fluid flow was Hopf (1)\* who observed film thickness, surface velocity and wave formation in a rectangular channel. The Reynolds number range of 150 to 600 was larger than that with which one is commonly concerned in heat transfer problems because the films considered were in general thicker. Hopf's theoretical analysis never considered the effects of surface tension. He showed that provided the channel width was considerably larger than the film thickness,  $\delta$ , then the mean flow per wetted perimeter was given by

$$Q = \frac{\rho g^3 \sin \theta}{3} \left(1 - \frac{0.635}{W} \right) \frac{\rho}{\mu} \quad 2.3.1$$

where  $\theta$  is the angle of inclination, and  $W$  is the width of the channel.

Nusselt (2) developed the first useful hydrodynamic analysis of film flow. He studied the equations of motion of an element in the liquid film. If the flow is steady, uniform, two dimensional and draining under the action of an acceleration field the Navier-Stokes equations reduce directly to the very simple differential equation

$$\frac{d^2 y}{dy^2} + \frac{\rho \sin \theta}{\gamma} = 0 \quad 2.3.2$$

where  $y$  is the coordinate perpendicular to the surface over which the liquid is flowing. Solution of equation 2.3.2 with the boundary conditions

- i)  $V = 0$  at  $y = 0$  (no slip at the wall)
- ii)  $\frac{dV}{dy} = 0$  at  $y = \delta$  (no drag at vapour interface)

produced the semi-parabolic equation for the velocity profile

\*References given in section 7.0

$$v = \frac{g \rho}{2\mu} (2y\delta - y^2) \sin \theta \quad 2.3.3$$

with the maximum velocity at the surface, when  $y = \delta$

$$v_s = \frac{g \delta^2 \rho \sin \theta}{2\mu} \quad 2.3.4$$

By integrating equation 2.3.3 over the film thickness, the mean velocity was found to be

$$v_{av} = \frac{g \delta^2 \rho \sin \theta}{3\mu} \quad 2.3.5$$

and hence the ratio of the two velocities is given by

$$\frac{v_s}{v_{av}} = \frac{3}{2} \quad 2.3.6$$

The mean film thickness,  $\delta_m$ , may then be calculated from

$$\delta_m = \left[ \frac{3\mu Q}{\sin \theta g \rho} \right]^{\frac{1}{3}} \quad 2.3.7$$

Jeffrey's (3) contributed to our knowledge of channel flow with small inclination by observing the instability of the flow over a large range of Reynolds numbers. He made measurements of velocities and film thicknesses. Using a dye tracer; laminar sub-layer thickness, eddy viscosity and friction factors were observed. A theoretical analysis of wave motion and 'bores' was also attempted. Further experimental data was produced by Chwang (4) for water and oil flowing on plates inclined up to 13 degrees to the horizontal, encompassing a Reynolds number range of 0.9 to 110.

Cooper, Drew and McAdams (5) correlate the data of the other workers already mentioned in the form of a friction factor plot. They plot results from isothermal flow of liquids on smooth vertical and inclined plates in the Reynolds number range of 1.5 to 150,000. They conclude that turbulence in the liquid layer played a greater part in the heat transfer when the Reynolds number exceeded 2500.

Kirkbride (6) studied wavy flow on the outside of tubes measuring the peak film thickness employing a micrometer technique. The range of Reynolds number varied from 0.04 to 2000 and the information obtained was used in his work concerned with condensation.

Friedman and Miller (7) experiment on the onset of wavy flow on the inside of tubes, the Reynolds number range was 0.02 to 115. In order to study the character of this flow the authors inject a dye in a stream of the fluid, as a means of discovering the maximum velocity of flow. They showed the velocity of spread of dye to be half as large as the velocity of flow of the external layer of fluid.

Grimley (8) also investigated the flow of fluid on the inside of tubes and in channels. He developed theoretical predictions of the onset of rippling on the surface of a film when the effect of surface tension was allowed for. Measurements were made for several fluids and the critical Reynolds number correlated by the dimensionless equation

$$\frac{\sigma^3}{\mu^4 g} = 0.3 (Re)^8 \quad 2.3.8$$

The investigation was with particular reference to liquid behaviour in packed towers and surface contacting equipment.

A more fundamental and general approach to the subject was introduced by Kapitsa (9). He was the first worker to attempt the solution of the equations of motion for the case of two dimensional wavy flow. He confined himself to the case when the wavelength was much larger than the film thickness. For this case it was assumed that the semi-parabolic velocity distribution of wave flow was the same as that for plane flow, that is

$$v_x = 1.5 v \left( 1 - \frac{y^2}{\delta^2} \right) \quad 2.3.9$$

where  $v$  is the velocity averaged over the cross-section, determined by

$$v = \frac{1}{3} \int_0^{\delta} v_x \, dy \quad 2.3.10$$

The simplified Navier-Stokes equation was

$$\frac{\partial v_x}{\partial t} + \frac{1}{2} \frac{\partial v_x^2}{\partial x} = -\frac{1}{\rho} \frac{\partial p}{\partial x} + g + \nu \nabla^2 v_x \quad 2.3.11$$

and the continuity equation expressed as

$$\frac{\partial \delta}{\partial t} = -\frac{\partial}{\partial x} \left( \int v_x \, dy \right) \quad 2.3.12$$

Substituting the velocity distribution, given by equations 2.3.9 and 2.3.10 into equation 2.3.11, and assuming the pressure at the free surface was due to surface tension effects, that is

$$\frac{\partial p}{\partial x} = -\sigma \frac{\partial^3 \delta}{\partial x^3}, \quad 2.3.15$$

and then averaging over the film thickness by integrating with respect to  $y$  and dividing by  $\delta$ , it was found that

$$\frac{\partial v}{\partial t} + \frac{g}{10} \frac{v \delta v}{\delta x} = \frac{\sigma}{\rho} \frac{\partial^3 \delta}{\delta x^3} + g \quad 2.3.14$$

While equation 2.3.12 becomes

$$\frac{\partial \delta}{\partial t} = -\frac{\partial (v \delta)}{\partial x} \quad 2.3.15$$

The equation of the free surface of the flowing layer was determined by that of the curve

$$y = \delta_0 \phi \quad 2.3.16$$

The thickness of the layer was equal to

$$\delta = \delta_0 (1 + \phi) \quad 2.3.17$$

The quantity  $\phi$  is a function of  $x$  and  $t$  with  $\delta_0$  as the mean film thickness. It is found that solutions to these equations in the form of surface waves are possible. In mathematical terms, a new variable  $x - C't$  can be introduced, where  $C'$  represents the phase velocity of waves travelling over the surface. After various rearrangements the equation for solution, to the first approximation, became

$$\begin{aligned}
 - \frac{\sigma}{\rho} \frac{\partial^3 \phi}{\partial x^3} - (C' - v) \frac{(9v - C') \partial \phi}{10 \partial x} - \frac{3\gamma}{\delta_0^2} (C' - 3v) \phi \\
 + g - \frac{3\gamma v}{\delta_0^2} = 0
 \end{aligned}
 \tag{2.3.18}$$

Solution of this equation to the first approximation gave

$$v = \frac{\delta_0^2 g}{3\gamma} \quad \text{and} \quad C' = 3v
 \tag{2.3.19}$$

In order to estimate the wave amplitude Kapitza considered that energy dissipation would take place only as a consequence of viscosity. After the onset of waves in the flow, the amplitude of the waves increased until the energy supplied by the gravity force is balanced by the viscous forces, whilst the thickness of the flow reduced to a minimum for a given flowrate. From this analysis Kapitza determined that in steady periodic undulatory flow at the same flowrates the mean film thickness,  $\delta_0$ , was 7 percent less if the waves were absent and the film was of uniform thickness. The wave amplitude for all flowrates had an approximate value of 0.46 of the mean film thickness,  $\delta_0$ , while the phase velocity amounted to 2.4 of the velocity  $v$  in the mean cross-section. Kapitza predicted that the onset of waves would occur at

$$Re = 2.43 \left[ \frac{\sigma \delta_0^3}{\mu^4 g} \right]^{\frac{1}{11}}
 \tag{2.3.20}$$

Kapitza and Kapitza (10) study wavy flow on the outside of tubes using a shadowgraph technique and produced data which gave good agreement with Kapitza's theory (9) at low flowrates. They showed that the relative change in wavelength for flow on a tube of radius  $R$  compared with that of a flat surface at the same flowrate was

$$\frac{\Delta \lambda}{\lambda} = \frac{1}{2} \left( \frac{\lambda}{2\pi R} \right)^2
 \tag{2.3.21}$$

which is small except for small values of  $R$ .

When two super-imposed fluids of different densities are accelerated in a direction perpendicular to their interface wave like

disturbances occur at the interface. Taylor (11) and Lewis (12) found that the surface was stable or unstable according to whether the acceleration was directed from the heavier to the lighter fluid or vice versa. Their experiments were confined to accelerations from air to some other fluids and where the film thickness was greater than one third of the wavelength of ripples produced.

A new theoretical analysis, applicable when part or all the flow in the fluid layer was turbulent was developed by Dukler and Bergelin (13). The new equations assumed the applicability of pipe flow universal velocity profiles suggested by Von Karman (14). The universal velocity distribution was defined by two parameters  $u^+$  and  $y^+$ , which were given as

$$u^+ = \frac{u}{u^*} \quad \text{and} \quad y^+ = \frac{u^* \rho_L y}{\mu_L} \quad 2.3.22$$

where  $u^*$  was the friction velocity and related to the wall shear by

$$u^* = \left( \frac{\tau_w g}{\rho_L} \right)^{\frac{1}{2}} \quad 2.3.23$$

Then for full pipe flow, for the laminar sub-layer

$$u^+ = y^+ \quad , \quad 0 < y^+ < 5 \quad 2.3.24$$

for the transition zone,

$$u^+ = -3.05 + 5.0 \ln y^+ \quad , \quad 5 < y^+ < 30 \quad 2.3.25$$

and lastly for the turbulent layer

$$u^+ = 5.5 + 2.5 \ln y^+ \quad , \quad 30 < y^+ < \eta \quad 2.3.26$$

where  $\eta$  is the magnitude of the universal distance parameter at the liquid surface given by

$$\eta = \frac{u^* \rho_L \delta}{\mu_L} \quad 2.3.27$$

The liquid flowrate per unit length of wetted periphery was given by

$$\Gamma = \mu_L \int_0^{\eta} u^+ dy^+ \quad 2.3.28$$

For the case of zero flowrate in the gas phase the equations reduce to give the film thickness as a function of flowrate and physical properties over the complete viscous to turbulent flow range

$$\frac{\Gamma}{\mu_L} + 64 = 3.0\eta + 2.5\eta \ln \eta \quad 2.3.29$$

It was shown that the transition from laminar to turbulent film flow occurred at a Reynolds number of 1080. Experimental results were obtained from the flow of water over the surface of a vertical plate.

Jackson (15) analysed wave flow on the inner wall of a vertical tube. He postulated that waves appeared when the Froude number exceeded unity and that viscosity had a much greater effect on wave inception than surface tension. Wave inception and film thickness were measured for six different liquids and the range of Reynolds numbers encompassed was 4 to 5,000.

Yih (16) investigated the stability of parallel laminar flow with respect to wave formation at the free surface. Taking the origin at the undisturbed free surface, measuring  $x$  downstream along that surface and  $y$  downward in a direction normal to the solid boundary, and denoting the velocity components by  $u$  and  $v$  respectively, the Navier-Stokes equations were

$$\frac{\partial u}{\partial t} + u \frac{\partial u}{\partial x} + v \frac{\partial u}{\partial y} = -\frac{1}{\rho} \frac{\partial p}{\partial x} + g \sin \beta + \nu \Delta u \quad 2.3.30$$

$$\frac{\partial v}{\partial t} + u \frac{\partial v}{\partial x} + v \frac{\partial v}{\partial y} = -\frac{1}{\rho} \frac{\partial p}{\partial y} + g \cos \beta + \nu \Delta v \quad 2.3.31$$

and the continuity equation as

$$\frac{\partial u}{\partial x} + \frac{\partial v}{\partial y} = 0 \quad 2.3.32$$

By making suitable non-dimensional substitutions the above equations were made dimensionless. A perturbation technique was used together with boundary conditions to obtain the well known Sommerfeld-Orr equation

$$(U - C)(\phi'' - \alpha^2 \phi) - U''\phi = \frac{1}{i\alpha Re} (\phi'''' - 2\alpha^2 \phi'' + \alpha^4 \phi) \quad 2.3.33$$

$U$  is the dimensionless value of the velocity component in the  $x$  direction and where  $\phi$  is a function of  $y$ ,  $C$  is the non-dimensional wave velocity and  $\alpha$  is the wave number defined by

$$\alpha = \frac{2\pi\delta}{\lambda} \quad 2.3-34$$

The solution of equation 2.2.33 was achieved by a series expansion in ascending powers of the Reynolds number. The conclusions drawn from these computations for vertical flow were

- (i) that increasing viscosity always tended to stabilise flow.
- (ii) that the flow became unstable at low Reynolds number and the approximate critical value was calculated to be 1.5.
- (iii) that for neutral disturbances the phase velocity of the waves propagated increased with increasing wavelength.

A purely experimental check on the onset of wave formation on a film of water flowing down a vertical plane was carried out by Binovic (17). Distilled water was allowed to flow down the outside of a pipe of diameter 1.045 inch by 5 feet long. The flowrate was adjusted until the water film was only just disturbed by a train of travelling waves. The flowrate was then determined by diverting and weighing the discharge. The discharge per unit width of tube circumference was found to be  $6.9 \times 10^{-3}$  in<sup>3</sup>/s at a temperature of 19°C, the corresponding Reynolds number was calculated to be 4.4. When the train of travelling waves had been initiated eighty-three pictures were obtained at 0.047 second intervals using a flash technique developed by Brown (18). Measurements were made from the photographs and the average values of the wavelength and velocity were about 0.45 inch and  $5\frac{1}{2}$  inch/s respectively.

So far no mention has been made of the types of wave patterns which appear at the free surface of the flowing film. Numerous

investigators have made observations of wave patterns on thin film flow. In general, the wave patterns may be described qualitatively as follows

- (i) At very low flowrates the film surface is completely smooth and mirror like, disturbed only occasionally by small random 'dimples' which are rapidly damped out in the direction of flow.
- (ii) At a slightly increased flowrate, small, symmetrical, regular waves appear. The wave fronts are almost straight and perpendicular to the direction of flow.
- (iii) Further increase of flowrate causes the regular symmetrical wavelets to become less regular, and the cross-section of the wave assumes the non-symmetrical shape usually described as a 'roll wave', with a steep front and a long gently sloping tail. Frequently these waves are preceded by a number of small waves which move as a group with the main wave. In this zone of flow the wave fronts are no longer straight but show a tendency to form bulges or split to overtake each other. This latter appearance has led to these patterns also being referred to as 'curtain type' waves.
- (iv) As the liquid flowrate is increased a stage is reached when the main waves and the accompanying small waves become so randomly mixed the surface appears to be covered with a mass of small jagged 'turbulent' waves. A number of photographs have been published that show this type of pattern e.g. Dukler and Bergelin (13).

The theoretical analysis of the problem was taken a step further by Brooks Benjamin. His paper (19) dealt with the hydrodynamic stability

of film flow characterised by small values of the Reynolds number. The formation of the problem resembled that of Yih (16), but the method of solution differed. This difference occurs in the solution of the Sommerfeld-Orr equation, 2.3.33, which was then rearranged into the form below where  $C$  is wave velocity divided by the surface film velocity,

$$\phi''' = (n - Cn - ny^2)\phi'' + (2n - \alpha^2 + C\alpha^2n - \alpha^4 + \alpha^2ny^2)\phi' \quad 2.3.35$$

and then

$$\phi''' = (p + qy^2)\phi'' + (r + s^2y^2)\phi' \quad 2.3.36$$

by first putting  $n$  in terms of the wave number

$$n = \frac{i\alpha u_0 \delta}{\gamma} = \frac{3i\alpha Re}{2} \quad 2.3.37$$

and then

$$\begin{aligned} p &= n - Cn + 2\alpha^2; & q &= -n; \\ r &= 2n - \alpha^2n + C\alpha^2n - \alpha^4; & s^2 &= \alpha^2n \end{aligned} \quad 2.3.38$$

A solution was obtained by expressing the function of  $\phi$  in the form

$$\phi(y) = \sum_{N=0}^{\infty} A_N y^N \quad 2.3.39$$

then this series constituted a solution of 2.3.36 when the coefficients

$A_N$  were made to satisfy the recurrence relation

$$\begin{aligned} N(N-1)(N-2)(N-3)A_N &= (N-2)(N-3)pA_{N-2} + \\ & \left[ r + (N-4)(N-5)q \right] A_{N-4} + s^2 A_{N-6} \end{aligned} \quad 2.3.40$$

for  $N > 3$ . A third order approximation to the series solution 2.3.39 as calculated by means of 2.3.40, and expressing the boundary equations in terms of the coefficients of  $A_N$  yielded for real  $C$ ,

$$C = 2(1 - \alpha^2 + \frac{11\alpha^4}{6} + 0.0077531\alpha^2 Re^2 - 3.3555556\alpha^6) \quad 2.3.41$$

The imaginary part yielded the relation between Reynolds number and for neutral stability and was expressed as

$$\begin{aligned} \frac{4\alpha^2}{3^{3/2} Re^{3/2}} + \frac{4 \cot \theta}{3Re} - \frac{8}{5} + 5.5289142\alpha^2 \\ - 0.0000639\alpha^2 Re^2 - 14.6352952\alpha^4 = 0 \end{aligned} \quad 2.3.42$$

where  $\zeta$  is defined by

$$\zeta = \Gamma (g \sin \theta)^{-\frac{1}{3}} \nu^{\frac{2}{3}} \tag{2.3.43}$$

and  $\Gamma$  is the kinematic surface tension.

A simplified treatment was given for long waves, where the wave number approaches zero, then  $C$  reduces to 2 the same value as that obtained by Kapitza employing a different form of argument. The optimum value of the wave number was found to be

$$\alpha_m^2 = \frac{45 u_0^2}{5 \Gamma} \tag{2.3.44}$$

where  $u_0$  is the mean velocity. In terms of Reynolds number

$$\alpha_m = 1.12 (\nu^{\frac{2}{3}} g^{\frac{1}{6}} \Gamma^{-\frac{1}{2}}) Re^{\frac{2}{3}} \tag{2.3.45}$$

The corresponding wavelength for the most unstable wave number was given by

$$\alpha_m = 3.11 (\Gamma^{\frac{1}{2}} g^{-\frac{1}{2}}) Re^{-\frac{1}{2}} \tag{2.3.46}$$

It must be remembered that this analysis assumes that  $\alpha$  is fairly small.

Belkin et al (20) obtained experimental data about wave formation on the surface of a smooth vertical rod. The range of Reynolds number investigated was 200 to 30,000. The film thickness was estimated by taking a photograph of the dry and wetted rod from the same position. Then the difference in area is related to the film thickness by

$$\text{Area wet} - \text{Area dry} = 2.5L \tag{2.3.47}$$

where  $L$  was the length of the wetted rod on the photograph.

Bushmanov (21) considered the flow of a liquid layer on a vertical wall under the influence of gravitation. The stability of the plane flow preceding wave formation was the starting point of the investigation. The solution was executed on similar lines to that of Yih except that the Sommerfeld-Orr equation was expressed in a different form, and solved by a series approximation continued only as far as

the fifth term. The analysis yields a critical Reynolds number given by

$$Re = \frac{8}{3} \frac{g \delta^3}{2\nu^2} \quad , \quad 2.3.48$$

for water a value of 72 was computed. Bushmanov argued that as the flowrate was increased no waves appeared at  $Re = 22$ , which was the value of critical  $Re$  predicted by Kapitsa, but at  $Re = 72$  waves would run upward at 15.1 cm/s. This would occur in the absence of any artificial perturbations. The waves occurring at  $Re = 72$  were not stable and only existed for a short time, however, they did disturb the plane flow so that waves running downward could appear and stable wave patterns could be established. Then wave flow would persist as the flowrate was decreased to  $Re = 22$ , when plane flow was again established. A more rigorous treatment of Kapitsa's equation was attempted in lieu of equation 2.3.11 Bushmanov obtained

$$\frac{\partial v_x}{\partial t} + v_x \frac{\partial v_x}{\partial x} + v_y \frac{\partial v_x}{\partial y} = -\frac{1}{\rho} \frac{\partial p}{\partial x} + \nu \nabla^2 v_x \quad 2.3.49$$

The solution of which yielded the relationship for the critical Reynolds number

$$Re = 7.32 \left( \frac{\sigma \delta \rho}{g \mu^4} \right)^{\frac{1}{11}} \quad 2.3.50$$

Thus he disagrees with Kapitsa as to the lower limit of stable wave flow.

Dukler (22) rejected theories that looked for a transitional  $Re$  applicable to the whole film and proposed a model which assumed a liquid film could be partially laminar, close to the solid surface, and partially turbulent permitting both types of flow to be taken into account. As in Dukler and Bergelin's work (19) use was made of universal velocity profiles. Solution of the equations was carried out and the results were then employed in his heat transfer analysis which will be described in a later section. In a further paper (23) Dukler

compared theoretical and experimental film thicknesses which showed good agreement with other workers in the field.

Binnie (24) completed further experimental work on the flow of laminar travelling waves on the surface of an open water channel inclined downwards over a range of 1 to  $2\frac{3}{4}$  degrees. The Reynolds number at their first appearance was observed, and measurements were obtained of their velocities and wavelengths. Correction had to be made to the results to allow for surface tension effects at the side walls, since waves observed did not extend right across the channel. Laminar wave inception was found to occur experimentally at Reynolds numbers, 29, 37, and 56 the theoretical minimums being 17, 24, and 48 for 1, 2 and  $2\frac{3}{4}$  degree slopes respectively.

Brooke-Benjamin's next contribution (25) extended his earlier work to cover the case of three dimensional stability. He assumed that a wave comprised a general harmonic of three dimensional small disturbances, and introduced a double Fourier integral to represent a bounded disturbance whose initial distribution over the free surface was arbitrarily prescribed. The theoretical analysis postulated that disturbances were effectively confined within an expanding elliptical region and carried downstream at a group mean velocity. Experimental observation, by photography, of the phenomena in question showed that the approximate theory could be applied. In the experimental arrangement a thin film was formed on an inclined sheet of glass which constituted the base of the channel. The results obtained from the above tended to confirm the earlier results.

A further paper (26) by Yih admitted that the numerical computational solution produced in his earlier paper (16) was incorrect and that Brooke-Benjamin's analytical solution (19) gave values for wave

speed which were more in accord with Dinnie's experiments (17). The Sommerfeld-Orr equation 2.3.33 was again the basis of the theory formed by the perturbation technique and a set of boundary conditions in a similar form. An initial solution for long waves was made by putting the wave number,  $\alpha$ , equal to zero directly which yielded the result that the ratio of the wave velocity to the average film velocity or dimensionless velocity,  $C$ , equalled 3. This was 1.5 times greater than that derived by Brooke-Benjamin. However, this was because the latter used the film surface velocity as the reference velocity whereas this paper by Yih used the film average velocity of the primary flow. The two results were thus actually in agreement. The question of large values of the wave number were discussed. The pertinent result obtained was that viscosity could have a de-stabilising effect on the flow. Shear at the free surface and variable surface tension effects were also briefly discussed.

An experimental study of film thickness and velocity in films on vertical surfaces was carried out by Portalski (27,28). The investigations considered the film characteristics of thirteen liquids, employing a hold-up technique to obtain average film thickness measurements. These film thickness measurements were compared with average film thicknesses computed from theories by Kapitza (9), Musselt (2) and Dukler and Bergelin (13). In all the cases considered the theory by Kapitza approximated to the experimental results better than Musselt's theory in the region for which these theories were intended. On the other hand both these theories compared unfavourably with the universal velocity treatment of Dukler and Bergelin. The latter's theory led to the prediction of the average film thicknesses within fair agreement to those experimentally determined. In the second paper (28) Portalski measured the film surface velocity and the mean stream

velocity. He found that in laminar flow and in wavy flow, before the onset of turbulence, that the ratio of maximum velocity to mean stream velocity was very nearly equal to the value of 1.5. As the flowrate was increased and turbulence occurred the above ratio decreased until a steady value of 1.15 was reached for fully turbulent flow.

Fulford (29) compiled a very comprehensive survey of experimental theoretical work concerned with film flow up to 1965. He outlines the contradictions occurring in the literature between the various theoretical solutions and experimental techniques.

The next modification to the Kapitza-Bushmanov equations was made by Massot et al (30) who included terms neglected in the earlier work. The term  $\delta^2 v/dx^2$  was included and the variation of film thickness in the 'x' direction was taken into account. The Navier-Stokes equation became

$$\begin{aligned} \frac{\partial v_x}{\partial t} + v_x \frac{\partial v_x}{\partial x} + v_y \frac{\partial v_x}{\partial y} &= \frac{\partial^2 v_x}{\partial x^2} + \frac{\partial^2 v_x}{\partial y^2} + g - \frac{1}{\rho} \frac{\partial p}{\partial x} \\ \frac{\partial v_y}{\partial t} + v_x \frac{\partial v_y}{\partial x} + v_y \frac{\partial v_y}{\partial y} &= \frac{\partial^2 v_y}{\partial x^2} + \frac{\partial^2 v_y}{\partial y^2} + g - \frac{1}{\rho} \frac{\partial p}{\partial y} \end{aligned} \quad 2.3.51$$

These equations were solved by a method similar to Kapitza's except that the results were expressed in terms of Weber number as the governing dimensionless group. This treatment included as special cases the low Weber number analyses of Yih, Benjamin and Kapitza as well as the high Weber number theory of Ishihara, Iwagaki and Iwasa (31). Agreement with experimental observation was improved over that obtained from previous analyses.

Further work by Yih (32) considered steady flow between two parallel plates, one fixed and one moving in its own plane (couette flow) showing that a variation of viscosity in a fluid would cause instability. Anshus and Acrivos (33) examined more closely the use

of surface active agents to reduce surface tension, and showed that the growth rate of waves decreased, accompanied by an increase in wavelength in falling film systems.

A further treatment by Lee (34) attempted a more rigorous theoretical solution of the equations by Kapitsa. The solution was the same as that of Kapitsa but the equilibrium wave amplitude was deduced entirely from the dynamic equations by investigating the non-linear effect on the isolated class of basic wave motions pertaining to the linear system. In the analysis  $\phi$  was given a periodic solution of the form

$$\phi(x) = A \sin \alpha x \quad 2.3.52$$

where the wave number was given by  $\alpha = (3 We v^2)^{\frac{1}{2}}$ , which differed from Kapitsa's value of  $\alpha = (3.6 We v^2)^{\frac{1}{2}}$ . The following expressions for  $v$  and  $C$  were obtained

$$v = \frac{g \delta_0^2}{3\gamma} \left(1 + \frac{3A}{2}\right) \quad 2.3.53$$

$$C = 3v(1 + 3A/2)^{-1} \quad 2.3.54$$

The pertinent conclusions drawn from the whole analysis were that the equilibrium wave amplitude was linearly dependent on the film thickness  $\delta_0$  so that the wave amplitude decreased uniformly to zero as the flow-rate became small. The values for the wave amplitude  $A$  of equation 2.3.52, and the Reynolds number for equilibrium stability were given in the following form

$$A = (3 We)^{\frac{1}{2}} \quad 2.3.55$$

$$Re = 3^{\frac{1}{5}} \left[ \frac{\sigma^3 \rho}{g \mu^4} \right]^{\frac{1}{5}} \cdot We^{\frac{5}{3}} \quad 2.3.56$$

Again the Weber number ( $We$ ) was used as the dominant non-dimensional group. As Brooke-Benjamin predicted vertical film flow was found to be unstable at all practical Reynolds number.

A paper by Gollan and Sideman (35) was an extension of Massot et al's solution for a steady periodic wave motion. In this case, however, the normal stress induced by viscosity was included in the boundary conditions and the Navier-Stokes equations were solved by utilising the controlling interfacial velocities rather than by averaging the equations. Equation 2.3.14 was obtained in the form

$$\frac{3}{2} \frac{\partial \bar{u}}{\partial t} + \frac{9\bar{u}}{4} \frac{\partial \bar{u}}{\partial x} = \frac{9}{2} \frac{\partial^2 \bar{u}}{\partial x^2} + \frac{\sigma}{\rho} \frac{\partial^3 \zeta}{\partial x^3} - 3 \frac{\bar{u}}{\zeta^2} + g \sin \theta \quad 2.3.57$$

At this point the film thickness was expressed in terms of the average film thickness  $\zeta_0$  and the local amplitude  $\phi$ , that is

$$\zeta = \zeta_0(1 + \phi) \quad 2.3.58$$

also for  $\phi < 1$ ,  $\bar{u}$  was approximated to

$$\bar{u} \approx U_0 + (C' - U_0)\phi + (C' - U_0)\phi^2 \quad 2.3.59$$

where  $C'$  is the phase velocity of the waves and  $U_0$  the average velocity at the film thickness  $\zeta_0$ . This yielded a result in non-dimensional wave velocity,  $a = C'/U_0$

$$We = \frac{4}{9} \frac{(3 - a)}{(a - 1)(a^2 - 5/2a + 3/2)} \quad 2.3.60$$

$$= \frac{6\pi \zeta_0 (a - 1)^{1/2}}{(3/2(3 - a))^{3/2}} \quad 2.3.61$$

this particular analysis fitted the experimental data better than other analyses up until this time.

A recent thesis by Holgate (36) analysed film flow on the surface of a stationary  $60^\circ$  right cone and derived a modified Sommerfeld-Orr equation using a perturbation technique, which, in-conjunction with boundary conditions in a similar form, was solved for small wave numbers to give a stability criterion. The coordinate system defined the X direction parallel to the cone generator, Y direction perpendicular to the cone generator and  $\theta$  the angular direction traced out by the cone generator. For the undisturbed flow the velocity profile

was given by

$$U = \frac{3}{2} (2y - y^2) \quad 2.3.62$$

the variation in mean film thickness with distance down the cone is

$$\delta = \left( \frac{3 \gamma Q}{\pi g \sin 2\beta} \right)^{\frac{1}{3}} \frac{1}{X^{\frac{1}{3}}} \quad 2.3.63$$

the variation of mean velocity with distance down the cone is

$$\bar{U} = \left( \frac{g \cos \beta Q^2}{12 \pi^2 \gamma \sin^2 \beta} \right)^{\frac{1}{3}} \frac{1}{X^{\frac{2}{3}}} \quad 2.3.64$$

Consequently the variation in Reynolds number with distance down the cone is given by

$$Re = \frac{Q}{2\pi \gamma \sin \beta} \cdot \frac{1}{X} \quad 2.3.65$$

and the Froude number, given by

$$Fr = \left( \frac{1}{3} Re \cos \beta \right)^{\frac{1}{2}} \quad 2.3.66$$

displayed a similar decrease with passage down the surface of the cone.

For the disturbed flow the governing equations were solved and produced an instability criterion in which the flow will be unstable for

$$Re > \frac{\tan \beta + 7/4x}{\frac{9x}{8} \tan \beta + \frac{9}{4} + \frac{2 \cot \beta}{x} - \frac{\alpha^2 S}{3}} \quad 2.3.67$$

where  $x$  is the non-dimensional distance in the  $X$  direction and  $S$  is the reciprocal of the Weber number which was shown to be small. For non-extreme values of  $\beta$  and large values of  $x$  the criterion reduced to

$$Re > 8/9x \quad 2.3.68$$

which is small and thus in agreement with Brooke-Benjamin's conclusion for the inclined surface.

The experimental study of the behaviour of a liquid film on the surface of the cone showed that the mean film thickness was a function of Reynolds number only

$$\delta_{\text{mean}} = 0.0685 \text{ Re}^{\frac{1}{3}} \quad 2.3.69$$

Measurements of film thickness were made using a movable capacitance probe, discussed fully in Appendix A. The mean film thickness was found to be less than that of the undisturbed laminar film by some 7%, an estimate which accords with Kapitza's theoretical prediction. The range of the constant flows studied was from 10 to 100 gallons per hour, the mean film thickness measured at 460 mm. diameter were 0.145 mm. and 0.315 mm. respectively. The amplitude, wave speed and wavelength of the disturbances were measured at different stations down the cone generator. The wave speed was found to be greater than 2.4 times the mean film velocity, as proposed by Kapitza, but still less than the long wave speed of 3 times the mean film velocity deduced by Brooke-Benjamin.

#### 2.4 Condensate flow on stationary surfaces

The development of the present day theories and the predictions of heat transfer rates associated with laminar film condensation had its origins in the analysis presented by Nusselt (2) in 1916. In the previous section the velocity distribution in the film has been documented. During the condensation process filmwise conditions will only occur if the surface is wettable and once the film is established the energy transfer is dependent on the thickness of this film. The analysis was developed by considering an elemental strip in the fluid and equating the energy flow across the film, from the vapour to the solid surface, to the condensation rate through the specific enthalpy of the condensation. To simplify the mathematics the following assumptions were made

- (i) The film was in laminar flow along a smooth isothermal

surface under the action of gravity.

- (ii) Energy flow across the film was by Fourier conduction only.
- (iii) Fluid accelerations and inertia effects were neglected.
- (iv) Sub-cooling of the condensate was neglected.
- (v) The liquid-vapour interface temperature was assumed to be that of the saturation temperature of the vapour.
- (vi) The vapour was relatively stationary with respect to the surface and vapour drag was non-existent.
- (vii) The physical properties of the condensate were evaluated at mean film temperature.
- (viii) Non-condensable gases were not present in the vapour.

Then the energy flow through the film was given by

$$dq = h_{fg}.dm = \frac{k \Delta T dx}{\delta} \quad 2.4.1$$

where  $dm$  was given by

$$dm = \rho.d(\delta.V_{av}) \quad 2.4.2$$

$V_{av}$  is given in equation 2.3.5. Substituting this value into equation 2.4.2 one obtains

$$h_{fg}.dm = \frac{\rho^2}{\mu} \cdot \delta^2 d\delta \cdot h_{fg} \cdot g \cdot \sin \theta \quad 2.4.3$$

Equating 2.4.1 and 2.4.3, integrating the result and substituting the boundary condition of  $\delta=0$  at  $x=0$ , produced

$$\delta = \sqrt[4]{\frac{4 \mu k \Delta T x}{\rho^2 h_{fg} g \sin \theta}} \quad 2.4.4$$

showing that the thickness of the film increased only with the fourth root of  $x$ . The heat transfer coefficient was expressed as

$$h = \frac{k}{\delta} \quad 2.4.5$$

Substituting equation 2.4.4 for  $\delta$  yielded the result

$$h = \sqrt[4]{\frac{k^3 \rho^2 h_{fg} g \sin \theta}{4 \mu \Delta T x}} \quad 2.4.6$$

This coefficient applies to position  $x$ . A mean coefficient of heat transfer  $hm$  may be defined by

$$hm = \frac{4}{3} \sqrt[4]{\frac{k^3 \rho^2 \cdot h_{fg} \cdot g \cdot \sin \theta}{4 \mu H \Delta T}} \quad 2.4.7$$

where 'H' is the vertical height of the condensing surface. For comparison of heat transfer coefficients the non-dimensional group

$$Nu = \frac{hm H}{k} \quad 2.4.8$$

where  $Nu$ , known as the Nusselt number, is often used in energy transfer calculations and is a measure of the rate of heat transfer by convection.

Subsequently many modifications of the above analysis have appeared each one relaxing further the restrictive assumptions imposed in Nusselt's original treatment, but these did not begin until the 1930's. During the intervening years experimental work by Othmer (37), Kirkbride (6), and others confirmed that heat transfer coefficients were up to 1.28 times the Nusselt values.

Colburn (91) suggested a semi-theoretical relationship to account for turbulent flow in the film. A correlation between the turbulent friction factor and the heat transfer factor 'j' was used to derive the following equation for the mean heat transfer coefficient in the turbulent region of the film of condensate

$$\frac{hm}{k} \left( \frac{g \sin \theta}{g} \right)^{\frac{1}{3}} = \frac{Re}{\frac{22}{Pr^{\frac{1}{4}}} Re - 364 + 12,800} \quad 2.4.9$$

Colburn's analysis assumed a transitional Reynolds number of 1600 and the equation predicted that the mean heat transfer coefficient increased with both Reynolds number and Prandtl number in the turbulent region.

Experimental work of Carpenter and Colburn (82) investigated the effect of vapour velocity on the condensation of steam, methanol and ethanol on the inside of a vertical tube. They found that as the vapour

velocity increased the heat transfer coefficient became larger at lower Reynolds numbers and recommended the equation

$$h_m = 0.065 \left( \frac{c_p \rho k f}{2\mu \rho_{\text{vap}}} \right)^{\frac{1}{2}} G_m \quad 2.4.10$$

where 'G<sub>m</sub>' was the mass flow per unit time per unit surface area and 'f' the fanning friction for the vapour. It was then postulated that the increased vapour velocity caused the film to become turbulent at Reynolds numbers less than 2000.

Nusselt in his analysis neglected the effect of sub-cooling of the condensate. Both Bromley (40) and Rohsenow (41) investigated this effect and concluded that the heat capacity of the condensate could be taken into account by a simple modification of the Nusselt equations. This modification took the form of replacing the latent energy, 'h<sub>fg</sub>', by 'h<sub>fg</sub> + K.c<sub>p</sub>.ΔT'. The constant 'K' was calculated by Bromley to be 0.375 for laminar flow assuming a linear temperature across the condensate layer. Rohsenow's value for 'K' was 0.68, but this analysis assumes a parabolic temperature profile, to account for the addition of liquid at saturation temperature to the outer layers. A further paper by Rohsenow et al (42) considered the effects of vapour velocity on laminar and turbulent film condensation. The analysis assumed the existence of the Prandtl-Von Karman 'universal velocity profile' for turbulent flow. The values of heat transfer coefficients predicted agreed with those from the semi-empirical formula of Carpenter and Colburn in the range of Prandtl numbers from 2 to 5.

Labuntsov (43,44) studied both theoretically and experimentally the effect of convective and inertial terms in laminar and turbulent condensation and received empirical support by generalising a large quantity of experimental data by other authors. From these observations and calculations the proposed formula for heat transfer

coefficient was

$$\frac{h}{hn} = \psi \epsilon_t \epsilon_v \quad 2.4.11$$

' $hn$ ' was the coefficient of heat transfer calculated according to Nusselt's formula, all the physical characteristics of the condensate being referred to the saturation temperature and

$\psi$  was a correction for the effect of convective heat transfer and the inertial forces. In the region  $h_{fg}/cp\Delta T \geq 5$ , and  $Pr = 1$  then

$$\psi = 1$$

$\epsilon_t$  was a correction factor for the temperature relationship of the physical characteristics of the condensate, equal to

$$\epsilon_t = \left( \frac{k_w^3 \mu_s}{k_s^3 \mu_w} \right)^{\frac{1}{4}} \quad 2.4.12$$

$\epsilon_v$  was a correction for the character of flow of the condensate and equals

$$\epsilon_v = C_1 (K_f^{\frac{1}{n}} Re)^m \quad 2.4.13$$

$$\text{where } K_f = \frac{\sigma^3 \rho}{\mu^4 g}$$

The factor ' $K_f$ ' has already been shown by Kapitza, in 2.3.20, to be one which may be used to predict the onset of rippling. For many materials, water, ammonia and freon 12 for example,  $K_f$  values do not differ greatly. Thus for a first approximation the variations in  $K_f^{\frac{1}{n}}$  may be neglected i.e.

$$\epsilon_v = C Re^m \quad 2.4.14$$

Values of ' $C$ ' and ' $m$ ' were estimated from averaged data relating to water vapour condensation giving

$$\epsilon_v = 0.95 Re^{0.04} \quad 2.4.15$$

and  $Re$  was given in this instance by

$$Re = \frac{4 hn \Delta T L_c}{h_{fg} \rho \psi} \quad 2.4.16$$

where ' $L_c$ ' was the length of the condensing surface.

The condensation of vapours on a vertical plate, assuming laminar filmwise conditions existed and velocities in the vapour have no effect on the condensate film, were analysed by Sparrow and Gregg (45) using the mathematical techniques of boundary layer theory. The equations for conservation of mass, momentum, and energy were simplified, respectively, to

$$\frac{\partial u}{\partial x} + \frac{\partial v}{\partial y} = 0 \quad 2.4.17$$

$$\rho \left( u \frac{\partial u}{\partial x} + v \frac{\partial u}{\partial y} \right) = \varepsilon (\rho - \rho_v) + \mu \frac{\partial^2 u}{\partial y^2} \quad 2.4.18$$

$$\rho \text{ cp} \left( u \frac{\partial T}{\partial x} + v \frac{\partial T}{\partial y} \right) = \frac{\partial^2 T}{\partial y^2} \quad 2.4.19$$

By assuming a stream function  $\psi$  defined by

$$u = \frac{\partial \psi}{\partial y}, \quad v = -\frac{\partial \psi}{\partial x} \quad 2.4.20$$

and a new independent variable,  $\eta$ , together with dependent variables  $F(\eta)$  and  $\theta(\eta)$ , ordinary differential equations were obtained. An overall energy balance was evoked to relate the independent variable to the physical quantities. These quantities are defined by, respectively

$$\eta = \left[ \frac{\varepsilon \text{ cp} (\rho - \rho_v)}{4 \nu k} \right]^{\frac{1}{2}} \frac{x_1}{x^{\frac{1}{2}}}, \quad F(\eta) = \frac{\psi \rho \text{ cp}}{4x^{\frac{3}{2}} k}, \quad 2.4.21$$

$$\theta(\eta) = \frac{T - T_{\text{sat}}}{T_w - T_{\text{sat}}}, \quad \frac{\text{cp} \Delta T}{h_{fg}} = -\frac{3 F(\eta_s)}{\theta'(\eta_s)}$$

where ' $F(\eta_s)$ ' and ' $\theta'(\eta_s)$ ' are values when  $\eta = (\eta_s)$

The ordinary differential equations evolved were solved numerically for the parameters  $\text{cp} \Delta T / h_{fg}$  and Prandtl number. The solution showed that inclusion of inertial terms had little effect on the heat transfer for Prandtl numbers greater than ten, and that film thickness was still found to be proportional to  $x^{\frac{1}{2}}$ . It is shown that the temperature profile through the film varies as  $\text{cp} \Delta T / h_{fg}$  and that for small values of this parameter the form of the profile is essentially a straight line.

Dukler (46) presented a more ambitious approach of actually solving

the velocity profile using the eddy viscosity expressions of Deissler (47) and Von Karman. The solution was formulated assuming that the eddy viscosity  $\mathcal{E}$  and eddy thermal conductivity  $\mathcal{E}_H$  were equal. The basic equations for any position in the film were

$$\gamma = \frac{1}{\mathcal{E}_c} (\mu_L + \mathcal{E} \rho_L) \frac{dV}{dy} \quad 2.4.22$$

$$Re_{LX} = \frac{4 \rho_L}{\mu_L} \int_0^{\delta} v \cdot dy \quad 2.4.23$$

$$q = -(k_L + \mathcal{E}_H c_{pL} \rho_L) \frac{dt}{dy} \quad 2.4.24$$

The equations were solved by computer and graphical relationships which allowed the determination of the velocity distribution, the film thickness, local heat transfer coefficient and average coefficient over an entire condenser tube were presented for various interfacial shears. A correction to this approach was applied by Lec(48) who pointed out that in the Von Karman range the molecular thermal conductivity compared to the eddy conductivity was not negligible for low Prandtl numbers. The correction showed that heat transfer coefficients were not as low as those predicted by Dukler at small values of Prandtl number.

Heat transfer rates in laminar film condensation on the underside of horizontal and inclined surfaces were predicted by Gerstman and Griffiths (49). An experimental investigation showed that when the condensing surface was in a horizontal position condensing Freon-113 formed in discrete drops. At slight angles of inclination there were three regimes of flow. Near the leading edge was smooth waveless flow, next a region of longitudinal ridges in the direction of flow which as they increased in amplitude shed drops from the crests. At medium angles of inclination up to the vertical roll waves were present. The theoretical solution assumed quasi-steady flow of a bounded instability

where condensate removal was by steady flow into a plane sink located at the centre line of each ridge. The maximum film thickness was then assumed to be a function of the shortest unstable wavelength of the Taylor instability (11) :-

$$\delta_{max} = \left( \frac{\sigma}{g \cos \theta (\rho - \rho_v)} \right)^{\frac{1}{2}} \quad 2.4.25$$

The longitudinal flow along the ridge was assumed zero. The assumption of the plane sink reduced the problem to a two dimensional one which could be defined by

$$\frac{\partial p}{\partial x} = \mu \frac{\partial^2 v_x}{\partial z^2} \quad 2.4.26$$

$$p = p_{sat} - (\rho - \rho_v) g \cos \theta (\delta - z) - \frac{\partial^2 \delta}{\partial x^2} \quad 2.4.27$$

Continuity

$$\frac{\partial v_x}{\partial x} + \frac{\partial v_z}{\partial z} = 0 \quad 2.4.28$$

and

$$\frac{Q}{A} = \frac{k \Delta T}{\delta} \quad 2.4.29$$

where the 'x' direction was at right angles to that of the longitudinal ridge and 'z' direction perpendicular to the solid surface. Introducing non-dimensional terms and manipulating the governing equations produced a fourth order non-linear equation. The numerical solution of this equation, for various values of the controlling non-dimensional group, predicted wavelength, maximum film thickness ratio, Nusselt number and Rayleigh number. The Nusselt number was defined as

$$Nu = \frac{h}{k} \left( \frac{\sigma}{g(\rho - \rho_v) \cos \theta} \right)^{\frac{1}{2}} \quad 2.4.30$$

and the Rayleigh number as

$$Ra = \frac{g \cos \theta (\rho - \rho_v) h \sigma g}{k \mu \Delta T} \left( \frac{\sigma}{g(\rho - \rho_v) \cos \theta} \right)^{\frac{3}{2}} \quad 2.4.31$$

The experimental results were correlated in terms of these two

groups and theoretically may be expressed as

$$\bar{Nu} = \frac{0.9 (Ra)^{\frac{1}{6}}}{(1 + 1.1(Ra)^{-\frac{1}{6}})} \quad 2.4.32$$

if the Rayleigh number is greater than  $10^6$ . A similar solution assuming cylindrical symmetry as in the ridge analysis, was carried out for horizontal surfaces yielding

$$\begin{aligned} \bar{Nu} &= 0.81 (Ra)^{0.193} ; & 10^{10} > Ra > 10^8 \\ \bar{Nu} &= 0.69 (Ra)^{0.2} ; & 10^8 > Ra > 10^6 \end{aligned} \quad 2.4.33$$

Measured values of the heat transfer coefficients were in quite good agreement with values predicted by preceding equations.

Kuiken (50), although strictly speaking not a worker in the field of condensation, is worth mention since he has produced a theory using almost inviscid flows which allows for fluid addition of increasing amounts as one progresses downstream. Fluid enters the film at the outer edge by some mechanism, an example of which is condensation. The rate at which mass addition occurred was governed by some power law. The existence of a viscous boundary layer was also acknowledged which had at its outer edge a velocity  $u = \sqrt{2 g x}$ , whilst at the solid boundary  $u = 0$ .

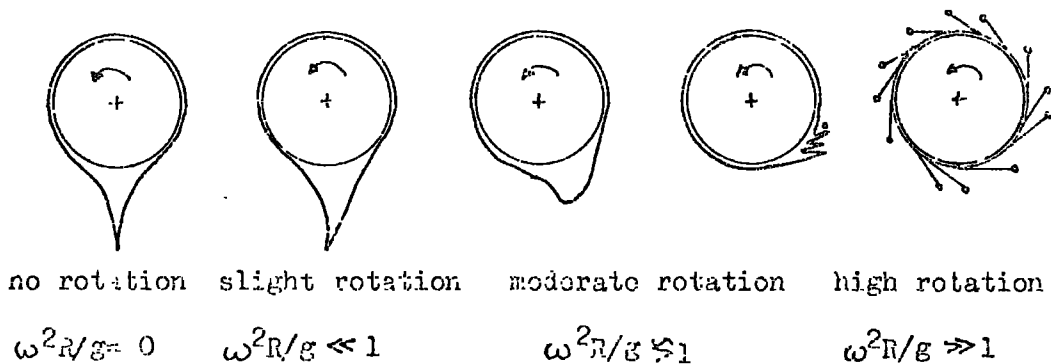
The information imparted in the preceding account is by no means a comprehensive one but does convey the various methods used in the development of condensation theory to define the phenomena occurring during film flow of condensate on stationary surfaces up to the present day.

## 2.5 Condensate flow on rotating surfaces.

### 2.5.1 Condensation and heat transfer on rotating cylindrical bodies.

One of the earlier studies of the transfer of energy to a rotating

surfaces, by condensing steam vapour, was carried out by Yeh (51). He examined the effect of surface speed on the heat transfer coefficients during filmwise condensation on a 0.0254 m diameter cylinder, rotating about its horizontal axis. Observation of the condensate surface, using high speed photography, showed that there were three phases of condensate flow. The first phase was a true film phase which existed up to 300 r.p.m. where the centrifugal force was not sufficient to throw off drops. The film was dragged round the cylinder in the direction of rotation and the drainage point was displaced in this direction from the downwards vertical where it would have occurred in the absence of rotation. Above 300 r.p.m. the centrifugal action becomes greater than the gravitational forces. At 554 r.p.m. some of the film on the surface began to break up and be thrown off in drops, initiated from the bottom quadrant on the leading side. Further increases of speed beyond 700 r.p.m. showed drops being shed almost tangentially. The sketches below indicate the general surface contours of the liquid film at varying speeds



The latter action continued up to a speed of 1500 r.p.m. at which point further increases in speed resulted in a fall in heat transfer coefficients. Photographs in this region showed that drops became pear shaped and tended to form streaks on the condensate surface. Vapour drag was suggested as the cause for the fall in heat transfer coef-

ficients but doubt has been cast on Yeh's equipment which had a faulty mechanical seal and was suspected of leaking air. The experimental data was presented in the form of a Nusselt versus Weber number plot

$$\text{Nu} = \frac{h D}{2k} \quad , \quad \text{We} = \frac{\rho D^3 \omega^2}{4 \sigma} \quad 2.5.1$$

A theoretical study of the drop size compared very well with measured drop size. The equation proposed for the size of droplet produced was

$$r^2 = \frac{3 \sigma g}{\rho ((V^2/R)^2 - g^2)} \quad 2.5.2$$

where V is the surface speed and R the cylinder radius. By assuming that the centrifugal forces were balanced by gravitational forces plus surface tension effects, a mean film thickness was theoretically deduced. The mean film thickness, given by  $Y_m$ , is

$$Y_m = \frac{\sigma g}{\rho ((V^2)^2 - (Rg)^2)^{1/2}} \quad 2.5.3$$

An experimental study of methods of improving heat transfer from condensing steam was performed by Birt et al (52). Of particular interest were observations reported concerning condensation on the surface of rotating vertical cylinders, 0.152 m and 0.216 m diameter, with filmwise condensate flow. With increase of speed the heat transfer coefficients were found to increase. Examination of photographs of the condensate surface showed that at low rotational speeds a system of longitudinal ridges were formed. As the speed of rotation was increased the ridges became unstable and drops were discharged, beginning at lower regions of the vertical cylinder and gradually moving upwards as the speed of rotation was further increased. A simple balance of forces in the system, surface tension versus centrifugal action suggested that

$$\delta = \frac{\sigma}{\omega^2 r^2 \rho} \quad 2.5.4$$

where  $\delta$  is the film thickness.

A linear relationship between heat transfer coefficients and the centrifugal acceleration was predicted from experimental results.

An analytical and experimental study of pure steam vapour condensing on a horizontal, rotating cylinder, 0.0254 m diameter was also performed by Singer and Preckshot (53). Their aim was to explain the result obtained by Yeh and to present physical and analytical models. Before attempting the analysis of condensation on a rotating tube observations were made of the hydrodynamic character of a liquid film by spraying water on to such a tube. At rotational speeds greater than about 250 r.p.m., a definite pattern of axially-symmetric waves were observed, with liquid sprayed off from the wave crests. This speed corresponded to a value of  $\omega^2 R/g$  of approximately 2.6. Three regimes of flow were found to exist corresponding to those observed by Yeh during condensation. The overall problem was thus reduced to three sub-problems, with models proposed to describe the phenomena. These cases were

- (i) The cylinder is rotating slowly so that gravitational forces are dominant, but centrifugal forces play a perturbing role.
- (ii) The cylinder is rotating rapidly so that gravitational forces are negligible in comparison with centrifugal forces, and vapour drag is not important. The condensate exists as a film.
- (iii) Same as (ii) except that the condensate also exists as drops.

The conclusions drawn from this analysis were

- (i) at low speeds the condensate drained by gravity and a 20% decrease in condensation heat transfer coefficient with increase in speed was noted.
- (ii) at moderate speeds a continuous film existed, characterised by ridge like waves displaced circumferentially, on the

cylinder surface. The heat transfer coefficient then increased to three times that of the stationary value.

- (iii) at high rotational speed drops were seen to be thrown from the surface of the condensate and that the heat transfer coefficient was reduced to that of the stationary cylinder.

The results were presented in the same form as in Yeh's work with Nusselt number plotted against Weber number and showed the same tendency. A better correlation of the results was produced by plotting

$$\text{Nu} \left( \frac{g D^3 h_{fg} \rho}{\nu k \Delta T} \right)^{-\frac{1}{4}} = \text{Nu} \quad 2.5.5$$

versus Weber number. The decrease of Nusselt number at high Weber numbers was thought to be due to interfacial drag. Thus the heat transfer data could be correlated by the following expressions

$$\text{Nu} = 0.0137(\text{We})^{0.735} \quad , \quad 250 < \text{We} < 900 \quad 2.5.6$$

$$\text{Nu} = 27.206(\text{We})^{-0.385} \quad , \quad 900 < \text{We} < 17000 \quad 2.5.7$$

The beginning of a series of experiments concerned with rotating energy transfer, whilst condensing steam vapour, was initiated by Hoyle (54) who was interested in thermal stressing of steam turbine rotors and shafts. The investigation by Matthews (55) was concerned with condensation of steam on horizontal rotating cylinders whose sizes were 0.1 m, 0.2 m, 0.254 m diameter and up to rotational speeds of 1500 r.p.m. The theoretical approach assumed that the gravitational force in the equation proposed by Nusselt for condensation on a stationary horizontal cylinder with quiescent vapour,

$$h = 0.733 \left( \frac{k^3 \mu h_{fg} g}{\nu^2 D \Delta T} \right)^{\frac{1}{4}} \quad 2.5.8$$

could be replaced by the centrifugal acceleration and rearranged to be presented in a more usable form. The equation was expressed in the new terms

$$\frac{h}{k} = B \left( \frac{1}{2} \frac{\omega^2}{\nu^2} \right)^{\frac{1}{4}} \left( \frac{\text{Pr}}{\text{cp}} \frac{h_{fg}}{\Delta T} \right)^{\frac{1}{4}} \quad 2.5.9$$

where 'B' replaced the constant 0.733 in the Nusselt equation and depended on rotational effects, defined by

$$B = 1.19 \frac{h}{k} \left( \frac{\nu}{\omega} \right)^{\frac{1}{2}} \left( \frac{\text{cp} \Delta T}{\text{Pr} h_{fg}} \right)^{\frac{1}{4}} \quad 2.5.10$$

A factor 'E' was then introduced to take into account effects of rotor curvature on the heat transfer coefficient

$$E = B \left( \frac{a \rho D^2}{3 \sigma} \right)^{\frac{1}{6}} \left( \frac{\omega^2 R}{g} \right)^{\frac{1}{4}} \quad 2.5.11$$

where 'a' equals the fractional coverage of the rotor surface by protrusions which were observed on the rotor during hydrodynamic tests using water sprayed onto the surface. Photographs of the condensate surface on the rotating cylinder indicated that it flowed towards protrusions on the condensate layer from which it eventually left in the form of discrete drops. The size of the protrusions was reduced as the rotational speed was increased and they appeared to cover only some 5% of the rotor surface area at all test speeds. The investigation observed either continuous film or continuous film with protrusions which at high rotational speeds were thrown from the surface.

In published work by Hoyle and Matthews (56,57) the experimental data was plotted on the basis of Nusselt versus Weber number. The results show no decrease in Nusselt number as the Weber number increased as did those of Singer and Preckshot and Yeh. The recommended equation for the heat transfer coefficient was

$$h = 1.5 \left( D \sqrt{\frac{g}{\sigma}} \right)^{-0.19} \left( 1.9 - \frac{0.9}{1.095} \frac{\omega^2 D}{g} \right) \left( \frac{k^3 g \rho^2 \text{cp}}{D \mu} \right)^{\frac{1}{2}} \left( \frac{h_{fg}}{\text{cp} \Delta T} \right)^{\frac{1}{2}} \quad 2.5.12$$

In the second paper the behaviour of the drops, the variation of their maximum size with rotational speed, and their number per unit area

were the subject of study. It was noted that the measured diameters were in some cases as much as 1.5 times greater than those calculated from Yeh's formula. Also that the area covered by protrusions reach a maximum when the acceleration at the surface was twenty times the acceleration due to gravity.

Nicol and Gacesa (59) study the condensation of steam on a rotating vertical cylinder 0.0254 m diameter, up to a maximum rotational speed of 2700 r.p.m. When the results were plotted in terms of the pertinent parameters of Nusselt and Weber numbers, the Nusselt number was found to be constant for Weber numbers below 500, and above this the correlating equation was

$$Nu = 6.13 We^{0.496} \quad 2.5.13$$

A similar correlation was predicted by Singer and Prockshot at high rotational speeds whose model assumed the surface was covered with hemispherical drops, which formed the controlling heat transfer resistance, and showed that

$$Nu \propto We^{0.5} \quad 2.5.14$$

No direct observation of the condensate surface was attempted.

### 2.5.2 Condensation and heat transfer on rotating discs.

An analysis was made by Sparrow and Gregg (59) for the condensation of pure saturated vapours on the surface of a rotating disc which revolves about a vertical axis. The problem was formulated as an exact solution of the Navier-Stokes and energy equations in cylindrical coordinates. The equations expressing conservation of mass, momentum, and energy for an incompressible, constant property fluid were

$$\frac{1}{r} \frac{\partial}{\partial r} (r V_r) + \frac{1}{r} \frac{\partial V_\phi}{\partial \phi} + \frac{\partial V_z}{\partial z} = 0 \quad 2.5.15$$

$$\left. \begin{aligned} \rho \left( \frac{Dv_r}{Dt} - \frac{v_\phi^2}{r} \right) &= - \frac{\partial p}{\partial r} + \mu \left( \nabla^2 v_r - \frac{2}{r^2} \frac{\partial v_\phi}{\partial \phi} - \frac{v_r}{r^2} \right) \\ \rho \left( \frac{Dv_\phi}{Dt} + \frac{v_r v_\phi}{r} \right) &= - \frac{1}{r} \frac{\partial p}{\partial \phi} + \mu \left( \nabla^2 v_\phi + \frac{2}{r^2} \frac{\partial v_r}{\partial \phi} - \frac{v_\phi}{r^2} \right) \\ \rho \frac{Dv_z}{Dt} &= - \frac{\partial p}{\partial z} + \mu \nabla^2 v_z \end{aligned} \right\} \quad 2.5.16$$

$$\rho \text{cp} \cdot \frac{DT}{Dt} = k \nabla^2 T \quad 2.5.17$$

Similar to the laminar boundary layer theory of condensation, on a stationary surface, by Sparrow and Gregg a new independent variable and dependent variables were evolved to transform the above partial differentials to ordinary differentials. These were; new independent variable

$$\eta = \left( \frac{\omega}{\nu} \right)^{\frac{1}{2}} z \quad 2.5.18$$

and dependent variables

$$\begin{aligned} F(\eta) &= \frac{v_r}{r \omega}, \quad G(\eta) = \frac{v_\phi}{r \omega}, \quad H(\eta) = \frac{v_z}{(\omega \nu)^{\frac{1}{2}}}, \quad P(\eta) = \frac{p}{\mu \omega} \\ \Theta(\eta) &= \frac{T_{\text{sat}} - T}{T_{\text{sat}} - T_w} = \frac{T_{\text{sat}} - T}{\Delta T} \end{aligned} \quad 2.5.19$$

The ordinary differential equations obtained were then solved numerically assuming the following boundary conditions:

- (i) The effect of gravity was neglected.
- (ii) Shear stresses at the surface produced by drag were assumed zero.
- (iii) Fluid temperatures at the solid surface and the liquid-gas interface assume the wall and saturated vapour temperatures respectively.
- (iv) The radial and axial velocity components are zero at the disc surface.

The solution showed that energy convection and acceleration terms were negligible and that temperature distribution across the film was

almost linear for low Prandtl number and  $cp\Delta T/h_{fg}$ . The Nusselt number was defined by

$$Nu = \frac{h}{k} \left( \frac{\nu}{\omega} \right)^{\frac{1}{2}} \quad 2.5.20$$

and that for small values of  $cp\Delta T/h_{fg}$  all the results were represented by

$$Nu = 0.904 \left( \frac{Pr h_{fg}}{cp\Delta T} \right)^{\frac{1}{4}} \quad 2.5.21$$

The predicted film thickness was found to be uniform over the disc and varying with Prandtl number and  $cp\Delta T/h_{fg}$  values. The following relationship was derived

$$\delta \left( \frac{\omega}{\nu} \right)^{\frac{1}{2}} = 1.107 \left( \frac{cp\Delta T}{Pr h_{fg}} \right)^{\frac{1}{4}} \quad 2.5.22$$

For a given fluid and a fixed temperature difference

$$\delta \sim \omega^{-\frac{1}{2}} \quad 2.5.23$$

The boundary conditions presupposed that the condensate surface remained smooth. In practice this is rarely found to be the case.

An experimental analysis was carried out by Nandapurkar and Beatty (60) who examined the condensation of pure vapours, of methanol, ethanol and Freon-113, on the surface of a rotating, horizontal, water cooled disc, 0.127 m diameter. A flow pattern study was carried out by introducing a methanol-water solution of pontamine blue dye through a size-20 hypodermic needle onto the rotating plate while methanol was being condensed. The dye flow followed spoke like radial paths having a slight curvature backward from the direction of rotation. Slight but definite ripples parallel to the dye paths were observed but it was not possible to determine whether such ripples were present originally or produced by the introduction of the dye itself. The data from tests on all three vapours was correlated to within  $\pm 15\%$  with the equation

$$h = 1.1 \left( \frac{k^3 \rho^2 h_{fg} (120\pi)^2}{\mu \Delta T} \right)^{\frac{1}{4}} R^{0.425} \quad 2.5.24$$

Measured coefficients were about 20% less than those predicted by Sparrow and Gregg, equation 2.5.20, and they were shown to increase in proportion to the rotational velocity raised to the power 0.425 rather than to the power 0.5 as the theory requires. The lower coefficient was possibly accounted for by drag of vapour on the ripples observed.

The effect of vapour drag on rotating condensation was analysed by Sparrow and Gregg (61) to supplement their work on the condensation of pure vapours on a rotating disc. The problem was attacked by simultaneous solution of the equations of motion in liquid and vapour. The partial differential equations were reduced to ordinary differential equations, as in their work (59) reported previously, and solved numerically on a computer. The analysis predicted that with thinner films energy transfer was increased and that with thick films energy transfer was reduced. They concluded that the effect of vapour drag on the analytical prediction of heat transfer as given in reference (59) was not significant so that the deviation between theory and experimental work by Nandapurkar and Beatty must be attributed to other causes. The solution of the governing equations was modified by the addition of the ratio  $\left[ (\rho\mu)_l / (\rho\mu)_v \right]^{\frac{1}{2}}$  where l refers to the liquid state and v to the vapour state. The effect of this ratio, for values between 50 and 650 was found to be negligible except for either very thin or very thick films.

A further theoretical and experimental analysis of the condensation of pure steam vapour on a rotating disc was performed by Espig and Hoyle (62,63). The disc, which was made of copper, was 0.25 m diameter and rotated about an axis in the horizontal plane at speeds up to 2500 r.p.m. A solution for the film thickness was formulated assuming semi-parabolic distributions for radial and tangential velocities

$$v_r = U \left[ 2\left(\frac{z}{\delta}\right) - \left(\frac{z}{\delta}\right)^2 \right] \quad 2.5.25$$

$$v = r\omega - v \left[ 2\left(\frac{z}{\delta}\right) - \left(\frac{z}{\delta}\right)^2 \right] \quad 2.5.26$$

which were substituted into equations expressing conservation of mass and momentum. For thin laminar films of condensate their analysis also gave

$$h = 0.903 \left( \frac{k^3 \rho^2 \omega^2 h_{fg}}{\mu \Delta T} \right)^{\frac{1}{3}} \quad 2.5.27$$

and for the film thickness they deduced that

$$\delta^4 = \frac{1.5 K^2 \left( \frac{\nu}{k\omega} \right) \left( \frac{3}{5} \frac{k\omega}{\nu} + 1 \right) \left( \frac{4}{5} \frac{k\omega}{\nu} + 1 \right)^2}{1 + \frac{4}{15} \frac{k\omega}{\nu} + \frac{8}{75} \left( \frac{k\omega}{\nu} \right)^2} \quad 2.5.28$$

where

$$K = \frac{k \Delta T}{h_{fg} (1 + 0.375 c_p \Delta T / h_{fg})} \quad 2.5.29$$

These computations were carried for an isothermal surface and assumed streamline, non-wavy laminar flow.

The experimental data was obtained by measuring the inner and outer wall temperatures of the disc, thermocouples were held in grooves in the surfaces and were brought out of the rig through a slip-ring unit. The experimental heat transfer coefficients were found to be up to twice the value predicted by equation 2.5.27 and **experimental** was related to the theoretical one by the relationship

$$\frac{h_{\text{exp}}}{h} = 113 K^{-0.415} \Delta T^{-0.6} \quad 2.5.30$$

The surface of the condensate was found to support wave like disturbances and it was their effect which gave rise to the higher heat transfer coefficients.

Espig and Hoyle (64) investigated flow in films of water on a rotating disc to determine whether wave motion gave mean film thickness measurements of lower values than those predicted by laminar flow film theory analogous to those observed in studies of liquids flowing down

vertical surfaces. Nusselt's equation for the mean film thickness was written in the form

$$\delta \left( \frac{g}{\nu^2} \right)^{\frac{1}{3}} = 0.909 \text{ Re}^{\frac{1}{3}} \quad 2.5.31$$

for the disc rotating at an angular velocity,  $\omega$ , it was proposed that  $\frac{1}{2}D\omega^2$  should be substituted for  $g$ , that is

$$\delta \left( \frac{1}{2} \frac{D\omega^2}{\nu^2} \right)^{\frac{1}{3}} = 0.909 \text{ Re}^{\frac{1}{3}} \quad 2.5.32$$

Measurements were made of the film thickness using a micrometer and probe technique which allowed only the crests of the waves to be monitored. In the range covered by the experimental work, Reynolds numbers from 20 to 600, the maximum film thickness ( $\delta_m$ ) could be correlated by the equation

$$\delta_m \left( \frac{1}{2} \frac{D\omega^2}{\nu^2} \right)^{\frac{1}{3}} = 1.3 \text{ Re}^{\frac{1}{3}}. \quad 2.5.33$$

### 2.5.3 Condensation and heat transfer on rotating conical bodies.

Bromley (65) predicted the performance characteristics of a Hickman-Badger centrifugal boiler compression still. The liquid to be evaporated flows in a thin film outward along the inside of a rapidly rotating cone whilst the vapour generated was compressed and returned to the other side of the cone, where it condensed to supply energy for the evaporation taking place on the inside. A theoretical analysis assumed the Nusselt equation in which a cone of apex angle  $2\phi$  was used and 'g' replaced by  $4\pi^2 r N^2 \sin\phi$ . The equation for the overall heat transfer coefficient,  $\bar{U}$ , is given by

$$\bar{U} = 1.37 \left( \frac{k^3 e^2 N^2 D_o^2 \sin\phi}{w_f \mu} \right)^{\frac{1}{3}} \quad 2.5.34$$

where  $w_f$  was the feed flow to the rotor. The experimental results fell into a range of values +71% to -32% which were accepted as satisfactory.

A further analysis of condensation of pure vapours on rotating surfaces was carried out by Sparrow and Hartnett (66) who use the boundary layer technique to examine rotating cones. The approach was exactly the same as that for the disc analysis; new dependent and independent variables, transformation of the partial differential equations to ordinary differential equations and finally solution by numerical means. The conclusions drawn were that the deviations from heat transfer coefficients of the disc to those of the cone were not large and that the coefficients were related by

$$\frac{h_{\text{cone}}}{h_{\text{disc}}} = (\sin \alpha)^{\frac{1}{2}} \quad 2.5.35$$

where  $2\alpha$  is the apex angle of the cone. A similar relationship was found for the film thickness given by

$$\frac{\delta_{\text{cone}}}{\delta_{\text{disc}}} = (\sin \alpha)^{-\frac{1}{2}} \quad 2.5.36$$

The system considered cones which were not too slender and also no account was taken of the effect of gravity which became more important as the apex angle was reduced for lower rotational speeds.

In a paper by Howe and Hoyle (67) heat transfer to a cooled vertical cone with a 0.61 m diameter base and an apex angle of  $60^\circ$ , rotating at 100 to 700 r.p.m. in a steam atmosphere, has been studied and was discussed. The data was presented by plotting Nusselt number,  $hD/k$ , against  $D\sigma\rho/\mu^2$  for values of  $\frac{1}{2}D\omega^2/g$  varying from 0 to 77. From this data it was observed that as  $\frac{1}{2}D\omega^2/g$  was increased from zero to a value of approximately 2.5 the slope of the curves of Nu against  $D\sigma\rho/\mu^2$  decreased to a minimum but with further increases of  $\frac{1}{2}D\omega^2/g$ , from 2.5 to 8, the slope again increased. After  $\frac{1}{2}D\omega^2/g$  equalled 8 the slope remained constant. The empirical equation relating Nu to  $D\sigma\rho/\mu^2$  for  $\frac{1}{2}D\omega^2/g = 0$  is given by

$$\frac{hD}{k} = 2000 \left( \frac{D \sigma \rho}{\mu^2 \cdot 2.5 \times 10^8} \right) \quad 2.5.37$$

and for values of  $\frac{1}{2}D\omega^2/g$  between 2.45 and 77

$$\frac{hD}{k} = 3700 \left( \frac{D \sigma \rho}{\mu^2 \cdot 2.5 \times 10^8} \right)^{0.16} \frac{D\omega^2}{2g} \quad 2.5.38$$

all the fluid properties being evaluated at the Drew reference

$$\text{temperature:} \quad t_f = t_s - 0.75(t_s - t_w) \quad 2.5.39$$

It was concluded that heat transfer to a conical surface at this apex angle resembled that to a cylinder more closely than that to a disc.

An experimental study was made of the formation and drainage of a film of condensate on the surface of a rotating  $60^\circ$  right cone by Robson (68). He found that measurement could not be made directly whilst the cone was rotating and steam was condensing on it. An open flash technique was used to obtain still photographs of the condensate surface at various speeds. An estimation of the film thickness was attempted by using Holgate's apparatus (36) and film thickness measurements were made using the capacitance probe. It was assumed that the mean film thickness observed at a particular radius, speed of rotation and water flowrate was the same as that under the same flow conditions when steam was condensing. The water flowrate was varied between 0.009 and 0.127 m<sup>3</sup>/h and the rotational speed from zero to 660 r.p.m. Mean film thicknesses were measured from various stations along the cone generator line. Use was then made of Howe and Hoyle's heat transfer results (67) to obtain a condensate flowrate at a particular diameter. The condensate flow, cone rotation and diameter under consideration were matched to water flowrate, cone rotation and diameter to obtain a mean water film thickness which was then assumed to be the mean condensate film thickness. Nusselt's equation for film thickness was modified and the suggested form is

$$\delta \left( \frac{D \omega^2 \sin 30}{2g} \right)^{\frac{1}{3}} = 1.1 \text{ Re}^{\frac{1}{3}} \quad 2.5.40$$

which predicts mean film thicknesses 1.22 times greater than the Nusselt equation.

This analysis by Robson showed that there were waves of the curtain type on the condensate surface, similar to those observed by Holgate, when the cone was stationary. When the cone was rotated slowly these curtain type waves, which had a wavelength of between 0.01 m and 0.03 m, now descended in a spiral fashion. Increasing the rotational speed caused the wavelength to decrease and a ridge type flow to appear, doing so first at the largest radius. Further increases of speed reduced the wavelength more and ridge type flow extended to all regions of the surface. This showed that the ridge type flow was dependent on  $\frac{1}{2} D \omega^2 / g$ . Although at the higher rotational speeds some of the ridges coalesced or split into two, no drops were observed to be thrown from the surface. Over the range of rotational speeds observed, zero to 1400 r.p.m., the angle between the drainage path of the ridge and the generator of the cone was very nearly constant at about  $23^\circ$ . The point at which this ridge type flow occurred was dependent on  $\frac{1}{2} D \omega^2 / g$  and pressure, the latter determining the heat flux. A parameter developed was a Reynolds number based on the mean film thickness and the average heat transfer coefficient

$$\text{Re} = \frac{3 \cos \theta \delta h_{av} \Delta T \cos \alpha}{h_{fg} \mu} \quad 2.5.41$$

where  $\alpha$  is the angle between the ridge and the cone generator.

The surface of the  $60^\circ$  right cone was seen to support ridge like waves,  $\frac{1}{2} D \omega^2 / g$  values above 50, but no drops were seen to be thrown off at any speed up to 1400 r.p.m. The condensate removal on cylinders was observed to be in the form of drops discharged tangentially from the condensate surface above certain speeds. It was thought that cones with

smaller apex angles may display this same phenomenon and a further theoretical and experimental analysis was carried out by Howe (67).

The theoretical analysis was formulated with the usual Nusselt assumptions. Convection and inertia terms were neglected, and the acceleration field 'g' was replaced by  $a_x$  defined as

$$a_x = \frac{1}{2}D\omega^2 \sin\beta + g \cos\beta \quad 2.5.42$$

where  $D = (d + 2x\sin\beta)$  2.5.43

and  $d$  was the initial diameter of a truncated cone and  $x$  the distance in the X direction which is parallel to the cone generator. A balance of forces at a point in the fluid predicted a semi-parabolic velocity profile in the Y direction, which is perpendicular to the cone generator, in accordance with the usual Nusselt theory. That is

$$V_x = \frac{\rho}{\mu} a_x (3y - y^2/2) \quad 2.5.44$$

An energy balance was then performed and the governing equation for film flow during condensation on the surface of rotating cones was given by

$$a_x \delta^3 \frac{d\delta}{dx} + \frac{\delta^4}{3} \left( \frac{da_x}{dx} + \frac{3\gamma}{D} \frac{dD}{dx} \right) = \frac{cp\Delta T \omega^2}{Pr(h_{fg} + 0.375 cp\Delta T)} \quad 2.5.45$$

The equation 2.5.45 was solved numerically and the heat transfer coefficients were plotted against distance from the starting point of condensation, for rotational speeds varying from zero to 1000 r.p.m., on a  $60^\circ$  right cone and on  $20^\circ$  and  $10^\circ$  apex angled, truncated, cones.

The experimental results were presented in graphical form plotting the two groups

$$Nu (3\mu)^{\frac{1}{3}} \left( \frac{\omega \sin\beta}{g \cos\beta} \right)^{\frac{2}{3}} \quad 2.5.46$$

where  $h = \frac{cp\Delta T \omega^2}{Pr(h_{fg} + 0.375 cp\Delta T)}$  2.5.47

and  $\frac{\chi \omega^2 \sin^2\beta}{k \cos\beta}$  2.5.48

and recommended equations for each cone which were derived from the

curves drawn through the experimental points and had the general form

$$\text{Nu}_{\text{exp}} \cdot (3H)^{\frac{1}{4}} \cdot \frac{(\omega \sin \beta)}{g \cos \beta} = A_1 \left( X \frac{\omega^2 \sin^2 \beta}{g \cos \beta} \right)^{1/2} \quad 2.5.49$$

where  $A_1$  and  $A_2$  are constants depending on the apex angle of the cone.

The theoretical curves were plotted on the same graphs and showed in general that the experimental heat transfer was greater than that predicted by laminar theory.

The laminar film thickness on a cone can be calculated by solving equation 2.5.45. A further analysis was performed by Howe to allow the film thickness to be calculated from the starting point of condensation which may occur at any given distance from the apex. Equation 2.5.45 was rearranged into the following form

$$E = \frac{\delta}{X} \frac{d}{dX} \left[ \frac{\delta^3 X (\omega^2 \sin^2 \beta + g \cos \beta)}{\gamma^2} \right] \quad 2.5.50$$

where  $E = \frac{\delta \text{ cp } \Delta T}{\text{Pr}(h_{fg} + 0.375 \text{ cp } \Delta T)}$  2.5.51

After introducing a dimensionless variable  $L$  to characterise the distance along the cone generator line from the starting point of the film

$$L = \frac{X}{e} \quad \text{hence} \quad \frac{dX}{dL} = e \quad 2.5.52$$

and  $\gamma$  to characterise the film thickness at any value of  $L$

$$\gamma = \frac{\delta}{\delta} \quad \text{hence} \quad \frac{d\delta}{d\gamma} = \delta \quad 2.5.53$$

The definitions chosen for  $\delta$  and  $e$  are

$$\delta = \left( \frac{\gamma}{\sin \beta} \right)^{\frac{1}{2}} E^{\frac{1}{4}} \quad 2.5.54$$

$$e = \frac{g \cos \beta}{\omega^2 \sin^2 \beta} \quad 2.5.55$$

Substitution of equations 2.5.54 and 2.5.55 reduce equation 2.5.50

to

$$\frac{\gamma}{L} \frac{d}{dL} \left[ \gamma^3 L(L+1) \right] = 1 \quad 2.5.56$$

which has the solution

$$\eta^4 L^{4/3} (L + 1)^{4/3} = \frac{4}{3} \int_0^L L^{4/3} (L + 1)^{1/3} dL \quad 2.5.57$$

The dimensionless film thickness,  $\eta$ , is related to the dimensionless distance along the cone generator line from its apex by

$$\eta^4 = \frac{4}{3} \frac{\int_{L_0}^L L^{4/3} (L + 1)^{1/3} dL}{L^{4/3} (L + 1)^{4/3}} \quad 2.5.58$$

where  $L_0$  is the distance of the starting point of the film along the cone generator line from the apex as shown in figure 1.

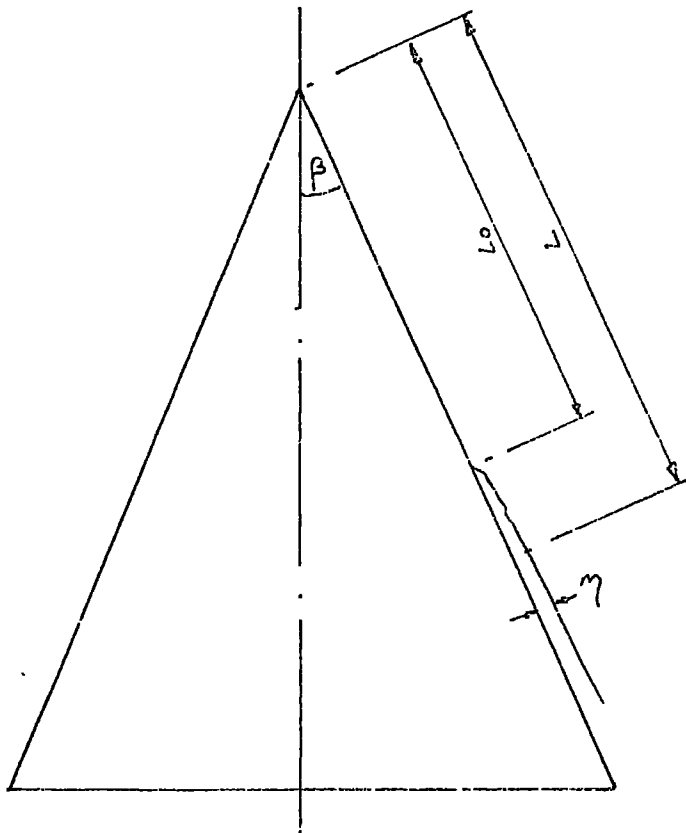


Figure 1. Laminar film thickness model.

The condensate film was found to support various patterns of waves as it drained along the surface of the  $10^\circ$ ,  $20^\circ$  and  $60^\circ$  cones. A description of these wave patterns was given for the  $10^\circ$  and  $20^\circ$  cones. At rotational speeds below 100 r.p.m. the condensate film supported waves

of the curtain type. Above 100 r.p.m. the wave formation changed to that of a ridge type which were spaced circumferentially around the cone surface. The angle these ridges formed with the cone generator varying as the speed of rotation was increased. The drainage was assisted at higher speeds by the formation and detachment of drops from the crests of the ridges. The photograph in figure 2. shows the drainage pattern on the surface of the  $10^\circ$  included angled cone rotating at 350 r.p.m. in a steam atmosphere at 2.5 bars absolute.

## 2.6 Present work.

It can be seen from the preceding sections that the laminar theory of filmwise condensation is established for both stationary and rotating surfaces. The survey shows that no direct measurement of condensate films have been attempted on rotating surfaces. Estimates which have been made are based on the flow of cold water over a rotating solid of comparable shape, for example Espig (62) and Robson (63). This procedure is far from satisfactory for true fluid flow studies and it was the purpose of this work to develop a measurement technique capable of wave motion and film thickness observations during the condensation process.

A theoretical analysis of the condensate film profile was attempted to clarify the action of centrifugal acceleration, surface tension and coriolis forces. The particular points to be examined are the effect of speed of rotation and condensation rate on the regimes of waves supported by the condensate film. The general analysis will be concerned with predicting wavelength, minimum and maximum film thicknesses and heat transfer coefficients and comparing these to those predicted by laminar theory.

3.0 THEORY

### 3.1 - Introduction.

In Howe's thesis (69) the appearance of the condensate flow on the surface of  $60^\circ$ ,  $20^\circ$  and  $10^\circ$  included angled cones has been described. Three regimes of flow were shown to exist on the condensate surface of the  $10^\circ$  cone. At low rotational speeds, up to 60 r.p.m., waves of the curtain type which have a small spiral motion down the cone surface were observed. The angle of the spiral increased as the rotational speed increased. As the speed was further increased, the condensate drainage pattern changed to that of ridge like waves which give the appearance of smooth streams flowing down spiral tracks making a small angle with the generating lines of the cone, as shown in figure 2. These ridges appeared around the whole circumference of the cone in a quasi-steady state condition. There were however points of discontinuity where some ridges disappeared and then reappeared further down the surface and some ridges coalesced whilst others split into two. The latter appeared to be commoner at higher rotational speeds. These higher rotational speeds produced less stable conditions due to imperfections and added drag from the vapour phase. Further increases in speed produced a condition where drops could be seen to be thrown from the ridge profile itself. These drops were thrown from lower radii first and as the speed increased the point of drop departure moved up the generator line.

Since the only quasi-steady state conditions occurred during the regime of ridge type flow, before the stage is reached when drops are being thrown from the surface of the ridges, this is the condition which can be readily modelled. The ridge model assumed is shown in figure 3., where  $\bar{\lambda}$  is the non-dimensional wavelength and  $\delta$  the film thickness.

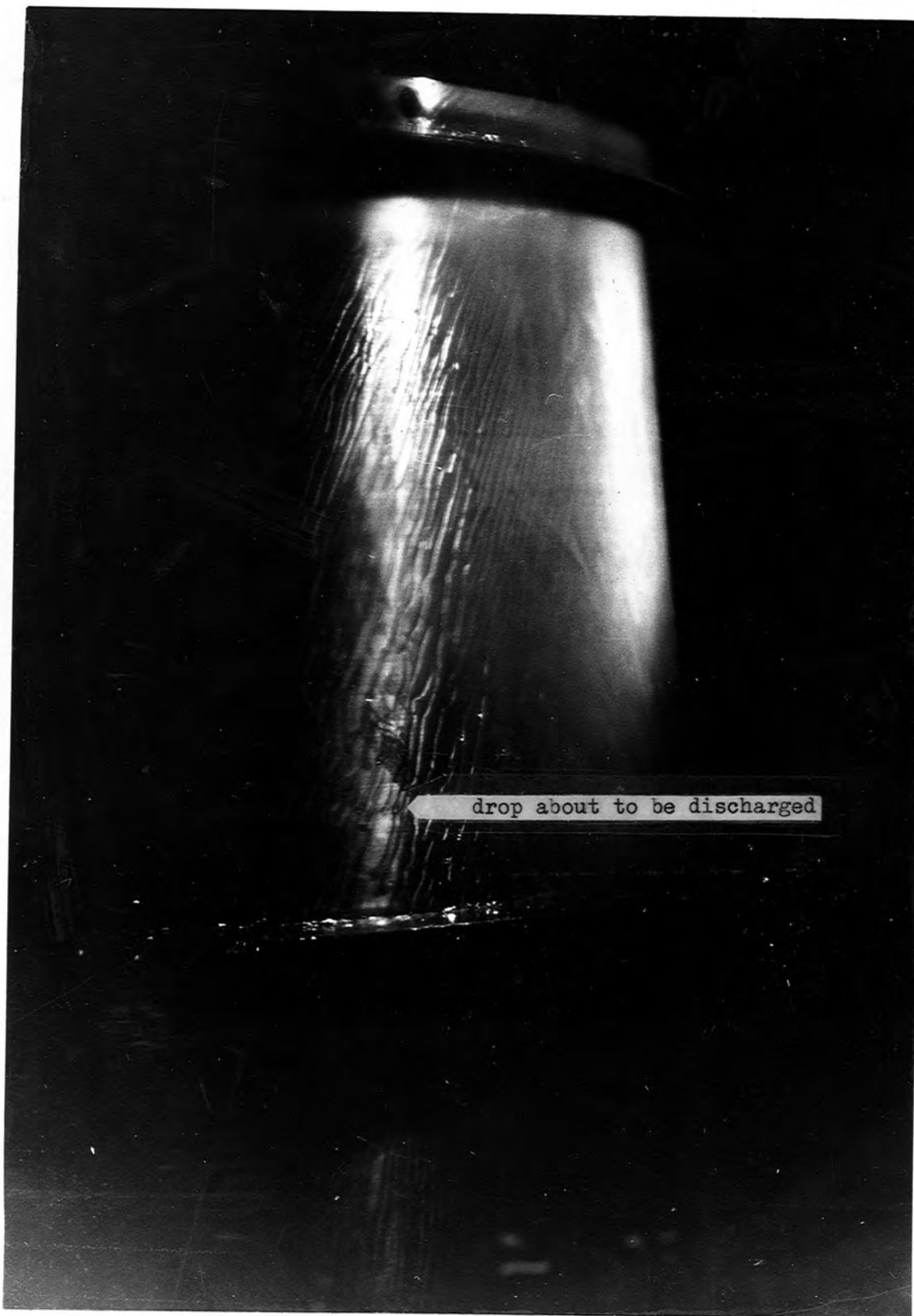


Figure 2. 'Ridge' type condensate flow on rotating cones.

Rotational speed 350 r.p.m. Steam pressure 2.5 bar abs.

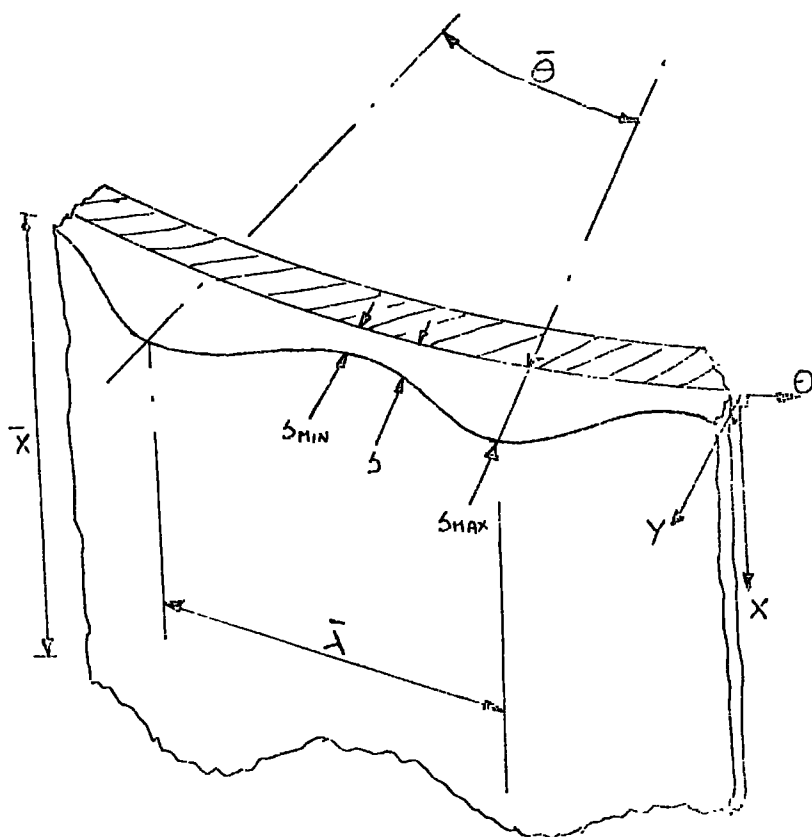


Figure 3. Model of surface profile.

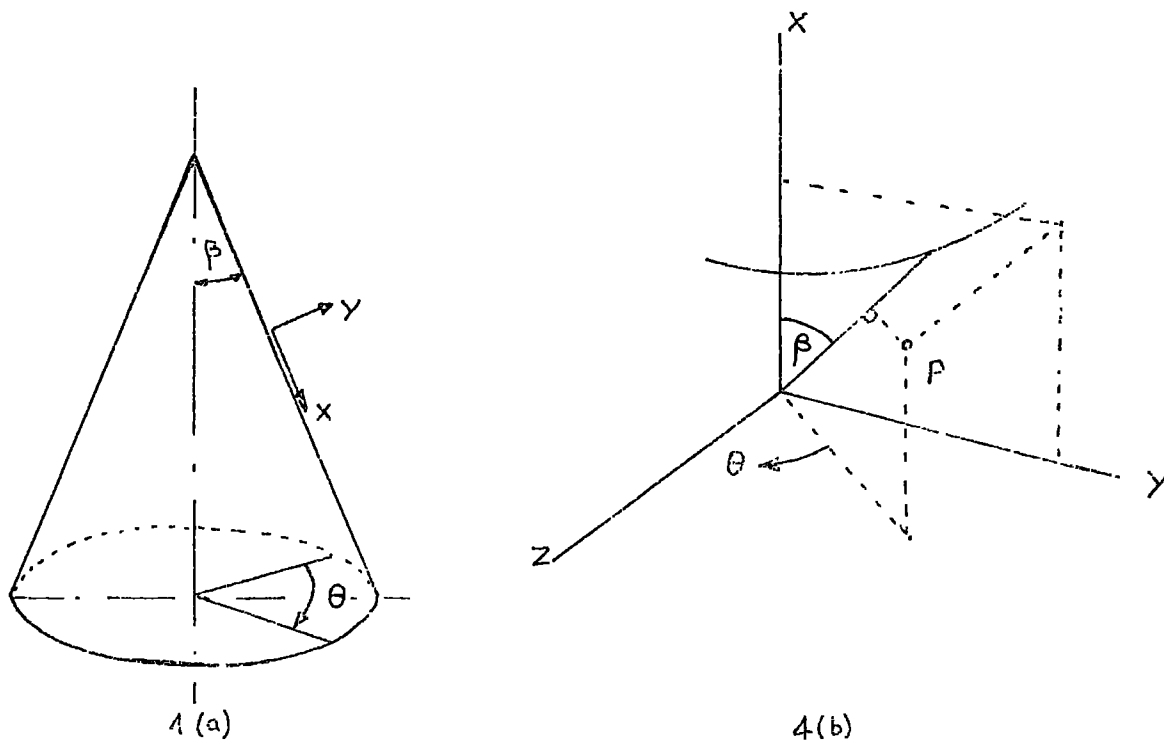


Figure 4. Coordinate system for the cone.

### 3.2 Coordinate system and equations of motion.

The coordinate system is shown diagrammatically in figure 4(a). Coordinates 'X' and 'Y' are parallel and perpendicular to the cone surface generator line respectively. Coordinate 'θ' traces out the circular movement of a point on the surface generator line when rotated about a vertical axis. These three coordinates are everywhere mutually perpendicular and thus form an orthogonal system.

The equations of motion must be derived in this new coordinate system. The equations of motion are given in general vectorial form;

$$\frac{\partial \vec{V}}{\partial t} - \vec{V} \times \vec{\omega} = -g \text{grad} \left( \frac{P}{\rho} + \frac{1}{2} \vec{V} \cdot \vec{V} + \Omega \right) + \nabla \left( g \text{grad} \text{div} \vec{V} - \text{curl} \cdot \text{curl} \vec{V} \right) \quad 3.2.1$$

where  $\omega$  is the vorticity and,  $P$ , the body force equals  $-g \text{grad} \Omega$ .

The fundamental equations necessary for expressing the equations of motion in any set of orthogonal coordinates are to be found in text books of hydrodynamics (e.g. Lamb (86)). In curvilinear coordinates the rectilinear coordinates (x,y,z) of any point are expressed as functions of the new coordinates  $(\alpha_1, \alpha_2, \alpha_3)$ ,

$$\alpha_1 = \alpha_1(x, y, z), \quad \alpha_2 = \alpha_2(x, y, z), \quad \alpha_3 = \alpha_3(x, y, z) \quad 3.2.2$$

The lengths of elements of arcs in the new directions are denoted by  $h_1 d\alpha_1$ ,  $h_2 d\alpha_2$  and  $h_3 d\alpha_3$ . The linearizing factors  $h_1$ ,  $h_2$  and  $h_3$  are calculated considering a point P distance  $r$  above the surface of the cone and finding its position vector  $r$ , where

$$h_1 = \left| \frac{dr}{d\alpha_1} \right|, \quad h_2 = \left| \frac{dr}{d\alpha_2} \right|, \quad h_3 = \left| \frac{dr}{d\alpha_3} \right|$$

For our coordinate system the position vector  $r$ , from figure 4(b), is given by

$$r = (X \sin \beta + Y \cos \beta) \cos \theta i + (X \sin \beta + Y \cos \beta) \sin \theta j + (X \cos \beta - Y \sin \beta) k \quad 3.2.3$$

In order to find  $h_1$ ,  $h_2$ , and  $h_3$  the modulus of the partial integrals of  $r$  with respect to  $X$ ,  $Y$  and  $\Theta$  respectively are required.

$$\frac{\partial r}{\partial X} = \sin\beta \cos\theta i + \sin\beta \sin\theta j + \cos\beta k$$

$$\left| \frac{\partial r}{\partial X} \right| = \sqrt{\sin^2\beta \cos^2\theta + \sin^2\beta \sin^2\theta + \cos^2\beta}$$

$$= \sqrt{\sin^2\beta (\cos^2\theta + \sin^2\theta) + \cos^2\beta}$$

$$h_1 = \sqrt{\sin^2\beta + \cos^2\beta} = 1 \quad 3.2.4$$

with  $\frac{\partial r}{\partial Y} = \cos\beta \cos\theta i + \cos\beta \sin\theta j - \sin\beta k$

$$\left| \frac{\partial r}{\partial Y} \right| = \sqrt{\cos^2\beta \cos^2\theta + \cos^2\beta \sin^2\theta + \sin^2\beta}$$

$$h_2 = \sqrt{\cos^2\beta + \sin^2\beta} = 1 \quad 3.2.5$$

and  $\frac{\partial r}{\partial \Theta} = -(X \sin\beta + Y \cos\beta) \sin\theta i + (X \sin\beta + Y \cos\beta) \cos\theta j$

$$\left| \frac{\partial r}{\partial \Theta} \right| = \sqrt{(X \sin\beta + Y \cos\beta)^2 \sin^2\theta + (X \sin\beta + Y \cos\beta)^2 \cos^2\theta}$$

$$h_3 = X \sin\beta + Y \cos\beta = R \quad 3.2.6$$

The three linearizing factors are

$$h_1 = 1, \quad h_2 = 1, \quad \text{and} \quad h_3 = R$$

The mathematical expressions necessary for inclusion in the equation of motion in vectorial form are :-

$$(i) \quad \text{grad} \equiv \frac{1}{h_1} \frac{\partial}{\partial \alpha_1}, \quad \frac{1}{h_2} \frac{\partial}{\partial \alpha_2}, \quad \frac{1}{h_3} \frac{\partial}{\partial \alpha_3} \quad 3.2.7$$

(ii) curl, whose three components are

$$\omega_1 = \frac{1}{h_2 h_3} \left[ \frac{\partial}{\partial \alpha_2} (h_3 u_3) - \frac{\partial}{\partial \alpha_3} (h_2 u_2) \right]$$

$$\omega_2 = \frac{1}{h_3 h_1} \left[ \frac{\partial}{\partial \alpha_3} (h_1 u_1) - \frac{\partial}{\partial \alpha_1} (h_3 u_3) \right] \quad 3.2.8$$

$$\omega_3 = \frac{1}{h_1 h_2} \left[ \frac{\partial}{\partial \alpha_1} (h_2 u_2) - \frac{\partial}{\partial \alpha_2} (h_1 u_1) \right]$$

$$(iii) \quad \text{div} = \frac{1}{h_1 h_2 h_3} \left[ \frac{\partial}{\partial \alpha_1} (h_2 h_3 u_1) + \frac{\partial}{\partial \alpha_2} (h_3 h_1 u_2) + \frac{\partial}{\partial \alpha_3} (h_1 h_2 u_3) \right] \quad 3.2.9$$

For our coordinate system let

$$\left. \begin{aligned} \alpha_1 &= X & \alpha_2 &= Y & \alpha_3 &= \Theta \\ \text{and } u_1 &= v_x & u_2 &= v_y & u_3 &= v_\theta + \omega r_s \end{aligned} \right\} \quad 3.2.10$$

To simplify matters the terms in equation 3.2.1 will be taken separately and also split up into the component directions.

(i) curl.curl  $\vec{V}$

$$\omega_1 = \frac{1}{R} \left[ \frac{\partial}{\partial Y} [R(V_\theta + \omega R_s)] - \frac{\partial}{\partial \theta} (V_y) \right]$$

multiplying out

$$= \frac{1}{R} \left[ \frac{\partial}{\partial Y} (R V_\theta + \omega R R_s) - \frac{\partial}{\partial \theta} (V_y) \right]$$

carrying out the differentiation

$$= \frac{V_\theta}{R} \cos \beta + \frac{\partial V_\theta}{\partial Y} + \frac{\omega X \cos \beta \sin \beta}{R} - \frac{1}{R} \frac{\partial V_y}{\partial \theta} \quad 3.2.11$$

Similarly for  $\omega_2$  and  $\omega_3$

$$\begin{aligned} \omega_2 &= \frac{1}{R} \left[ \frac{\partial}{\partial \theta} (V_x) - \frac{\partial}{\partial X} (R V_\theta + \omega R R_s) \right] \\ &= \frac{1}{R} \frac{\partial V_x}{\partial \theta} - \frac{\partial V_\theta}{\partial X} - \frac{V_\theta}{R} \sin \beta - \frac{2\omega X \sin^2 \beta}{R} - \frac{\omega Y \sin \beta \cos \beta}{R} \end{aligned} \quad 3.2.12$$

and 
$$\omega_3 = \frac{\partial}{\partial X} (V_y) - \frac{\partial}{\partial Y} (V_x)$$

$$= \frac{\partial V_y}{\partial X} - \frac{\partial V_x}{\partial Y} \quad 3.2.13$$

Taking the curl a second time

X direction

$$\begin{aligned} \frac{1}{R} \left[ \frac{\partial}{\partial Y} \left( R \frac{\partial V_y}{\partial X} - R \frac{\partial V_x}{\partial Y} \right) - \frac{\partial}{\partial \theta} \left( \frac{1}{R} \frac{\partial V_y}{\partial \theta} - \frac{V_\theta}{R} \sin \beta - \frac{\partial V_\theta}{\partial X} \right. \right. \\ \left. \left. - \frac{2\omega X \sin^2 \beta}{R} - \frac{\omega Y \sin \beta \cos \beta}{R} \right) \right] \end{aligned}$$

differentiating the above term gives

$$\begin{aligned} \frac{1}{R} \left[ \left( R \frac{\partial^2 V_y}{\partial X \partial Y} + \frac{\partial V_y}{\partial X} \cos \beta - R \frac{\partial^2 V_x}{\partial Y^2} - \frac{\partial V_x}{\partial Y} \cos \beta \right) \right. \\ \left. - \left( \frac{1}{R} \frac{\partial^2 V_y}{\partial \theta^2} - \frac{\partial V_\theta}{\partial \theta} \frac{\sin \beta}{R} - \frac{\partial^2 V_\theta}{\partial X \partial \theta} \right) \right] \end{aligned}$$

and simplifying

$$\begin{aligned} \frac{\partial^2 V_y}{\partial X \partial Y} + \frac{\partial V_y}{\partial X} \frac{\cos \beta}{R} - \frac{\partial^2 V_x}{\partial Y^2} - \frac{\partial V_x}{\partial Y} \frac{\cos \beta}{R} \\ - \frac{1}{R^2} \frac{\partial^2 V_y}{\partial \theta^2} + \frac{\partial V_\theta}{\partial \theta} \frac{\sin \beta}{R^2} + \frac{1}{R} \frac{\partial^2 V_\theta}{\partial X \partial \theta} \end{aligned} \quad 3.2.14$$

Y - direction

$$\frac{1}{R} \left[ \frac{\partial}{\partial \theta} \left( \frac{\partial V_{\theta}}{\partial Y} + \frac{V_{\theta} \cos \beta}{R} + \frac{\omega X \sin \beta \cos \beta}{R} - \frac{1}{R} \frac{\partial V_y}{\partial \theta} \right) - \frac{\partial}{\partial X} \left( R \left( \frac{\partial V_y}{\partial X} - \frac{\partial V_x}{\partial Y} \right) \right) \right]$$

differentiating and simplifying the above term one obtains

$$\begin{aligned} & \frac{1}{R} \frac{\partial^2 V_{\theta}}{\partial \theta \partial Y} + \frac{\partial V_{\theta}}{\partial \theta} \frac{\cos \beta}{R^2} - \frac{1}{R^2} \frac{\partial^2 V_y}{\partial \theta^2} - \frac{\partial^2 V_y}{\partial X^2} \\ & - \frac{\partial V_y}{\partial X} \frac{\sin \beta}{R} + \frac{\partial^2 V_x}{\partial X \partial Y} + \frac{1}{R} \frac{\partial V_x}{\partial Y} \sin \beta \end{aligned} \quad 3.2.15$$

$\Theta$  direction

$$\begin{aligned} & \frac{\partial}{\partial X} \left( \frac{1}{R} \frac{\partial V_x}{\partial \theta} - \frac{\partial V_{\theta}}{\partial X} - \frac{V_{\theta} \sin \beta}{R} - \frac{2\omega X \sin^2 \beta}{R} - \frac{\omega Y \sin \beta \cos \beta}{R} \right) \\ & - \frac{\partial}{\partial Y} \left( \frac{V_{\theta}}{R} + \frac{\partial V_{\theta}}{\partial Y} + \frac{\omega X \cos \beta \sin \beta}{R} - \frac{1}{R} \frac{\partial V_y}{\partial \theta} \right) \end{aligned}$$

differentiating and simplifying the above term one obtains

$$\begin{aligned} & \frac{1}{R} \frac{\partial^2 V_x}{\partial X \partial \theta} - \frac{\partial V_x}{\partial \theta} \frac{\sin \beta}{R^2} - \frac{\partial V_{\theta}}{\partial X} \frac{\sin \beta}{R} + \frac{V_{\theta} \sin^2 \beta}{R^2} - \frac{\partial^2 V_{\theta}}{\partial X^2} \\ & + \frac{2\omega Y \sin^2 \beta \cos \beta}{R^2} + \frac{\omega Y \sin^2 \beta \cos \beta}{R^2} - \frac{1}{R} \frac{\partial V_{\theta}}{\partial Y} + \frac{V_{\theta} \sin \beta}{R^2} - \frac{\partial^2 V_{\theta}}{\partial Y^2} \\ & + \frac{\omega X \cos^2 \beta \sin \beta}{R^2} + \frac{1}{R} \frac{\partial^2 V_y}{\partial \theta \partial Y} - R \frac{\partial V_y}{\partial \theta} \frac{\cos \beta}{R^2} \end{aligned} \quad 3.2.16$$

(ii) In a similar manner  $\text{grad} \left( \frac{1}{2} \vec{V} \cdot \vec{V} \right) - \vec{V} \times \vec{\omega}$  are calculated where the components of  $\vec{V} \times \vec{\omega}$  are

$$-u_2 \omega_3 - u_3 \omega_2, \quad u_3 \omega_1 - u_1 \omega_3, \quad \text{and} \quad u_1 \omega_2 - u_2 \omega_1$$

in the X, Y and  $\Theta$  directions respectively.

X direction

$$\begin{aligned} & \frac{\partial}{\partial X} \left( \frac{1}{2} V_x^2 + \frac{1}{2} V_y^2 + \frac{1}{2} (V_{\theta} + \omega R_s)^2 \right) - V_y \left( \frac{\partial V_y}{\partial X} - \frac{\partial V_x}{\partial Y} \right) \\ & + (V_{\theta} + \omega R_s) \left( \frac{1}{R} \frac{\partial V_x}{\partial \theta} - \frac{V_{\theta} \sin \beta}{R} - \frac{\partial V_{\theta}}{\partial X} - \frac{2\omega X \sin^2 \beta}{R} - \frac{\omega Y \sin \beta \cos \beta}{R} \right) \end{aligned}$$

differentiating the above term one obtains

$$\begin{aligned} & V_x \frac{\partial V_x}{\partial X} + V_y \frac{\partial V_y}{\partial X} + V_{\theta} \frac{\partial V_{\theta}}{\partial X} + \frac{\partial V_{\theta}}{\partial X} \omega R_s + V_{\theta} \omega \sin \beta + \omega^2 X \sin^2 \beta \\ & - V_y \frac{\partial V_y}{\partial X} - V_y \frac{\partial V_x}{\partial Y} + \frac{V_{\theta}}{R} \frac{\partial V_x}{\partial \theta} - \frac{V_{\theta}^2 \sin \beta}{R} \end{aligned}$$

$$\begin{aligned}
 & -V_{\theta} \frac{\partial V_{\theta}}{\partial X} - \frac{2\omega V_{\theta} X \sin^2 \beta}{R} - \frac{\omega V_{\theta} Y \sin \beta \cos \beta}{R} + \frac{\omega \frac{\partial V_x}{\partial \theta} R_s}{R} \\
 & - \frac{\omega V_{\theta} \sin \beta R_s}{R} - \omega R_s \frac{\partial V_{\theta}}{\partial X} - \frac{2\omega^2 X R_s \sin^2 \beta}{R} - \frac{\omega^2 R_s Y \sin \beta \cos \beta}{R}
 \end{aligned}$$

Then simplifying and rearranging into the following form

$$\begin{aligned}
 & V_x \frac{\partial V_x}{\partial X} + V_y \frac{\partial V_y}{\partial Y} + \frac{V_{\theta}}{R} \frac{\partial V_x}{\partial \theta} - \frac{V_{\theta}^2}{R} \sin \beta - \frac{\omega^2 X \sin^2 \beta}{R} (2R_s - 1) \\
 & + V_{\theta} \omega \sin \beta \left(1 - \frac{R_s}{R}\right) + \frac{\omega \frac{\partial V_x}{\partial \theta} R_s}{R} - \frac{V_{\theta} \sin \beta \omega}{R} (2X \sin \beta - Y \cos \beta) \\
 & \quad - \frac{\omega^2 Y \sin \beta \cos \beta R_s}{R} \qquad \qquad \qquad 3.2.17
 \end{aligned}$$

Y direction

$$\begin{aligned}
 & \frac{\partial}{\partial Y} \left[ \frac{1}{2} V_x^2 + \frac{1}{2} V_y^2 + \frac{1}{2} (V_{\theta} + \omega R_s)^2 \right] - (V_{\theta} + \omega R_s) \left[ \frac{V_{\theta} \cos \beta}{R} \right. \\
 & \left. + \frac{\partial V_{\theta}}{\partial Y} + \frac{\omega X \cos \beta \sin \beta}{R} - \frac{1}{R} \frac{\partial V_y}{\partial \theta} \right] + V_x \left[ \frac{\partial V_y}{\partial X} - \frac{\partial V_x}{\partial Y} \right]
 \end{aligned}$$

Differentiating and simplifying as for the X direction one obtains

$$\begin{aligned}
 & V_x \frac{\partial V_y}{\partial Y} + V_y \frac{\partial V_y}{\partial Y} + \frac{V_{\theta}}{R} \frac{\partial V_y}{\partial \theta} + \frac{\omega R_s}{R} \frac{\partial V_y}{\partial \theta} - \frac{V_{\theta}^2}{R} \cos \beta \\
 & + \frac{\omega R_s V_{\theta} \cos \beta}{R} + \frac{\omega V_{\theta} X \cos \beta \sin \beta}{R} - \frac{\omega^2 X R_s \cos \beta \sin \beta}{R} \qquad \qquad \qquad 3.2.18
 \end{aligned}$$

\theta direction

$$\begin{aligned}
 & \frac{1}{R} \frac{\partial}{\partial \theta} \left[ \frac{1}{2} V_x^2 + \frac{1}{2} V_y^2 + \frac{1}{2} (V_{\theta} + \omega R_s)^2 \right] - V_x \left[ \frac{1}{R} \frac{\partial V_x}{\partial \theta} \right. \\
 & \left. - \frac{\partial V_{\theta}}{\partial X} - \frac{V_{\theta}}{R} - \frac{2\omega X \sin^2 \beta}{R} - \frac{\omega Y \sin \beta \cos \beta}{R} \right] + \\
 & V_y \left[ \frac{V_{\theta} \cos \beta}{R} + \frac{\partial V_{\theta}}{\partial Y} + \frac{\omega X \cos \beta \sin \beta}{R} - \frac{1}{R} \frac{\partial V_y}{\partial \theta} \right]
 \end{aligned}$$

Again differentiating and simplifying one obtains

$$\begin{aligned}
 & V_x \frac{\partial V_{\theta}}{\partial X} + V_y \frac{\partial V_{\theta}}{\partial Y} + \frac{V_{\theta}}{R} \frac{\partial V_{\theta}}{\partial \theta} + \frac{\omega R_s}{R} \frac{\partial V_{\theta}}{\partial \theta} + \frac{V_{\theta}}{R} (V_x + V_y \cos \beta) \\
 & + \frac{\omega \sin \beta}{R} (2V_x X \sin \beta + V_y X \cos \beta + V_x Y \cos \beta) \qquad \qquad \qquad 3.2.19
 \end{aligned}$$

(iii) Finally the terms of  $\text{grad div } \vec{V}$  are calculated as follows

X direction

$$\frac{\partial}{\partial X} \left[ \frac{1}{R} \left( \frac{\partial (R V_x)}{\partial X} + \frac{\partial (R V_y)}{\partial Y} + \frac{\partial (V_{\theta})}{\partial \theta} \right) \right]$$

The differentiation of the term for the X direction gives

$$\frac{\partial}{\partial X} \left[ \frac{1}{R} \left( R \frac{\partial V_x}{\partial X} + V_x \sin \beta + R \frac{\partial V_y}{\partial X} + V_y \cos \beta + \frac{\partial V_\theta}{\partial \theta} \right) \right]$$

Simplifying this term and differentiating a second time gives

$$\begin{aligned} \frac{\partial^2 V_x}{\partial X^2} + \frac{\partial V_x}{\partial X} \frac{\sin \beta}{R} - \frac{V_x \sin^2 \beta}{R^2} + \frac{\partial^2 V_y}{\partial X \partial Y} + \frac{\partial V_y}{\partial X} \frac{\cos \beta}{R} \\ - \frac{V_y \cos \beta \sin \beta}{R^2} + \frac{1}{R} \frac{\partial^2 V_\theta}{\partial X \partial \theta} - \frac{1}{R} \frac{\partial V_\theta}{\partial \theta} \frac{\sin \beta}{R} \end{aligned} \quad 3.2.20$$

Y direction

$$\frac{\partial}{\partial Y} \left[ \frac{1}{R} \left( \frac{\partial (R V_x)}{\partial X} + \frac{\partial (R V_y)}{\partial Y} + \frac{\partial (V_\theta)}{\partial \theta} \right) \right]$$

differentiating once gives

$$\frac{\partial}{\partial Y} \left[ \frac{1}{R} \left( R \frac{\partial V_x}{\partial X} + V_x \sin \beta + R \frac{\partial V_y}{\partial Y} + V_y \cos \beta + \frac{\partial V_\theta}{\partial \theta} \right) \right]$$

then performing the differentiating a second time and simplifying, the term becomes

$$\begin{aligned} \frac{\partial^2 V_x}{\partial X \partial Y} + \frac{1}{R} \frac{\partial V_x}{\partial Y} \frac{\sin \beta}{R} - \frac{V_x \cos \beta \sin \beta}{R^2} + \frac{\partial^2 V_y}{\partial Y^2} \\ + \frac{\partial V_y}{\partial Y} \frac{\cos \beta}{R} - \frac{V_y \cos^2 \beta}{R} + \frac{1}{R} \frac{\partial^2 V_\theta}{\partial Y \partial \theta} - \frac{1}{R} \frac{\partial V_\theta}{\partial \theta} \frac{\cos \beta}{R} \end{aligned} \quad 3.2.21$$

$\theta$  direction

$$\frac{1}{R} \frac{\partial}{\partial \theta} \left[ \frac{1}{R} \left( \frac{\partial (R V_x)}{\partial X} + \frac{\partial (R V_y)}{\partial Y} + \frac{\partial (V_\theta)}{\partial \theta} \right) \right]$$

differentiating twice and simplifying gives

$$\frac{1}{R} \frac{\partial^2 V_x}{\partial X \partial \theta} + \frac{1}{R} \frac{\partial V_x}{\partial \theta} \frac{\sin \beta}{R} + \frac{1}{R} \frac{\partial^2 V_y}{\partial X \partial \theta} + \frac{\partial V_y}{\partial \theta} \frac{\cos \beta}{R} + \frac{1}{R^2} \frac{\partial^2 V_\theta}{\partial \theta^2} \quad 3.2.22$$

The terms 3.2.14, 3.2.17 and 3.2.20 can then be substituted into 3.2.1 to produce the equation of motion in the X direction for the coordinate system.

$$\begin{aligned} \frac{\partial V_x}{\partial t} + \left[ V_x \frac{\partial V_x}{\partial X} + V_y \frac{\partial V_x}{\partial Y} + \frac{V_\theta}{R} \frac{\partial V_x}{\partial \theta} - \frac{V_\theta^2 \sin \beta}{R} - \omega^2 X \sin^2 \beta \left( \frac{2R_s}{R} - 1 \right) \right. \\ + V_\theta \omega \sin \beta \left( 1 - \frac{R_s}{R} \right) + \omega \frac{\partial V_x}{\partial \theta} \frac{R_s}{R} - \frac{V_\theta \sin \beta \omega}{R} (2X \sin \beta - Y \cos \beta) \\ \left. - \frac{\omega^2 Y \sin \beta \cos \beta R_s}{R} \right] = F_x - \frac{1}{\rho} \frac{\partial P}{\partial X} + \gamma \left[ \left( \frac{\partial^2 V_x}{\partial X^2} \right) \right] \end{aligned}$$

$$\begin{aligned}
 & + \frac{1}{R} \frac{\partial V_x}{\partial X} \sin \beta - \frac{V_x}{R^2} \sin^2 \beta + \frac{\partial^2 V_y}{\partial X \partial Y} + \frac{\cos \beta}{R} \frac{\partial V_y}{\partial X} \\
 & - \frac{V_y \cos \beta \sin \beta}{R^2} + \frac{1}{R} \frac{\partial^2 V_\theta}{\partial X \partial \theta} - \frac{1}{R^2} \frac{\partial V_\theta}{\partial \theta} \sin \beta \left( \frac{\partial^2 V_y}{\partial X \partial Y} + \frac{\partial V_y}{\partial X} \frac{\cos \beta}{R} \right) \\
 & - \left. \frac{\partial^2 V_x}{\partial Y^2} - \frac{\partial V_x}{\partial Y} \frac{\cos \beta}{R} - \frac{1}{R^2} \frac{\partial^2 V_y}{\partial \theta^2} + \frac{\partial V_\theta}{\partial \theta} \frac{\sin \beta}{R^2} + \frac{1}{R} \frac{\partial^2 V_\theta}{\partial X \partial \theta} \right]
 \end{aligned}$$

Simplifying and rearranging, the equation becomes

$$\begin{aligned}
 & \frac{\partial V_x}{\partial t} + V_x \frac{\partial V_x}{\partial X} + V_y \frac{\partial V_x}{\partial Y} + \frac{V_\theta}{R} \frac{\partial V_x}{\partial \theta} - \frac{V_\theta^2}{R} \sin \beta + \omega \frac{\partial V_x}{\partial \theta} \\
 & + V_\theta \omega \sin \beta \left( 1 - \frac{R_s}{R} \right) - \frac{V_\theta \sin \beta \omega}{R} \cdot (2X \sin \beta + Y \cos \beta) \\
 & - \omega^2 \sin \beta \left[ X \sin \beta \left( 2 \frac{R_s}{R} - 1 \right) + \frac{Y \cos \beta R_s}{R} \right] = F_x \\
 & - \frac{1}{\rho} \frac{\partial p}{\partial X} + \gamma \left[ \frac{\partial^2 V_x}{\partial X^2} + \frac{\partial^2 V_x}{\partial Y^2} + \frac{1}{R^2} \frac{\partial^2 V_y}{\partial \theta^2} \right. \\
 & \left. + \frac{1}{R} \left( \frac{\partial V_x}{\partial X} \sin \beta + \frac{\partial V_x}{\partial Y} \cos \beta \right) - \frac{\sin \beta}{R^2} \left( 2 \frac{\partial V_\theta}{\partial \theta} + V_x \sin \beta + V_y \cos \beta \right) \right] \quad 3.2.23
 \end{aligned}$$

Similarly for the Y direction the equation becomes

$$\begin{aligned}
 & \frac{\partial V_y}{\partial t} + V_x \frac{\partial V_y}{\partial X} + V_y \frac{\partial V_y}{\partial Y} + \frac{V_\theta}{R} \frac{\partial V_y}{\partial \theta} - \frac{V_\theta^2}{R} \cos \beta - \frac{\omega X \cos \beta \sin \beta V_\theta}{R} \\
 & + \frac{\omega R_s}{R} \frac{\partial V_y}{\partial \theta} - \frac{\omega R_s V_\theta \cos \beta}{R} - \frac{\omega^2 R_s X \cos \beta \sin \beta}{R} = F_y \\
 & - \frac{1}{\rho} \frac{\partial p}{\partial Y} + \gamma \left[ \frac{\partial^2 V_y}{\partial X^2} + \frac{\partial^2 V_y}{\partial Y^2} + \frac{1}{R^2} \frac{\partial^2 V_y}{\partial \theta^2} + \frac{1}{R} \left( \frac{\partial V_y}{\partial X} \sin \beta + \frac{\partial V_y}{\partial Y} \cos \beta \right) \right. \\
 & \left. - \frac{\cos \beta}{R^2} \left( V_x \sin \beta + V_y \cos \beta \frac{\partial V_\theta}{\partial \theta} \right) \right] \quad 3.2.24
 \end{aligned}$$

and for the  $\theta$  direction the equation becomes

$$\begin{aligned}
 & \frac{\partial V_\theta}{\partial t} + V_x \frac{\partial V_\theta}{\partial X} + V_y \frac{\partial V_\theta}{\partial Y} + \frac{V_\theta}{R} \frac{\partial V_\theta}{\partial \theta} + \frac{V_\theta}{R} (V_x + V_y \cos \beta) \\
 & + \frac{\omega \sin \beta}{R} (2V_x X \sin \beta + V_y X \cos \beta + V_x Y \cos \beta) = F_\theta \\
 & - \frac{1}{\rho} \frac{\partial p}{\partial \theta} + \gamma \left[ \frac{\partial^2 V_\theta}{\partial X^2} + \frac{\partial^2 V_\theta}{\partial Y^2} + \frac{1}{R^2} \frac{\partial^2 V_\theta}{\partial \theta^2} + \frac{2}{R^2} \left( \frac{\partial V_x}{\partial \theta} \sin \beta + \frac{\partial V_y}{\partial \theta} \cos \beta \right) \right. \\
 & \left. + \frac{1}{R} \left( \frac{\partial V_\theta}{\partial X} \sin \beta + \frac{\partial V_\theta}{\partial Y} \cos \beta \right) - \frac{1}{R^2} \left( V_\theta \sin^2 \beta + V_\theta \sin \beta - \omega Y \sin^2 \beta \cos \beta \right. \right. \\
 & \left. \left. + \omega X \cos^2 \beta \sin \beta \right) \right] \quad 3.2.25
 \end{aligned}$$

### 3.3 Gravitational forces and pressure terms.

For the rotating cone centrifugal force terms and other inertial forces are contained within the general Navier-Stokes equations 3.2.23, 3.2.24 and 3.2.25. Gravity acts as a body force, of dominating importance at low rotational speeds and becoming less important as the speed increases. The gravity terms are given by

$$F_x = g \cos \beta, \quad F_y = -g \sin \beta, \quad F_\theta = 0 \quad 3.3.1$$

Pressure terms are kept separate from centrifugal and gravity terms at this stage because the former will be considered as dependent on changes of local surface effects such as surface tension.

### 3.4 Development of governing equations.

In their complete form the Navier-Stokes equations would be almost, if not entirely intractable, but in the present case they can be simplified in a number of ways by the following assumptions

- (i) During each test a constant speed will be assumed. This means that

$$\frac{\partial v_i}{\partial t} = 0 \quad 3.4.1$$

where  $i = X, Y$  and  $\theta$

- (ii) Drag forces on the surface are considered to be zero, thus the surface shear stress can be assumed zero.
- (iii) We must now look more closely at the form of the Navier-Stokes equations. The lefthand side of equations 3.2.23, 3.2.24 and 3.2.25 consist of inertia terms. In the rotating framework coriolis and centrifugal terms are included. For water and organic liquids Sparrow and Gregg (45) employing a boundary layer type of analysis showed that the inertia forces

resulting from the acceleration of the liquid parallel to the solid surface are negligible compared with for instance viscous forces. However, the centrifugal forces due to the rotation of the cone, and coriolis forces due to the change in the cone radius as the fluid flows down it, are not negligible, and must be retained.

- (iv) when dealing with thin films the order of magnitude of terms in the general equations can often be evaluated by considering the order of magnitude of the changes in the three dimensions. Following the usual boundary layer argument that the typical film thickness  $\delta$  is much smaller than the characteristic length  $X$ , we can assign the relative orders of 1 and  $\xi$  ( $\ll 1$ ) to the magnitude of the changes in the  $X$  and  $Y$  directions respectively. For example on the right-hand side of equation 3.2.23 the term  $\frac{\partial^2 V_x}{\partial Y^2}$  has the order  $\xi^{-2}$  whereas the other viscous terms are no greater than  $\xi^{-1}$  and are also  $X$  dependent, thus the latter terms in comparison with the former are negligible.

- (v) It will be assumed that changes occurring in the  $X$  direction will be small for this particular model. Nusselt showed from his analysis that the increase in film thickness was only of the order  $X^{\frac{1}{4}}$ . Also due to the increase in radius the thinning action tends to counteract the former increase. These two factors mentioned strengthen the assumption that changes in the  $X$  direction occur only slowly.

Applying these assumptions then equation 3.2.6,

$$R = X \sin\beta + Y \cos\beta,$$

reduces to

$$R = X \sin\beta = R_s \quad 3.4.2$$

and the equations 3.2.23, 3.2.24 and 3.2.25 reduce, respectively, to

X direction

$$-2\omega V_{\theta} \sin\beta - \omega^2 R \sin\beta = g \cos\beta - \frac{1}{\rho} \frac{\partial p}{\partial x} + \nu \frac{\partial^2 V_x}{\partial y^2} \quad 3.4.3$$

Y direction

$$-2\omega V_{\theta} \cos\beta - \omega^2 R \cos\beta = -g \sin\beta - \frac{1}{\rho} \frac{\partial p}{\partial y} + \nu \frac{\partial^2 V_y}{\partial y^2} \quad 3.4.4$$

$\theta$  direction

$$2\omega V_x \sin\beta = -\frac{1}{\rho R} \frac{\partial p}{\partial \theta} + \nu \frac{\partial^2 V_{\theta}}{\partial y^2} \quad 3.4.5$$

### 3.5 General assumptions and Boundary conditions.

Throughout the rest of the solution of the governing equations the following will be assumed

- (i) that only pure vapour condenses. This allows the fluid surface temperature to be considered to be that of the steam saturation temperature. The effects of non-condensables on the condensation rate has been widely discussed, for example N.E.L. reports (79). A non-condensable gas tends to accumulate on the liquid-vapour interface and thus to produce a barrier to diffusion of the vapour. The result being an increased temperature drop from the bulk of the vapour to the interface.
- (ii) the physical properties of the film will be evaluated at the Drew reference temperature. This temperature is calculated by the addition of the wall surface temperature and one quarter of the temperature difference across the condensate film

$$T_{drew} = T_w + 0.25(T_s - T_w) \quad 3.5.1$$

McAdams (70) recommended that the viscosity should be

evaluated at this temperature.

- (iii) the velocity of the fluid at the solid boundary is zero, that is no slip at the wall.
- (iv) the flow is laminar at all positions.
- (v) the pressure in the liquid film is hydrodynamic and that the pressure just below the surface is reduced by

$$\sigma \left[ \frac{\frac{1}{R^2} \frac{\partial^2 \zeta}{\partial \theta^2}}{\left(1 + \left(\frac{1}{R} \frac{\partial \zeta}{\partial \theta}\right)^2\right)^{3/2}} \right] \quad 3.5.2$$

- (vi) the velocity profiles throughout the solution will be assumed to be semi-parabolic. The net effect of assumptions (iii), (iv) and (v) is to make the velocity profiles similar at all sections. This is one of the major assumptions in the solution. In the subsequent procedure a point occurs where it is possible to seek a solution without assuming the semi-parabolic velocity profile (3.6.4). This decision must be tolerated to keep the solution within the bounds of computing time available. The non semi-parabolic profile solution also introduces further non-dimensional terms creating extra difficulties in interpreting the results.

### 3.6 Velocity Profiles.

#### 3.6.1 Velocity profile in the X direction.

The equation 3.4.3 can be integrated directly with the initial assumption that  $-2\omega V_\theta \sin \beta$  is small compared with the other term in the equation,  $\omega^2 R \sin \beta + g \cos \beta$ , because  $V_\theta \omega$  is much smaller than  $\omega^2 R$ . Pressure changes in the X direction may be assumed small thus eliminating  $\frac{\partial P}{\partial X}$ , then equation 3.4.3 becomes

$$\rho (\omega^2 R \sin \beta + g \cos \beta) + \mu \frac{\partial^2 V_x}{\partial y^2} = 0 \quad 3.6.1$$

which may be rewritten

$$\frac{\partial^2 V_x}{\partial Y^2} = -\frac{\rho}{\mu} (\omega^2 R \sin \beta + g \cos \beta) \quad 3.6.2$$

Integrating this equation once

$$\frac{\partial V_x}{\partial Y} = -\frac{\rho}{\mu} (\omega^2 R \sin \beta + g \cos \beta) Y + A' \quad 3.6.3$$

One of the boundary conditions is that at the condensate-vapour interface the shear stress is zero, i.e.

$$\text{at } y = \delta, \quad \frac{\partial V_x}{\partial Y} = 0$$

the constant,  $A'$ , becomes

$$A' = \frac{\rho}{\mu} (\omega^2 R \sin \beta + g \cos \beta) \delta$$

Integrating equation 3.6.3, gives the velocity in the X direction :

$$V_x = -\frac{\rho}{\mu} (\omega^2 R \sin \beta + g \cos \beta) \frac{Y^2}{2} + \frac{\rho}{\mu} (\omega^2 R \sin \beta + g \cos \beta) \delta Y + B'$$

At the wall the velocity in the X direction is assumed zero, i.e.

$$V_x = 0 \quad \text{when } \delta = 0$$

Thus the constant,  $B'$ , must be zero. Substituting the value of the constant  $B'$ , into the equation for  $V_x$  and rearranging into a more convenient form

$$V_x = \frac{\rho}{\mu} (\omega^2 R \sin \beta + g \cos \beta) \left( Y \delta - \frac{Y^2}{2} \right) \quad 3.6.4$$

This is the semi-parabolic velocity distribution normally assumed by other workers.

### 3.6.2 Relative circumferential velocity, $V_\theta$ .

For the relative circumferential velocity,  $V_\theta$ , the governing equation, 3.4.5, is:

$$0 = -\frac{1}{R} \frac{\partial P}{\partial \theta} - 2 \rho V_x \omega \sin \beta + \mu \frac{\partial^2 V_\theta}{\partial Y^2}$$

This equation contains the term  $V_x$  as a component. Since the former velocity itself varies with the film thickness it would make the

following equations unmanageable if it were left in its present form. This may be seen by substituting equation 3.6.4 directly into equation 3.4.5 the result is :-

$$\begin{aligned} -\frac{1}{R} \frac{\partial P}{\partial \theta} - \frac{2\rho^2}{\mu} (\omega^2 R \sin \beta + g \cos \beta) \left( Y\delta - \frac{Y^2}{2} \right) \omega \sin \beta \\ + \mu \frac{\partial^2 V_\theta}{\partial Y^2} = 0 \end{aligned} \quad 3.6.5$$

Integrating the above equation twice, and assuming the equation 3.6.16 has already been derived, together with the boundary conditions of;

$V_\theta = 0$ , when  $Y = 0$ , and  $\frac{\partial V_\theta}{\partial Y} = 0$ , when  $Y = \delta$ , one obtains

$$\begin{aligned} V_\theta = \frac{\rho}{R} (\omega^2 R \cos \beta - g \sin \beta) \left( Y\delta - \frac{Y^2}{2} \right) + \frac{\sigma}{R^3} \frac{\partial^3 \delta}{\partial \theta^3} \left( Y\delta - \frac{Y^2}{2} \right) \\ - \frac{\rho^2}{\mu} (\omega^2 R \sin \beta + g \cos \beta) \omega \sin \beta \left( Y\delta^3 - \frac{Y^3 \delta}{3} \right) \\ + \frac{\rho^2}{3\mu} (\omega^2 R \sin \beta + g \cos \beta) \omega \sin \beta \left( Y\delta^3 - \frac{Y^4}{4} \right) \end{aligned} \quad 3.6.6$$

It has already been mentioned that this destroys our semi-parabolic velocity distribution and causes extra difficulties in the subsequent solution of the final equations plus the impossible task of correlating the extra non-dimensional groups so introduced. It is therefore proposed that its effect can be simulated by using the average value of  $V_x$ , given by

$$\begin{aligned} \frac{1}{\delta} \int_0^\delta V_x dY &= \frac{1}{\delta} \int_0^\delta \frac{\rho}{\mu} (\omega^2 R \sin \beta + g \cos \beta) \left( Y\delta - \frac{Y^2}{2} \right) dY \\ &= \frac{1}{\delta} \left[ \frac{\rho}{\mu} (\omega^2 R \sin \beta + g \cos \beta) \left( \frac{Y^2 \delta}{2} - \frac{Y^3}{6} \right) \right]_0^\delta \\ &= \frac{\delta^2}{3} \frac{\rho}{\mu} (\omega^2 R \sin \beta + g \cos \beta) \end{aligned} \quad 3.6.7$$

Equation 3.4.5 then becomes

$$-\frac{1}{R} \frac{\partial P}{\partial \theta} - \frac{2\rho^2 \delta^2 \omega \sin \beta}{3\mu} (\omega^2 R \sin \beta + g \cos \beta) + \mu \frac{\partial^2 V_\theta}{\partial Y^2} = 0$$

which may be rewritten

$$\frac{\partial^2 V_\theta}{\partial Y^2} = \frac{1}{R\mu} \frac{\partial P}{\partial \theta} + \frac{2\rho^2 \delta^2 \omega \sin \beta}{3\mu^2} (\omega^2 R \sin \beta + g \cos \beta) \quad 3.6.8$$

To obtain an expression for the pressure distribution through the film equation 3.4.4 can be used. Since the film is assumed to be everywhere thin then  $\frac{\partial^2 v_y}{\partial y^2}$  can be neglected. The term  $-2\omega v_0 \cos\beta$  may be assumed small compared with the centrifugal term  $\omega^2 R \cos\beta - g \sin\beta$  and so may be neglected in this instance. Then we have

$$\frac{\partial P}{\partial y} = \rho (\omega^2 R \cos\beta - g \sin\beta) \quad 3.6.9$$

Integrating with respect to  $Y$  gives

$$P = \rho (\omega^2 R \cos\beta - g \sin\beta) Y + \text{CONSTANT}$$

The pressure immediately above the film surface is  $P_0$ , just below the surface the pressure is reduced by

$$\sigma \left[ \frac{\frac{1}{R^2} \frac{\partial^2 \delta}{\partial \theta^2}}{\left(1 + \left(\frac{1}{R} \frac{\partial \delta}{\partial \theta}\right)^2\right)^{\frac{3}{2}}} \right] \quad 3.6.10$$

where  $\delta$  is the film thickness, and  $\sigma$  is the surface tension. Since  $\left(\frac{1}{R} \frac{\partial \delta}{\partial \theta}\right)^2$  is negligible, by the order of magnitude criterion, this equation,

3.6.10, reduces to  $\frac{\sigma}{R^2} \frac{\partial^2 \delta}{\partial \theta^2}$  giving :-

$$P = P_0 - \frac{\sigma}{R^2} \frac{\partial^2 \delta}{\partial \theta^2} \quad 3.6.11$$

Then at the surface where  $Y = \delta$ , and the pressure is given by the above equation then we may write

$$P_0 - \frac{\sigma}{R^2} \frac{\partial^2 \delta}{\partial \theta^2} = \rho (\omega^2 R \cos\beta - g \sin\beta) \delta + \text{CONSTANT}$$

$$\text{CONSTANT} = P_0 - \frac{\sigma}{R^2} \frac{\partial^2 \delta}{\partial \theta^2} - \rho (\omega^2 R \cos\beta - g \sin\beta) \delta \quad 3.6.12$$

For simplicity throughout this solution, let

$$\omega^2 R \cos\beta - g \sin\beta = a_y \quad 3.6.13$$

$$\omega^2 R \sin\beta + g \cos\beta = a_x \quad 3.6.14$$

Equation 3.6.12 may be rewritten,

$$\text{CONSTANT} = P_0 - \frac{\sigma}{R^2} \frac{\partial^2 \delta}{\partial \theta^2} - \rho a_y \delta$$

then

$$P = \rho a_y Y + P_0 - \frac{\sigma}{R^2} \frac{\partial^2 \delta}{\partial \theta^2} - \rho a_y \delta$$

$$P = \rho a_y (\gamma - \delta) + P_0 - \frac{\sigma}{R^2} \frac{\partial^2 \delta}{\partial \theta^2} \quad 3.6.15$$

Equation 3.6.15 is then the pressure distribution through the film.

Differentiating the equation with respect to  $\theta$  produces,

$$\frac{\partial P}{\partial \theta} = -\rho a_y \frac{\partial \delta}{\partial \theta} - \frac{\sigma}{R^2} \frac{\partial^3 \delta}{\partial \theta^3}$$

$$\text{then } \frac{1}{R} \frac{\partial P}{\partial \theta} = -\frac{\rho a_y}{R} \frac{\partial \delta}{\partial \theta} - \frac{\sigma}{R^3} \frac{\partial^3 \delta}{\partial \theta^3} \quad 3.6.16$$

Substituting equation 3.6.16 into equation 3.6.8 gives

$$\frac{\partial^2 V_\theta}{\partial \gamma^2} = \frac{1}{\mu} \left[ -\left( \frac{\rho a_y}{R} \frac{\partial \delta}{\partial \theta} + \frac{\sigma}{R^3} \frac{\partial^3 \delta}{\partial \theta^3} \right) + \frac{2}{3} \frac{\delta^2 \rho^2}{\mu} \omega \sin \beta a_x \right] \quad 3.6.17$$

Integration of the above equation requires,

$$\frac{\partial V_\theta}{\partial \gamma} = \frac{1}{\mu} \left[ \frac{2}{3} \frac{\delta^2 \rho^2}{\mu} \omega \sin \beta a_x - \left( \frac{\rho a_y}{R} \frac{\partial \delta}{\partial \theta} + \frac{\sigma}{R^3} \frac{\partial^3 \delta}{\partial \theta^3} \right) \right] \gamma + A_0$$

when,  $\gamma = \delta$ ,  $\frac{\partial V_\theta}{\partial \gamma} = 0$  then the constant is :-

$$A_0 = -\frac{1}{\mu} \left[ \frac{2}{3} \frac{\delta^2 \rho^2}{\mu} \omega \sin \beta a_x - \left( \frac{\rho a_y}{R} \frac{\partial \delta}{\partial \theta} + \frac{\sigma}{R^3} \frac{\partial^3 \delta}{\partial \theta^3} \right) \right] \delta \quad 3.6.18$$

Integrating once more gives,

$$V_\theta = \frac{1}{\mu} \left[ \frac{2}{3} \frac{\delta^2 \rho^2}{\mu} \omega \sin \beta a_x - \left( \frac{\rho a_y}{R} \frac{\partial \delta}{\partial \theta} + \frac{\sigma}{R^3} \frac{\partial^3 \delta}{\partial \theta^3} \right) \right] \frac{\gamma^2}{2} + A_0 \gamma + B_0 \quad 3.6.19$$

$$\text{when, } \gamma = 0, V_\theta = 0, \text{ then } B_0 = 0 \quad 3.6.20$$

Substituting the constants, given by 3.6.18 and 3.6.20, into equation 3.6.19 we have

$$V_\theta = \frac{1}{\mu} \left[ -\frac{2}{3} \frac{\delta^2 \rho^2}{\mu} \omega \sin \beta a_x + \left( \frac{\rho a_y}{R} \frac{\partial \delta}{\partial \theta} + \frac{\sigma}{R^3} \frac{\partial^3 \delta}{\partial \theta^3} \right) \right] \left( \gamma \delta - \frac{\gamma^2}{2} \right) \quad 3.6.21$$

In general terms we now have equations for both  $V_x$  and  $V_\theta$ , given in equations 3.6.4 and 3.6.21 respectively.

### 3.7 Continuity Equation

We must now turn our attention to the question of continuity of flow. Consider an elemental segment shown in figure 5.

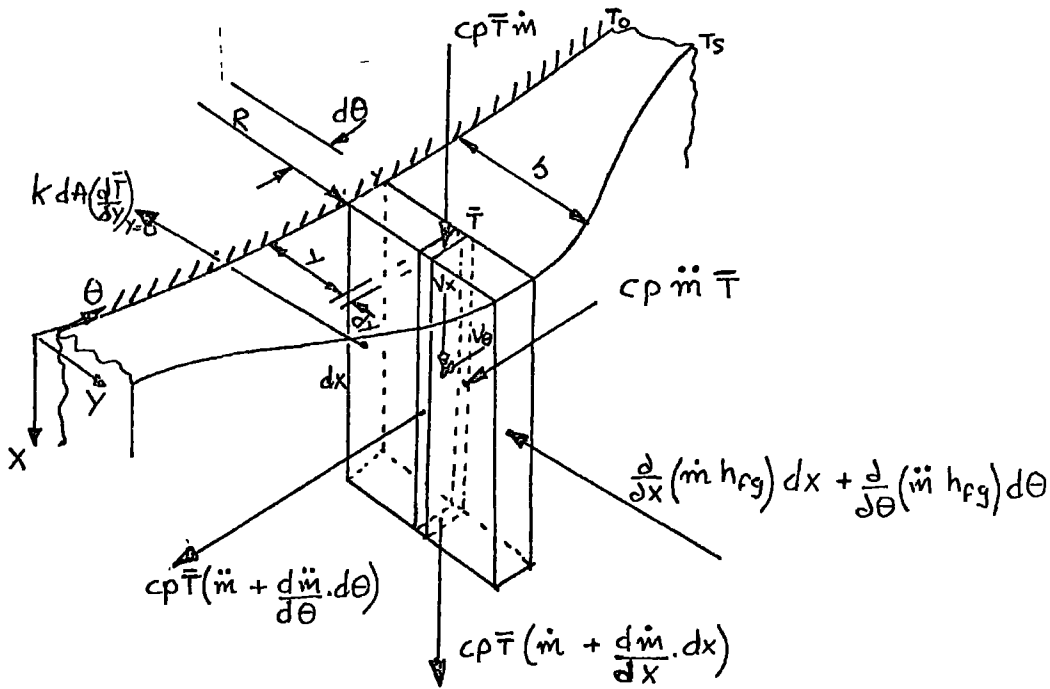


Figure 5. Elemental segment in model surface.

$$\dot{m} = \int_0^s \rho V_x R d\theta dy \quad 3.7.1$$

$$\dot{m} = \int_0^s \rho V_\theta dx dy \quad 3.7.2$$

Equating the energy transferred across the element

$$\begin{aligned} dQ &= \frac{\partial}{\partial x} \left[ \dot{m} h_{fg} + c_p \dot{m} (T_s - \bar{T}) \right] dx \\ &+ \frac{\partial}{R \partial \theta} \left[ \dot{m} h_{fg} + c_p \dot{m} (T_s - \bar{T}) \right] R d\theta \\ &= k R d\theta dx \left( \frac{\partial \bar{T}}{\partial y} \right)_{y=0} \end{aligned}$$

Introducing 3.7.1 and 3.7.2

$$\begin{aligned} &\frac{\partial}{\partial x} \left[ \rho h_{fg} \int_0^s V_x R d\theta dy + \rho c_p \int_0^s V_x R d\theta dy (T_s - \bar{T}) \right] dx \\ &+ \frac{\partial}{R \partial \theta} \left[ \rho h_{fg} \int_0^s V_\theta dx dy + \rho c_p \int_0^s V_\theta dx dy (T_s - \bar{T}) \right] R d\theta \end{aligned}$$

$$= k R d\theta dx \left( \frac{\partial \bar{T}}{\partial Y} \right)_{Y=0} \quad 3.7.3$$

### 3.8 Solution of the Equation

Rohsenow (42) showed that a linear temperature profile was an excellent approximation for most flows, confirmed by Koh, Sparrow and Hartnett (86)

$$(T_s - \bar{T}) = \Delta T \left( 1 - \frac{Y}{S} \right) \quad 3.8.1$$

Simplifying equation 3.7.3 and introducing 3.8.1 together with the equations for  $V_x$  and  $V_\theta$ , 3.6.4 and 3.6.21 respectively, we have

$$\begin{aligned} & \frac{\partial}{\partial X} \left[ \rho h_{fg} R \int_0^S \frac{\rho a_x}{\mu} \left( YS - \frac{Y^2}{2} \right) dY + \rho c_p R \int_0^S \frac{\rho a_x}{\mu} \left( YS - \frac{Y^2}{2} \right) \Delta T \left( 1 - \frac{Y}{S} \right) dY \right] \\ & + \frac{\partial}{\partial \theta} \left[ \rho h_{fg} \int_0^S \frac{1}{\mu} \left( -\frac{2}{3} \frac{S^2}{\mu} \rho^2 \omega \sin \beta a_x + \frac{\rho a_y}{R} \frac{\partial s}{\partial \theta} + \frac{\sigma}{R^3} \frac{\partial^3 s}{\partial \theta^3} \right) \left( YS - \frac{Y^2}{2} \right) dY \right. \\ & \quad \left. + \rho c_p \int_0^S \frac{\Delta T}{\mu} \left( -\frac{2}{3} \frac{S^2}{\mu} \rho^2 \omega \sin \beta a_x + \frac{\rho a_y}{R} \frac{\partial s}{\partial \theta} + \frac{\sigma}{R^3} \frac{\partial^3 s}{\partial \theta^3} \right) \left( YS - \frac{Y^2}{2} \right) \left( 1 - \frac{Y}{S} \right) dY \right] \\ & = k R \left( \frac{\partial \bar{T}}{\partial Y} \right)_{Y=0} \quad 3.8.2 \end{aligned}$$

Performing the integration within the brackets

$$\begin{aligned} & \frac{\partial}{\partial X} \left[ \frac{\rho^2 h_{fg} R a_x}{\mu} \left( \frac{Y^2 S}{2} - \frac{Y^3}{6} \right)_0^S + \frac{\rho^2 c_p R a_x \Delta T}{\mu} \left( \frac{Y^2 S}{2} - \frac{Y^3}{3} - \frac{Y^3}{6} + \frac{Y^4}{8S} \right)_0^S \right] \\ & + \frac{\partial}{\partial \theta} \left[ \rho h_{fg} R \cdot \frac{1}{\mu} \left( -\frac{2}{3} \frac{S^2}{\mu} \rho^2 \omega \sin \beta a_x + \frac{\rho a_y}{R} \frac{\partial s}{\partial \theta} + \frac{\sigma}{R^3} \frac{\partial^3 s}{\partial \theta^3} \right) \left( \frac{Y^2 S}{2} - \frac{Y^3}{6} \right)_0^S \right. \\ & \quad \left. + \rho c_p \frac{\Delta T}{\mu} \left( -\frac{2}{3} \frac{S^2}{\mu} \rho^2 \omega \sin \beta a_x + \frac{\rho a_y}{R} \frac{\partial s}{\partial \theta} + \frac{\sigma}{R^3} \frac{\partial^3 s}{\partial \theta^3} \right) \left( \frac{Y^2 S}{2} - \frac{Y^3}{3} - \frac{Y^3}{6} + \frac{Y^4}{8S} \right)_0^S \right] \\ & = k \cdot R \left( \frac{\partial \bar{T}}{\partial Y} \right)_{Y=0} \end{aligned}$$

hence

$$\begin{aligned} & \frac{\partial}{\partial X} \left[ \frac{\rho^2 h_{fg} R a_x S^3}{\mu} + \frac{\rho^2 c_p a_x R \Delta T S^3}{\mu} \right] + \\ & \frac{\partial}{\partial \theta} \left[ \frac{\rho h_{fg}}{\mu} \left( -\frac{2}{3} \frac{S^2}{\mu} \rho^2 \omega \sin \beta a_x + \frac{\rho a_y}{R} \frac{\partial s}{\partial \theta} + \frac{\sigma}{R^3} \frac{\partial^3 s}{\partial \theta^3} \right) \frac{S^3}{3} \right. \\ & \quad \left. + \frac{\rho c_p \Delta T}{\mu} \left( -\frac{2}{3} \frac{S^2}{\mu} \rho^2 \omega \sin \beta a_x + \frac{\rho a_y}{R} \frac{\partial s}{\partial \theta} + \frac{\sigma}{R^3} \frac{\partial^3 s}{\partial \theta^3} \right) \frac{S^3}{8} \right] \\ & = k R \left( \frac{\partial \bar{T}}{\partial Y} \right)_{Y=0} \quad 3.8.3 \end{aligned}$$

Now  $R = X \sin\beta$  and  $a_x = \omega^2 R \sin\beta + g \cos\beta$

Performing the differentiation and simplifying

$$\begin{aligned} & \left[ \frac{\rho^2}{\mu} \left( 2 \omega^2 X \sin^2\beta + g \cos\beta \sin\beta \right) \frac{s^3}{3} \right. \\ & \quad \left. + \frac{\rho^2}{\mu} \left( \omega^2 X^2 \sin^3\beta + g X \cos\beta \sin\beta \right) \frac{s^2 ds}{dx} \right] \left[ h_{fg} + \frac{3c_p \Delta T}{8} \right] \\ & + \left[ -\frac{10s^4}{9} \frac{\rho^3}{\mu^2} \omega \sin\beta a_x \frac{ds}{d\theta} + \frac{\rho^2}{3R\mu} a_y \frac{d^2s}{d\theta^2} s^3 + \frac{\rho^2 a_y}{R\mu} \left( \frac{ds}{d\theta} \right)^2 s^2 \right. \\ & \left. + \frac{\rho \sigma}{3\mu R^3} \frac{d^4s}{d\theta^4} s^3 + \frac{\rho \sigma}{\mu R^3} \frac{d^3s}{d\theta^3} s^2 \right] \left[ h_{fg} + \frac{3c_p \Delta T}{8} \right] = k \cdot R \cdot \frac{\Delta T}{s} \end{aligned}$$

Rearranging the above equation we obtain

$$\begin{aligned} & \frac{\rho s^3}{3\mu} \left( 2 \omega^2 \sin^2\beta + g \frac{\cos\beta}{X} \right) + \frac{\rho a_x}{\mu} \frac{ds}{dx} s^2 \\ & - \frac{10}{9} \frac{\rho^2}{\mu^2} \frac{\omega \sin\beta}{R} a_x s^4 + \frac{\rho^2}{3R^2} \frac{a_y}{\mu} \frac{d^2s}{d\theta^2} s^3 + \frac{\rho a_y}{R^2 \mu} \left( \frac{ds}{d\theta} \right)^2 s^2 \\ & + \frac{\sigma}{3\mu R^4} \frac{d^4s}{d\theta^4} s^3 + \frac{\sigma}{\mu R^4} \frac{d^3s}{d\theta^3} s^2 = \frac{k \Delta T}{\rho h_{fg} \left( 1 + \frac{3c_p \Delta T}{8 h_{fg}} \right) s} \quad 3.8.4 \end{aligned}$$

The dimensionless group  $cp\Delta T/h_{fg}$  signifies the effect of sub-cooling which occurs in the condensate layer. The quantity  $h_{fg}$  is replaced by  $(h_{fg} + 0.375 cp\Delta T)$  but the additional term only becomes significant when dealing with liquid metals. The value of 0.375 in the formula can be replaced by 0.68 if a parabolic temperature profile is assumed instead of the linear one assumed here.

#### Formation of the non-dimensional equation

Equation 3.8.4 can be made dimensionless by defining the following new variables

$$\bar{s} = \frac{s}{s_{MIN}}, \quad \bar{\theta} = \frac{R\theta}{\left[ \frac{\sigma}{\rho a_y} \right]^{1/2}}, \quad \bar{x} = X \frac{\rho a_y^2 s_{MIN}}{\sigma a_x} \quad 3.8.5$$

Tackling equation 3.8.4 term by term for simplification and introducing the new variables gives :-

$$\begin{aligned} \frac{s^2}{\mu} \rho a_x \frac{ds}{dx} &= \frac{\bar{s}^2 s_{MIN}^2}{\mu} \frac{\rho a_x}{\sigma} \frac{s_{MIN}}{a_x} \frac{d\bar{s}}{d\bar{x}} \rho a_y^2 \frac{s_{MIN}}{\sigma} = \frac{\bar{s}^2 s_{MIN}^4}{\mu \sigma} \rho a_y^2 \frac{d\bar{s}}{d\bar{x}} \\ \frac{s^3}{3\mu} \frac{\rho a_y}{R^2} \frac{d^2s}{d\theta^2} &= \frac{\bar{s}^3 s_{MIN}^3}{3\mu} \frac{\rho a_y}{R^2} \frac{s_{MIN}}{\sigma} \frac{d^2\bar{s}}{d\bar{\theta}^2} R^2 a_y \rho = \frac{\bar{s}^3 s_{MIN}^4}{3\mu \sigma} \rho a_y^2 \frac{d^2\bar{s}}{d\bar{\theta}^2} \\ \frac{s^2}{\mu} \frac{\rho a_y}{R^2} \left( \frac{ds}{d\theta} \right)^2 &= \frac{\bar{s}^2 s_{MIN}^2}{\mu} \frac{\rho a_y}{R^2 \sigma} \frac{s_{MIN}^2}{\sigma} \left( \frac{d\bar{s}}{d\bar{\theta}} \right)^2 \rho a_y R = \frac{\bar{s}^2 s_{MIN}^4}{\mu \sigma} \rho a_y^2 \left( \frac{d\bar{s}}{d\bar{\theta}} \right)^2 \end{aligned}$$

$$\begin{aligned} \frac{\bar{s}^3}{3\mu} \frac{\sigma}{R^4} \frac{\partial^4 \bar{s}}{\partial \bar{\theta}^4} &= \frac{\bar{s}^3 \bar{s}_{MIN}^3}{3\mu} \frac{\sigma}{R^4} \frac{\partial^4 \bar{s}}{\partial \bar{\theta}^4} R^4 \frac{\rho^2 a_y^2 \bar{s}_{MIN}}{\sigma^2} = \frac{\bar{s}^3 \bar{s}_{MIN}^4}{3\mu \sigma} \frac{\rho^2 a_y^2}{\sigma^2} \frac{\partial^4 \bar{s}}{\partial \bar{\theta}^4} \\ \frac{\bar{s}^2}{\mu} \frac{\sigma}{R^4} \frac{\partial^3 \bar{s}}{\partial \bar{\theta}^3} \frac{\partial \bar{s}}{\partial \bar{\theta}} &= \frac{\bar{s}^2 \bar{s}_{MIN}^2}{\mu} \frac{\sigma}{R^4} \left( \frac{\partial^3 \bar{s}}{\partial \bar{\theta}^3} \right) \left( \frac{\partial \bar{s}}{\partial \bar{\theta}} \right) R^4 \frac{\rho^2 a_y^2 \bar{s}_{MIN}^2}{\sigma^2} = \frac{\bar{s}^2 \bar{s}_{MIN}^4}{\mu \sigma} \frac{\rho^2 a_y^2}{\sigma^2} \frac{\partial^3 \bar{s}}{\partial \bar{\theta}^3} \frac{\partial \bar{s}}{\partial \bar{\theta}} \\ \frac{10}{9} \frac{\bar{s}^4}{\mu^2} \frac{\rho^2 \omega \sin \beta}{R} \frac{a_x \partial \bar{s}}{\partial \bar{\theta}} &= \frac{10}{9} \frac{\bar{s}^4 \bar{s}_{MIN}^4}{\mu^2} \frac{\rho^2 \omega \sin \beta}{R} \frac{a_x}{R} \frac{\partial \bar{s}}{\partial \bar{\theta}} \left( \frac{\rho a_y}{\sigma} \right)^{\frac{1}{2}} \bar{s}_{MIN} R \\ &= \frac{10}{9} \frac{\bar{s}^4 \bar{s}_{MIN}^5}{\mu^2} \frac{\rho^2 \omega \sin \beta}{R} \frac{a_x}{R} \left( \frac{\rho a_y}{\sigma} \right)^{\frac{1}{2}} \frac{\partial \bar{s}}{\partial \bar{\theta}} \\ \frac{\rho \bar{s}^3}{3\mu} \left( 2\omega^2 \sin^2 \beta + g \frac{\cos \beta}{x} \right) &= \frac{\bar{s}^3 \bar{s}_{MIN}^3}{3\mu} \rho \left( 2\omega^2 \sin^2 \beta + \frac{\rho a_y^2 \bar{s}_{MIN} g \cos \beta}{x \sigma a_x} \right) \\ \frac{k \Delta T}{\rho h_{fg} \bar{s} \left( 1 + \frac{3c_p \Delta T}{8 h_{fg}} \right)} &= \frac{k \Delta T}{\rho h_{fg} \bar{s}_{MIN} \left( 1 + \frac{3c_p \Delta T}{8 h_{fg}} \right)} \end{aligned}$$

Re-combining the non-dimensional terms into 3.8.4 and rearranging by extracting the factor  $\frac{\bar{s}_{MIN}^4 \rho^2 a_y^2}{3\mu \sigma}$  we obtain :-

$$\begin{aligned} \frac{\bar{s}_{MIN}^4 \rho^2 a_y^2}{3\mu \sigma} \left( 3\bar{s}^3 \frac{\partial \bar{s}}{\partial \bar{x}} + \frac{2\bar{s}^3 \omega^2 \sin^2 \beta \sigma}{\bar{s}_{MIN} \rho a_y^2} + \frac{\bar{s}^3 g \cos \beta}{x a_x} \right) + 3\bar{s}^3 \left( \frac{\partial \bar{s}}{\partial \bar{\theta}} \right)^2 \\ + \bar{s}^4 \frac{\partial^4 \bar{s}}{\partial \bar{\theta}^4} + 3\bar{s}^3 \frac{\partial^3 \bar{s}}{\partial \bar{\theta}^3} \frac{\partial \bar{s}}{\partial \bar{\theta}} - \frac{10}{3} \frac{\bar{s}^5}{\partial \bar{\theta}} \frac{\bar{s}_{MIN}}{\mu} \left( \frac{\sigma \rho}{a_y^3} \right)^{\frac{1}{2}} \omega \sin \beta a_x \\ = \frac{k \Delta T}{\rho h_{fg} \bar{s}_{MIN} \left( 1 + \frac{3c_p \Delta T}{8 h_{fg}} \right)} \end{aligned} \quad 3.8.6$$

In equation 3.8.6 there are three main non-dimensional groups. If the constant multiplier on the lefthand side of the equation is taken across to the other side we have a governing non-dimensional group which will be given the symbol  $\Lambda$  and is defined by

$$\Lambda = \frac{k \Delta T \mu \sigma}{h_{fg} \rho^3 a_y^2 \bar{s}_{MIN}^5 \left( 1 + \frac{3c_p \Delta T}{8 h_{fg}} \right)} \quad 3.8.7$$

It is of major importance because it embodies many of the system variables.

Two other groups which also appear in the equation are to be denoted by

$\Omega$  and  $\Theta$ . These are defined by

$$\Omega = \frac{\omega^2 \sin^2 \beta \sigma}{\bar{s}_{MIN} \rho a_y^2}$$

$$\text{and } \Theta = \frac{\omega \sin \beta a_x \bar{s}_{MIN}}{\left( \frac{\sigma \rho}{a_y^3 \mu^2} \right)^{\frac{1}{2}}} \quad 3.8.8$$

It may be seen that for any value of  $\Lambda$  both  $\Omega$  and  $\Theta$  may then be calculated.

Substituting these symbols for the non-dimensional groups in equation 3.8.6 gives

$$3\bar{z}^3 \frac{\partial \bar{z}}{\partial \bar{x}} + 2\Omega \bar{z}^3 + g \frac{\cos \beta}{\bar{x}} \frac{\bar{z}^3}{a_x} + \bar{z}^4 \frac{\partial^2 \bar{z}}{\partial \bar{\theta}^2} + 3\bar{z}^3 \left( \frac{\partial \bar{z}}{\partial \bar{\theta}} \right)^2 + \bar{z}^4 \frac{\partial^4 \bar{z}}{\partial \bar{\theta}^4} + 3\bar{z}^3 \frac{\partial^3 \bar{z}}{\partial \bar{\theta}^3} \frac{\partial \bar{z}}{\partial \bar{\theta}} - \frac{10}{3} \textcircled{H} \bar{z}^5 \frac{\partial \bar{z}}{\partial \bar{\theta}} = 3\Lambda \quad 3.8.9$$

In equation 3.8.9 the term  $\bar{z}^3 \left( 2\Omega + \frac{g \cos \beta}{\bar{x}} \frac{\bar{z}^3}{a_x} \right)$  is one of special mention. The reason being that throughout the proceeding computations the term has been replaced simply by  $\Omega \bar{z}^3$ . In this particular analysis the term is of relatively small importance compared with the other terms. The non-dimensional term  $\Omega$  is itself small order because it has as a multiplier  $\sin^2 \beta$  with a denominator of  $ay^2$ . The other non-dimensional term  $\frac{g \cos \beta \bar{z}^3}{\bar{x} a_x}$  may be neglected due to its dependence on changes in the 'X' direction which throughout this analysis have been considered as of small order compared with the circumferential direction.

The effect of making the simplification of  $\Omega \bar{z}^3$  causes an average reduction in the non-dimensional peak film thickness of less than 0.35% and in the non-dimensional wavelength of less than 0.17%. For a more fuller account of the above change see Appendix F.

It has already been assumed throughout the development and solution of the previous equations that rates of change in the 'X' direction were small. This being the case then we can say that

$$\bar{z} = \text{CONST.} (1 + \epsilon \bar{x}) \quad 3.8.10$$

where  $\epsilon$  is a small number. Thus the differential with respect to  $\bar{x}$  is

$$\frac{\partial \bar{z}}{\partial \bar{x}} = \epsilon \bar{z} \quad 3.8.11$$

This is a major assumption because at this point we loose all information about what will happen as we move in the 'X' direction. What we are now saying is that for a small distance, governed by  $\epsilon$ , each side of a chosen value of radius there is no significant change in the film thickness relationship which will now be solved for the 'Y' and ' $\theta$ ' directions. That is we have reduced our system from one of

three-dimensions to that of two. Consequently, substituting 3.8.11 into equation 3.8.9 we obtain

$$\begin{aligned} 3 \varepsilon \bar{z}^4 + \bar{z}^4 \frac{\partial^2 \bar{z}}{\partial \bar{\theta}^2} + 3 \bar{z}^3 \left( \frac{\partial \bar{z}}{\partial \bar{\theta}} \right)^2 + \bar{z}^4 \frac{\partial^4 \bar{z}}{\partial \bar{\theta}^4} + \Omega \bar{z}^3 \\ + 3 \bar{z}^3 \left( \frac{\partial^3 \bar{z}}{\partial \bar{\theta}^3} \right) \left( \frac{\partial \bar{z}}{\partial \bar{\theta}} \right) - \frac{10}{3} \Theta \bar{z}^5 \frac{\partial \bar{z}}{\partial \bar{\theta}} = 3 \Lambda \end{aligned} \quad 3.8.12$$

Finally, if primes are used to signify differentiation with respect to  $\bar{\theta}$  the equation may be rewritten

$$\begin{aligned} \bar{z}''' = \frac{3 \Lambda}{\bar{z}^4} - \bar{z} \bar{z}'' - \frac{3 (\bar{z}')^2}{\bar{z}} - \frac{3 \bar{z}'' \bar{z}'}{\bar{z}} \\ - 3 \varepsilon - \frac{\Omega}{\bar{z}} + \frac{10}{3} \Theta \bar{z} \bar{z}' \end{aligned} \quad 3.8.13$$

By taking  $\delta_{\min}$  as the characteristic dimension of the film thickness, it is possible to specify completely the problem as an initial value one. Two of the initial values are obtained from consideration of symmetry, namely that the first and third derivatives must be zero at the point of minimum film thickness. A third was that, at minimum film thickness the non-dimensional film thickness must be unity. Fourthly, that at the point of minimum film thickness the curvature vanishes, i.e. the rate of change of curvature is zero. Written in our non-dimensional terminology these initial values become

$$\bar{z} = 1, \quad \bar{z}' = 0, \quad \bar{z}'' = 0, \quad \text{and} \quad \bar{z}''' = 0 \quad 3.8.14$$

Employing the initial conditions set out above the equation, 3.8.13, was solved numerically using the I.B.M. S/360 Continuous System Modelling Program (C.S.M.P.) (82). The program was run on an I.B.M. 360/67 digital computer.

One of the initial problems encountered when using the modelling program was that on each run the value of  $\varepsilon$  had to be evaluated which gave a full cyclic condition. After exhaustive runs it was found that over one half of a wavelength the effect of not having a full

cyclic run was less than 0.1% change in  $\bar{z}_{max}$ . Typical curves for  $\bar{z}$  against  $\bar{\theta}$  for two values of  $\epsilon$  are given in figure 30. These curves show that although values of  $\epsilon$  are not critical a method of evaluating their size with varying conditions is necessary. The method is fully described in Appendix C.

The analysis proved that given a set of conditions, cone speed, cone angle and physical properties of the fluid; a certain wavelength and corresponding ratio of peak film thickness to that of trough film thickness,  $\bar{z}_{max}$ , would be predicted.

### 3.9 Parameter Variation.

The dimensionless parameters  $\Lambda$ ,  $\Theta$  and  $\Omega$  occur in the governing equation 3.3.13 and their nominal value must be known before a numerical solution is attempted. The quantity  $\Lambda$  has a greater influence on the solution than  $\Theta$  and  $\Omega$  which can be calculated from it. It is difficult to put an exact interpretation on  $\Lambda$  because it is a function of virtually all the variables involved in condensation on rotating surfaces. It is related to the energy level by the condensate film temperature difference, to a balance of inertia forces by the acceleration in the Y direction and surface tension and also to the surface configuration by the minimum film thickness, that is the film thickness in the trough. The physical properties of the condensate also have a certain amount of influence in determining  $\Lambda$ .

The quantity  $\Theta$  is not such a powerful term because by substituting for  $z_{min}$  we obtain

$$\Theta = \frac{\omega}{a_y} \frac{S_{11}\beta}{a_y} \left( \frac{k \Delta T}{(1 + 0.375 \frac{c_p \Delta T}{h_{fg}}) h_{fg} \Lambda} \right)^{\frac{1}{5}} \left( \frac{\sigma^7 a_y}{\mu^8 e} \right)^{\frac{1}{10}}$$

which shows that it is only dependent on  $\Lambda$  to the power 0.2. It is a

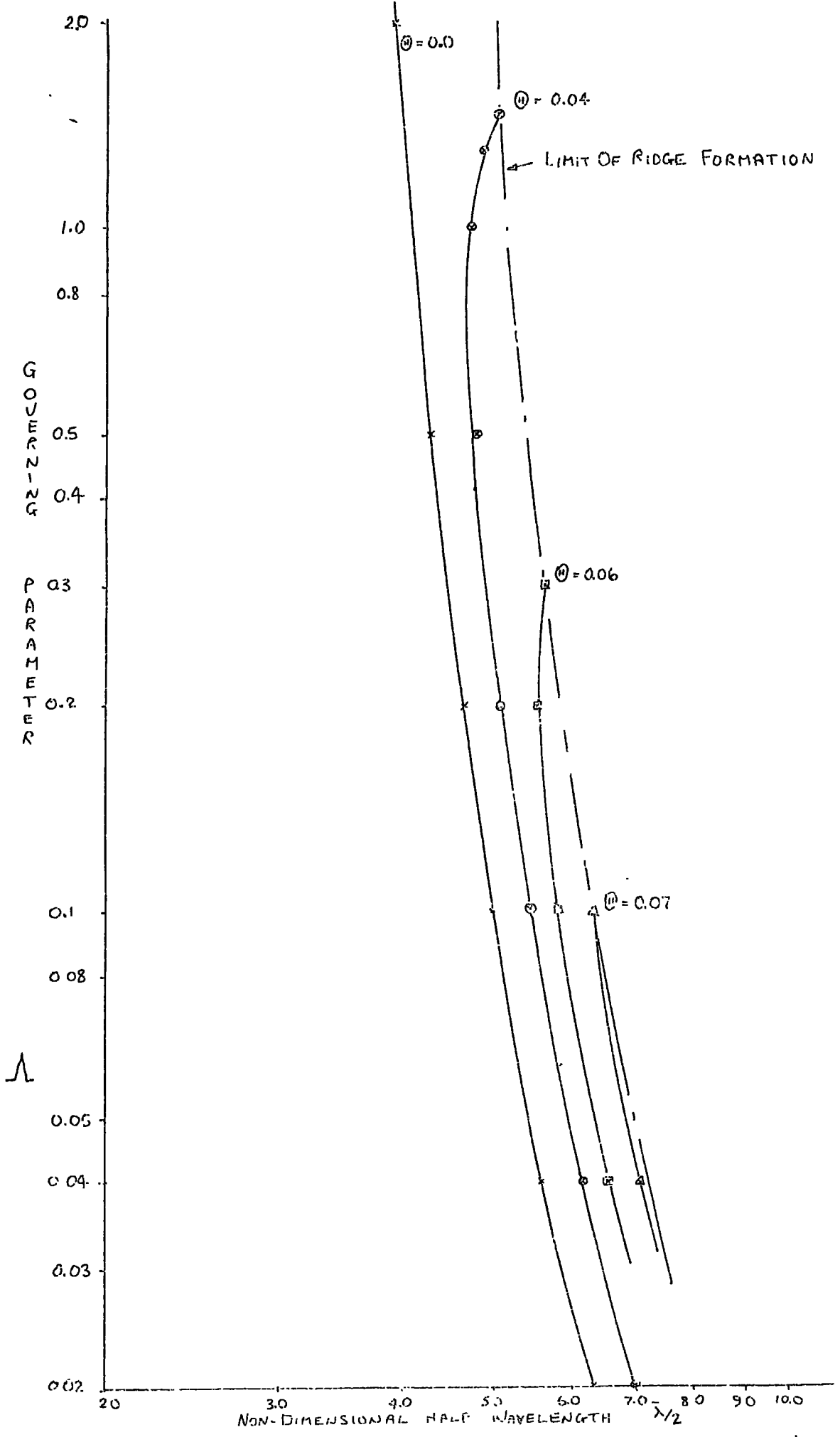


FIGURE 6. VARIATION OF NON-DIMENSIONAL HALF WAVELENGTH WITH  $\lambda$ .

quantity which qualifies the Coriolis term in the governing equation and it may thus be said that the effect of Coriolis will not be great. The final parameter  $\Omega$  is derived from the term in the general equation concerned with the reciprocal of the non-dimensional film thickness alone. For our slender cones the numerical value is small because  $\sin^2 \beta$  is of small value. Compared with  $\Lambda$  it is negligible but included for completeness.

The range of  $\Lambda$  investigated was 0.02 to 10.0. This range was chosen because it covers the values of wavelength and film thickness found in practice. The maximum practical value of  $\Theta$ , which occurred at low rotational speed was found to be 0.07. The working range examined was 0.0 to 0.07. The solution of equation 3.8.13 for the above range of  $\Lambda$  and  $\Theta$  was performed on an I.B.M. computer using the C.S.M.P. package. A full description of this program and its operation is given in Appendix D. The results of these computations are shown in figures 6. and 7. Figure 6. shows the variation of dimensionless half wavelength with  $\Lambda$  and  $\Theta$ , and figure 7. the variation of dimensionless film thickness, the ratio of peak film thickness to that at the bottom of a trough.

Data presented in figure 6. reveals that a family of curves exists for the relationship between  $\Lambda$  and non-dimensional half wavelength, with varying  $\Theta$ . A limit of stability exists for the prediction of ridge type waves. Generally as the parameter  $\Theta$  becomes smaller, which is determined mainly by the acceleration in the Y direction,  $a_y$ , squared, the greater the range of  $\Lambda$  for ridge like waves to exist. It is not possible for ridge type waves to be formed when  $\Theta$  is greater than 0.071. This limiting value is dependent on many factors but as mentioned above the most important being the acceleration in the Y direction. A factor involved in this parameter is the ratio of the

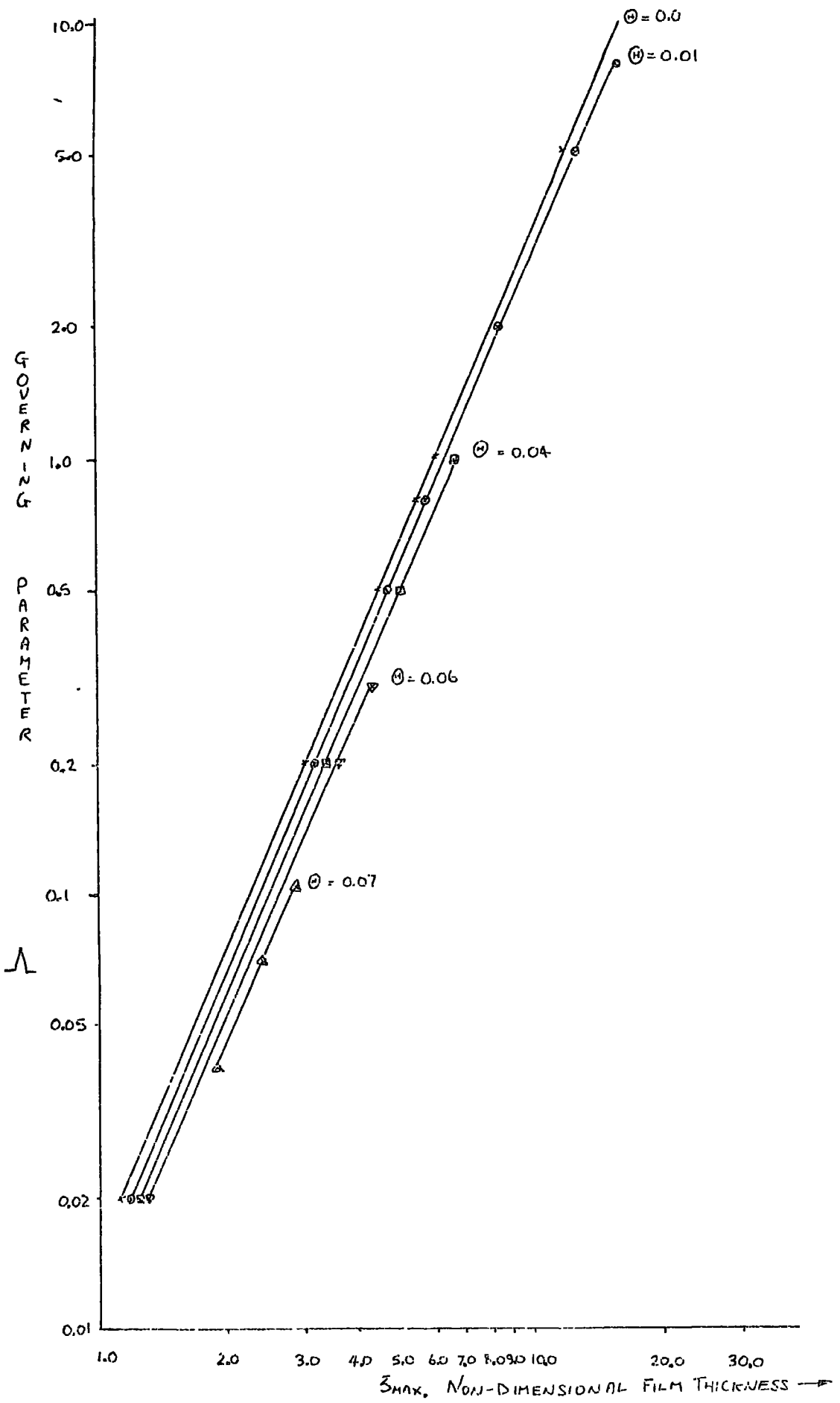


FIGURE 7. VARIATION OF NON-DIMENSIONAL FILM THICKNESS WITH  $\lambda$ .

acceleration in the Y direction to that in the X direction,  $a_y/a_x$ , which will be used later as a variable for distinguishing the limits for which certain type and ridge like regimes continue, and the point at which drops commence leaving the ridge peaks.

The relationship between  $\Lambda$  and the non-dimensional film thickness,  $\bar{z}_{\max}$ , is an almost linear one on a log-log scale. The effect of increasing  $\Lambda$  is one of increasing the ratio of the peak film thickness to that of trough film thickness,  $\bar{z}_{\max}$ . From figure 7. we can see that increase of  $\Lambda$  also increases the ratio  $\bar{z}_{\max}$ . The length of the lines, for varying  $\Theta$ , show the limits of  $\Lambda$  for which the ridge like waves will be predicted.

The quantity  $\Lambda$  is very sensitive to changes in the minimum, or trough, film thickness. This means that to calculate  $\Lambda$  an accurate measurement of  $\bar{z}_{\min}$  would be necessary. It is difficult to draw any direct conclusions from figures 6 and 7 because the effect of each variable is very complex and impossible to analyse singly.

Finally little mention has been made of the quantity  $\Omega$  other than to say it was of small importance. A check was made by neglecting it in one computer run with the result that no change occurred in the non-dimensional half wavelength and less than 0.1% change in  $\bar{z}_{\max}$ . Values of  $\Omega$  considered ranged from 0.0005 to 0.0016.

#### 4.0 EXPERIMENTAL WORK

#### 4.1 Apparatus.

The rig has been fully described in both Robson's thesis (68) and Howe's work (67,69). It consists essentially of a steel pressure vessel, which has seven observation ports, capable of withstanding dry saturated steam at a working pressure of 13.8 bar. The cone under test was mounted on a base plate inside the vessel. The base plate was connected to a hollow main shaft supported rigidly in two main bearings solidly earthed to the pressure vessel body. A mechanical seal was necessary at the point where the main shaft enters the pressure vessel, the seal was lubricated and cooled by having a constant flow of water supplied at a pressure one or two bar above the vessel working pressure. The main shaft was belt driven, at speeds varying between 50 to 2000 r.p.m., by an 11.5 kw direct current motor. The latter being controlled by a 400-440 volt, 3 phase, 50 Hz., thyristor fired bridge rectifier circuit. The general arrangement drawing is shown in figure 8.

The inner surface of the cone was cooled by water pumped from a closed loop circuit, introduced through a central pipe and finally sprayed onto the surface. The control on the spray unit, consisting of a gate valve on the line to each section of the spray unit, allowed for the regulation of the surface temperature over the inner surface. Ideally an isothermal inner surface was the aim during tests.

The steam was supplied by a Clayton steam generator which is oil fired and fully automatic; capable of producing 1430 kg/hr at pressures ranging from 5 to 13 bar. The supply to the rig was via a regulating valve, the boiler was set to produce steam at 10 bar and the regulating valve adjusted to provide the required test pressure. Steam quality could be checked using a throttling and separating calorimeter. A de-superheating section was provided since after passage through the

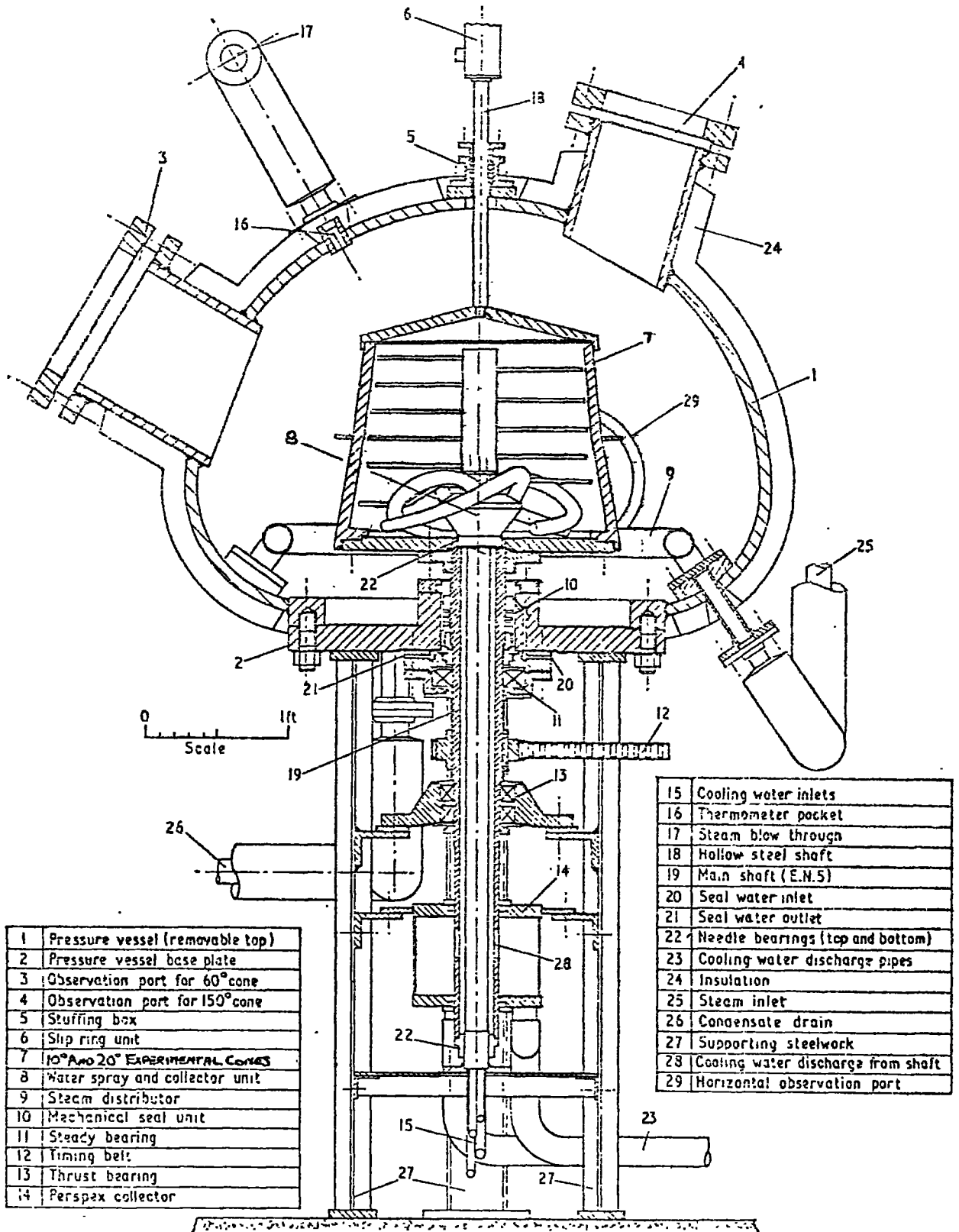


Figure 8. General arrangement of apparatus.

regulating valve the throttling action produced super-heated steam and dry saturated steam was needed for experiments. The steam was introduced into the vessel by a distribution pipe around the base of the vessel.

The experimental body consisted of  $10^\circ$ ,  $20^\circ$  and  $150^\circ$  conical surfaces, the main body was made up of the first two conical surfaces each having a truncated working length of 0.2 m and minor diameters of 0.493 m and 0.53 m respectively. Figure 9. shows the general arrangement of the cones. The wall thickness of both cones was 0.0172 m. The outer surface of the body was divided into three parts by two throwing rings, these prevented the condensate formed on one running down and interfering with the other surfaces. The  $150^\circ$  conical surface, not instrumented for this investigation, had a working length of 0.2 m and was 0.0175 m thick. A diaphragm fitted to the top of  $10^\circ$  truncated cone prevented cooling water reaching the  $150^\circ$  surface, thus minimising unwanted condensate.

Cooling water was removed from inside the body by scoops on the stationary inner supply pipe, the annulus between the latter and the main shaft acted as the drainage path. Condensate removal was via drainage pipes in the base of the vessel, taken to an auxiliary condenser working at a vacuum and finally through a measuring tank into the make up feed-water to the boiler. A line diagram of the system is shown in figure 10.

## 4.2 Instrumentation.

### 4.2.1 Film thickness measurement.

A review of methods capable of measuring liquid film thickness, detailed in Appendix A. indicated that two methods were possibly suitable for this application. These were

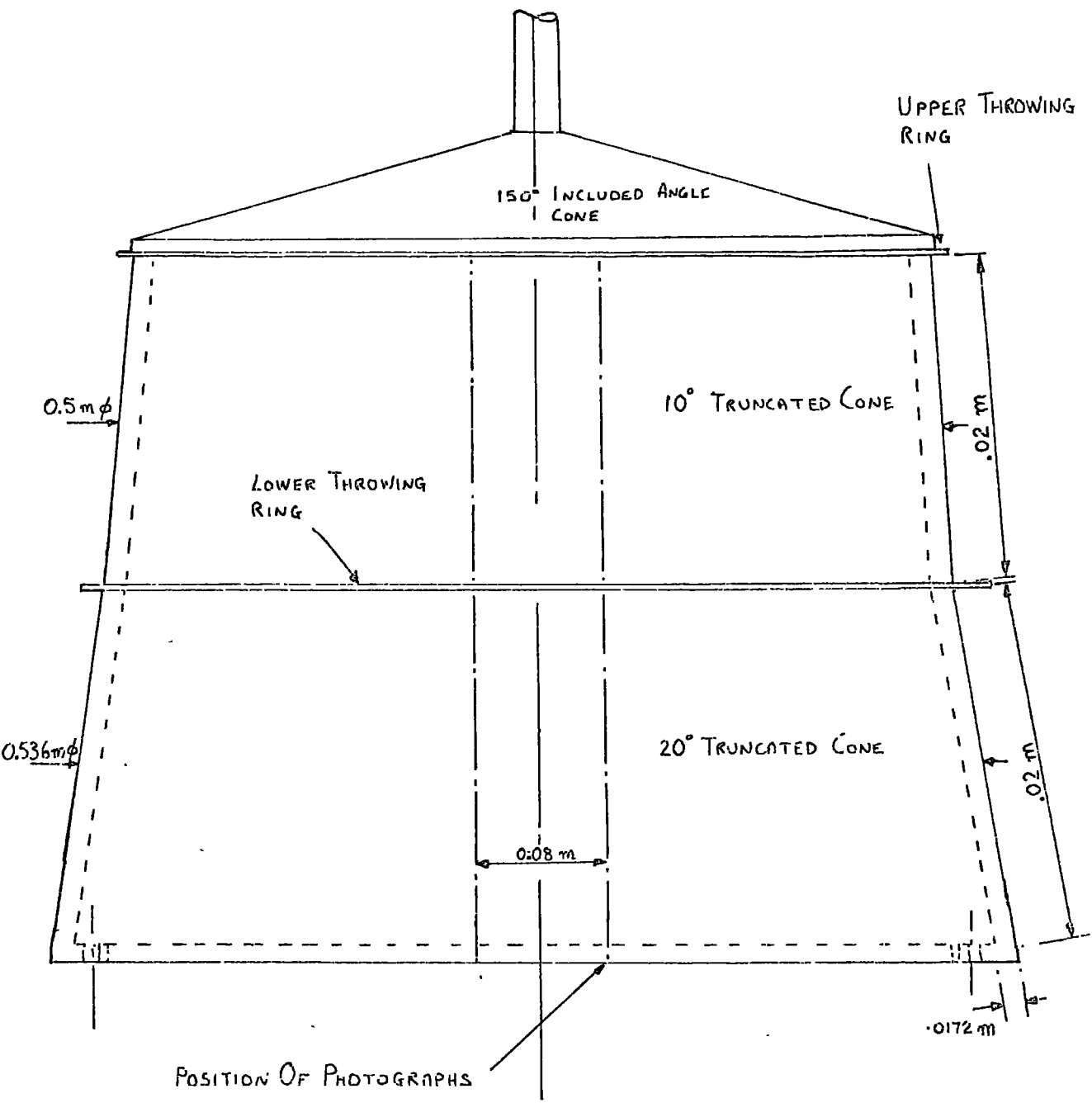


FIGURE 9. GENERAL ARRANGEMENT OF EXPERIMENTAL BODY

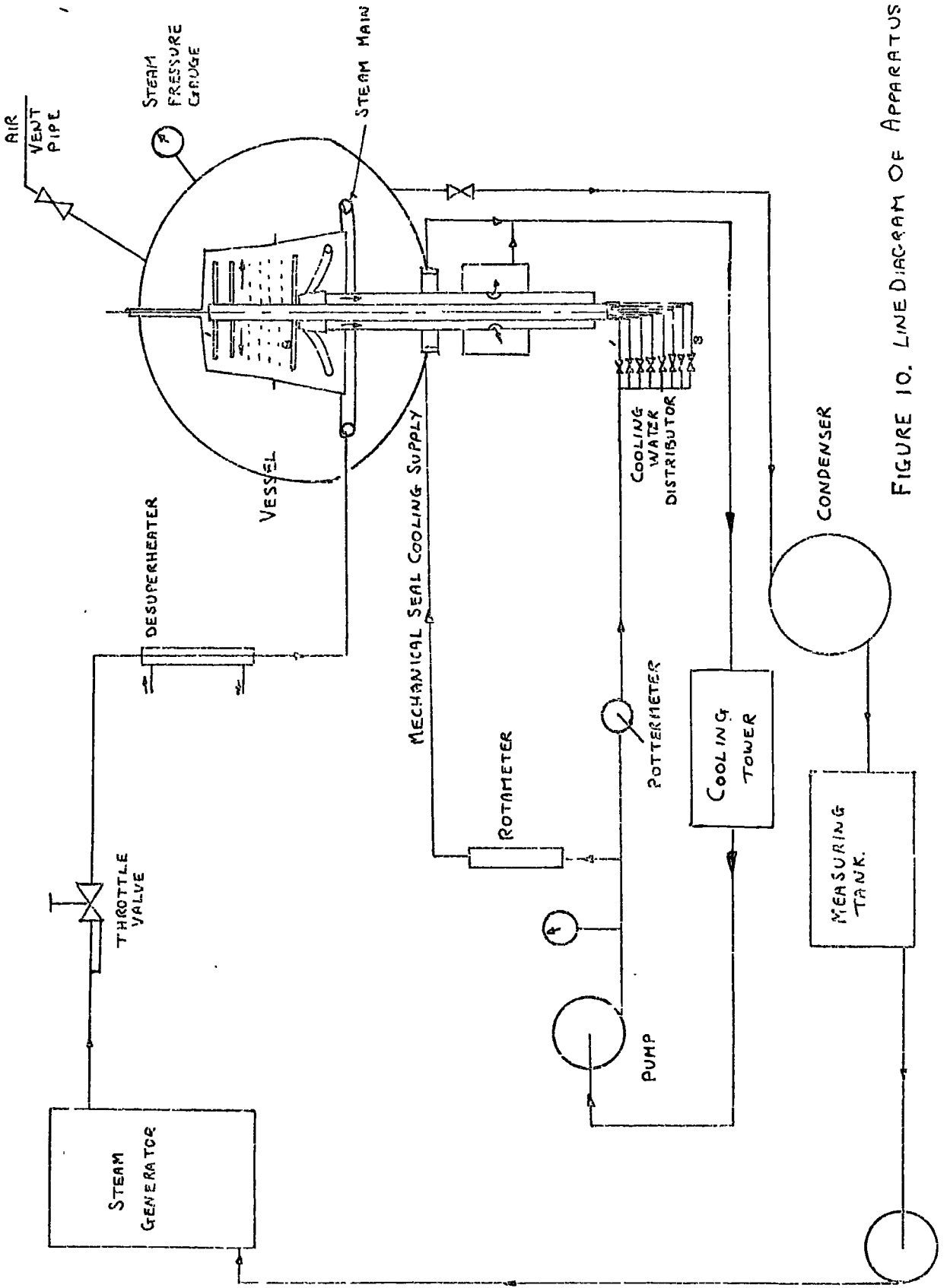


FIGURE 10. LINE DIAGRAM OF APPARATUS.

- (i) the measurement of electrical conductivity in the fluid film.
- (ii) direct observation by means of a probe, adjusted until it contacted the peaks of the waves on the film surface.

The former of course if successful could give much more information than the latter. A detailed account of the conductivity dependent measuring device design and calibration is given in Appendix B. The design criteria were that the gauge must be sensitive enough to be able to

- (i) measure film thickness to a minimum of  $1 \times 10^{-5}$  m.
- (ii) resolve wavelength to a minimum of  $3 \times 10^{-3}$  m.

The system chosen was such that it gave a continuous output dependent on the resistance, or conductance, of the layer of fluid covering the electrode. The output was monitored directly on an oscilloscope or a permanent copy could be obtained by recording on an Ultra-violet (U.V.) chart recorder. From the U.V. recording the maximum and minimum film thickness could be obtained via the calibration chart and wave crest velocity could be found if timing marks were made on the chart recording.

The point method is basically described in Appendix A. The type of construction required for this application was more complicated because the test body was situated in a steam environment, its surface separated by a distance of 0.6 m from the nearest useful observation port and it was capable of being rotated at speeds up to 1400 r.p.m. Thus the particular design criteria were

- (i) a traversing mechanism with a measuring system
- (ii) a sealing system to prevent steam loss
- (iii) a suitably strong probe capable of electrical contact with the film surface but insulated from the steam atmosphere.

The first requirement was met by utilising part of the conductivity device calibration equipment for the traversing and measuring mechanism. The probe was constructed of mild steel having a tapering 'X' cross-

section which plugged into the former mechanism. Insulation of the probe was effected by using a silica rubber potting compound suitably aged and hardened to withstand the high steam temperatures.

The circuit employed to monitor contact with the film surface and the cone surface is shown in figure 11. The signal source chosen provided a 1000 Hz, 2 volt peak to peak output, the same one as used in the conductivity device calibration. The two positions of the switch were included for sensitivity. It is necessary to avoid direct contact to earth, which could cause a short circuit and possible destruction of some of the more sensitive components, when sensing the position of the cone surface which acts as a reference level. On the other hand the current flow when the probe was in contact with the condensate was of the order of 100 micro-ampere, so that one circuit could not be used for the same operation. A digital multimeter was employed as the sensing element, the probe was traversed towards the condensate surface until contact occurred. Immediately a current of magnitude depending on the film thickness flowed in the circuit. There was initially a small reading of 2 or 3 micro-amperes, due to leakage along the insulator surface, but this was insufficient to interfere with the observation of the point of contact. When the body was stationary and the sensing switch in position 2 the probe was traversed again until contact was obtained. The difference between the two positions was the peak film thickness.

The whole mechanism was mounted on the test rig by bolting to one of the nozzle blanks. By using the observation ports on each side of the vessel both  $10^{\circ}$  and  $20^{\circ}$  surfaces could be monitored. Rotation of the blank allowed measurements to be made at different distances down the cone generator line.

The accuracy of the measurement relied on the cone rotating true

on its central axis and very little bearing wear. These two were subsequently found to be suspect and measuring techniques had to be re-considered, the changes necessary are documented in section 4.3.

#### 4.22 Installation and testing of film thickness measuring equipment.

The size and construction of the film thickness measuring gauge is given in Appendix B. The method of fixing the gauges into the surface was one of extreme importance. The measurement of the film conductance depends on line contact of the insulation with the cone surface. This was accomplished by milling holes into the cone surface to hold the gauge and also drilling small holes through the cone wall for the lead out wires. The gauge was held in the surface of the cone by the insulator being a light force fit into the holes in the surface and an adhesive which was poured into the holes first. The metallic surface of the cone was prepared for the application of the adhesive by degreasing thoroughly and then etching for 30 seconds in an ammonium persulphate solution, 1 part of the latter to 4 parts by weight of water. The surface was rinsed with distilled water and then dried in an air stream at 20°C. The gauge once set in the surface was filed almost flush with the surface and finally brought flush with the surface with wet and dry emery cloth.

The number of measuring points chosen was eight. The orientation of these gauges is shown in figure 13. Four measuring points on each of 10° and 20° cones was thought to be sufficient to fully describe the surface profile. Too many gauges may weaken the cone and also the number of sliprings required to carry the signals out was limited.

Initial tests of the film thickness measuring gauges were carried out in conjunction with tests made by Howe (75). To begin with some contamination in the system caused dropwise condensation. During the process of dropwise condensation all gauges showed that no liquid film

was present or at least so thin as to be undetectable by the technique in use. When the central electrode made contact instantaneously with a drop running down the surface a reading of the current was possible. This reading showed that the gauges were functioning. It was only when the cone had run on a number of occasions that true filmwise condensation was observed. Once filmwise condensation was fully established further tests were conducted. These showed that of the original eight gauges only four were reading correctly. The undulating character of the surface film was clearly shown by the signal from these four gauges on the oscilloscope. The latter was found more convenient during preliminary tests than the U.V. recorder.

Owing to the fact that Howe (69) needed many more results for his heat transfer work further tests were discontinued. Re-commencement of tests after some 60 hours condensation showed that only one gauge remained in working order. This eventually proved faulty because it would only function under no-load, on the introduction of steam and rotation of the cone the gauge 'shorted' to earth other than by the condensate film alone.

Analysis revealed that all gauges failed for the same reason, the formation of a path to earth other than through the film alone. Further checks revealed that some of the thermo-couples had also open-circuited and some had even lifted from the grooves in which they had been held. It was concluded that the adhesive had broken down under high temperature and stress. Communication with S.I.R.A. (71) disclosed that epoxy resin adhesives age hardened at high temperature and brittleness was inevitable. Brittleness was accelerated by thick adhesive layers and even more by the addition of high stress. Thus the line contact around the gauge, which gave the gauge its particular 'constant', could not be held. The extra parallel earth paths have the effect of decreasing

the apparent resistance and hence the current flow in the circuit is increased. A further earth path was unfortunately introduced due to adhesive failure because at a breakage point the insulation on the copper output wires could be damaged. Thus the conductivity measuring gauges had to be discarded and the point method adopted to make all film thickness measurements.

When testing the point method further complications were encountered. Some wear was detected in the main bearings causing the cone to run out of true. This wear was considered appreciable since measurements with a dial test indicator showed that movement was of the same order as the film thickness. The  $10^{\circ}$  cone movement was 0.0002 m compared with the film thickness which was estimated to be of the order 0.0001 m. The above test also showed that, as well as the movement in the bearing, the cone was not running true on its axis, figure 12. This coupled with the thermo-couple failures resulted in a major overhaul of the rig having to be carried out.

#### 4.2.3 Temperature measurement.

The measurement of temperature throughout the rig was by copper-constantan thermo-couples. The thermo-couples were constructed from 0.3155 mm diameter copper and constantan wires, both double glass fibre wrapped and varnished, bound together with glass fibre braid and varnished. The insulation was capable of withstanding temperatures up to  $200^{\circ}\text{C}$ . The junction was formed by twisting together a short length of the two wires and soldering. The outer surface temperature was measured by thermo-couples held in grooves machined in the surface. These grooves were machined 0.5 mm wide but widened slightly to just accept one conductor plus insulation; their depth was made equal to twice their width. This procedure ensured minimum adhesive thickness

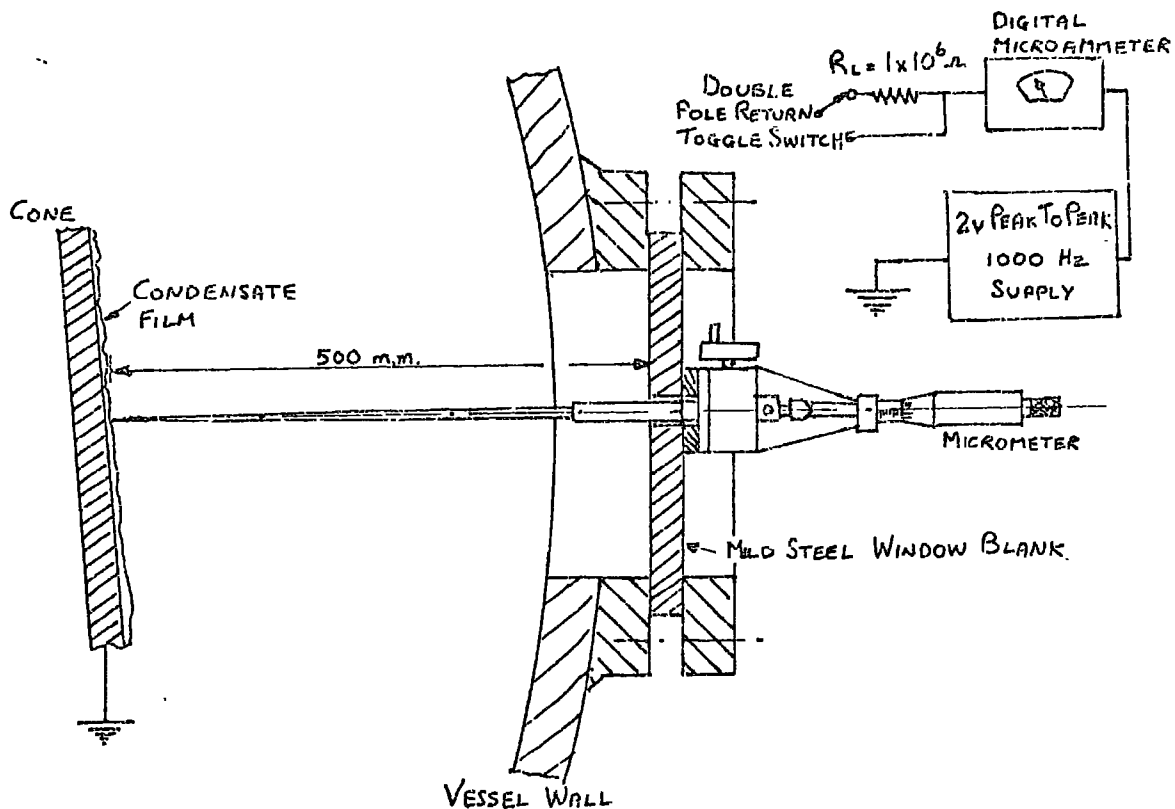


FIGURE 11. POINT MEASURING CIRCUIT

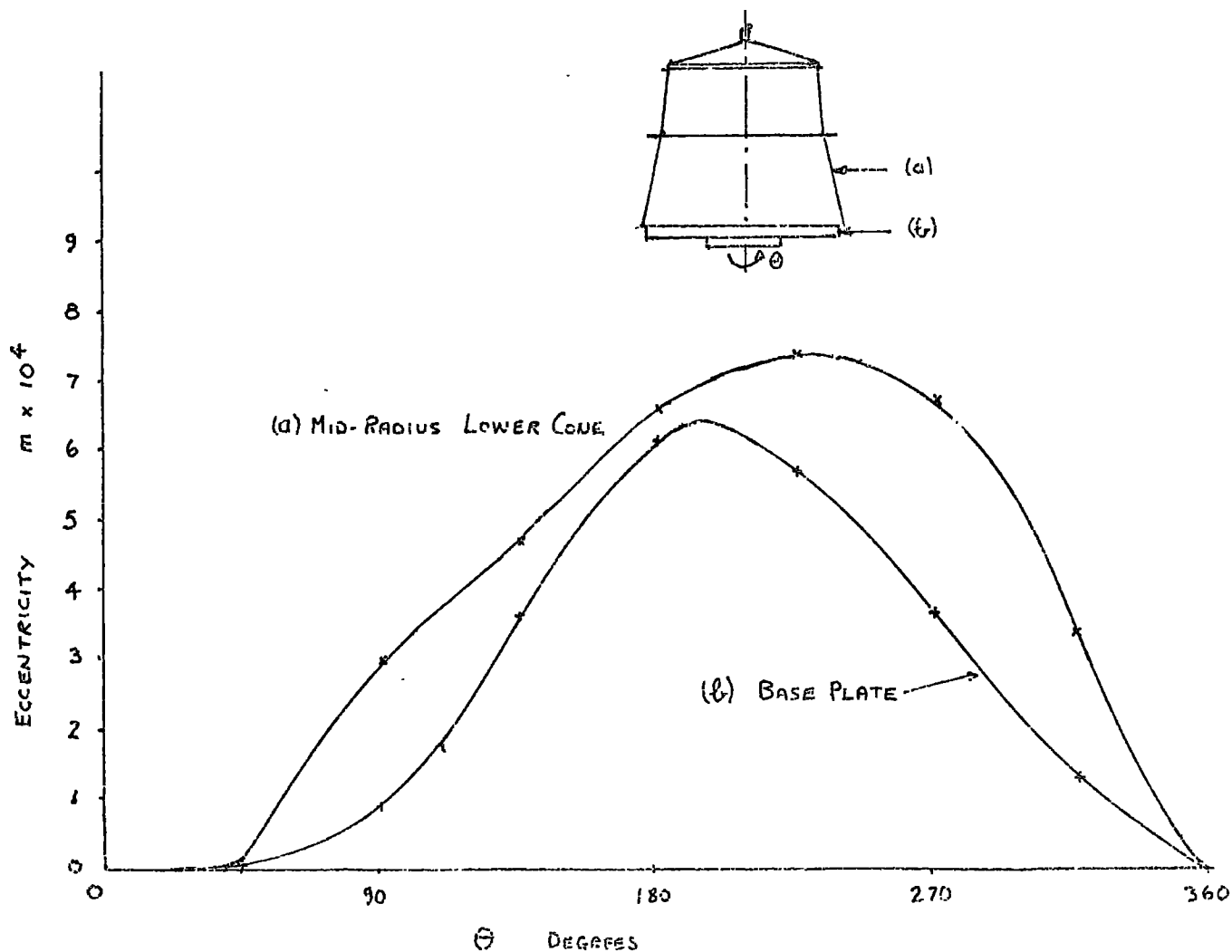


FIGURE 12. ECCENTRICITY OF EXPERIMENTAL BODY

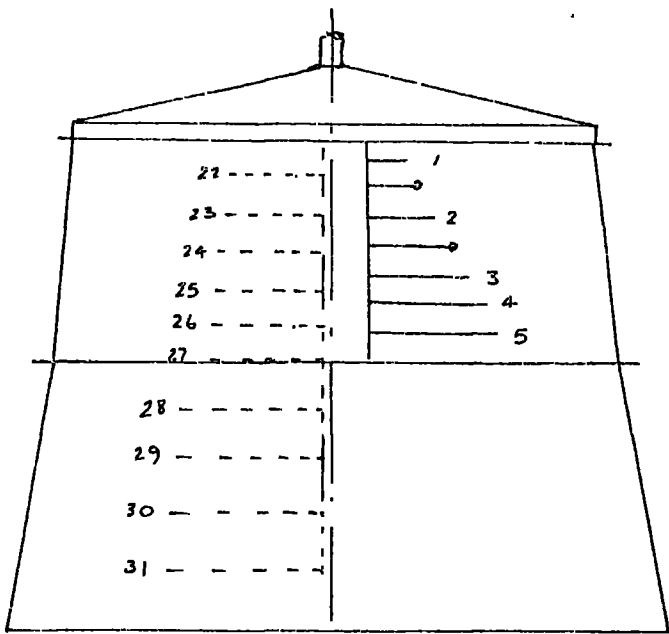
which was of prime importance. The thermo-couples were placed in an isothermal region, this meant that the grooves were made at least 0.05 m in length before the thermo-couples were passed through a 1 mm hole to the inside surface. The adhesive used to fix the thermo-couples was Bostik 1160, an alcohol based product which needed drying for 1 hour at 27°C and curing for 20 minutes at 140°C to attain maximum strength.

The arrangement of the thermo-couples, nine on the 10° cone surface and ten on the 20° cone surface are shown in figure 13. The thermo-couples on the outer surfaces all pass through the wall and are taken up the inside wall of the cones, through the small hollow shaft to the slipping unit. There are eleven thermo-couples attached to the inner cone surfaces, five on each of the 10° and 20° surfaces and one at the junction of the two. The junctions were soldered to the body wall then the leads were adhered to it before being taken through the small shaft to the slipping unit. The thermo-couples were connected to two slipping units, one a 40 way unit the other a 12 way unit. The latter was the one intended for use with the conductivity measuring gauges. One cone surface was fully instrumented at any one time because there were not sufficient slippings to carry all the thermo-couples. The thermo-couples were then taken to a switch unit. This was a break before make unit which connected each thermo-couple in turn into the measuring circuit. A line diagram is given in figure 14. The output from a thermo-couple was measured with a sensitive digital voltmeter, a cold junction was provided by a mixture of ice and water at atmospheric pressure, the temperature attained was 0°C to +1°C.

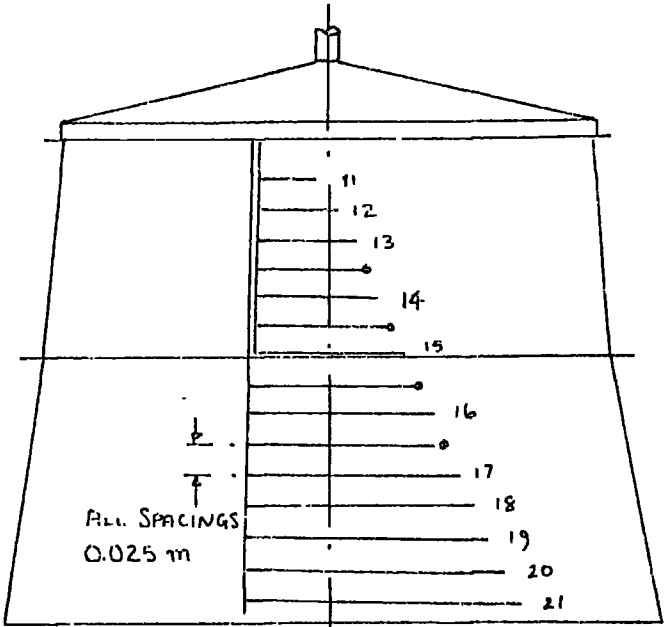
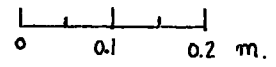
The other temperatures measured were

(i) the surrounding air temperature. Two methods were used to obtain this temperature

(a) a thermo-couple connected through the large slipping unit



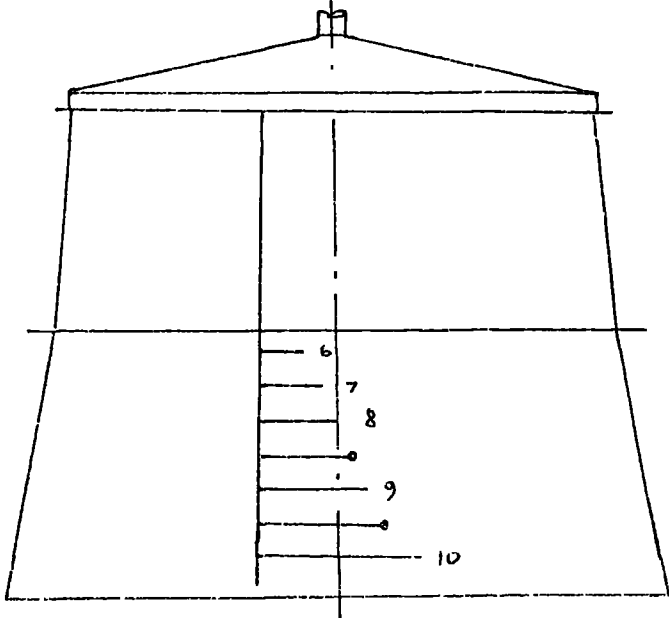
10° CONE



10° CONE

20° CONE

- CONDUCTANCE FILM THICKNESS MEASURING DEVICES
- THERMOCOUPLES
- - - INSIDE THERMOCOUPLES



20° CONE

FIGURE 13. THERMOCOUPLE AND FILM THICKNESS MEASURING GAUGE ORIENTATION

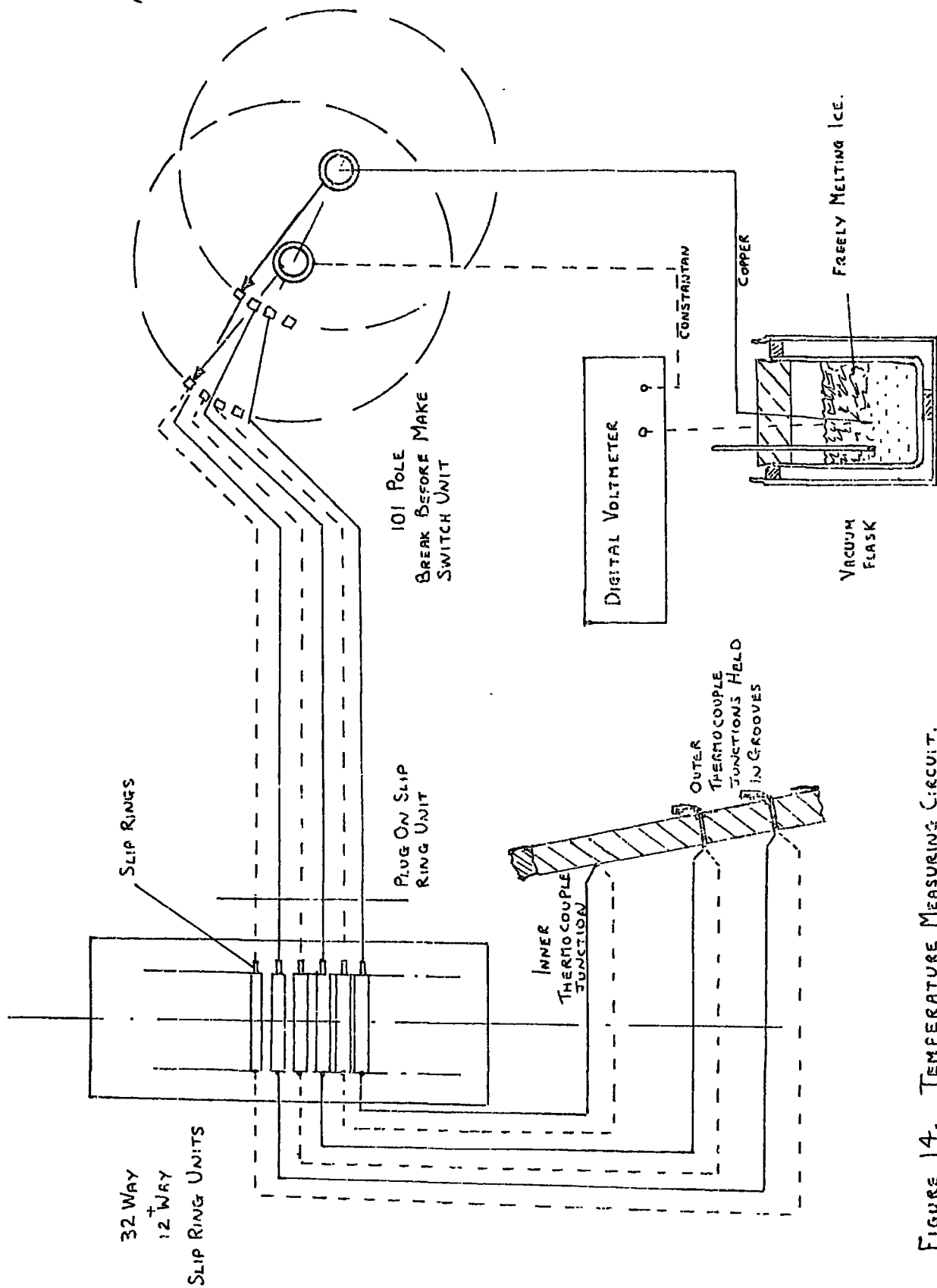


FIGURE 14. TEMPERATURE MEASURING CIRCUIT.

- reading the temperature of the air close to the input terminals of the large slipring unit.
- (b) a thermo-couple situated close to the input terminals of the large slipring unit.
- (ii) the pressure vessel wall temperature using a thermo-couple attached to one of the observation port flanges.
- (iii) the steam saturation temperature by a thermo-couple protruding into the steam space.
- (iv) the inlet and outlet cooling water temperatures. The latter was obtained from an average of four thermo-couples attached to the inner and outer portions of the scoops.
- (v) the temperatures at the input and output terminals of the large and small slipring units.

The readings of the temperatures at the input and output terminals, plus the two surrounding air temperatures were necessary because it was noticed that surface temperature readings through the slipring units became depressed at high speed runs. An absolute temperature was important because the accuracy of the temperature difference across the film governs the accuracy of the heat transfer coefficients. The depression of the readings through the slipring unit was caused by a difference of temperature at the constantan-silver junctions, at input and output terminals, which introduced a secondary e.m.f. By measuring the input and output terminal temperatures and applying the following procedure derived by Benedict (72) the secondary e.m.f. could be corrected. The difference in the input and output terminal temperatures was computed. If the input terminal temperature of the slipring unit was the higher of the two then the computed temperature difference was added to the conc surface temperatures. A check on this correction could be made by observing the two readings of surrounding air temperature.

The thermo-couples were calibrated in an oil bath and a calibration chart drawn up. This calibration chart showed that all the thermo-couples were within  $\pm 1\%$  of the Standard Calibration for copper-constantan junctions, as given in B.S. 1828-1961.

#### 4.2.4 Pressure measurement.

Pressure measurements were made using standard calibrated bourdon gauges. The accuracy with which this type of instrument can be read depends on the range of pressure measured. The gauges used on the rig were a 0 to 7 bar and a 0 to 20 bar, having reading accuracies of  $\pm 0.02$  and  $\pm 0.1$  bar respectively. The calibration of the gauges can be checked at intervals on a dead weight testing machine.

#### 4.2.5 Flow measurement.

The cooling water flowrate was measured by a commercially available instrument called a 'Pottermeter' installed in the input line. This instrument depends in principle on the measurement of the number of rotations of a propellor placed in the path of the inflow. By allowing each blade of the propellor to pass through a magnetic field a series of pulses were produced. These pulses were counted by a digital totaliser. It was necessary to use a stopwatch to obtain a time averaged pulse count. The 'Pottermeter' had already been calibrated at the factory and a 'constant factor' given, this was 110,213.195 pulses per  $m^3$ .

The design flowrate was 1 to 23  $m^3/s$  with a quoted accuracy of  $\pm 0.5\%$ . Averaging the pulse count over the fifteen minute test reduces the inaccuracy in starting and stopping the stopwatch and totaliser simultaneously to a minimum.

Total condensate flowrate measurement during an experimental period,

including that from both stationary and rotating parts, could be performed via a measuring tank through which all condensate passed whilst being returned to the boiler feedwater hotwell. This was carried out by timing the amount of condensate collected in the tank over the fifteen minute period.

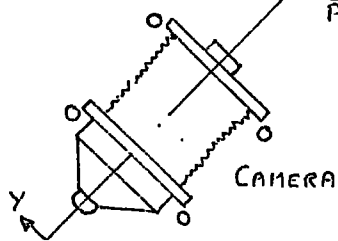
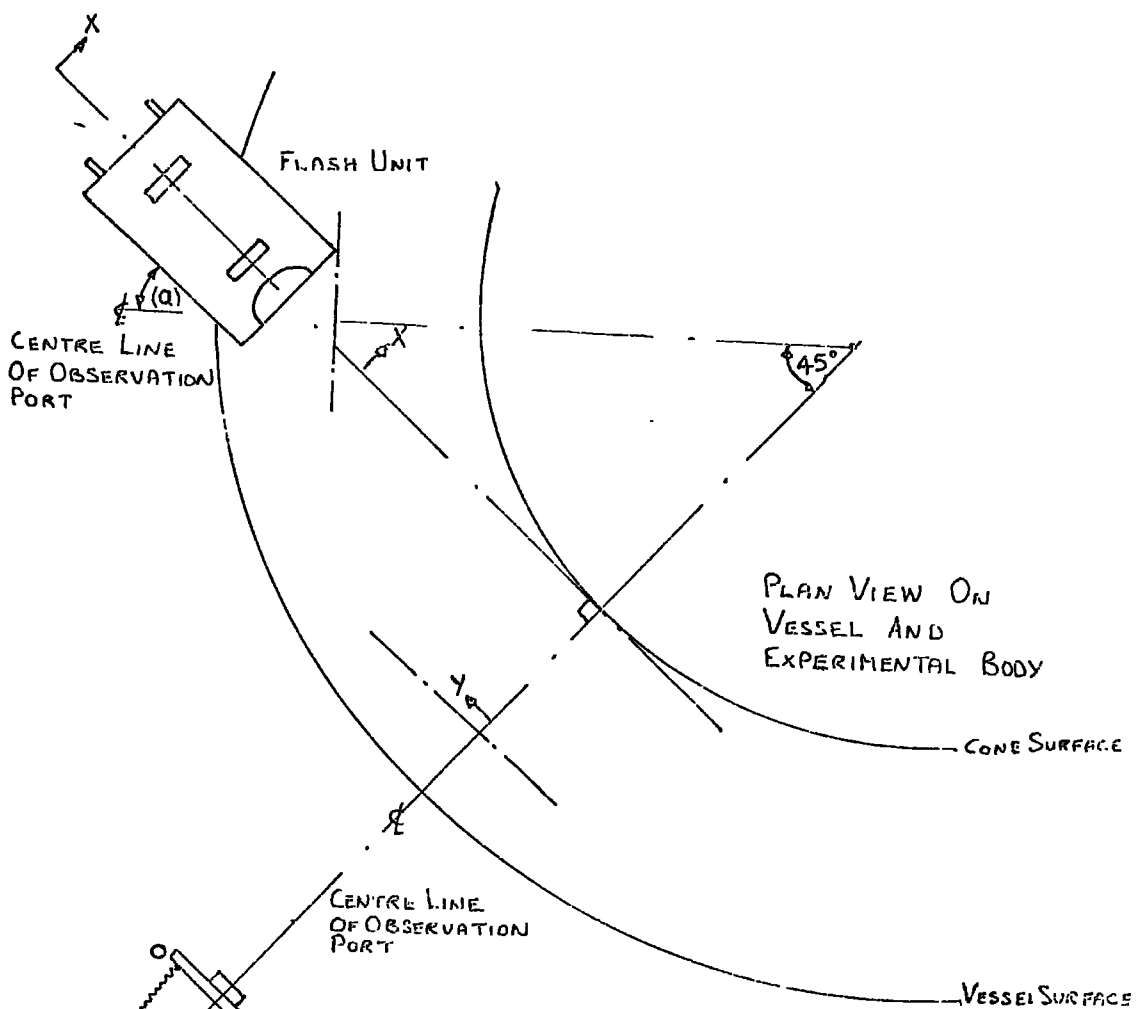
A more accurate method of individual condensate measurement for each conical surface would have been invaluable, however, such a system impeded the flow of steam and obscured the condensate surface. The latter was particularly objectionable because the condensate flow pattern could not be observed.

#### 4.2.6 Photography.

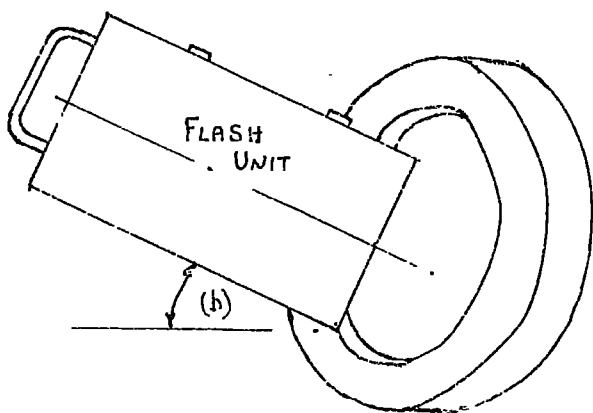
Observation of the condensate surface was carried out by two methods. Firstly to ascertain the general behaviour of the condensate film a stroboscope was used. The stroboscope was particularly useful for detecting whether a complete film existed. When the flash rate of the stroboscope coincides with the rotation rate of the cone, successive observations of the same area of condensate surface can be made.

A permanent record of the surface profile was obtained in the form of a photograph. The camera employed was of monorail construction, this allowed maximum use to be made of its robustness to withstand the high temperature operation in the filming position. It also permitted a variety of lenses to be used so that focussing over a range of distances was possible. A further advantage was that the camera could accept photographic plates. The plates used, were 100 x 125 mm, Ilford H.P.4, gave minimum distortion during exposure and the enlarging process.

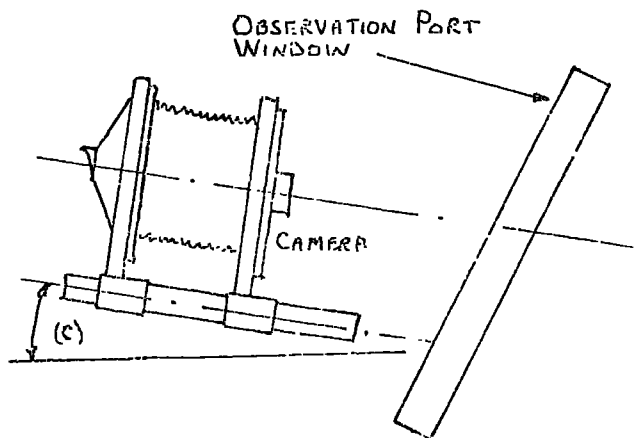
To enable measurements to be obtained from the plates it was necessary to align the camera and lighting source so that a satisfactory



ANGLES	a	10° CONE	20° CONE
		38	25
	b	29	50
	c	5	10



SECTION ON XX



SECTION ON YY

FIGURE 15. LIGHTING AND CAMERA POSITIONING



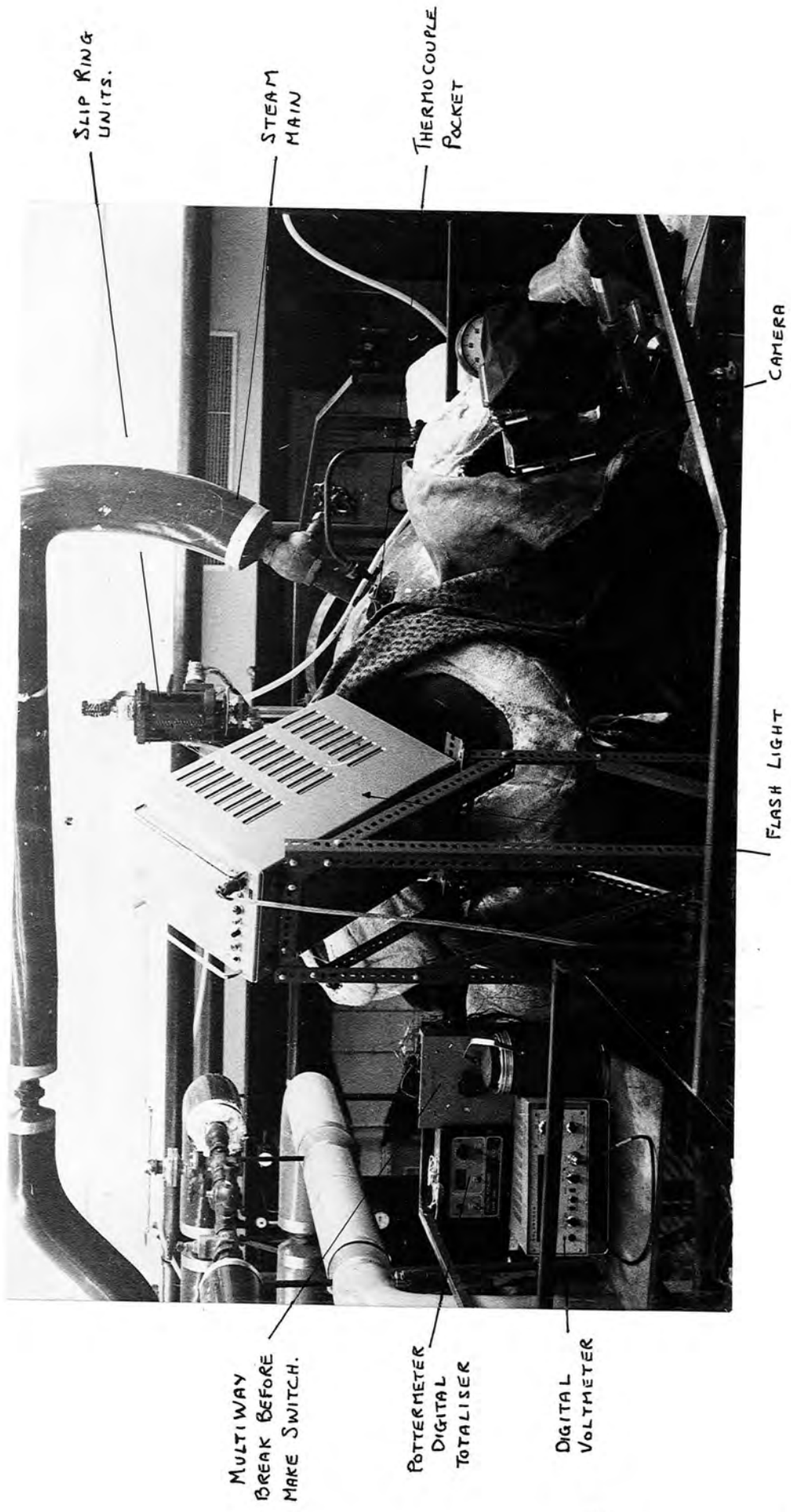


FIGURE 16. LIGHTING AND CAMERA POSITIONS FOR THE 20° CONE.

photograph could be taken perpendicular to the cone generator line. This was a difficult task because the porting arrangements had not been designed for this procedure. After many trial lighting and camera positions the arrangements shown in figure 15. were adopted. Two positions were necessary because the camera must be set perpendicular to the cone generator line. The most difficult problem encountered was to produce a directional light source of sufficient intensity and short duration. The light source chosen was a 2 micro-second, single flash unit of 40 joules output. An open flash technique was adopted, this consisted of blacking out all the vessel windows, the camera shutter was then fully opened and the flash unit triggered.

The above technique was found satisfactory if the camera shutter was set at f5.6 and the plates subsequently developed for ten minutes in a high activity developer, in this case Ilford Microphen.

The photograph, in figure 16., shows the general layout of the various components already mentioned. The difficulty involved with the actual orientation of the flash unit and camera, with reference to the porting arrangements, is demonstrated. As well as this complicated outside arrangement the inside surface of the port nozzle was lined with aluminium foil to reflect light to the point of interest. Also shown are the positions of the temperature measuring equipment.

#### 4.2.7 Rotational speed.

Measurement of rotational speed was made using a hand tachometer which was placed directly onto the electric motor shaft. The accuracy of measurement of the rotational speed was within  $\pm 2$  r.p.m.

#### 4.3 Preliminary test runs.

After the major overhaul preliminary test runs were necessary for four reasons, these are

- (i) to check that all the thermo-couples were functioning correctly.
- (ii) to practise using the film thickness measuring technique. This consisted of bringing the probe up to the condensate surface, whilst the cone was rotating and when contact was made a reading on the micrometer was taken. The high spots, which were apparent on the conical surfaces, were clearly marked so that when the cone was stationary these points could be brought beneath the probe. At this position the probe was then moved up to the surface. When contact occurred another reading was taken. The difference between the two readings was the peak film thickness. This procedure was repeated several times with reasonable consistency.
- (iii) to obtain a consistent surface condition. This is essential in order to compare the condensate surface profiles. In practical conditions no treatment is given to the component surfaces. Once an oxide layer has formed then this will be the normal running condition. With the test body certain contaminants in the oxide layer required removal by wet and dry paper. If cleaning in this manner was required frequently, at each cleaning a fresh oxide layer would have to be formed. Thus these preliminary runs produced cone surface conditions which could be practically representative.
- (iv) to produce filmwise condensation. Previous workers had found that contamination caused dropwise condensation during initial runs. This was found to be the case again. After the cleaning of the cone surface with wet and dry paper as above filmwise

condensation was observed at the beginning of the test run, however, after ten minutes contamination had caused dropwise condensation. When the test was completed and the vessel had cooled down sufficiently one of the port observation glasses was removed and the test body completely soaked in a detergent called Decon 75. It took four such soakings to obtain a satisfactory film.

#### 4.4 Test procedure.

Before commencing a test run a series of pre-run checks were made. Firstly one of the port glasses had to be removed and the test body sprayed with water to ensure a fully wettable surface. At the same time all the observation port glasses used for inspection and photography were cleaned by spraying with water. The port glass was replaced and all the black out conditions checked. The camera and flash unit were checked for alignment. Once placed in one of the two positions for observing the condensate film care was exercised not to disturb the system so that all negatives and prints would be directly comparable and no geometrical corrections would be necessary. The focussing of the camera was performed only once and a check made at the beginning of each test.

At the same time as the above were being performed the Clayton boiler, which took about fifteen minutes to be fully operational, was flashed up. After the pre-run checks the following procedures were carried out on the test apparatus. Both the cooling water stop valve and drain valve were opened and the water pump started, and cooling water was supplied to the inner surface of the cone by opening the main valve at the distribution manifold. The pressurised water supply

to the mechanical seal was adjusted to  $0.5 \text{ m}^3/\text{h}$ . The cooling air was supplied to the slipping units and the motor control unit switched on, adjusting the latter to obtain the desired rotational speed. The blow-off valve and the vessel drain valve were opened before the introduction of the steam. This was necessary to assist air purging. When the Clayton boiler was fully operational steam was admitted to the vessel through the regulating valve. The blow-off valve was left open for about five minutes but the drain valve was closed after about one minute. When the blow-off valve was closed the steam pressure was slowly raised to the test pressure. Once the test pressure had been attained the blow-off and drain valves were again opened to purge the system. The valves were then closed and the system allowed to settle down for several minutes.

Adjustment of the individual distribution manifold valves was then carried out to obtain as uniform an inner surface temperature as possible. This was done for the initial test only, and the rate of flow of the cooling water was not varied for the remaining tests. It was found that the inner surface temperature of the cone could not be varied very much, the objective could only be to make this temperature the same at all points.

The condensate was allowed to build up in the well of the vessel to a pre-determined level and the condensate drain valve was then adjusted to maintain this level. The rotational speed and the pressure were checked and if necessary adjusted to the test values. These test conditions were maintained for ten to fifteen minutes to enable the temperatures of the cone and pressure vessel to become steady. The steam blow-off valve was opened for ten seconds whilst observing the thermo-couple e.m.f. readings in order to check for the presence of non-condensables prior to a test run.

The measured quantities during one particular test run consisted of

- (i) pressure and saturation temperature, checked at regular intervals.
- (ii) cooling water flowrate, timed over ten to fifteen minute intervals.
- (iii) speed of rotation checked at regular intervals.
- (iv) point temperature readings from the inner and outer surfaces of the cone. Plus; input and output slipping unit terminal temperatures, cooling water inlet and outlet temperatures. These were read at the beginning and finish of each test run.
- (v) peak film thickness measurement, readings taken twice during each test run.
- (vi) a still photograph taken after the surface had been illuminated with a stroboscope to ensure filmwise condensation existed.

For one pressure setting a series of rotational speeds were chosen when each of the observations (iv) to (vi) were made for each speed.

## 4.5 Results.

### 4.5.1 Limits of experimental tests.

The parameter  $\Lambda$  developed in the theoretical analysis contains the independent variables condensate temperature difference and the acceleration in the  $Y$  direction. The range of temperature difference is catered for by increase in pressure which is directly related to the increase in energy transfer. The pressure range chosen was 1.5, 2, 2.5, 3 and 4 bar absolute.

The speed of rotation of the cones was varied between 120 and

400 r.p.m. for the  $10^\circ$  included angled cone and 200 to 600 r.p.m. for the  $20^\circ$  included angled cone. The range of values of the acceleration in the Y direction are 60 to 350 and 110 to 1000  $\text{m/s}^2$  for the  $10^\circ$  and  $20^\circ$  cones respectively. The speed range was varied by 50 r.p.m. up to 400 and 600 r.p.m. respectively for each of the five pressures quoted.

The film thickness measurements were performed at a point mid-way between the maximum and minimum diameters of each test section. A number of tests were carried out on the  $10^\circ$  included angle cone with the probe re-positioned 0.135 m down the cone generator line.

The character and geometry of the condensate film were observed photographically for each set of experimental conditions. A careful check was necessary to ensure that the photographic record in each condition was correctly identified. From the photographic negative plates the wavelength and the angle formed by a ridge and the generator line were measured. Prints were taken from certain negatives to display the patterns of the condensate layer with changes of rotational speed and steam pressure. The extent of the surface which the photographs cover are shown in figure 9. by the dotted lines.

#### 4.5.2 Measurements from photographic negative plates.

The measurements were made from the negative plates by holding each in the enlarger and projecting an image onto a sheet of white paper. The ridge pattern, at the same position as the film thickness measurements were made, was carefully marked. The distance between a series of peaks or ridges was then measured with a travelling microscope. For the larger wavelengths it was satisfactory to confine the measurement to three successive peaks, but for short wavelengths a better result could be obtained by measuring over six successive peaks. The enlargement factor was calculated by identifying two thermo-couple

grooves and dividing the measurement taken from the enlargement by the measurement made directly from those situated on the cone surface.

The ridge angle was found by marking the full ridge onto a sheet of white paper using the image cast by the enlarger and a flexible 'French' curve to follow the profile. The sheet of paper was transferred to a table which had a vernier measuring scale giving a reading accuracy of  $\pm 6$  minutes of arc. The principal inaccuracies in this kind of measurement are introduced from errors in aligning the tangent to the curve with the cross-wires as observed through the magnifying eyepiece of the instrument.

All measurements were made from ridges as near as possible to the point where the normal to the surface coincides with the direction of observation. In this position errors due to the surface curvature of the cone are minimal. The largest wavelength measured was 0.0069 m. Then the difference between the length measured, the chord length of 0.0204 m, and the surface arc length which is 0.020483 m is less than 0.5% error. The positioning of the peaks and subsequent measurement could be estimated to be  $\pm 0.0005$  m over the 0.024 m section, a percentage error of  $\pm 2.5\%$ .

The experimental results are given in Tables 1. and 2. for  $10^\circ$  and  $20^\circ$  cone surfaces respectively.

#### 4.6 Error analysis.

Some of the errors in the experimental work have already been mentioned, for example those in ridge angle and wavelength measurements and those in individual instruments. Other measurements which will be used in the discussion section are condensate film and wall temperature differences and film thickness. The most serious error occurring in the

cone surface temperature is the uncertainty of the position of the thermo-couple junction in the groove. Howe (69) used an electrical analogue and found that if the thermo-couple junction was at the bottom of a groove a  $2^{\circ}\text{K}$ , per  $100^{\circ}\text{K}$  temperature difference across the wall, error was possible. Also because the slipping terminals could not be kept at the same temperature an error in estimating the secondary e.m.f. correction of  $\pm 1^{\circ}\text{K}$  can occur. An average wall temperature difference of  $60^{\circ}\text{K}$  was attained throughout most tests. Thus, allowing a further  $\pm 1\%$  for thermo-couple calibration error, a percentage error of  $\pm 4.5\%$  results. The temperature differences measured for the condensate film varied between  $9^{\circ}$  and  $22^{\circ}\text{K}$ , then the percentage error must also vary. At  $9^{\circ}\text{K}$  an error of  $\pm 29\%$  can occur whereas at  $22^{\circ}\text{K}$  this is reduced to  $\pm 12\%$ . The latter include an allowance of  $\pm 0.1^{\circ}\text{K}$  in steam temperature measurement.

Values calculated in the discussion include energy per unit area transferred through the wall and heat transfer coefficients. The former is given by Fourier conduction through the cone wall

$$q = - \frac{k \Delta T_w}{\delta_w}$$

The thermal conductivity of the cone material was found experimentally by Howe. The method employed was to calculate the resistivity of a sample of material made when the cone was being cast. The resistivity curves were calculated whilst the sample was held in an oil bath which allowed the temperature dependency to be found. The equation for the thermal conductivity of copper alloys is given in a paper (84) by Powell in the form

$$k_t = C_1 \sigma_t T + C_2$$

where

$$\sigma_t = \text{electrical conductivity of the metal} \quad \frac{1}{\Omega}$$

$$T = \text{absolute temperature}$$

$$C_1 = 2.39 \times 10^8 \quad \text{w}\Omega/\text{K}^2$$

$$C_2 = 7.5 \quad \text{w/mK}$$

Typical derivation of thermal conductivity for the material can be taken as  $\pm 5\%$ .

Measurements were difficult on the conc wall metal thickness because of its curved profile and also the depth of the face. For this reason an error in the wall thickness of  $\pm 1\%$  must be tolerated.

The error in the calculated quantities may now be estimated. For any quantity  $X$ , which is a function of several variables  $a, b, c, \dots, n$

$$\text{i.e. } X = f(a, b, c, \dots, n)$$

then the maximum possible error is given by

$$\frac{\Delta X}{X} \max = \sum \frac{\partial X}{\partial n} \cdot \frac{n}{X} \cdot \frac{\Delta n}{n}$$

all terms in the summation being given the same sign. Then the sum of the component errors is the error in the quantity under consideration. The error in the energy transfer per unit area,  $q$ , becomes  $\pm 10.5\%$ . The heat transfer coefficient is given by

$$h = q / \Delta T_f$$

The error in  $\Delta T_f$  has already been calculated to be  $\pm 28\%$  when  $\Delta T_f$  is  $9^\circ\text{K}$  and  $\pm 12\%$  when  $\Delta T_f$  is  $22^\circ\text{K}$ . Thus the two errors in the heat transfer coefficient when  $\Delta T_f$  is  $9^\circ\text{K}$  and  $22^\circ\text{K}$  are  $\pm 38.5\%$  and  $\pm 22.5\%$  respectively.

However a more realistic estimation of errors can be obtained by calculating the root mean square values. The root mean square error is given by

$$\left(\frac{\Delta X}{X}\right)^2 = \sum \left(\frac{\partial X}{\partial n}\right)^2 \left(\frac{n}{X}\right)^2 \left(\frac{\Delta n}{n}\right)^2$$

Substituting the errors of each of the components; thermal conductivity, temperature difference and wall thickness into the above form results in an expected error of  $\pm 7\%$  in the heat flux. The errors in the heat transfer coefficient become  $\pm 29\%$  and  $\pm 14\%$  when the condensate film temperature difference is  $9^\circ\text{K}$  and  $22^\circ\text{K}$  respectively.

Film thickness measurements were made using an accurate micrometer

which allowed an absolute error of  $\pm 0.0025$  mm. However, during re-assembly of the rig the main bearings showed some play, of the order 0.025 mm. Thus the worst possible error in the reading for peak film thickness could be  $\pm 37\%$ . When the system was rotating some of the play would be taken up and a much smaller error incurred. Tests with Wayne-Kerr capacitance measuring equipment confirmed that a more realistic error would be  $\pm 10\%$ . A systematic error of  $\pm 15\%$  appeared because of the electrical contact method of detecting the condensate surface. This error took the form of pointer vibration due to drops from the throwing rings and also general rig vibration. This causes premature contact with the condensate film. Also when sensing the cone surface, due to the irregular shape of the cone a further error could be incurred. Electrical contact is made slightly more inefficient in this application because of the leakage path via the condensate layer along the pointer masking the initial contact. Therefore an overall measurement error of  $\pm 25\%$  must be accepted.

5.0 DISCUSSION.

## 5.1 Description of condensate behaviour.

### Introduction.

The observation of the condensate surface for a pressure variation of 1.5 to 4 bar absolute and a speed variation of zero to 600 r.p.m. leads to the following general conclusions :-

- (i) The condensate layer supports four regimes of flow in the speed range considered
  - (a) When the cone is stationary waves of the curtain type exist on the condensate layer and are similar to those observed by Holgate (36) and Robson (68). These curtain type waves are shown on the lower half of the photograph in Figure 17(a) for condensate flow on the  $10^\circ$  included angle, truncated cone (the latter being referred to as the  $10^\circ$  cone throughout the rest of the text, similarly the  $20^\circ$  cone refers to the  $20^\circ$  included angle, truncated cone). The photograph only shows the waves on the  $10^\circ$  cone but similar waves occur on the  $20^\circ$  cone. The poor quality of the photograph presented arises from the fact that the camera and the illuminating flash were orientated in order to produce the optimum result for the ridge type waves observed at higher speed and not for curtain waves. The lower portion however shows a system of waves which occur in groups of one prominent wave followed by a series of smaller wavelets.
  - (b) In the range 60 to 100 r.p.m., for all pressures observed, the surface was covered by curtain type waves which travel down the surface in a helix action. Again the characteristic pattern consisted of a main wave front followed by ripples of shorter wavelength, very similar to the stationary case except that they flowed in a helix pattern of 60 to 70 degrees

to the cone generator line.

- (c) An increase of speed above 100 r.p.m. brings about a complete change in the pattern of condensate drainage. Ridge like waves are formed at certain speeds depending on the steam pressure and hence the condensation rate. These ridge like waves flow in the X direction forming a small angle to the cone generator line, approximately  $10^\circ$  at inception, and are circumferentially displaced around the cones. With an increase in speed a reduction in wavelength occurs and in general the ridge angle increases.
- (d) Further increases in speed produced a condition where condensate removal was assisted by drops leaving the crests of ridges. The rotational speed at which the latter occurred was also pressure dependent. Initially drops were seen to leave the condensate surface at larger radii i.e. lower on the cone, increasing the rotational speed caused the drop departure point to move to a smaller radius.

In general terms the above occurs on both the  $10^\circ$  and  $20^\circ$  cones.

- (ii) Increase of pressure causes ridge type flow to be formed and drops to be thrown from the condensate surface at lower rotational speeds.

### 5.1.1 Variation of speed at constant pressure.

#### $10^\circ$ Cone

A series of photographs, Figure 17(b) and Figures 18(a) to 22(a), show the effect of speed variation at a constant steam pressure of 2 bar absolute for the  $10^\circ$  cone. In Figure 17(b) the rotational speed is 135 r.p.m. This is a valuable photograph as it shows that there is no clear



Figure 17. Variation of condensate layer profile with change of speed at constant steam pressure.

cut value of the acceleration perpendicular to the cone generator,  $a_y$ , at which ridge like waves will form. At about mid-way down the surface a discontinuity point occurs where the curtain type waves exist above this point and ridge like waves are forming below it. As mentioned previously the illuminating flash and camera were not set up to observe waves of the curtain type, but it can perhaps just be observed that the clear upper region contains curtain waves. A small portion of curtain type regime is visible in the centre of the photograph. The ridge waves that have formed still bear some of the characteristics of the curtain waves; the usual small ripples behind the larger wavefronts which are clearly discernable on ridges on the right-hand side. Observation of the ripples on the ridges suggests the helix angle which the curtain type waves were pursuing. No ridges are visible on the left-hand side of the photograph and thus this photograph is one which enables the limiting conditions for curtain waves to be defined.

The value of  $a_y$ , calculated assuming the mid-point radius, at which the ridges form for this pressure is  $48.92 \text{ m/s}^2$ . The corresponding value of  $a_y/a_x$  (the ratio of acceleration perpendicular to the cone generator to that parallel to the cone generator) is 5.46. The phenomena of ridge type flow has also been observed on the underside of a surface slightly inclined from the horizontal. This is a similar process where the accelerations involved have their largest component tending to remove the condensate vertically downwards and being resisted by surface tension forces. The slope at which ridges first became apparent was between 15 and 17 degrees to the horizontal, no nearer estimation could be deduced from the paper by Gerstman and Griffiths (49), corresponding to a range of  $a_y/a_x$  of 3.6 to 4.4.

The next speed of rotation observed was 200 r.p.m., the surface configuration is shown in Figure 18(a). It is obvious that the ridge

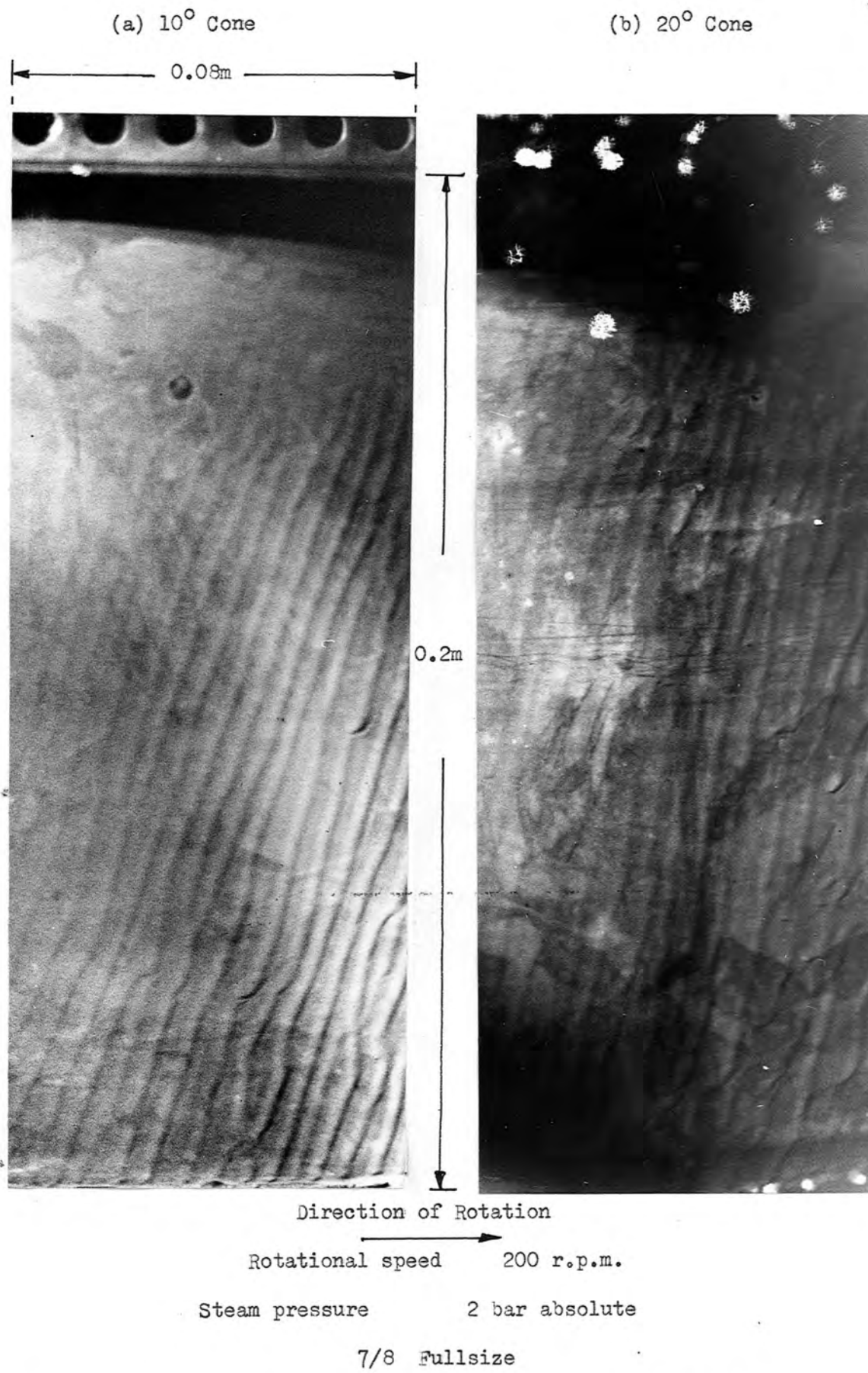


Figure 18. Variation of condensate layer profile with change of speed at constant steam pressure.

formation is fully developed, and some ridges can be traced the full length of the cone surface. Examination of the photograph reveals that formation of ridge type flow is dependent to a large extent on the condensate present on the surface. Ridges are not visible for at least 25 mm from the start of condensation. It is not possible to detect whether waves of the curtain type exist. It can be seen that motion of the ridges is very sensitive to the condition of the cone surface over which they flow. Where an irregularity of the surface, such as a blow-hole occurs, the ridge tends to bend around it. Such imperfections no doubt account for the occurrence of irregularities in the ridge pattern. A detailed examination shows several places in which some ridges intersect and continue as one whereas others split up and continue as two. In this photograph three adjacent ridges are involved. Two ridges merge and continue as one until a little further down when the third ridge splits up into two. In the upper right-hand corner two or three have merged and proceeding down the surface one can see that the enlarged ridge is about to split up. From these observations it is possible to say that there is a stable wavelength, that is a constant number of ridges present on the surface at any one speed, but due to surface imperfections the orientation of some ridges are subject to abrupt local changes.

Figure 19(a) displays the surface configuration at 250 r.p.m. The wavelength of the ridges is noticeably smaller than the previous speeds, and the angle which these ridges make with the cone generator line has increased. The photograph shows the pattern of ridges existing on a part of the cone which has a large amount of blow-holes. These blow-holes were formed during casting and although they were sealed with a non-contaminating compound visible discolouration of the surface around these points, and the appearance of non-wettable areas, led to

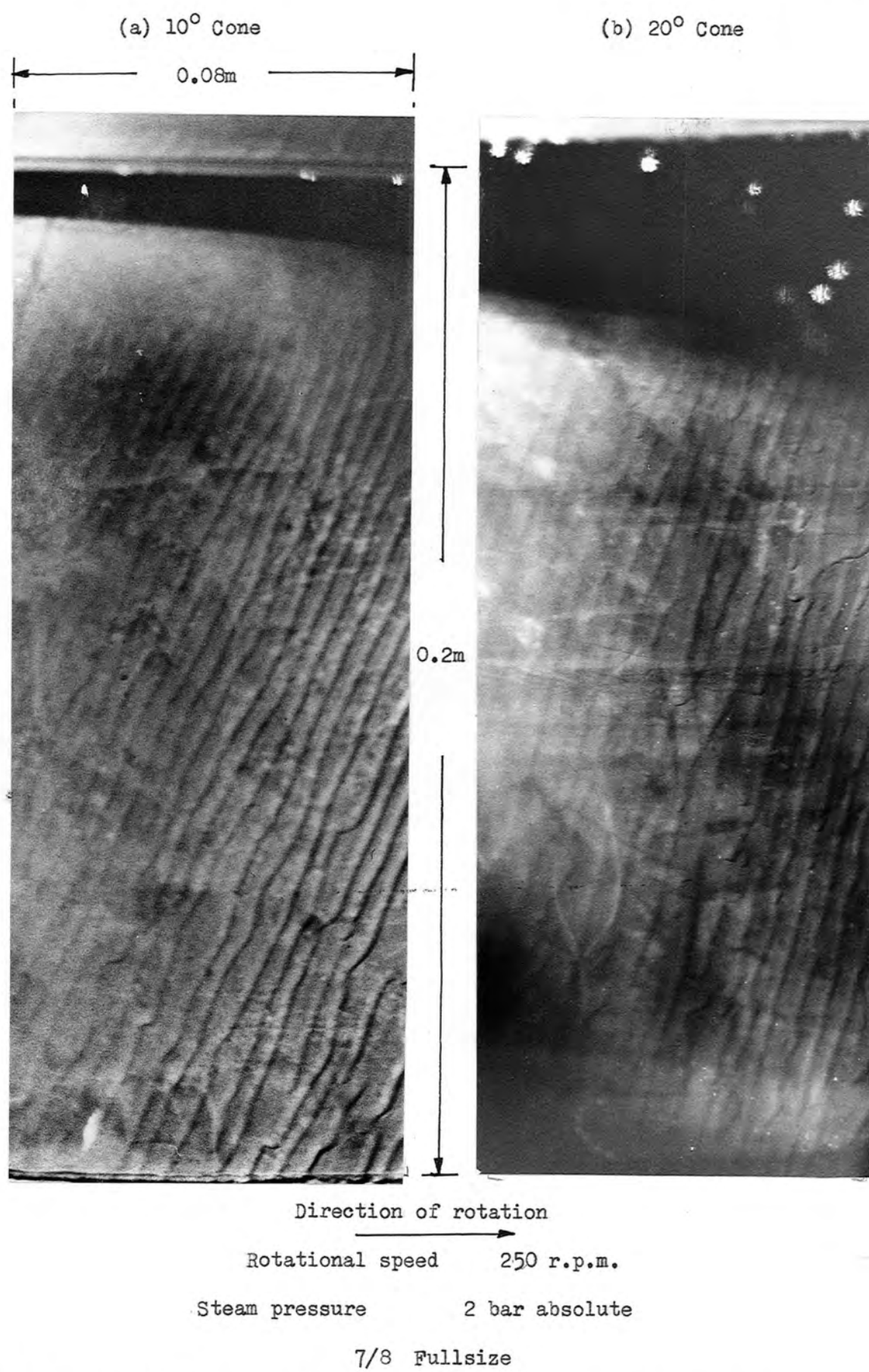


Figure 19. Variation of condensate layer profile with change of speed at constant steam pressure.

the conclusion that some leaching of a contaminant occurred. The surface needed to be cleaned periodically by soaking with Decon 75 (a propriety brand decontaminant). The point of ridge initiation has also moved closer to the starting point of condensation, and experimental results show that an increase in heat transfer rate which implies a higher condensation rate also. The ridge formation on the lower part of the cone has become slightly irregular in that ridges 'snake' down the surface. This suggests that the ridges are approaching a condition in which they permit the maximum possible flow of condensate. The value of  $a_y/a_x$  at this position is 7.04.

A further increase of speed to 300 r.p.m. produced the surface pattern shown in Figure 20(a). Another reduction in wavelength has occurred and the angle of inclination of the ridge to the cone generator line has increased considerably. The irregularity of the ridges is more pronounced and near the lower left-hand corner a protrusion has appeared on one of the ridges. Increasing the rotational speed to 350 r.p.m. results in the irregularity occurring at a smaller radius. The photograph in Figure 21(a) shows well developed protrusions having appeared in greater number although it is not clear whether any protrusions have been detached. The ridges are closely spaced and have a definite peaky appearance. The ratio of  $a_y/a_x$  for the protrusion which appears at the smallest radius is 7.78.

Examination of Figure 22(a), rotational speed 400 r.p.m., confirms that the protrusions become unstable and drops are thrown from the peaks of the ridges. At a position 0.04 m from the lower edge and 0.02 m from the left-hand side of this photograph a drop can be seen. This is considered to be a drop because it has the same 'starred' appearance exhibited by drops being shed from the throwing rings. Tracing the movement of the drop almost horizontally to the right a position can

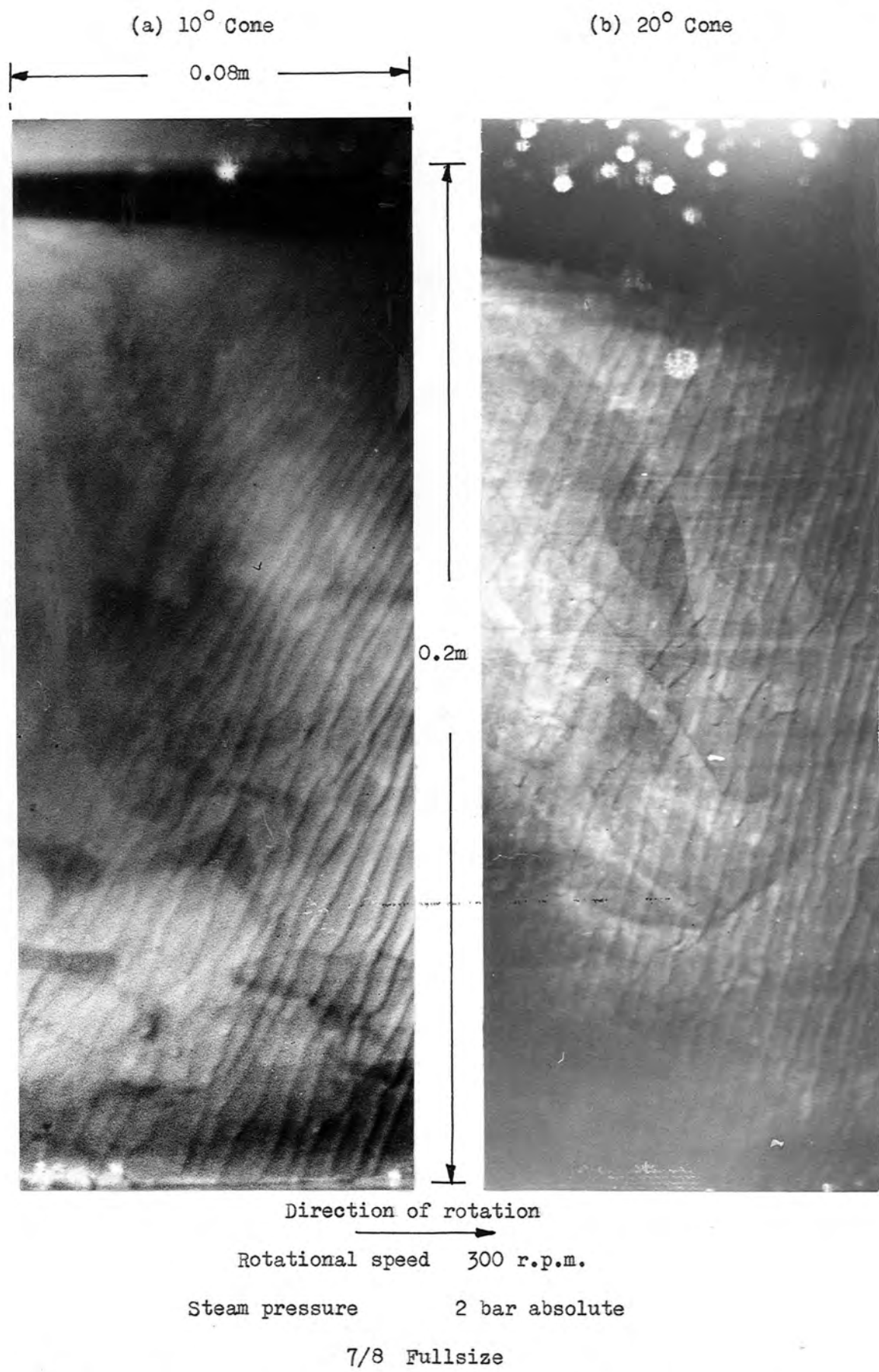


Figure 20. Variation of condensate layer profile with change of speed at constant steam pressure.

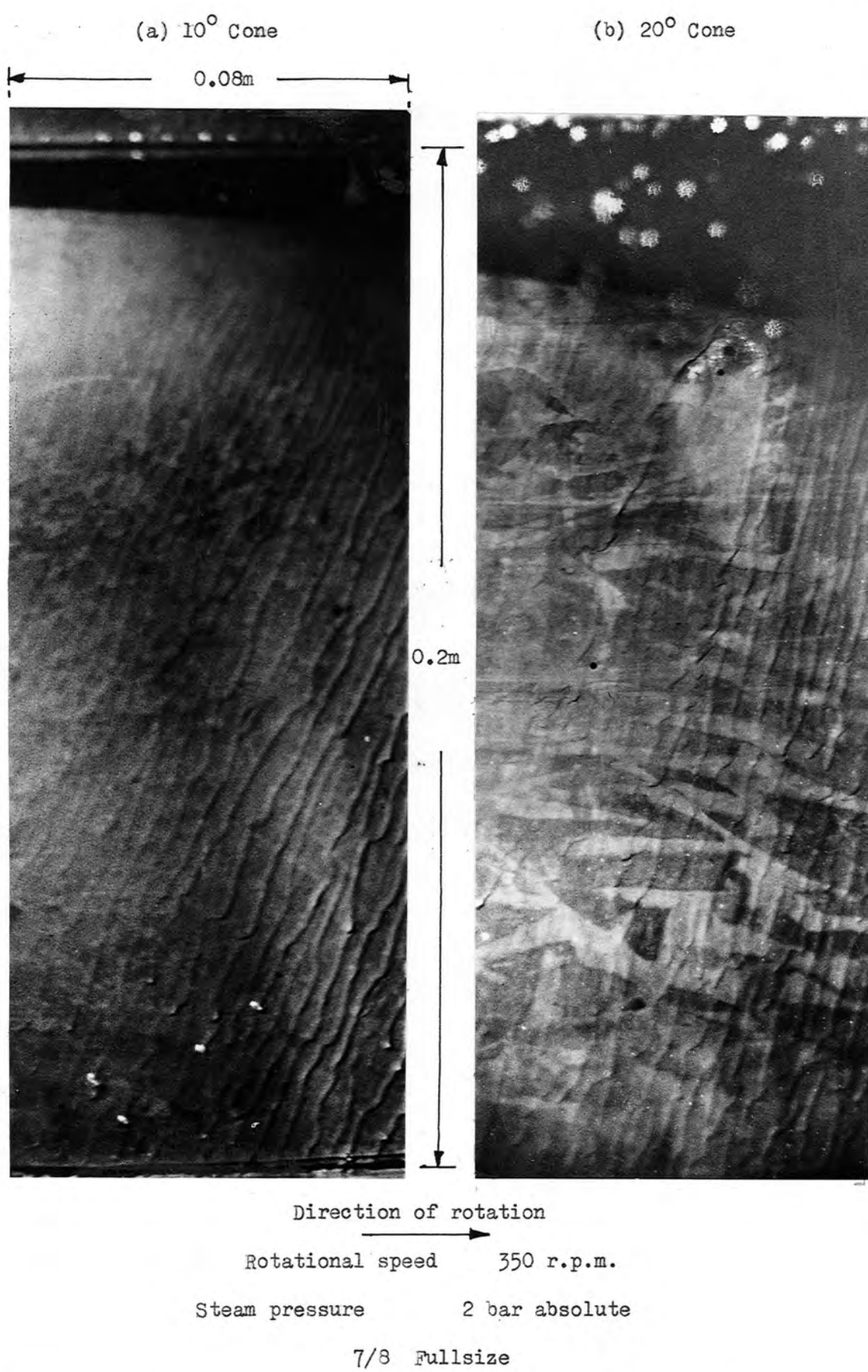


Figure 21. Variation of condensate layer profile with change of speed at constant steam pressure

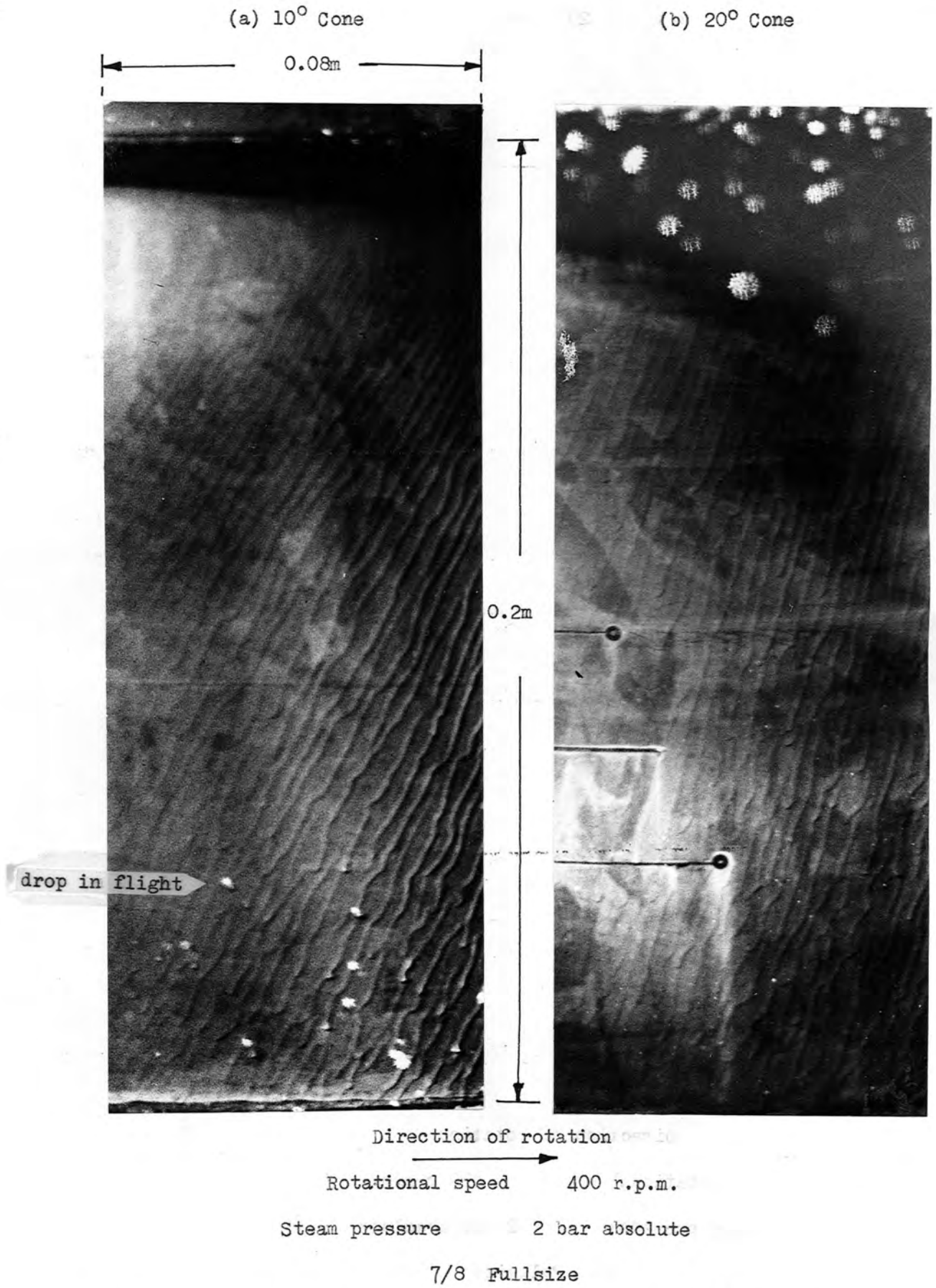
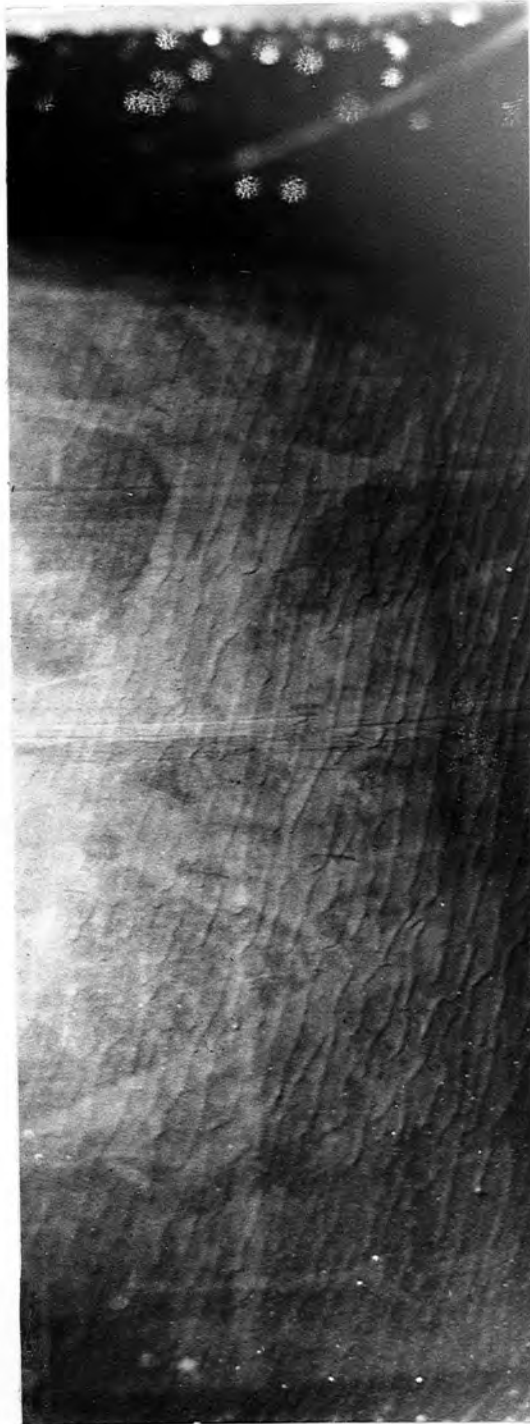


Figure 22. Variation of condensate layer profile with change of speed at constant steam pressure.



Direction of rotation

Rotational speed 450 r.p.m.

Steam pressure 2 bar absolute

7/8 Fullsize

Figure 23. Variation of condensate layer profile with change of speed at constant steam pressure.

be found where a ridge suddenly disappears. The drop has a vertical fall of approximately 2.5 mm and is 29 mm to the left of the above ridge. It may be assumed that the drop leaves the ridge crest tangentially with a velocity of  $\omega R$ . However, it will also have a velocity in the X direction due to the ridge flow itself. It is not certain why the ridge disappears entirely except to say that we are dealing with extremely thin films and once a drop has been precipitated the action of the neighbouring ridges may be such that they now drain the flow in preference. The ratio of the acceleration in the Y direction to that in the X direction at the point the drop was thrown off was calculated to be 10.41.

### 20° Cone

The quality of the observations made on this surface was drastically reduced because the photographs had to be taken through a haze of droplets formed when the condensate from the 10° cone is dispersed at the throwing ring. This caused a reduction in light intensity at the 20° surface. However, observation of drop departure from the ridges is not entirely prevented because the depth of field employed was such that any drop more than 0.2m from the surface was a meaningless blurr. Thus drops which had just left the surface could be positively identified.

For the given pressure the first speed at which ridge type waves were observed was 200 r.p.m., Figure 18(b) presents the photograph of the condensate surface pattern. It is immediately apparent that increase of apex angle has delayed the transition to ridge type waves. Characteristic of all the photographs of the 20° cone is the shadow cast by the throwing ring and the large white blurr formed by the drops discharged from it. The ridges shown have a characteristic feature in common with those on the 10° cone surface at 135 r.p.m. in that ripples are discernable on their surfaces. This speed corresponds to a  $a_y/a_x$

ratio of 3.85 which is larger than that of the  $10^\circ$  cone but may be explained on the grounds that the ridge flow is further developed on the  $20^\circ$  surface.

The next speed investigated was 250 r.p.m. and the photograph of this configuration is shown in Figure 19(b). The change into stable ridge type formation has not yet occurred. There is still evidence of what appears to be ripples on the ridges and also near the top, left-hand, corner a helical roll wave is visible. It would appear from these observations that it requires a larger speed range to produce stable ridge type flow.

At 300 r.p.m. the ridge type flow has become fully established. Figure 20(b) shows the surface configuration and it must be acknowledged that the ridges are not as well formed as those on the  $10^\circ$  cone at the same speed. Unfortunately the  $20^\circ$  cone surface has more porous areas than the  $10^\circ$  cone and it was found that one area of the surface was nearly always non-wettable. The only time it was fully wettable was immediately following a soaking with Decon 75 but this condition only lasted a short time. The irregular formation of the ridges can perhaps be accounted for on this ground. A contributing factor may arise from the presence in the best areas of the surface of the thermo-couple grooves. These have been filled with adhesive but the eroding action of the condensate causes a step like cut in the surface. The angle the ridge makes with the cone generator line can now be seen to be increasing more rapidly with speed. At this point it is possible to make a general comparison with results obtained from the  $10^\circ$  cone. The angle made by the ridges with the cone generator on the  $20^\circ$  cone are all generally smaller than those on the  $10^\circ$  cone. The wavelength also appears larger on the  $20^\circ$  cone but these and the ridge angles will be discussed fully in section 5.4.

Demonstration of the effect of the non-wettable areas on the ridge like waves is shown in Figure 21(b). The rotational speed of the cone is 350 r.p.m. To the right of a large porosity hole the ridges have a smooth appearance similar to those on the  $10^\circ$  cone. Those ridges whose path is interrupted by a non-wettable area tend to bypass it and those which actually traverse such an area 'snake' across it in a disorderly manner. However the effect appears only local as below this section the ridges once more attain a uniform configuration.

A further increase of speed to 400 r.p.m., shown in Figure 22(b), brings about a visible reduction in wavelength and an increase in the angle which the ridge makes with the cone generator. Some discolouration of the surface around the thermo-couple ends and conductance film thickness measuring gauges suggests some leakage of a contaminant.

The final photograph, shown in Figure 23, was taken at 450 r.p.m. Examination of the ridges shows that there is no apparent change in either wavelength or the angle of inclination to the cone generator. At the lower right-hand corner there is a ridge which has a protrusion on it. The  $a_y/a_x$  ratio at this point is 5.19. The same type of protrusion appeared on the  $10^\circ$  cone but it was only after a further 50 r.p.m. increase in speed before drops were observed to be leaving the crests of the ridges. In another series of tests, at 3.0 bar steam pressure, drops were seen to be thrown from the surface. The speed of rotation at which this occurred was 600 r.p.m. corresponding to an  $a_y/a_x$  of 5.32. The increase in condensation rate was not very large so that these rates would not be expected to be very different from that occurring at a pressure of 2.0 bar. It can be seen that the ratio is much lower than that at which drops left the  $10^\circ$  cone. This could be due to the relative speeds of the ridges themselves. On the  $10^\circ$  cone surface the ridge velocity is determined by an  $a_x$  value of  $48 \text{ m/s}^2$  at

400 r.p.m. whereas an acceleration of  $202 \text{ m/s}^2$  occurs on the  $20^\circ$  cone surface at 600 r.p.m. This would make any protrusion formed much more unstable.

### 5.1.2 Variation due to pressure changes at constant speed.

The rotational speed was held constant at 350 r.p.m. and the pressures observed were 1.5, 2.5, 3, and 4 bar absolute. A further series of photographs, Figures 24 to 27, (a) and (b), show the effect of pressure variation at constant speed.

#### $10^\circ$ Cone.

The surface configuration for the ridge formation which occurs at 1.5 bar is shown in Figure 24(a). The photograph is unfortunately marred by discontinuities produced by porosity marks. However the general picture is adequately represented and shows that the condensate flows completely along the surface. At the larger radii small protrusions can be seen to have formed. These protrusions could be due to the discontinuities at the upper radii. An increase in pressure to 2.5 bar, Figure 25(a), indicates no drastic change in the method of drainage except that in the left-hand lower corner a drop may have been thrown off but the photograph is not clear enough to be certain. At 3 bar absolute, photograph shown in Figure 26(a), there is a slight increase in wavelength and drops are being thrown off at a position some 40 or 50 mm from the bottom of the surface. The pattern is very distinct and reveals that as the ridges build up in size they become generally unstable and 'snake' down the surface.

Finally at 4 bar, the photograph of the surface is presented in Figure 27(a), drops are being shed at radii up to the mid-point of the cone surface. This is not a particularly good example because again a porous area at upper radii produce smearing and collision of ridges

which may prematurely overload a single ridge allowing drops to be thrown off at a smaller radius than would have been expected. It may be concluded that changes in the angle made by the ridge with the cone generator and the wavelength brought about by changes of pressure are not as large as those with speed. It appears that it is the size of the ridge, due to rapid build up of condensate at higher condensation rates, which induces drops to be precipitated at smaller radii as the pressure is increased. That is the condensate flow builds up quickly to the point where it permits the maximum amount of flow, a small instability is then enough to cause a drop to be precipitated and thus relieve the ridge and allow the condensate flow to build up again.

#### 20° Cone.

The speed of 350 r.p.m. was maintained for the 20° cone and the condensate surface configuration, at the first steam pressure of 1.5 bar, is given in Figure 24(b). Description of the surface form for the 20° cone is best accomplished by comparison with the previous description of the 10° cone results. The wavelength appears longer and the ridges less peaky than those shown in Figure 24(a). No protrusions are visible and the regime is quite orderly with the angle of inclination of the ridges to the cone generator slightly less than on the 10° cone.

The photograph for the next pressure of 2 bar is shown in Figure 21(b). Comparison with that for the 10° cone confirms that the angle the ridges make with the cone generator are smaller. This photograph has already been described in a previous section. The non-wettable area prevents any direct conclusions being drawn from this figure. There is very little change in the condensate surface configurations for the next two pressures of 2.5 and 3 bar, which are shown in Figures 25(b) and 26(b) respectively. However, it is clear that the angle between the direction of the ridges and the cone generator increases with the semi-

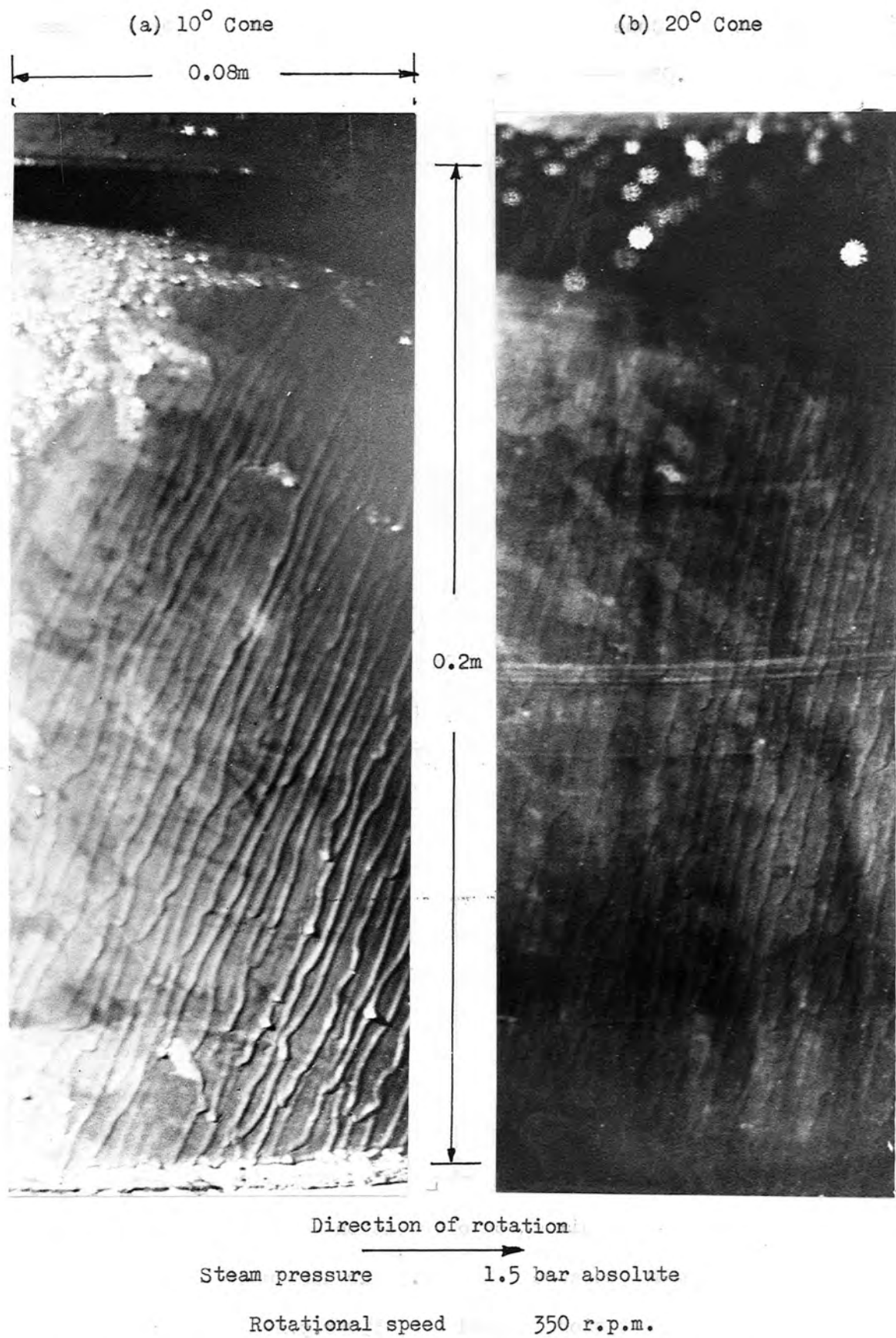
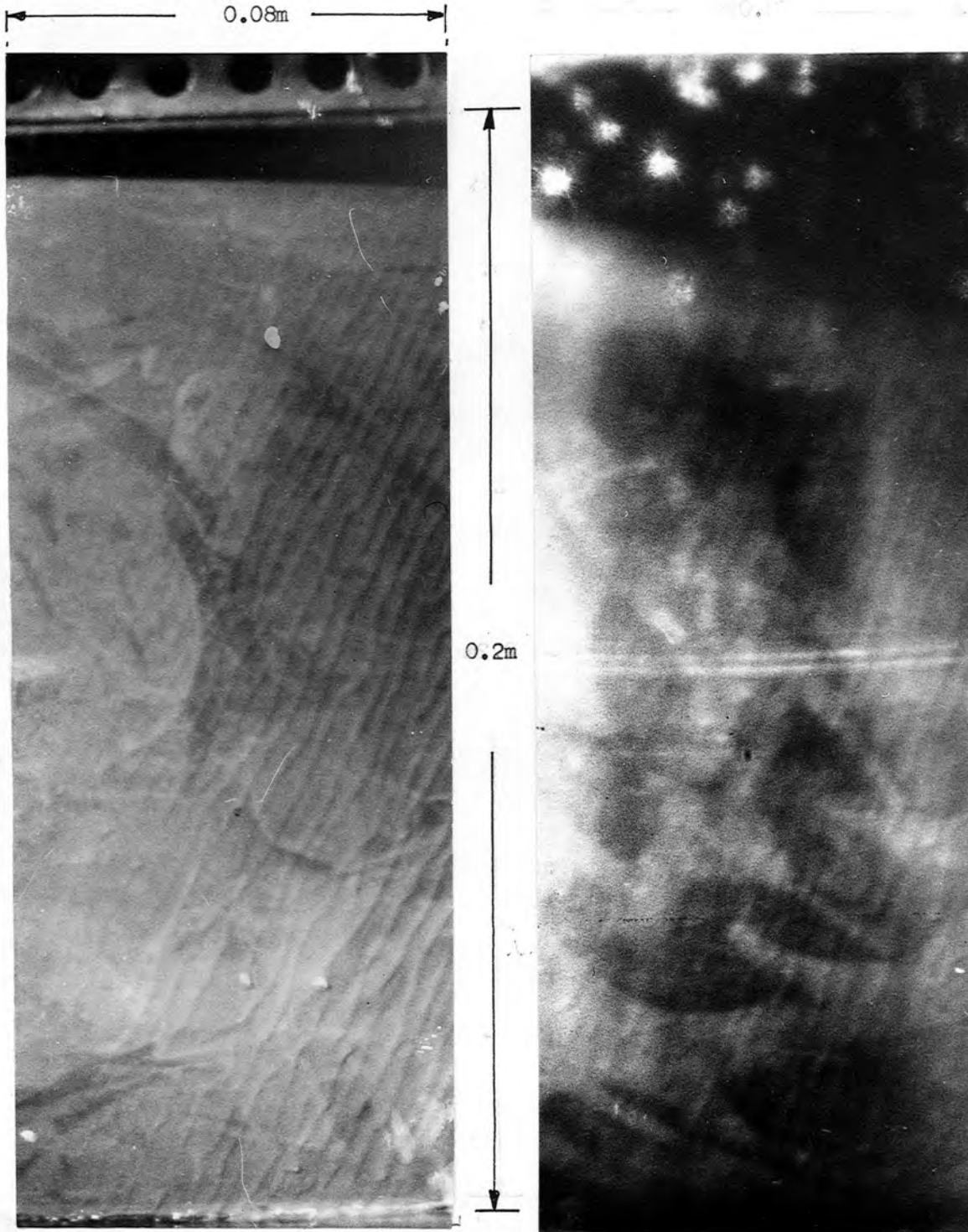


Figure 24. Variation of condensate layer profile with change of pressure at constant speed

(a)  $10^\circ$  Cone

(b)  $20^\circ$  Cone



Direction of rotation

Steam pressure 2.5 bar absolute

Rotational speed 350 r.p.m.

7/8 Fullsize

Figure 25. Variation of condensate layer profile with change of steam pressure at constant speed.

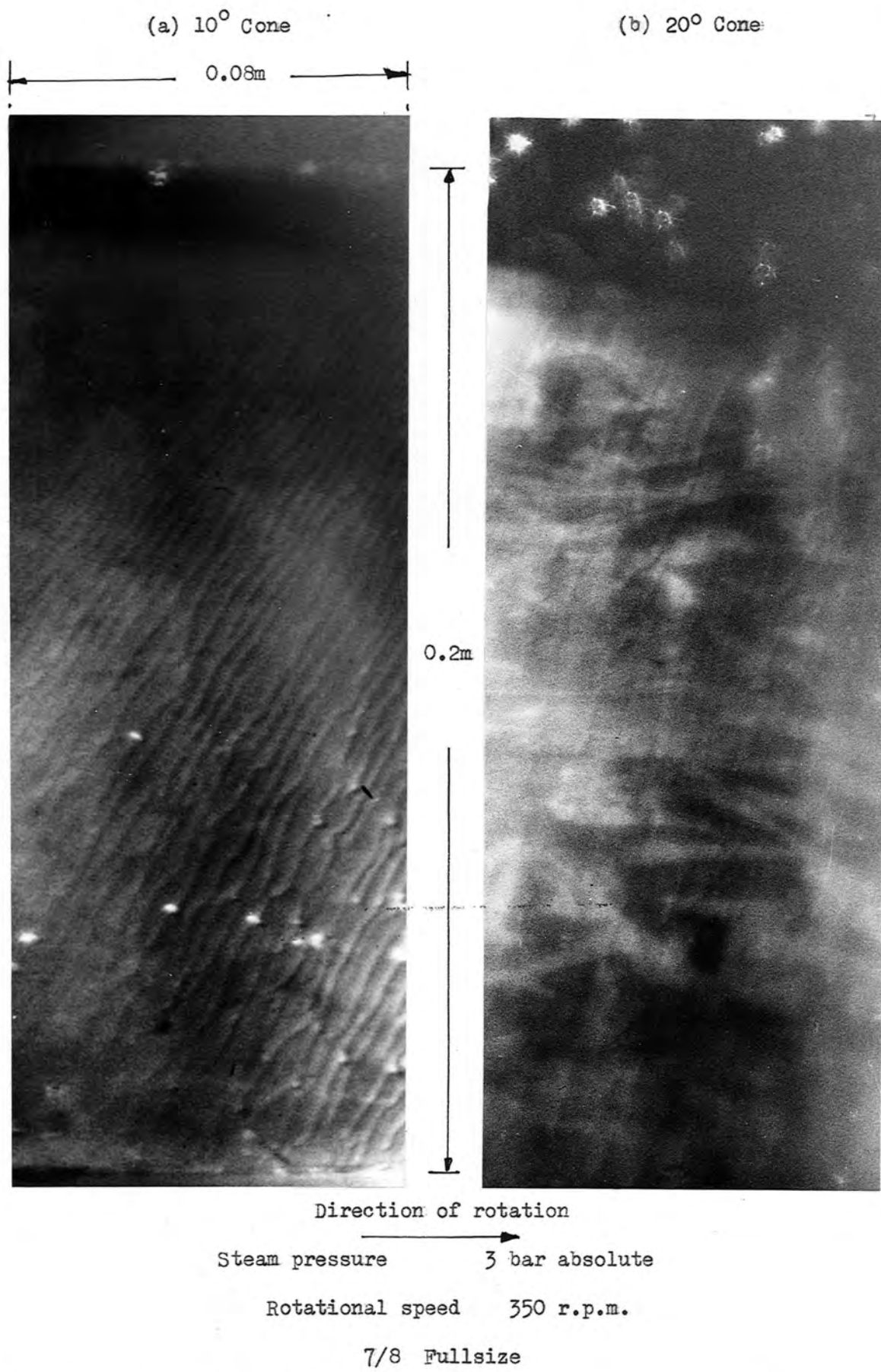


Figure 26. Variation of condensate layer profile with change of steam pressure at constant speed.

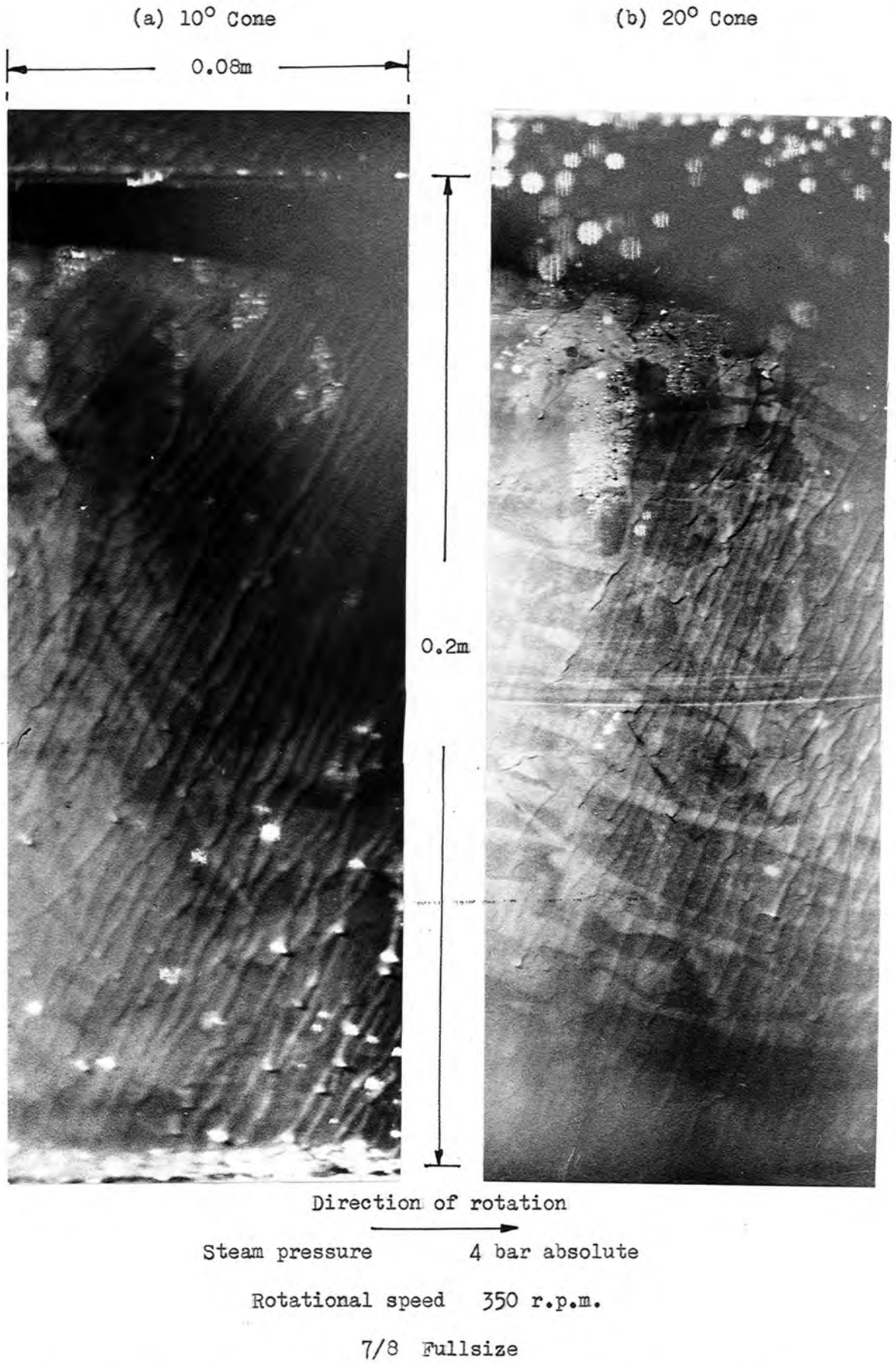


Figure 27. Variation of condensate layer profile with change of steam pressure at constant speed.

angle at the apex of the cone. Apparently, therefore, this angle is not determined solely by Coriolis forces, but that inertia forces and perhaps drag forces from the vapour phase may play a part. No protrusions are visible on the 3 bar photograph but the lower portion is very blurred. This blurring is due to dispersion of the incident light by small drops.

The last photograph included, presented in Figure 27(b), was taken at 4 bar absolute. This is a clearer photograph but is marred by a non-wettable patch which has appeared in the upper left-hand corner. A more stable section of the ridge formation occurs in the bottom right-hand corner. This section shows that protrusions have appeared on the ridges. A further increase in the angle of inclination of the ridges to the cone generator has occurred. Summarising the information gained for the  $20^\circ$  cone, a small increase in wavelength and an increase in angle of inclination of the ridges occurs as the pressure was increased from 1.5 to 4 bar. The photographs shown for the  $20^\circ$  cone were the most presentable ones acquired. All the others allowed only the ridge angle and wavelength to be obtained with some difficulty. It must therefore be borne in mind that the  $20^\circ$  cone results are not as reliable as those obtained from the  $10^\circ$  cone photographs.

## 5.2 Initiation speeds for ridge formation and drop departure.

It was possible for the  $10^\circ$  cone to observe closely, with the aid of a stroboscope, the speeds at which ridges appeared and disappeared and also the rotational speeds at which drops were seen to be thrown from the ridges at all test pressures. The results are presented graphically in Figure 28. The measurement of rotational speeds at which drops begin to leave the ridges are not as reliable as those at which the ridge formation appears because the background also contained

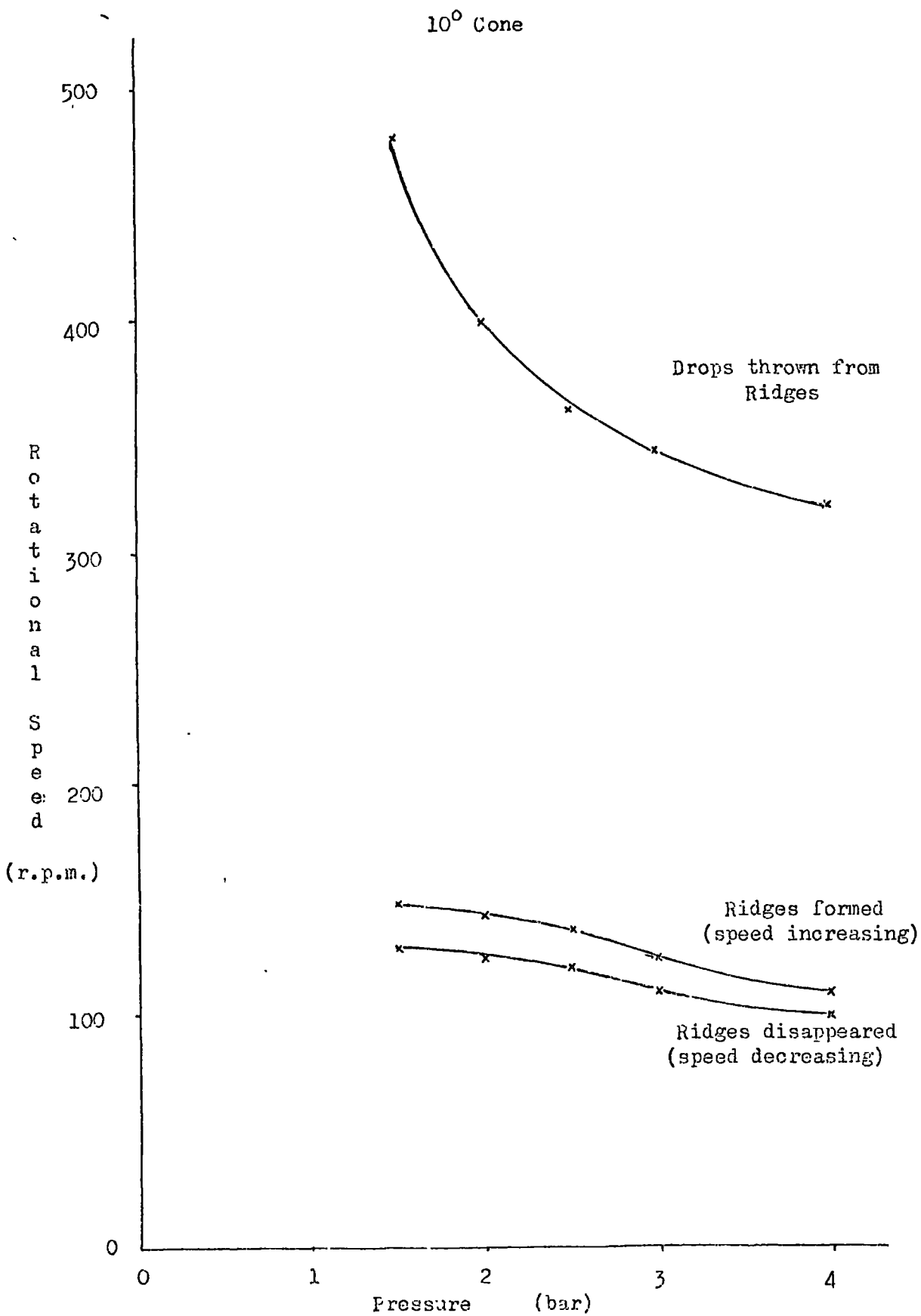


Figure 23. Ridge initiation and drop formation speeds.

drops which were produced by the throwing ring. The initiation of the ridge regime is dependent on condensation rate which is directly proportional to the pressure. This is to be expected since the more condensate on the surface the greater the inertial forces. The hysteresis effect manifests itself in a difference between the limiting conditions at which ridge waves first appear, and those at which they disappear, shown in Figure 28, may be due to

- (i) difference in the effect of surface tension in the two cases.
- (ii) drag forces due to the vapour phase may hold the curtain type regime.
- (iii) the actual mechanism which first produces the ridge type flow, which may only be postulated, is not reversible.

The curtain type waves, or roll waves, even when the cones are stationary do not follow a consistent pattern. Once the cones begin to rotate the roll waves appear to take on a helix like action. From the observations made this helix action does not appear to change from 50 r.p.m. to the point of change into the ridge like regime. The roll waves shorten in wavelength, that is there are more wave fronts on the condensate surface.

In the stationary case drainage of the condensate is governed by gravity and the angle of inclination of the surface with respect to the vertical is important. When the cone is rotating the drainage force in the X direction is increased by the term  $\omega^2 R \sin \beta$ . At the same time a component now exists which is trying to pull the film away from the surface. Increasing the rotational speed increases the film velocity in the X direction and also the centrifugal pull away from the surface causes the flow to become more unstable. Kapitza has shown that the wave velocity is 2.4 times the mean film velocity thus the roll waves are travelling more rapidly. This unstableness in the wave front takes

the form of jagged sheets.

The jagged appearance of the main roll wave fronts may be the initiation of the ridge type flow. The rotational speed has become too large to support this type of flow and another more stable form must be attained. Surface tension forces are too large to allow drops to be thrown from the surface. Each of these jagged waves is a triangle pointing in the direction of flow. The sharper the apex angle of these triangles become the greater the action of acceleration terms causing the condensate flowing in the wave itself to break away in pockets. Thus if these spear shaped pockets begin to coalesce in the X direction then the beginnings of ridges occur. This may be one interpretation put on the appearance of the surface in Figure 17(b). The shape and wavelength of these ridges then being determined by the centrifugal acceleration in the Y direction.

The changes in the regimes so far have been plotted on a rotational speed basis, Figure 28. It can be seen that the two curves appear to become asymptotic. A non-dimensional variable may now be introduced which has such a relationship with increase of speed. This is the ratio of the acceleration in the Y direction to that in the X direction,  $a_y/a_x$ . For cones this ratio approaches the limit of  $1/\tan \beta$ , the limits are

- (i) for the  $10^\circ$  cone,  $a_y/a_x = 11.4$
- (ii) for the  $20^\circ$  cone,  $a_y/a_x = 5.6$
- (iii) for the  $60^\circ$  cone,  $a_y/a_x = 1.74$

For cylinders  $a_y/a_x$  can increase without limit, that is it equals  $\frac{1}{2}D\omega^2/g$ . The speed range in which we are interested has a maximum value of  $a_y/a_x$  equal to 9.65 and 5.45 for the  $10^\circ$  and  $20^\circ$  cones respectively. For a horizontal cylinder the term  $a_y/a_x$  is somewhat artificial since the flow is circumferential and condensate flows from the lower face in the form

of drops to begin with. The term can be replaced by  $\frac{1}{2}D\omega^2/g$ , which is used by Hoyle and Matthews (56), and the change of drainage pattern considered to have occurred when drops leave the surface tangentially at all positions.

The action of the two components of the centrifugal acceleration are important throughout the range of the ridge like flow. The component of acceleration in the Y direction,  $a_y$ , is attempting to pull the film away from the cone surface and is being resisted by surface tension forces. The component of acceleration in the X direction,  $a_x$ , causes the condensate to be drained along the ridge and at moderate speeds tends to help stabilise the pattern. Increasing speed will at some point cause the ridge type flow to become unstable. The velocity in the ridge must be very complex since we have flow in the X direction, a circumferential flow draining the trough of each ridge and also condensation on the surface of the ridge itself. Thus any instability may be enough to break the hold of the surface tension forces and allow the ridge to be relieved of condensate in the form of drops.

Another variable which must have some bearing on the regimes of flow is the distance in the X direction or for cones an increase in radius. That is the further downstream one travels the greater the likelihood of change of regime because the film becomes thicker and ultimately turbulent.

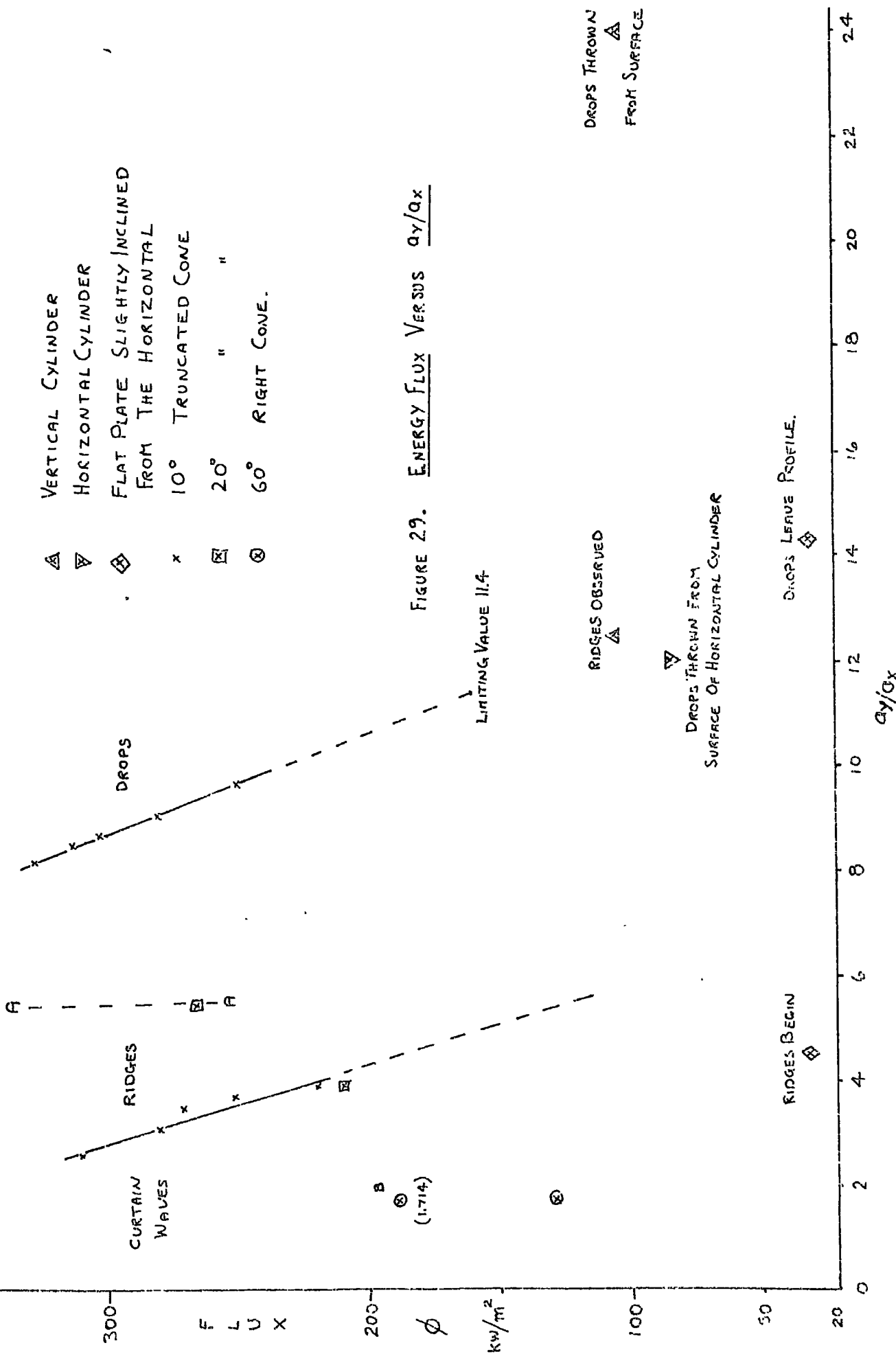
A similar pattern of disturbances were observed on the  $60^\circ$  rotating right cone reported by Robson (68). These 'ridges' were only formed at speeds between 600 and 1450 r.p.m. at radii greater than 0.35 m for the lower rotational speed. Photographs included in Robson's thesis showed that the 'ridge' formation was also pressure dependent. No accurate measurements could be made from the photographs but in terms of  $a_y/a_x$  and heat flux,  $\phi$ , two representative points were obtained. It was

possible to extract information from three rotational speeds providing an average value of  $a_y/a_x$  of 1.714 for an energy flux of  $1.89 \times 10^5 \text{ w/m}^2$ . A second point of  $a_y/a_x$  equalling 1.713 and energy flux,  $\phi$ , of  $1.29 \times 10^5 \text{ w/m}^2$  was also obtained.

A formation of ridges was also noted by Birt et al (52) on the condensate layer on the surface of a rotating vertical cylinder, of 0.1524 m diameter, at low speeds. A photograph in the above paper shows ridges on the condensate layer which are formed at 337 r.p.m. and an energy flux of  $1.075 \times 10^5 \text{ w/m}^2$ . The ratio  $a_y/a_x$  is a direct ratio of centrifugal acceleration to the drainage acceleration in the X direction, which the acceleration due to gravity and has a value of 12.5.

Although no direct observation of the ridge patterns forming was carried out for the  $20^\circ$  cone photographic evidence in Figure 18(b) allows one to say that this speed is not greatly above the initial formation speed. During an earlier series of tests, prior to the major overhaul, a photograph taken at 185 r.p.m still showed waves of the curtain type on the condensate layer. All the above mentioned points are plotted in Figure 29. Finally a value of  $a_y/a_x$  at an energy flux of  $30 \times 10^4 \text{ w/m}^2$ , is included for ridge formation of a condensate layer on the underside of a slightly horizontal plate. As explained in section 2.0 this is only an average value because not enough information was included in Gerstman and Griffith's paper (49).

The second consideration was to identify the point at which drops were thrown from the condensate layer. It was not possible to predict this point theoretically. However from the experimental results a plot of  $a_y/a_x$  versus energy flux allows a line to be drawn on one side of which the ridge regime exists, with the condensate flowing wholly along the surface, and on the other condensate removal is enhanced by drops being thrown from the condensate layer. The experimental results



are plotted in Figure 28. Only a single point was available for the  $20^\circ$  cone and this was taken from a drop shown in a photograph taken at 600 r.p.m. and a steam pressure of 3 bar absolute. A line, A - A, may be drawn because changes in values of  $a_y/a_x$  above 500 r.p.m. are small. Protrusions formed on the surface of horizontal, rotating cylinders were reported to be discharged tangentially when a ratio of  $\frac{1}{2}D\omega^2/g$  equal to 12 was reached. Birt et al show that for a vertical cylinder condensate removal by drops occurs when  $\frac{1}{2}D\omega^2/g$  is approximately equal to 24, this value may not be the lowest speed for drop formation, however, no other information was given. Finally the angle of inclination to which a plate must be inclined from the horizontal for drops to detach themselves from ridges is about  $4^\circ$ . This angle corresponds to a value of  $a_y/a_x$  of 14.5.

Examination of Figure 29 shows that the experimental points divide the range of  $a_y/a_x$  into three distinct regimes. Comparing other workers findings the first comment which can be made concerning the  $60^\circ$  cone is that all the values obtained fall within the roll wave, or waves of the curtain type regime. This coupled with the fact that no sudden change in condensate surface pattern occurs tends to suggest that this is not true ridge type flow but more of a squeezing together of helical roll waves. The vertical cylinder appears to require the greatest ratio of  $a_y/a_x$  to obtain both ridge formation and drop departure. This conclusion is made because ridges are observed on the cylinder when the value of  $a_y/a_x$  is outside the upper limit for the  $10^\circ$  cone. From the above analysis certain fundamental conclusions can be drawn. Firstly, increase of condensation rate causes drops to be thrown from the condensate layer at progressively lower speeds. This point also suggests that the length of condensing surface is important to drop departure. This may be deduced from Nusselt's theory where if the condensing is long enough the film becomes thicker until turbulence occurs. Since the

shedding of drops is essentially due to inertia forces the build up of condensate will lead to drops being thrown off at lower speeds. This then could account for the discrepancy in ridge and drop  $a_y/a_x$  ratios. The distance along the condensing surface when drops were seen to fly from the condensate layer, for the  $10^\circ$  and  $20^\circ$  cones, is approximately 0.18 m. No distance is given in Birt et al's paper(52) so that one may be looking at a drop thrown from a point much closer to the start of condensing surface which would mean a higher rotational speed to obtain removal of condensate by drops thrown from the condensate layer than at a distance of 0.18 m. This means that the lines in Figure 29 are not unique, that for comparison with each other and also other bodies a distance parameter is necessary.

At the outset of the project it was hoped that the theory would allow the prediction of both ridge like wave initiation and drop detachment speeds. Unfortunately the theory suggests that no stable wave-form exists at low rotational speeds and thus there may be no definite point of initiation of ridge type flow. A point however exists below which the wavelength predicted becomes infinite. The stability line is shown in Figure 6. This may be a consequence of the neglect in the theory of the presence of curtain type waves on the surface of the condensate before ridge flow is initiated. Thus a separate theory is necessary in order to develop the progress of curtain type waves from zero speed upwards. The results of this analysis could be used as a boundary condition for the ridge type flow. A separate theory was investigated, of the solution of the governing equations in spherical coordinates by a perturbation technique, but the final equations obtained were so complicated that no satisfactory means of solving them has been found.

The theory will predict an instability as the speed is increased through the ridge type flow range. As speed increases,  $S_{max}/S_{min}$ , the

ratio of film thickness at the wave crests to that in the troughs increases and finally reaches a value which is clearly not possible in practice. This occurred on the  $20^\circ$  cone at 600 r.p.m. where  $\delta_{\max}/\delta_{\min}$  attained the value of 16.4 to obtain the required heat flux experimentally present. The reason for this anomaly is that the sudden change in heat flux when a drop is detached cannot be taken into account in the theory.

### 5.3 Comparison of theoretical and experimental work.

The theoretical section has already dealt with the general solution of equation 3.8.13 in terms of parameters  $\Lambda$  and  $\Theta$ , but in order to check the prediction of wavelength and film thickness, given certain quantities, the measurements of maximum and minimum film thicknesses are required. Failure of the proposed method of measuring film thickness by the conductivity of the condensate layer, as described in Appendix B, had the consequence that measurements of the film thickness at the wave crests were available. The minimum value was necessary to calculate  $\Lambda$ ,  $\Theta$  and  $\Omega$ . Once these were known the equation 3.8.13 could be solved using the Continuous System Modelling Programme package as described in Appendix D. To overcome this difficulty a computer programme, also given in Appendix D, was developed within the C.S.M.P. package which, using an iterative technique, predicted either  $\bar{\delta}$  and wavelength using energy per unit area transferred as a convergence factor or wavelength and heat transfer coefficient employing the measured maximum film thickness as the convergence factor. The former computation predicting  $\bar{\delta}$  and wavelength assumes a starting value  $\Lambda$ , and hence  $\Theta$  and  $\Omega$ , then solving equation 3.8.13 in finite steps until a maximum value of  $\bar{\delta}$  is found which corresponds to one half

non-dimensional wavelength. Assuming Fourier conduction through the condensate film a heat transfer coefficient for each finite strip was calculated and integrating over half a wavelength a mean heat transfer coefficient evaluated. From the experimental results a local film temperature difference and wall temperature difference were obtained and hence a heat transfer coefficient. The two heat transfer coefficients could then be compared and an iterative procedure adopted which increases  $\Lambda$  until the former two are equal or more practically when they are within  $\pm 5\%$ . The second method also assumes an initial value of  $\Lambda$  but this time calculates  $\bar{z}$  from the measured value peak film thickness divided by the value of  $z_{\min}$  calculated from  $\Lambda$ . The non-dimensional half wavelength and theoretical  $\bar{z}$  are obtained from the solution of equation 3.8.13 and an iteration performed until both  $\bar{z}$ 's are equal or more practically within  $\pm 5\%$ . The computer programme is fully described in Appendix D.

The two above methods should be of equal importance. During development of the programme it was found that because of the large error in calculating the experimental heat transfer coefficient and an unexpected poor convergence at low rotational speeds the programme took too long to run. Thus to check the theoretical solution the convergence using the measured value of maximum film thickness was adopted. The programme evolved, Appendix D, calculates the theoretical wavelength, minimum, mean and laminar film thicknesses. Processing the previous information further; heat transfer coefficients, Nusselt and Taylor numbers and inertial effects were computed.

### 5.3.1 Wavelength.

It has been assumed that the ridge formation has a regular, almost sinusoidal, appearance and that to model the ridge exactly the initial

FIGURE 30 DIMENSIONLESS FILM THICKNESS VERSUS DIMENSIONLESS WAVELENGTH

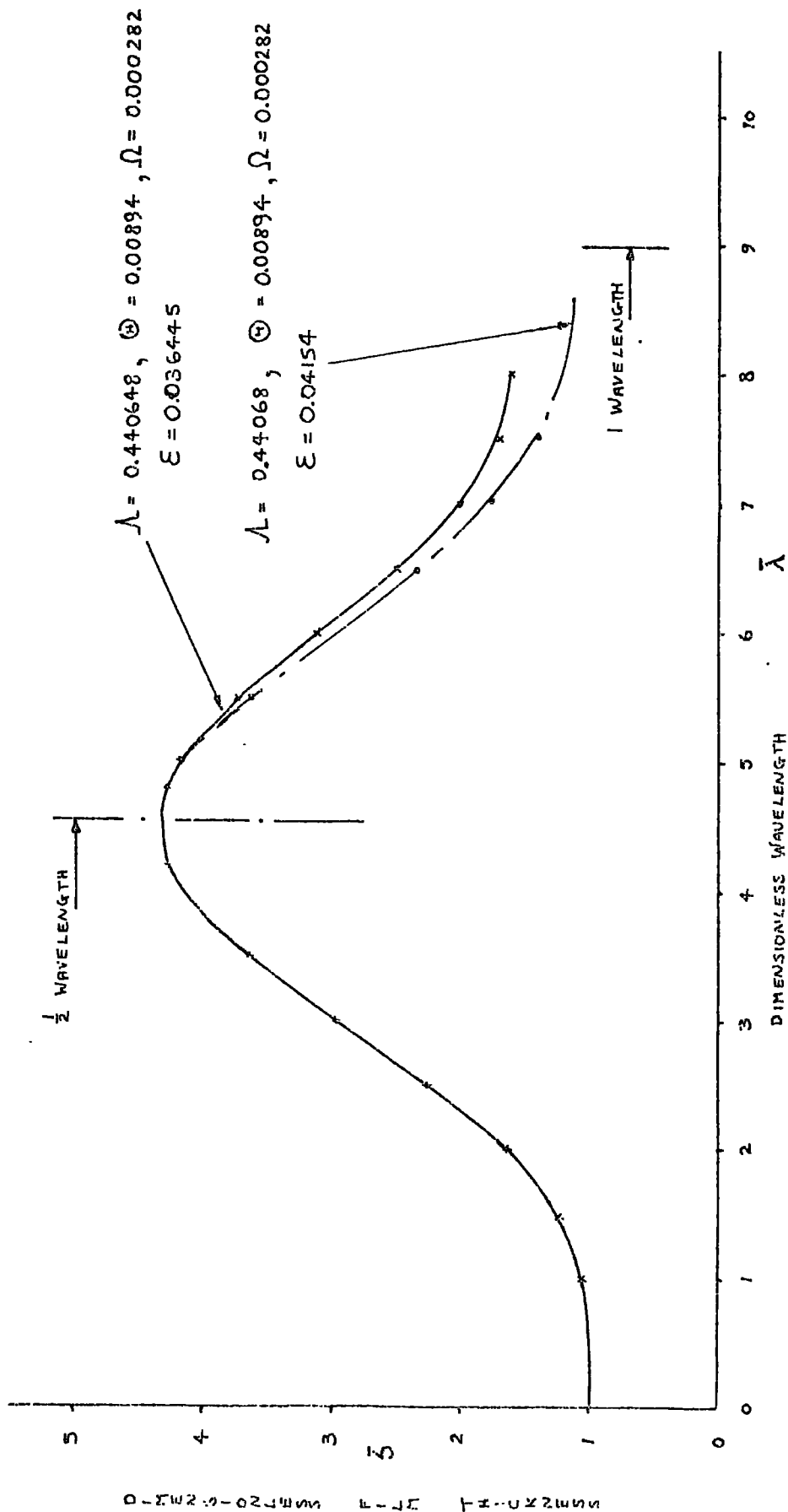
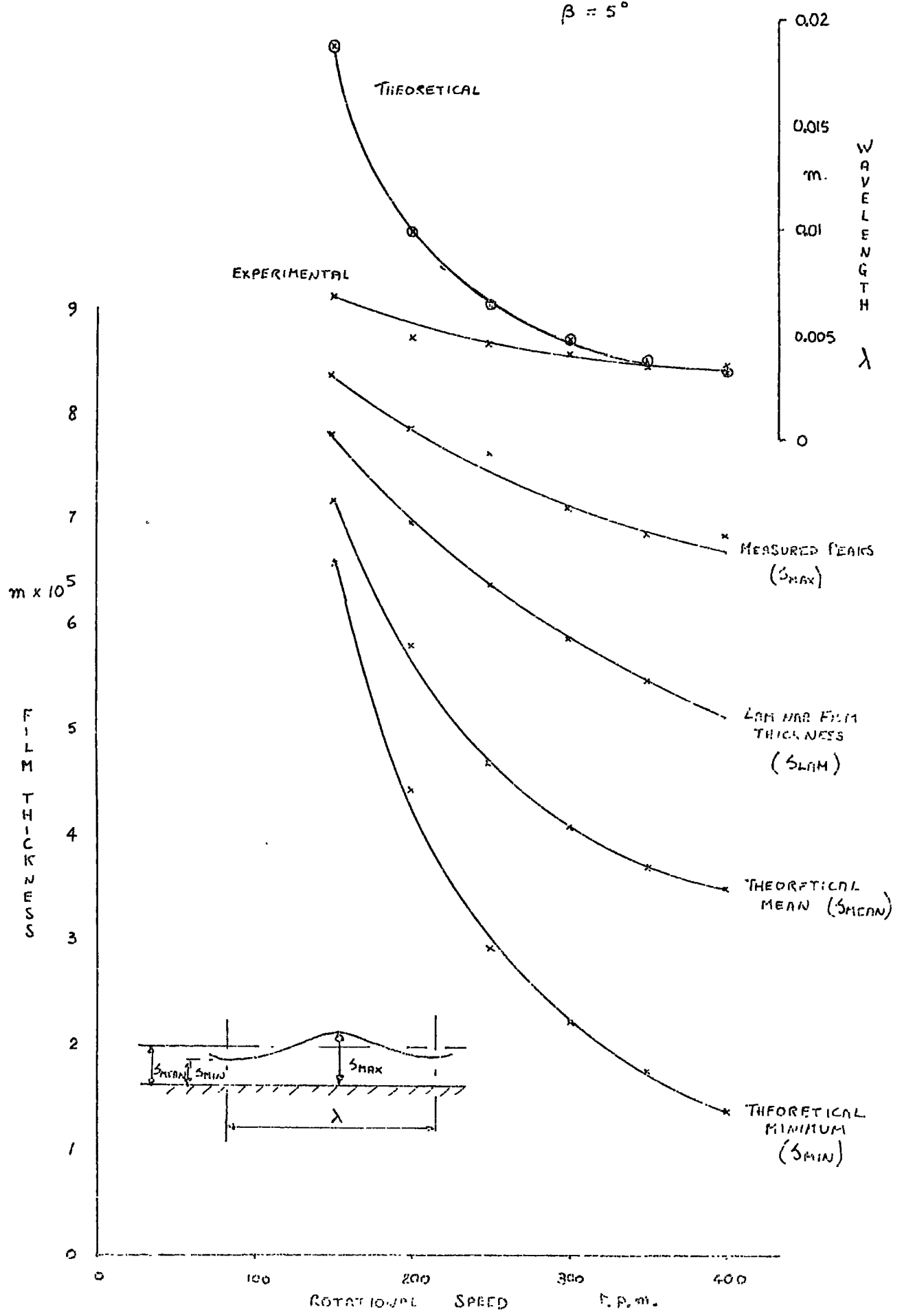


FIGURE 31 TYPICAL WAVELENGTH AND FILM THICKNESS VERSUS ROTATIONAL SPEED

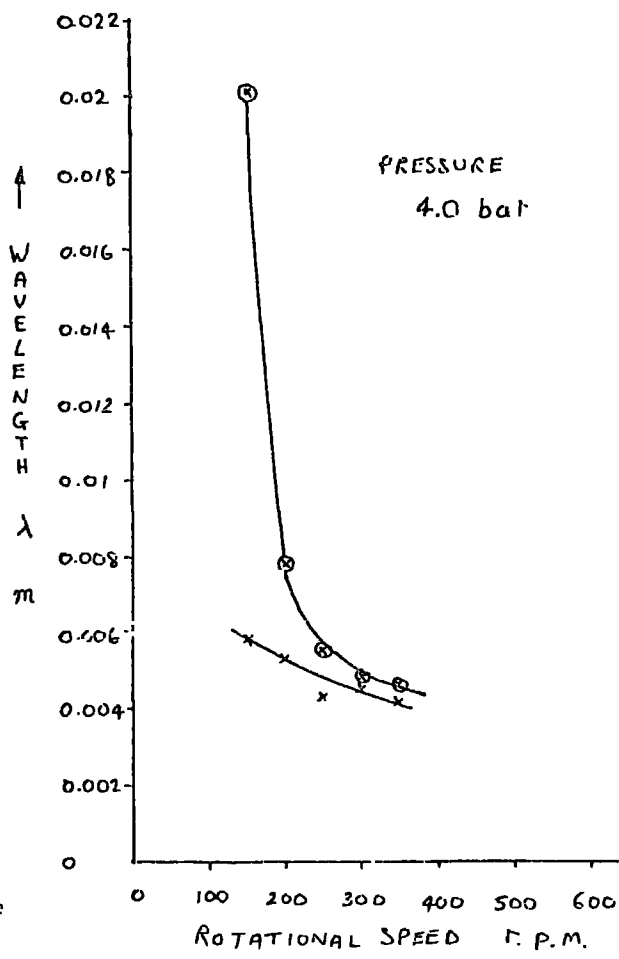
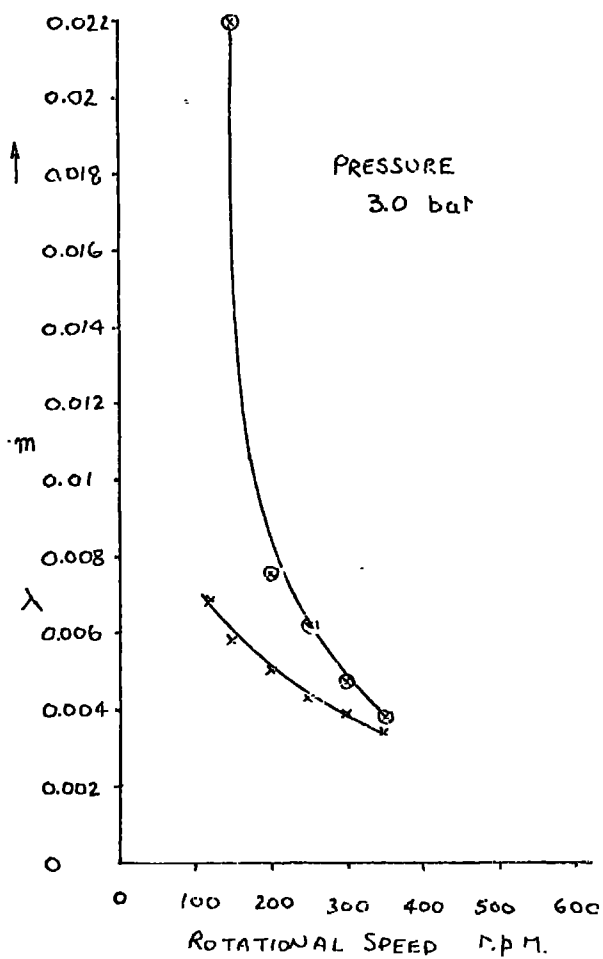
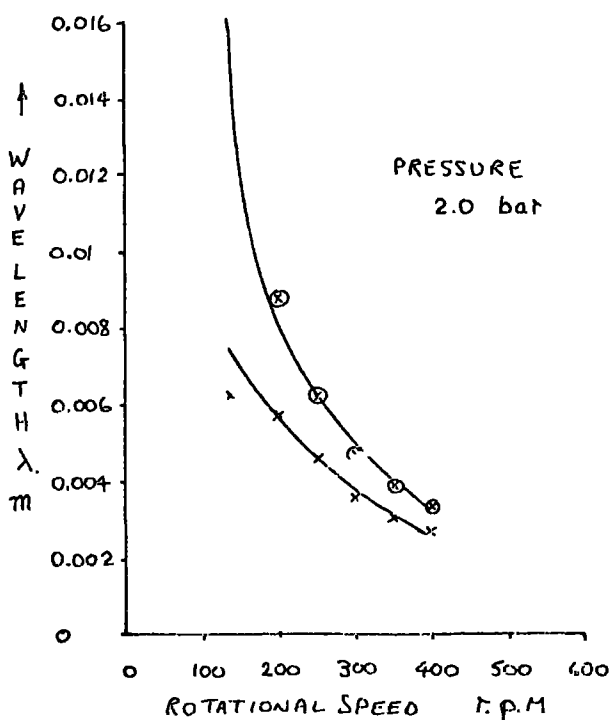
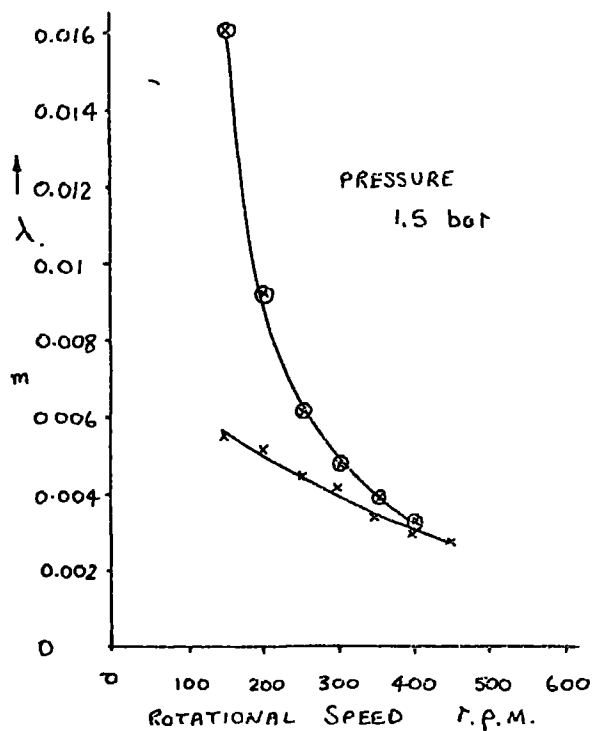
PRESSURE  $2\frac{1}{2}$  bar abs. APEX ANGLE  $10^\circ$   
 $\beta = 5^\circ$



boundary conditions must result after one complete wavelength. After many runs it was found that this was not the case. The programme output showed that one wavelength was not twice the half wavelength and that sometimes the final value of  $\bar{\lambda}$  was either less than or greater than unity. This inherent error indicates that some of the simplifications and assumptions affect the repeatability of the waveform. Figure 30 depicts a typical ridge profile produced by the computer programme.

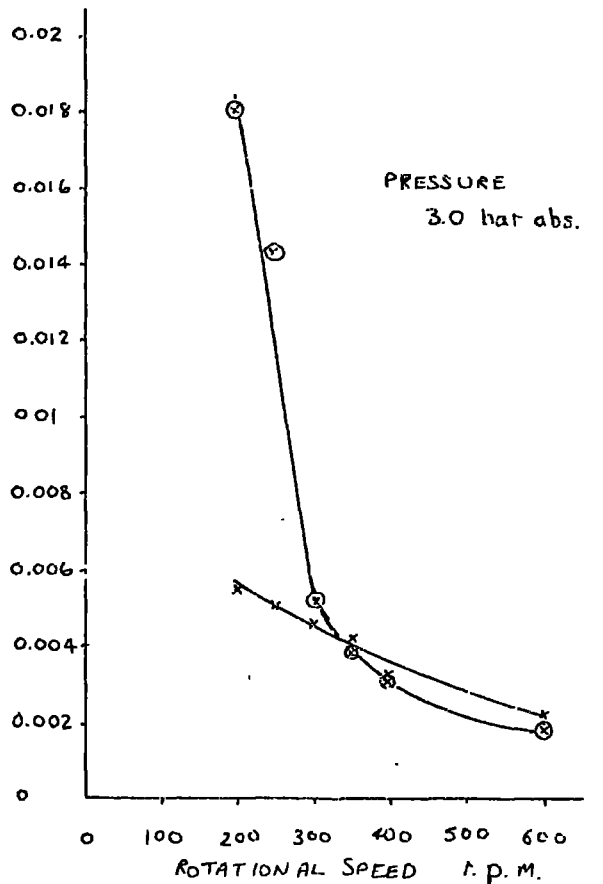
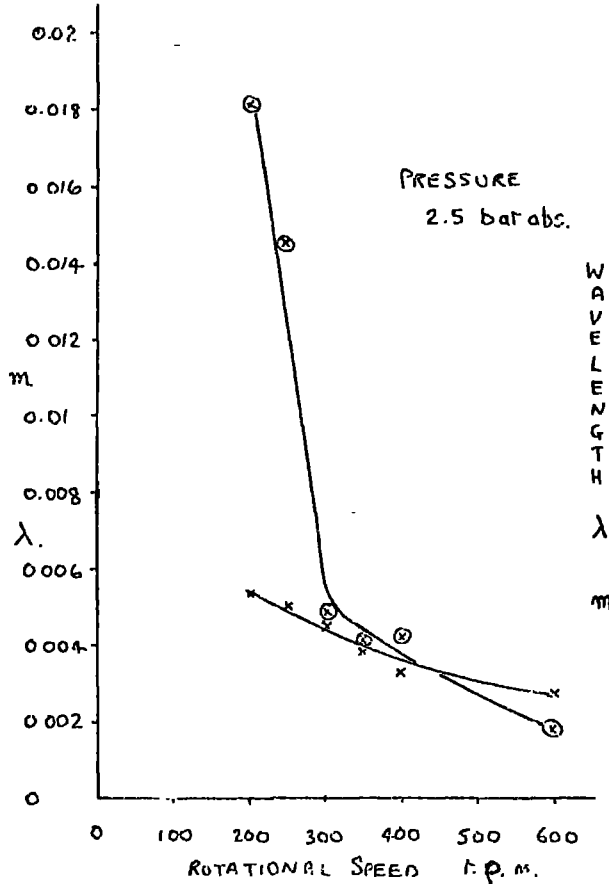
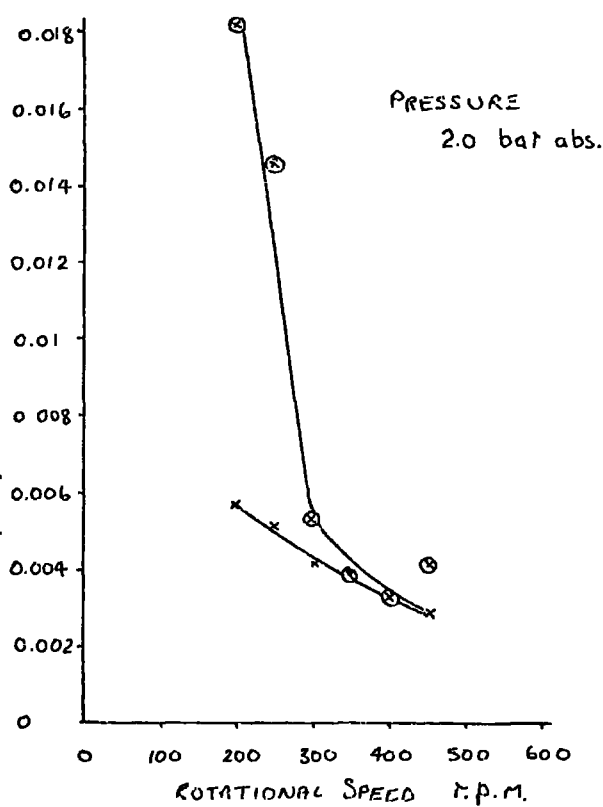
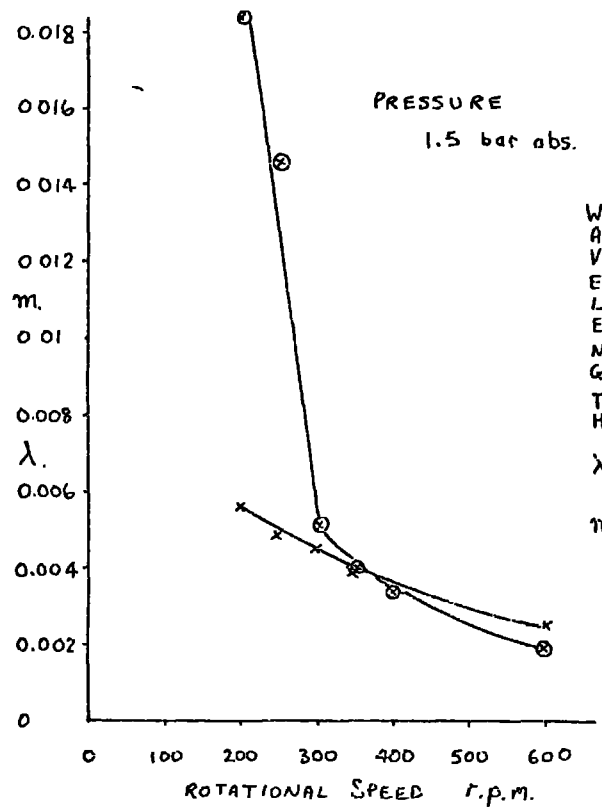
A comparison of theoretical and experimental wavelengths for a steam pressure of 2.5 bar formed on the  $10^\circ$  cone are shown in Figure 31. It is immediately apparent that at low rotational speed there is a large discrepancy between theoretical prediction and the measured value. As the rotational speed is increased the discrepancy is reduced until at 400 r.p.m. there is good agreement. The other results, for comparison of theoretical and experimental wavelengths on both  $10^\circ$  and  $20^\circ$  cones, are given in Figures 32 and 33 respectively. The numerical values for the experimental results are given in Tables 1 and 2, for the theoretical ones in Tables 3 and 4, for the  $10^\circ$  and  $20^\circ$  cones respectively. All the graphs follow the same trend as that in Figure 31. Those of the  $20^\circ$  cone however appear to be less stable than the  $10^\circ$  cone because they need a greater speed range to settle down.

In general the theoretical and experimental wavelengths decrease with increase of speed. From equation 3.8.13 the governing factor was found to be  $\Lambda$ . This factor is a complex one containing the two conflicting quantities surface tension and centrifugal acceleration in the Y direction. If now instead of rotational speed the experimental wavelengths are plotted against the acceleration in the Y direction,  $a_y$ , on log-log graph paper an almost linear relationship is observed, Figure 34. Both  $10^\circ$  and  $20^\circ$  cones have a similar linear relationship except that the gradient of the  $20^\circ$  cone is slightly greater than that



—x—x—x— EXPERIMENTAL POINTS  
 —⊗—⊗—⊗— THEORETICAL VALUES  
 10° CONE      β = 5°

FIGURE 32 ROTATIONAL SPEED VERSUS WAVELENGTH



-x-x-x- EXPERIMENTAL POINTS  
 -⊙-⊙-⊙- THEORETICAL POINTS  
 20° CONE       $\beta = 10^\circ$

FIGURE 33      ROTATIONAL SPEED      VERSUS      WAVELENGTH

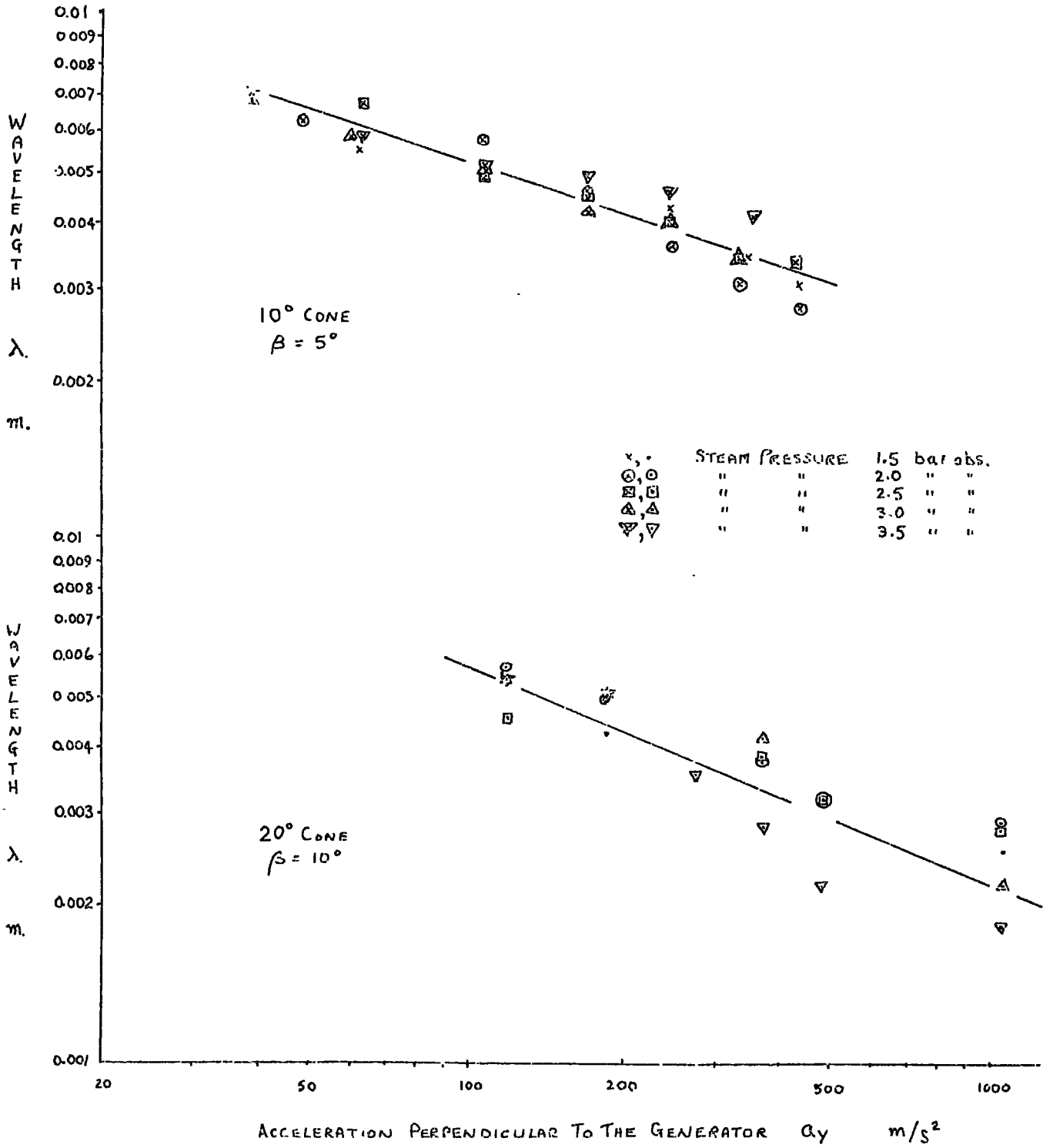


FIGURE 34. WAVELENGTH VERSUS PERPENDICULAR ACCELERATION

of the  $10^\circ$  cone. There is some separation of points plotted for different pressure ratings. The results are difficult to compare because the  $10^\circ$  cone wavelengths first decrease then increase again as the pressure increases. The  $20^\circ$  cone results are more consistent in that increase of pressure produces a continuous decrease in wavelength. This means that there are more ridges present on the surface at higher pressures. This is in accordance with general heat transfer data in that as the pressure increases the heat transfer coefficient is reduced. In general it appears that in order to keep a stable regime increase of pressure or rotational speed causes a reduction in wavelength.

The surface tension values assumed for calculation purposes are those for water and steam interfaces but no allowance has been made for 'pH' variation. This may cause some error in any computations made. Concern has been shown throughout the experimental work due to contamination of the cone surface. The nature of this contamination has not been traced successfully and it may produce some variation in the surface tension from test to test. Measurements of 'pH' values made in Appendix B showed that a variation of 5.8 to 6.6 were obtained.

A further point to note is that the theoretical analysis was formulated specifically with ridge type waves as the form of drainage. A precise point of discontinuity can be found in practice whereas for the theoretical analysis no such point exists. Prior to the ridge type flow there exists waves of the curtain type, however, theoretically the prediction is that of ridge type waves with a large wavelength. It must therefore be concluded that the equations developed do not perfectly model the ridge flow regime and that the transition point presents a problem that cannot be easily dealt with.

### 5.3.2 Film thickness.

One of the original aims of the present work was to develop a method of measuring condensate film thickness which would be applicable to the case of a rotating conical body. Two methods were developed, one using a conductance technique which could measure the transient film thickness, and a point method which could only measure the peak film thickness. Both methods are fully described in Appendix A. Unfortunately the conductance method failed due to adhesive breakdown during tests in the cone surface. The point method produced results which will be discussed in the following sections.

#### Peak film thickness.

Peak film thickness can be observed directly by means of an adjustable probe. The apparatus has already been described in the experimental section and Figure 11 shows the arrangement of the probe and the measuring sensing equipment.

The operation of the measuring equipment has also been described in the initial test runs. These measurements were taken at speeds of up to 300 r.p.m. on the  $10^\circ$  cone surface at low pressures. Subsequent measurements required to fulfill the test programme showed that

- (i) those measurements taken at the maximum rotational speeds are less consistent because droplets striking the probe caused it to oscillate and if during any downward motion contact is made with the film a thicker film than is actually present is observed. This effect is more pronounced for the  $20^\circ$  cone because of the larger angle and also the drops from the throwing ring at the highest condensation rate interfered to such an extent that readings were not available. The oscillations were so violent that the probe, on sudden contact

with the cone surface, was bent out of shape.

- (ii) the probe tip had to be made as thin as possible to reduce the effect of drag when contact with the condensate surface may produce oscillations which when amplified by successive collisions could cause damage to the probe.

The zero error of the measuring system was checked whilst the cone was rotating by closing the steam valve and slowly traversing the probe until contact was made with the cone surface. This test showed that an error of some 0.02 mm could occur between this and the stationary case which is the order of error anticipated. The rotational test was not carried out too often because the adhesive in the thermo-couple grooves had become slightly undercut. If the probe struck the edge of a groove the former could be severely damaged.

#### Results

All the measurements recorded were multiplied by the cosine of half the apex angle to obtain the true peak film thickness, the latter thicknesses are documented in Tables 1 and 2 for the  $10^\circ$  and  $20^\circ$  cones respectively. These peak film thicknesses are also recorded graphically in Figures 35 and 36 for  $10^\circ$  and  $20^\circ$  cone surfaces respectively. All the graphs show a decrease in film thickness with increase of speed through the whole pressure range for both  $10^\circ$  and  $20^\circ$  cone surfaces. The peak film thickness varies little with increase of pressure but it is noticeably that it appears thicker at higher pressures. The variations are, however, within the experimental error and so no certain conclusions can be drawn. The same holds true for the difference in peak film thickness between those measured on the  $10^\circ$  cone and those measured on the  $20^\circ$  cone surface. It would appear then that the only observations possible are that the film thickness decreases with increase of rotational speed and that a change in pressure or cone apex angle has only

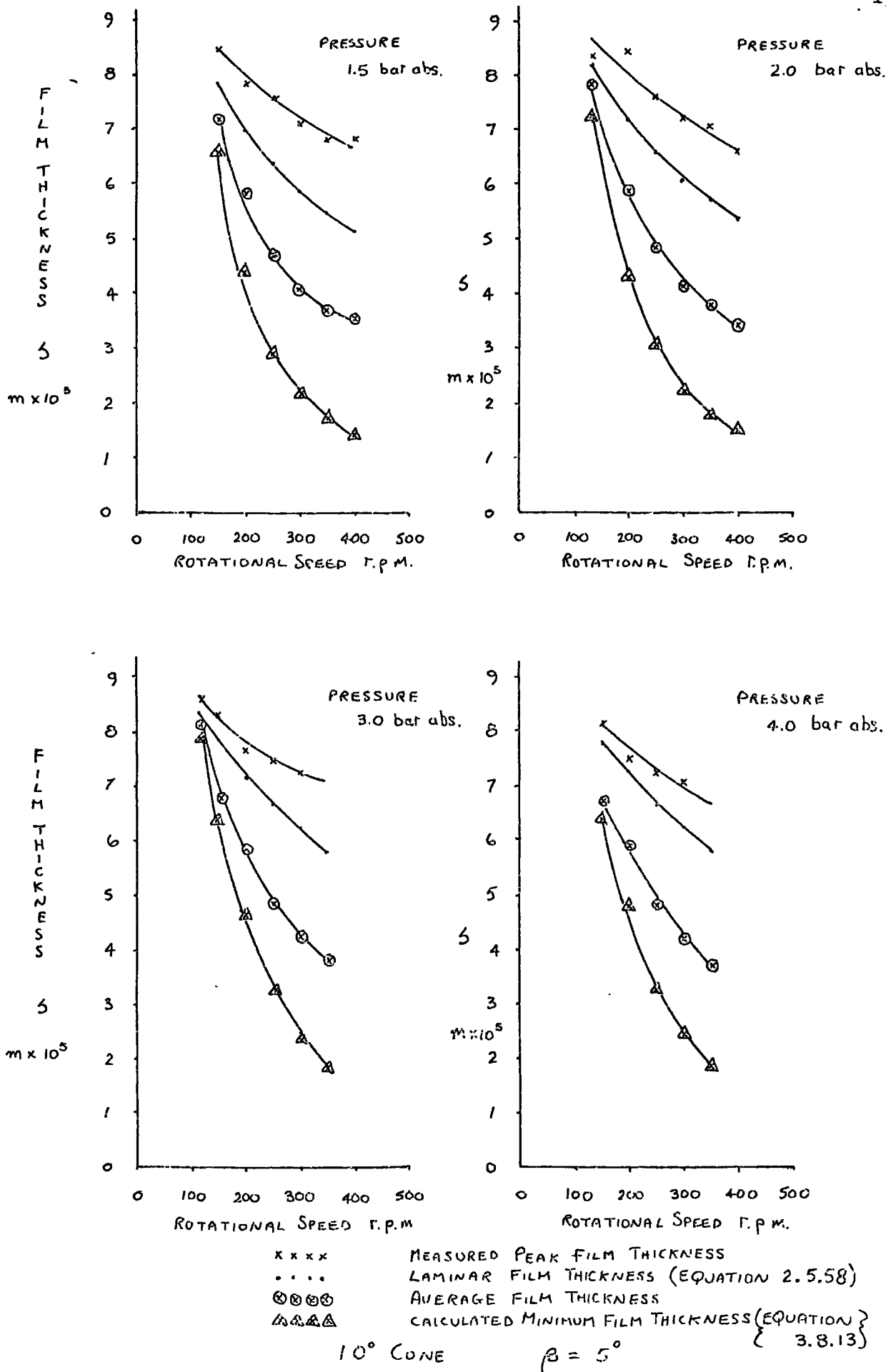
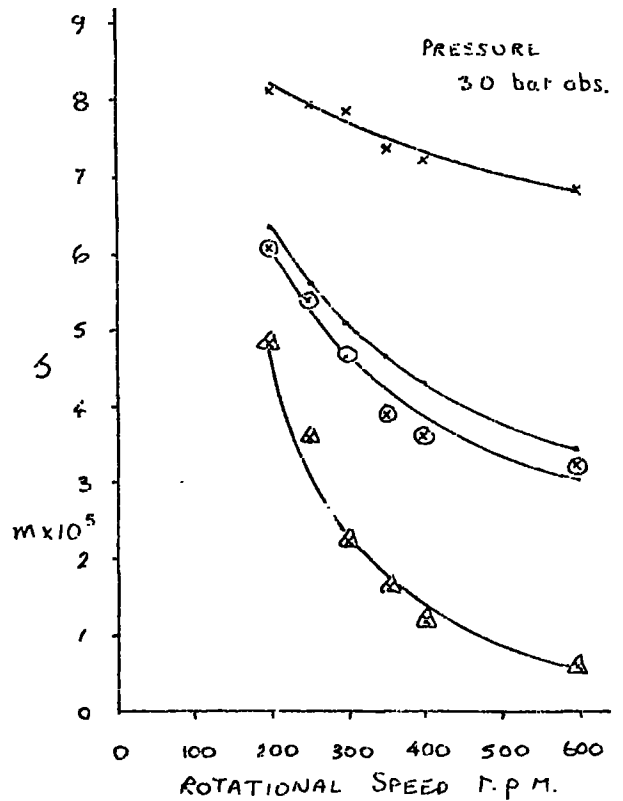
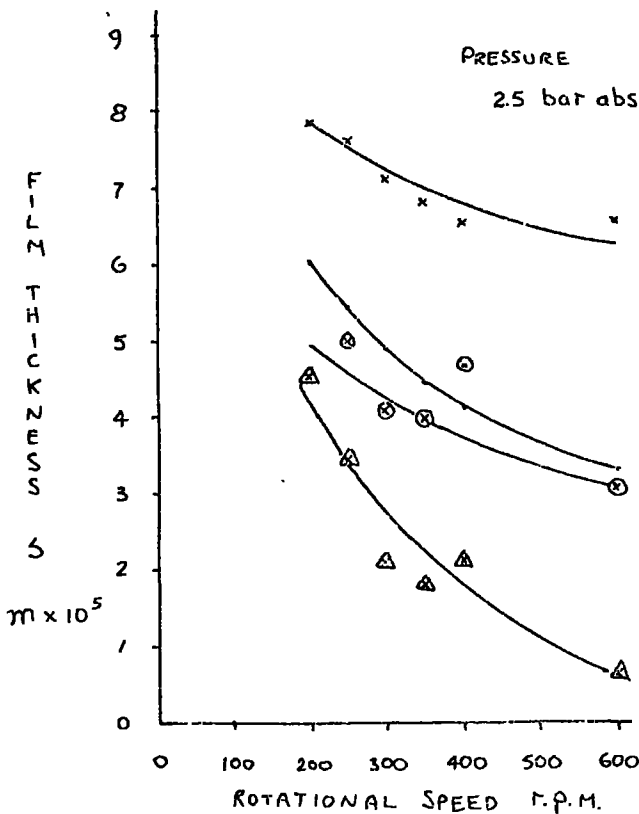
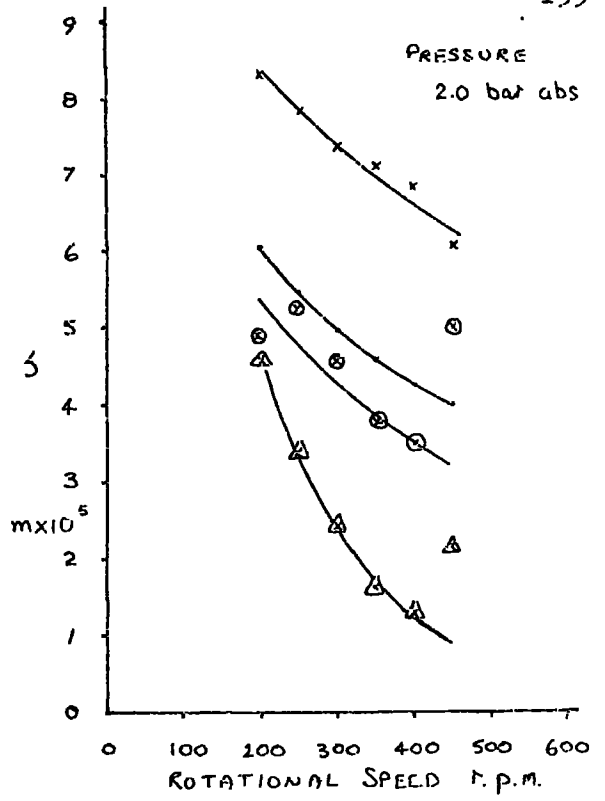
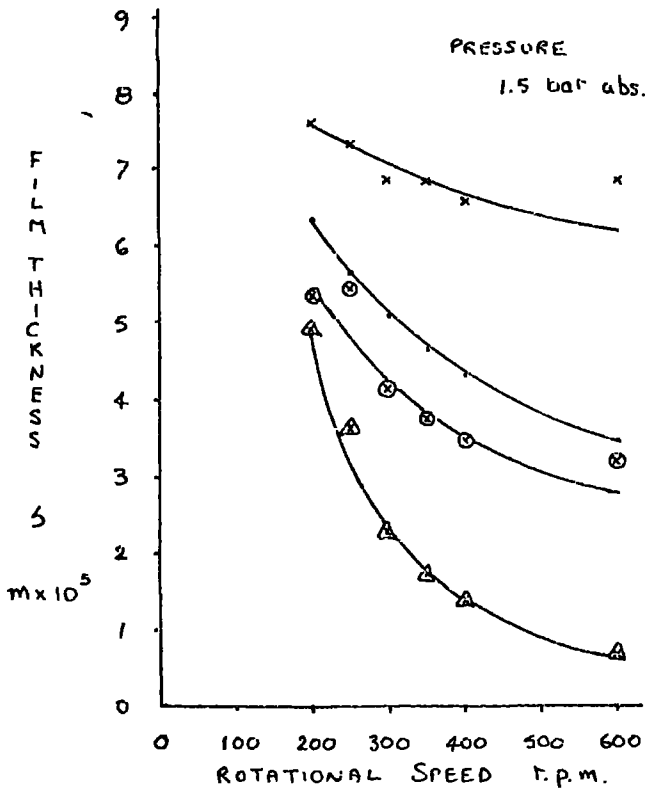


FIGURE 35. FILM THICKNESS VERSUS ROTATIONAL SPEED.



x x x x MEASURED PEAK FILM THICKNESS  
 · · · · LAMINAR FILM THICKNESS (EQUATION 2.5.58)  
 ⊙ ⊙ ⊙ ⊙ AVERAGE FILM THICKNESS  
 △ △ △ △ CALCULATED MINIMUM FILM THICKNESS (EQUATION 3.8.13)  
 20° CONE β = 10°

FIGURE 36 FILM THICKNESS VERSUS ROTATIONAL SPEED

a small effect in the range covered.

#### Minimum film thickness.

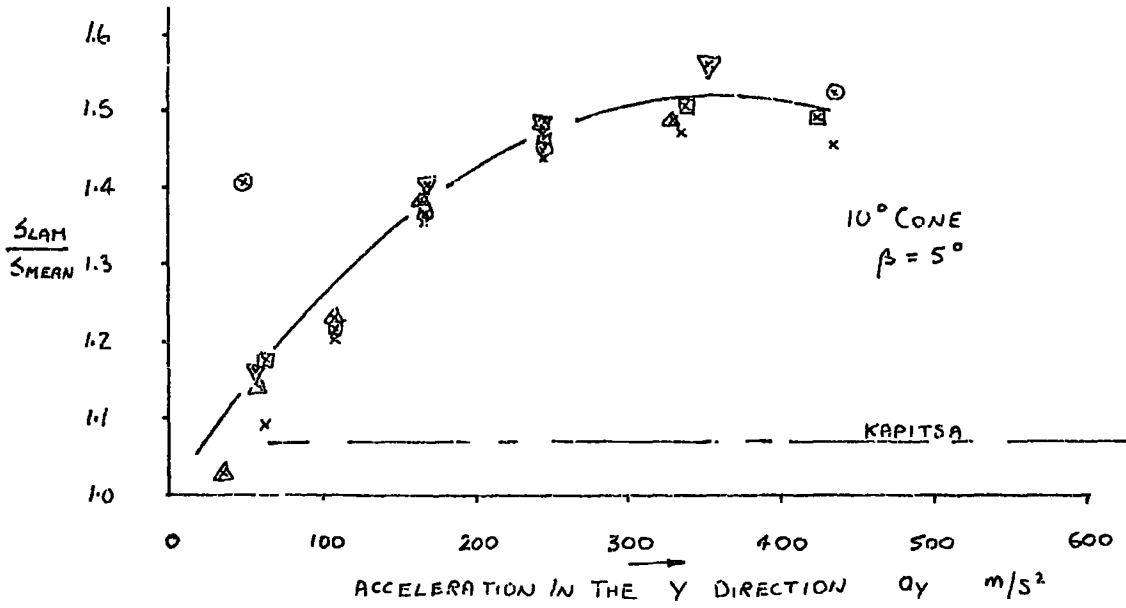
The minimum film thickness could not be observed directly, and must therefore be predicted from a theoretical approach. The programme developed to solve equation 3.8.13 for the experimental data predicts the wavelength of the ridge like waves using the ratio of peak film thickness divided by minimum film thickness as the controlling term. Thus a value of minimum film thickness corresponding to a predicted wavelength is given. This value is plotted for each speed for all tests in Figures 35 and 36 for  $10^\circ$  and  $20^\circ$  cones respectively. The minimum film thickness becomes thinner as the rotational speed is increased for the whole pressure range on the  $10^\circ$  cone and for all values except two on the  $20^\circ$  cone. The condensation may be considered as occurring in two regions, a region of thin film and a region of thick film. The bulk of the condensation occurs in the thin film region and flow will be governed by a balance of the surface tension and viscous forces. In the derivation of the theory one of the assumptions made was that fluid flowed transversely into the ridges. These ridges then acted as channels to drain the condensate. The drainage velocity could not be taken into account directly but could be related to the most important controlling term  $\mathcal{E}$  by the method described in Appendix C. It has already been shown that repeatability of the waveform was not possible and that adjustment of  $\mathcal{E}$  could bring this repeatability closer. This must then point to the fact that the circumferential velocity outward from the minimum film thickness is not truly transverse and that this must augment the velocity in the X direction.

It was shown in section 5.3.1 that increase of speed resulted in decrease in wavelength, so that more ridges appeared on the surface. At

the same time it is now clear that minimum, or trough, film thickness also decreases. The condensation rate does not increase to any extent, for constant pressure, so that a reduction in wave length means less condensate per trough and the increase in centrifugal acceleration increasing the velocity clearing the trough confirms the theoretical prediction of thinning minimum film thickness. A further confirmation can be drawn from direct observations of the shadows formed on each of the photographs. At low rotational speeds the shadow appears to indicate a slightly undulating condensate surface whereas at maximum rotational speed a much more marked peak effect is clearly visible. Figure 31 shows that peak film thickness decreases with increase of speed, then the minimum film thickness must be that much thinner. A similar effect was noted about the circumferential waves formed on the surface of a rotating disc by Espig and Hoyle (63). They observed that increasing the discs speed of rotation appeared to cause an increase of the wave depth at constant flowrate.

#### Mean and Laminar film thicknesses.

A mean film thickness is computed by integrating over a half wavelength and is plotted on each graph in Figures 35 and 36. Howe (69) has already developed an equation which predicted the laminar film thickness and this value is also plotted on the graphs in Figures 35 and 36. It can be seen that the calculated mean film thicknesses are thinner than the predicted laminar ones at any rotational speed and steam pressure. Figure 37 reveals the relationship between the ratio of laminar film thickness divided by mean film thickness and the acceleration in the Y direction,  $a_y$ . Kapitsa (9) showed that the mean film thickness of a film with surface waves is  $7\%$  less than the corresponding thickness of a uniform layer with laminar flow conditions.



Symbol	STEAM PRESSURE	Value
x, x	1.5 bar abs.	1.5
⊙, ⊙	" "	2.0
⊠, ⊠	" "	2.5
Δ, Δ	" "	3.0
▽, ▽	" "	4.0

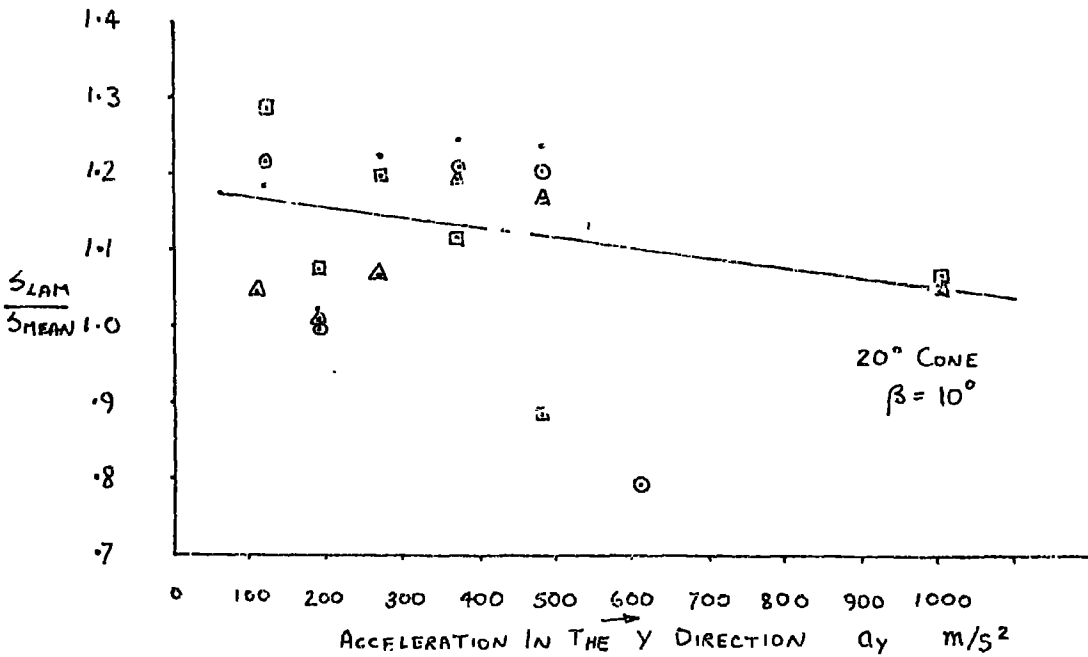


FIGURE 37. RATIO OF LAMINAR TO CALCULATED MEAN FILM THICKNESS  
VERSUS ACCELERATION PERPENDICULAR TO GENERATOR

In this case the ratio of laminar film thickness to that of mean film thickness ( $\delta_{lam}/\delta_{mean}$ ) increases to a maximum of 1.53 as the rotational speed is increased to 350 r.p.m. and then to decrease with further increases for the  $10^\circ$  cone surface. The  $20^\circ$  cone ratio of  $\delta_{lam}/\delta_{mean}$  increases continually as the speed increases and attains a value of 1.29 at 600 r.p.m. It is possible that the ridge like waves on the  $10^\circ$  cone surface have a more peaky appearance than that of the  $20^\circ$  cone and this may account for the difference in values. The reason for this may be due to the acceleration in the X direction for the  $20^\circ$  cone is larger and could have the effect of reducing the peakiness of the ridge like waves by draining the condensate more rapidly. The effect of mean film thickness being thinner than the predicted laminar one would account for the under estimation of the theoretical heat transfer coefficients, compared with experimental results in Howe's laminar treatment.

Film thickness estimates have been made by Robson (68) of a condensate layer on the surface of a rotating  $60^\circ$  right cone. These have already been discussed in section 2.5.3. Results extracted from this work show the mean film thickness at a radius of 0.305 m to be 0.07 mm at 200 r.p.m. reducing to 0.035 mm at 600 r.p.m. The curves drawn showed that increase of pressure produced small increase in film thickness. These figures compare fairly well with the film thicknesses measured in this work, however no exact conclusions may be drawn from the two values because of the lack of confidence in the method of measurement used by Robson. No other corroborative evidence of film thickness measurement on rotating system has been found.

In an attempt to allow prediction of minimum or peak film thickness the laminar film thickness was used as a reference value and after being divided by each of the former and the resulting numbers were plotted against the component of acceleration in the Y direction,  $a_y$ . Figure

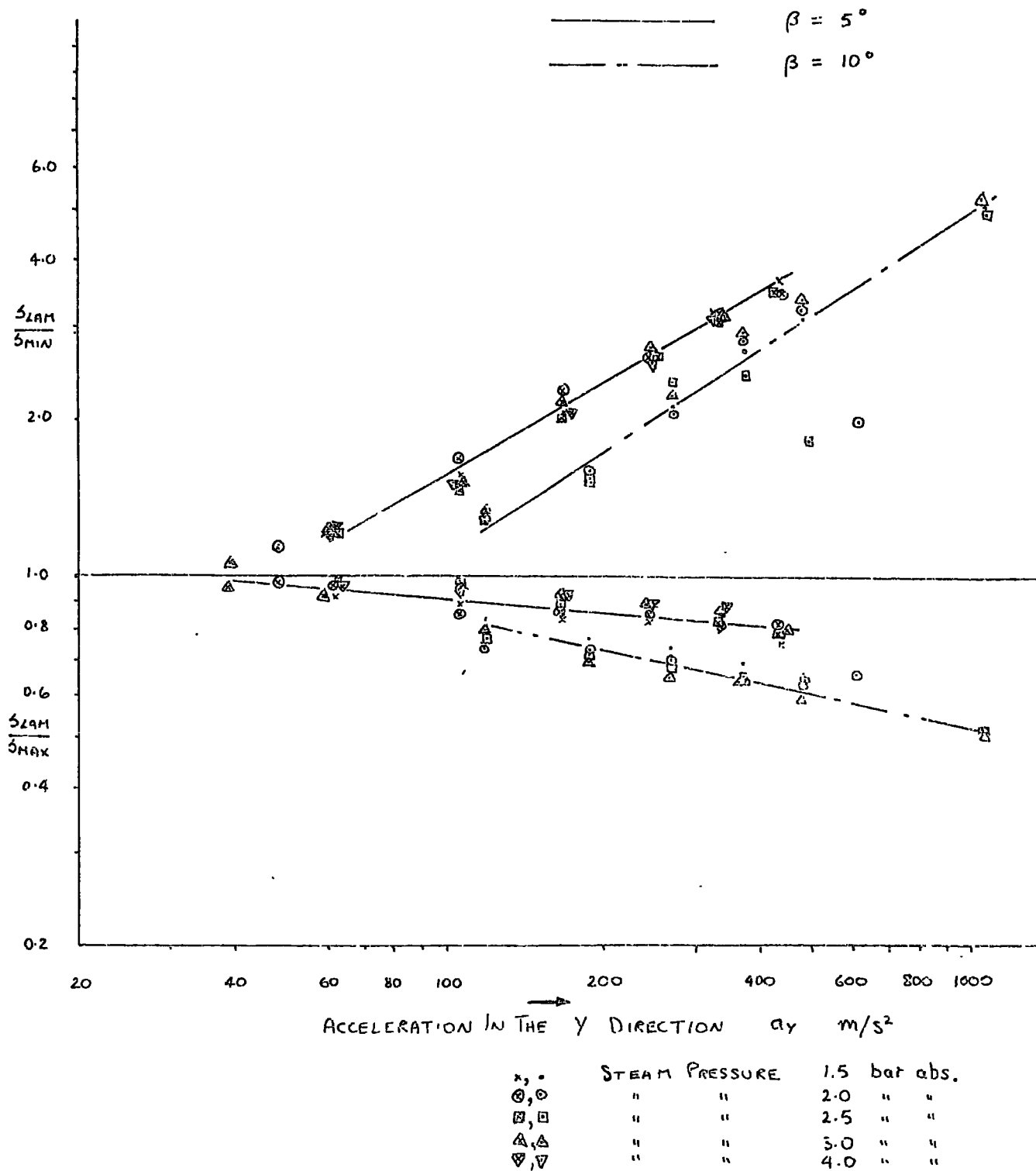


FIGURE 38. RATIO OF LAMINAR TO MINIMUM AND MEASURED PEAK FILM THICKNESS VERSUS ACCELERATION IN THE Y DIRECTION

38 shows the trend of each of the terms for  $10^\circ$  and  $20^\circ$  cones. For both  $10^\circ$  and  $20^\circ$  cones the ratios,  $s_{lam}/s_{min}$  and  $s_{lam}/s_{max}$  may be represented by first order polynomials. Plotted on log-log graph paper these are shown to be straight line relationships. Examination of Figure 38 reveals that scatter of various points is mainly pressure dependent and that all points in each group may be represented by a single line within  $\pm 16\%$ . These equations are

$$10^\circ \text{ cone} \quad \frac{s_{lam}}{s_{min}} = 0.1183 a_y^{0.5606} \quad 5.3.21$$

$$20^\circ \text{ cone} \quad \frac{s_{lam}}{s_{min}} = 0.0611 a_y^{0.6346} \quad 5.3.22$$

and for the peak film thickness

$$10^\circ \text{ cone} \quad \frac{s_{lam}}{s_{max}} = 1.33 a_y^{-0.0875} \quad 5.3.23$$

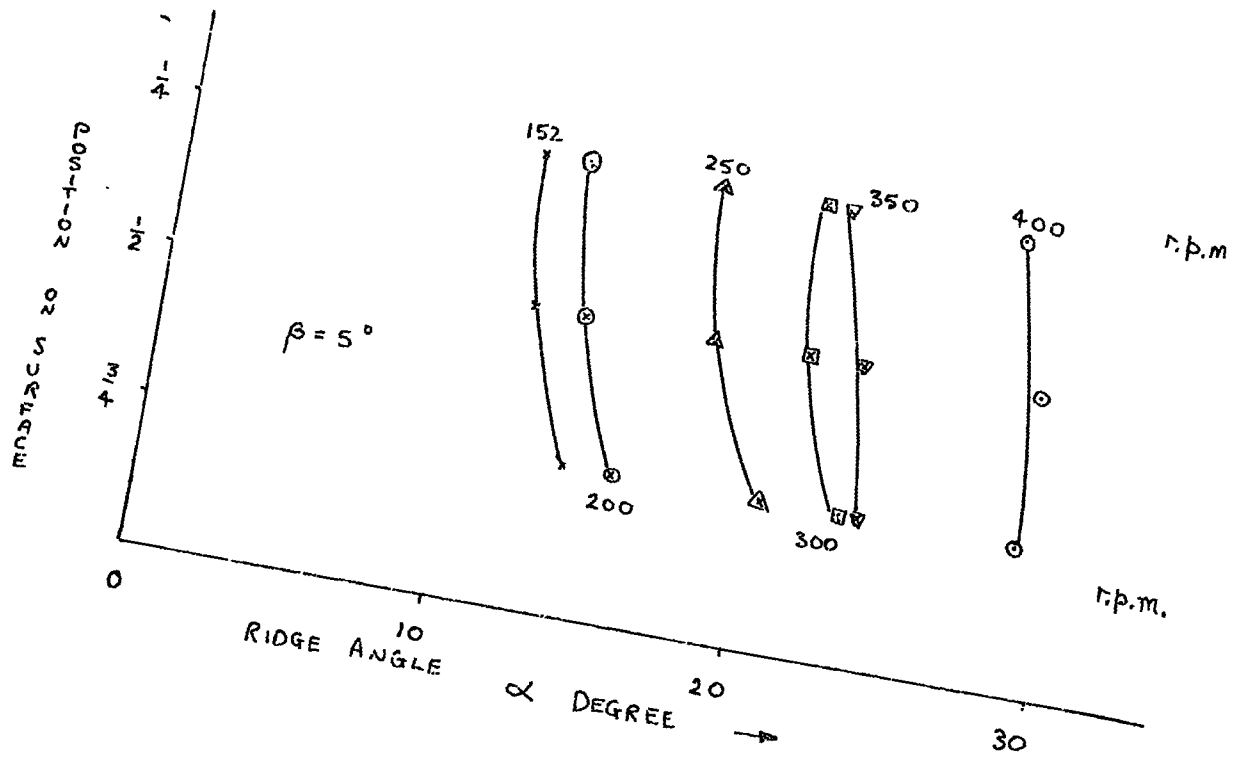
$$20^\circ \text{ cone} \quad \frac{s_{lam}}{s_{max}} = 2.177 a_y^{-0.2059} \quad 5.3.24$$

The dimensional value of acceleration in the Y direction was chosen as the dependent variable because it is a readily available, relevant, component. Thus given a particular speed a value of  $s_{lam}/s_{min}$  or  $s_{lam}/s_{max}$  may be found. Once these values have been obtained the more conventional laminar film thickness may be then calculated and hence  $s_{min}$  and  $s_{max}$  may be predicted. A similar prediction for the mean film thickness is not possible because of the scatter the points and the form the graphs take.

#### 5.4 Inertia forces and drag.

The photographic study of the condensate surface allowed an examination of the change in the angle which the ridge makes with the cone generator line with change in rotational speed and radius of the surface. Although there is some relationship between the ridge angle, radius and speed it may well be very complex. In Figures 39 to 43 a comparison of ridge angles on the  $10^\circ$  and  $20^\circ$  cones is given for variation of steam pressure, radius or distance down cone surface, and rotational speed. Examination of the graphs reveals that each of these factors has a different effect. Firstly, increase of speed generally has the overall effect of causing the ridge to follow a path having a increasing angle of descent. However, in some cases the angle can reach a maximum and then decrease with further increase of rotational speed. The change in ridge angle with progress down the cone surface is a much less predictable one. Most ridges have a shallower angle at the start of the condensation surface and movement down the cone surface causes the angle of inclination to increase. There are some ridges that do the opposite and have decreasing angles of inclination with progress down the cone surface, and others that increase to a maximum at a certain position and then on further progress downstream the angle of inclination decreases. Some of these may be due to random surface variations brought about by contamination or some other irregularity. The difference in orientation is more marked between the  $10^\circ$  and  $20^\circ$  cones. Those ridge angles on the  $20^\circ$  cone are much shallower than those on the  $10^\circ$  cone, even at 600 r.p.m. on the  $20^\circ$  cone the angle of inclination is some  $10^\circ$  less than those on the  $10^\circ$  cone at 400 r.p.m.

The effect of pressure variation is presented in Figures 44 (a) and (b) for the  $10^\circ$  and  $20^\circ$  cones respectively. Comparison of these two Figures shows the shallower angle of inclination of the ridge angles



STEAM PRESSURE 1.5 bar abs.

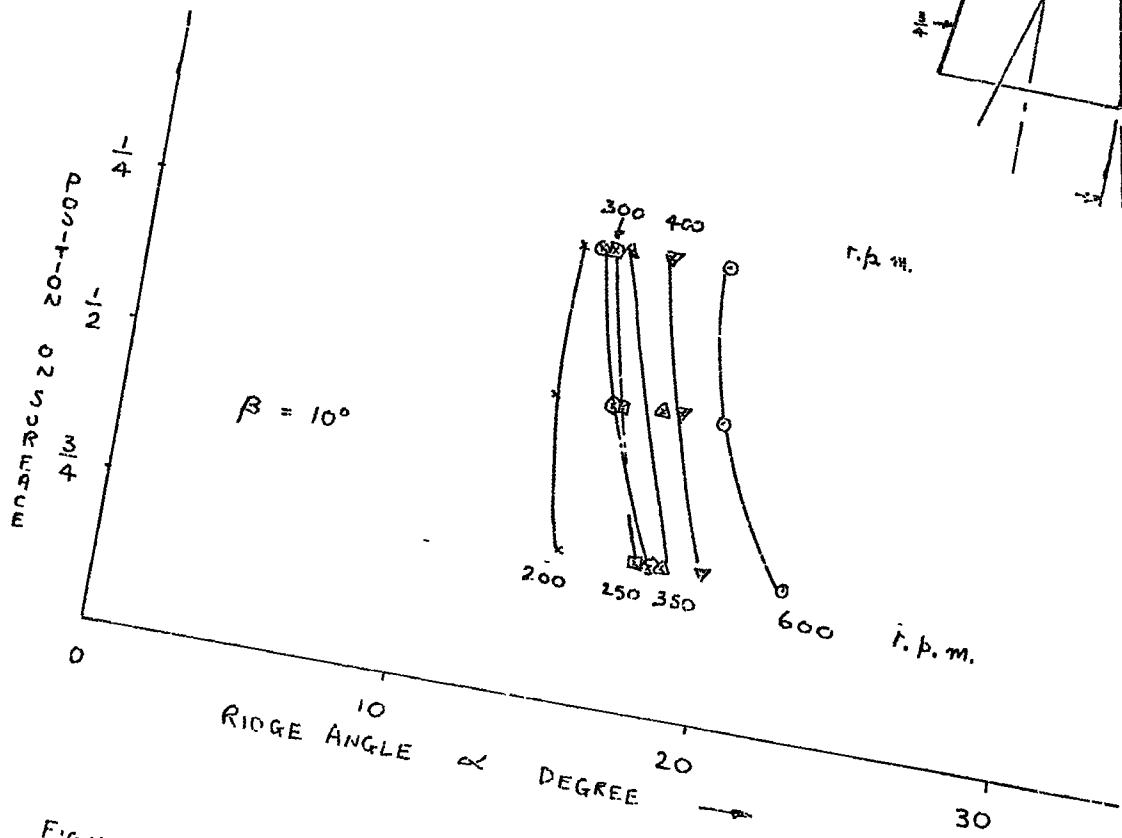
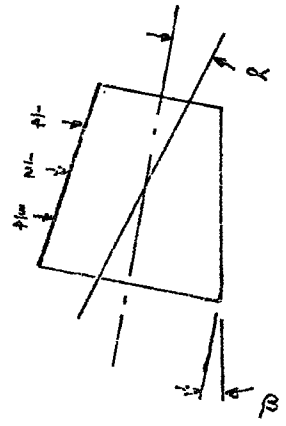


FIGURE 39 VARIATION OF RIDGE ANGLE ALONG CONE GENERATOR

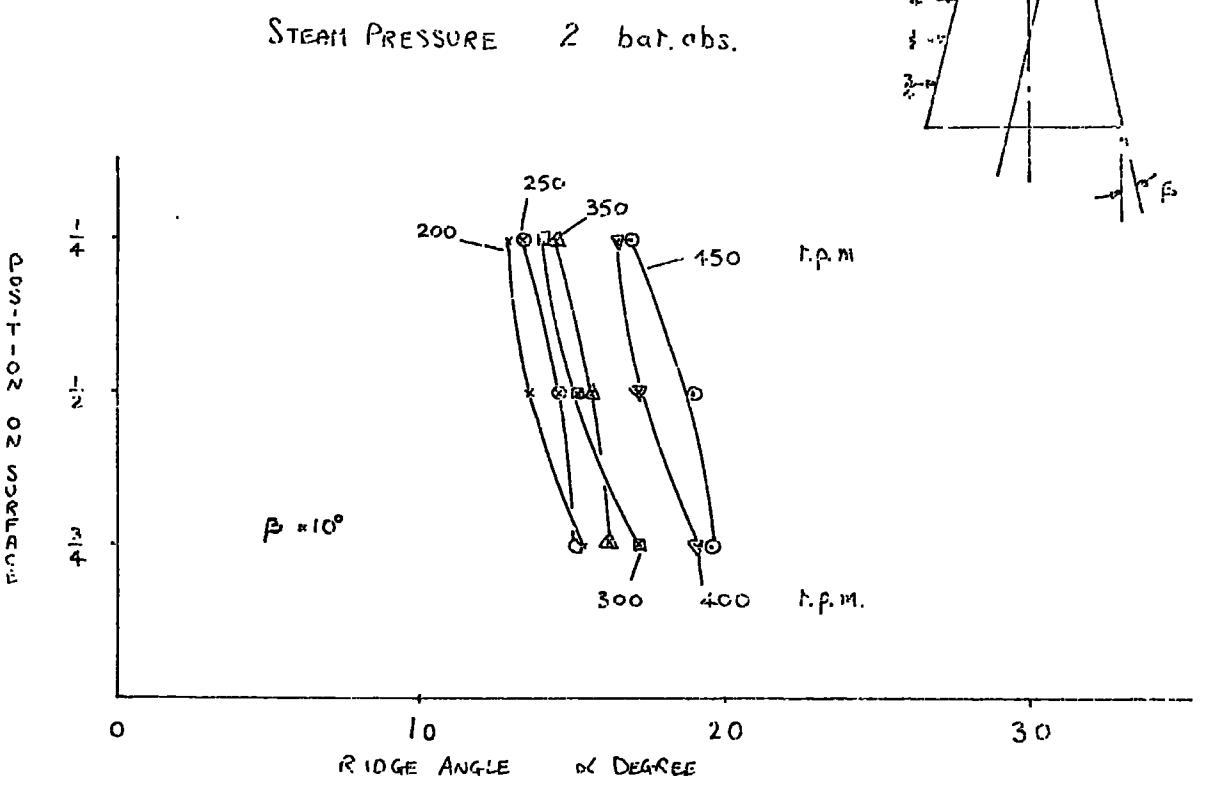
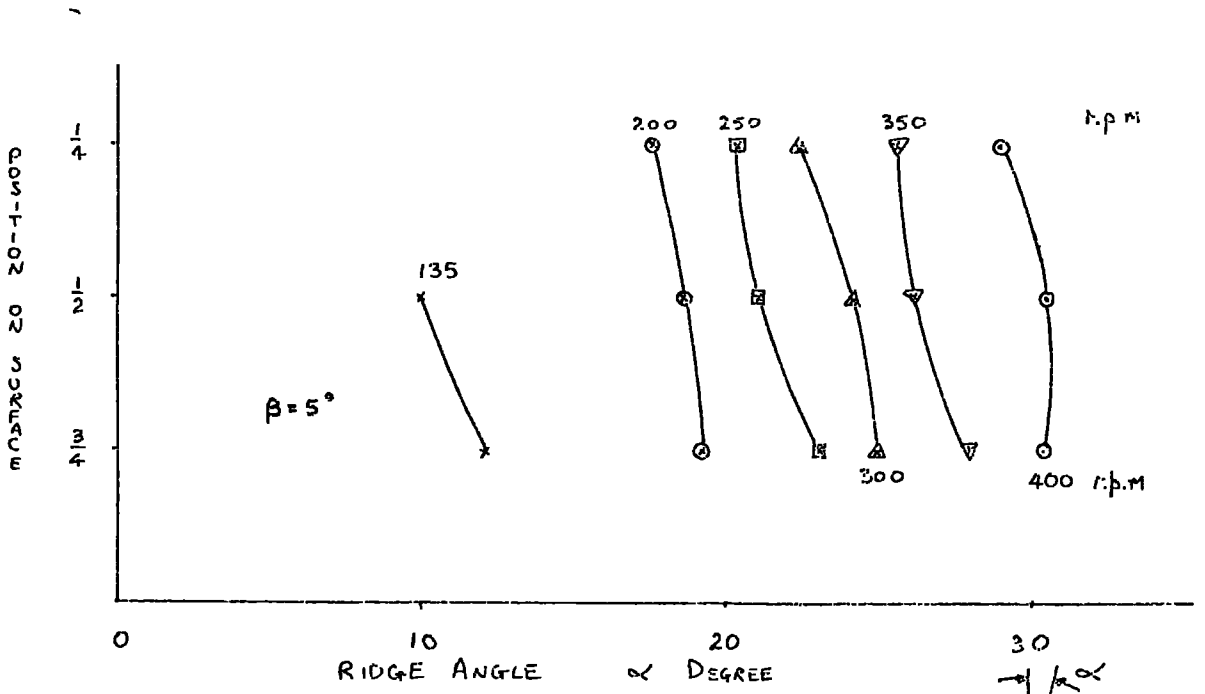
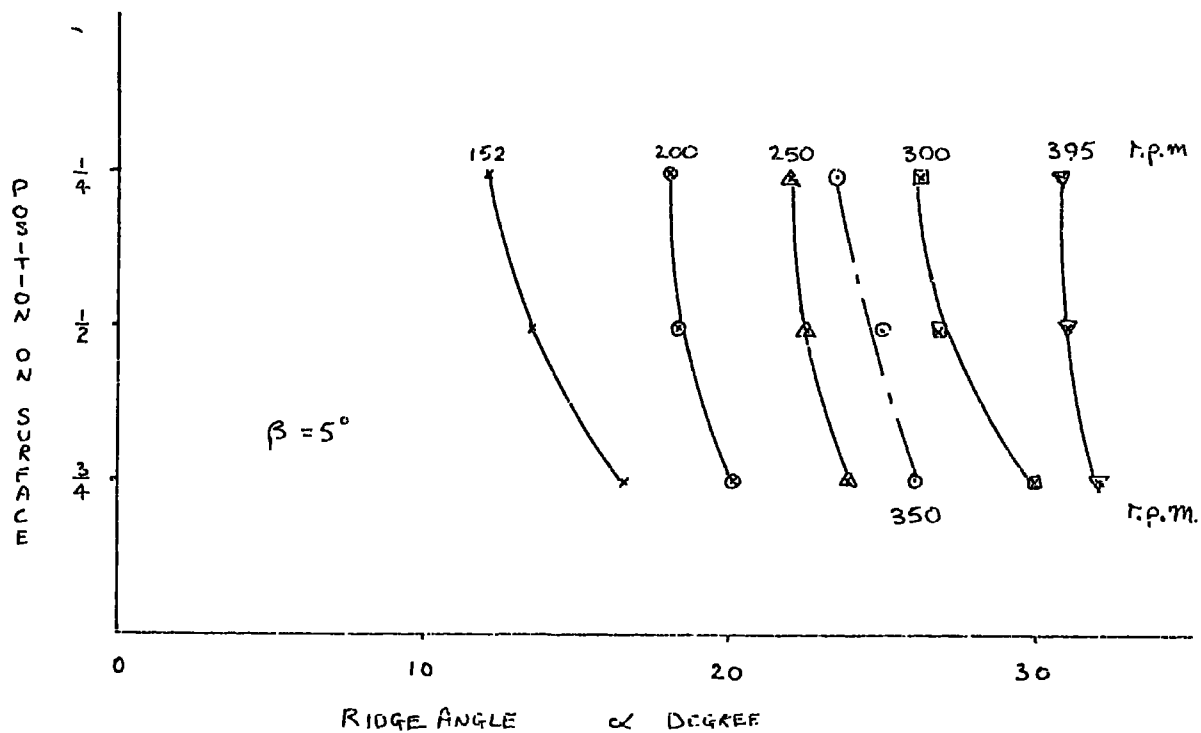


FIGURE 40 VARIATION OF RIDGE ANGLE ALONG CONE GENERATOR



STEAM PRESSURE 2.5 bar abs.

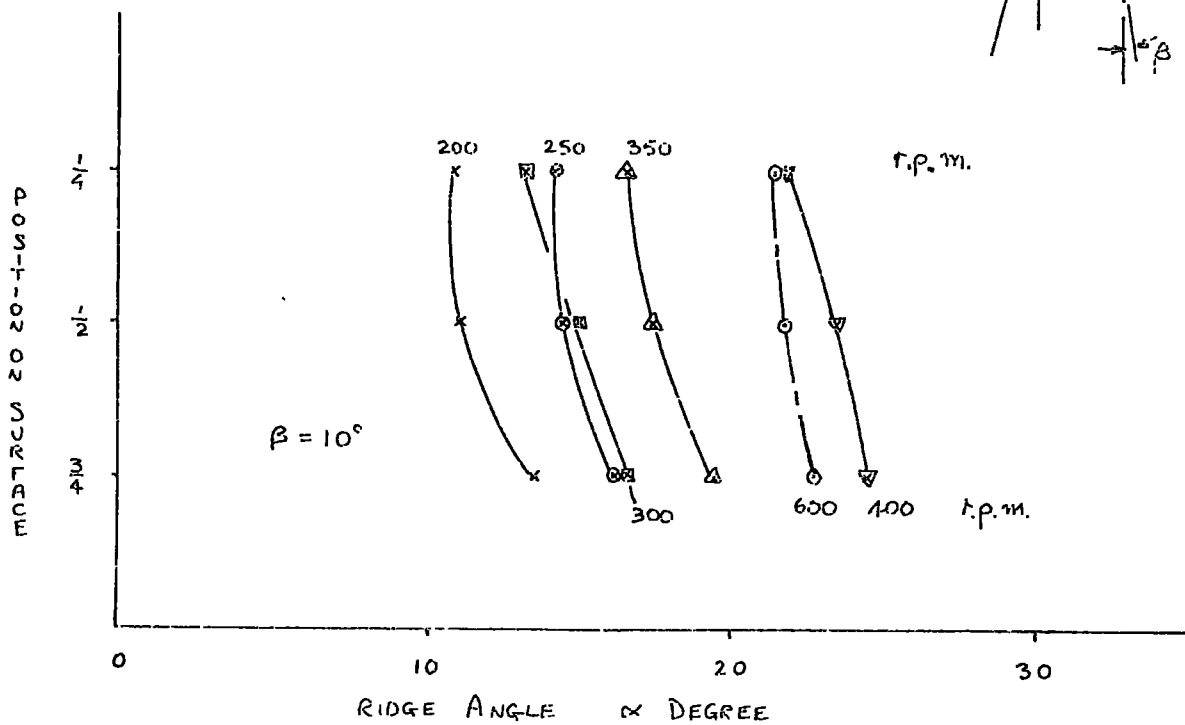
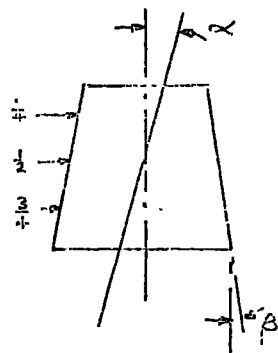


FIGURE 41. VARIATION OF RIDGE ANGLE ALONG CONE GENERATOR

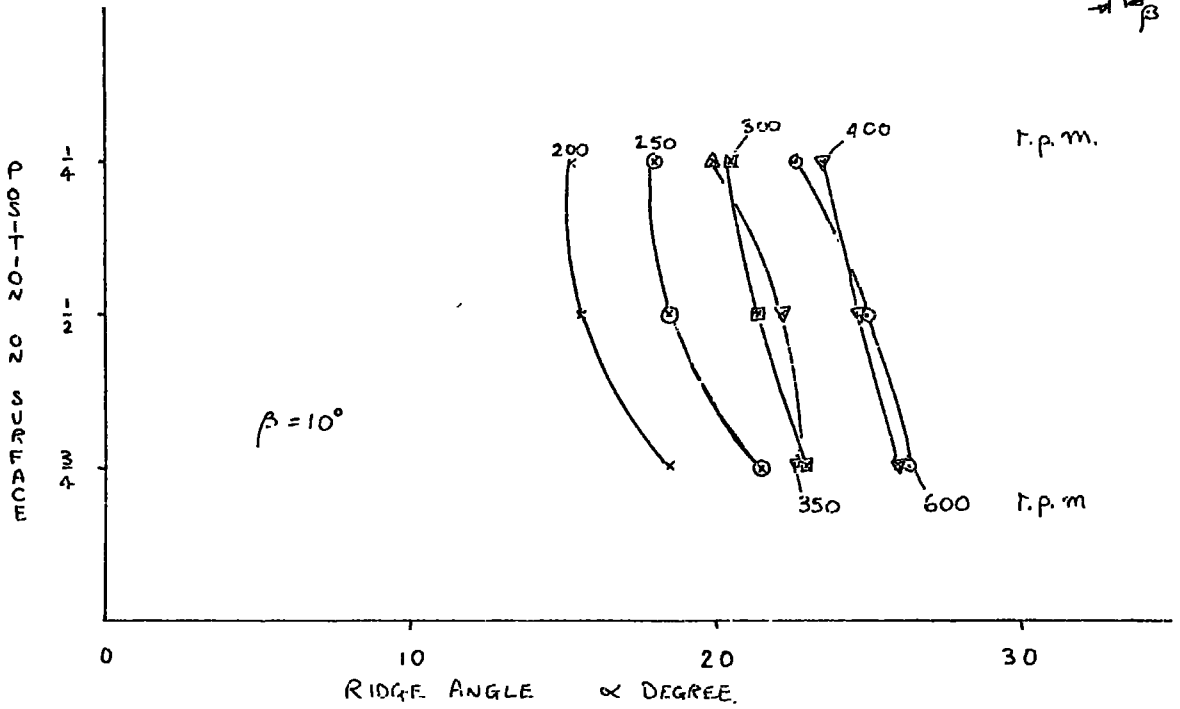
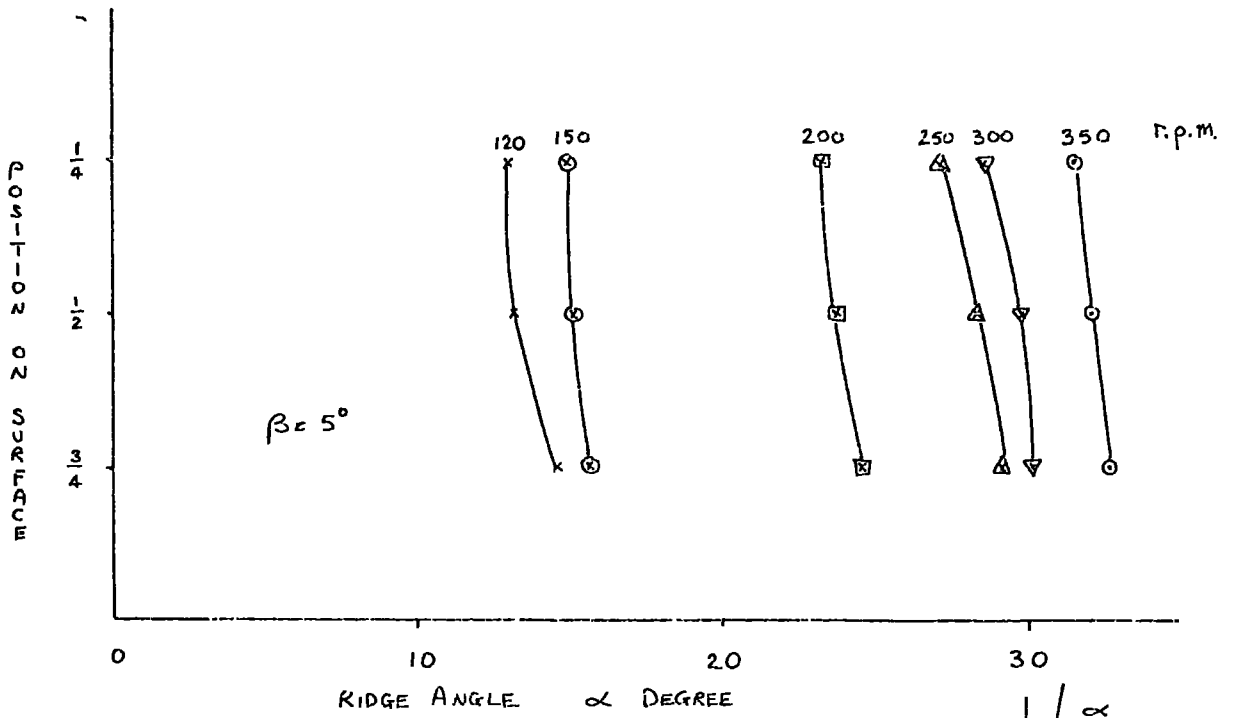
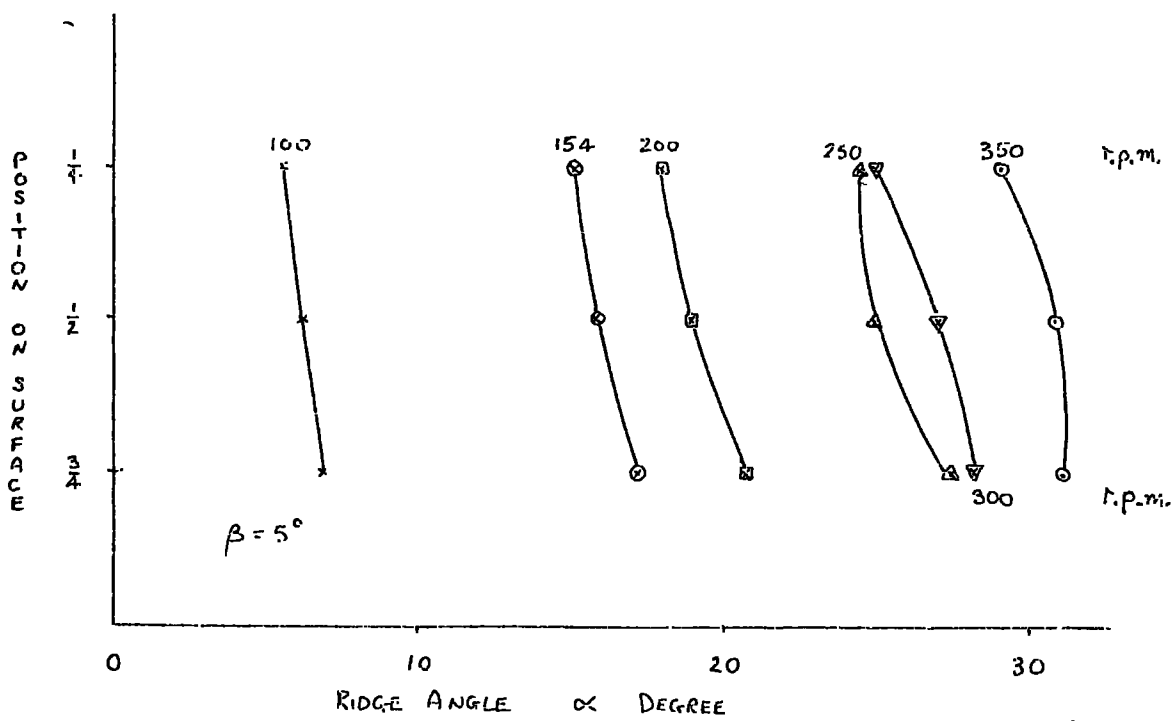


FIGURE 42. VARIATION OF RIDGE ANGLE ALONG CONE GENERATOR.



STEAM PRESSURE 4 bar abs.

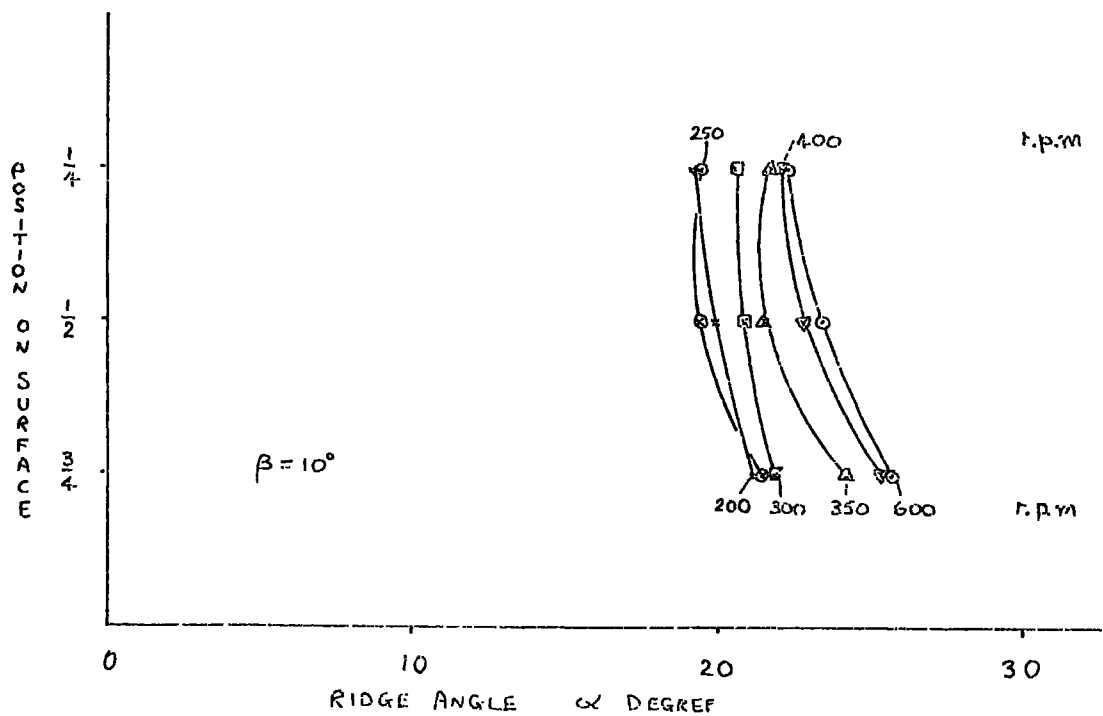
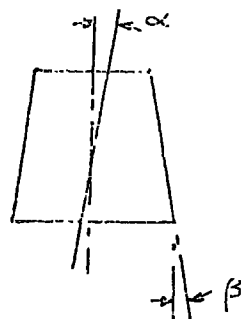


FIGURE 43. VARIATION OF RIDGE ANGLE ALONG CONE GENERATOR.

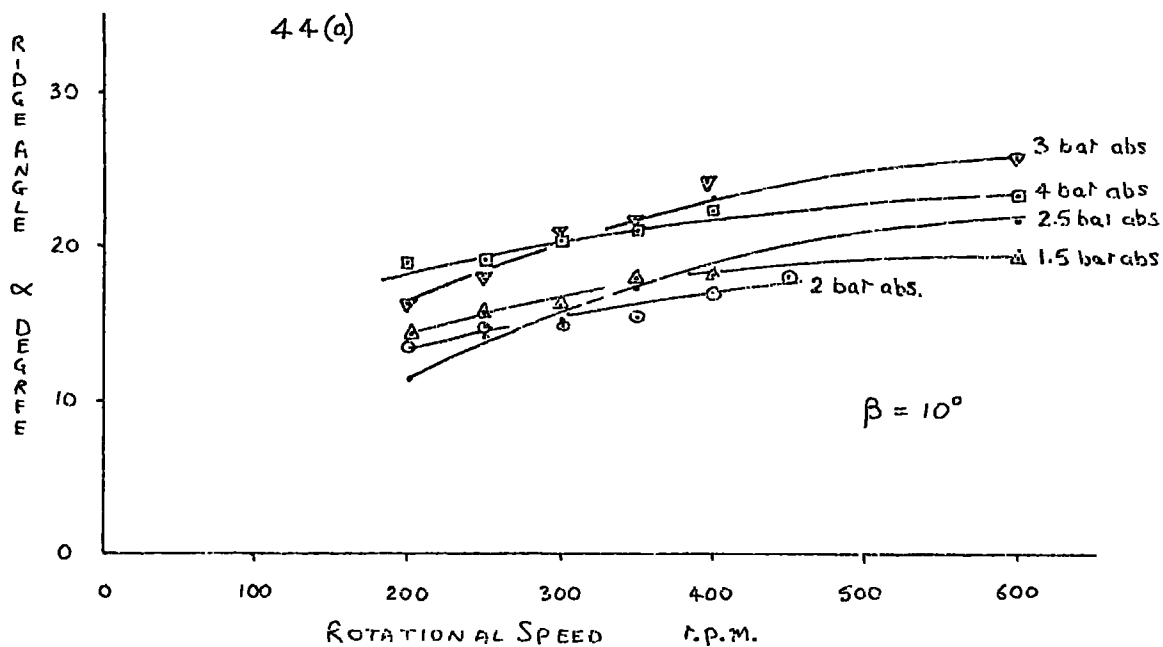
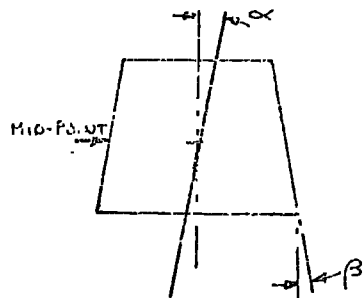
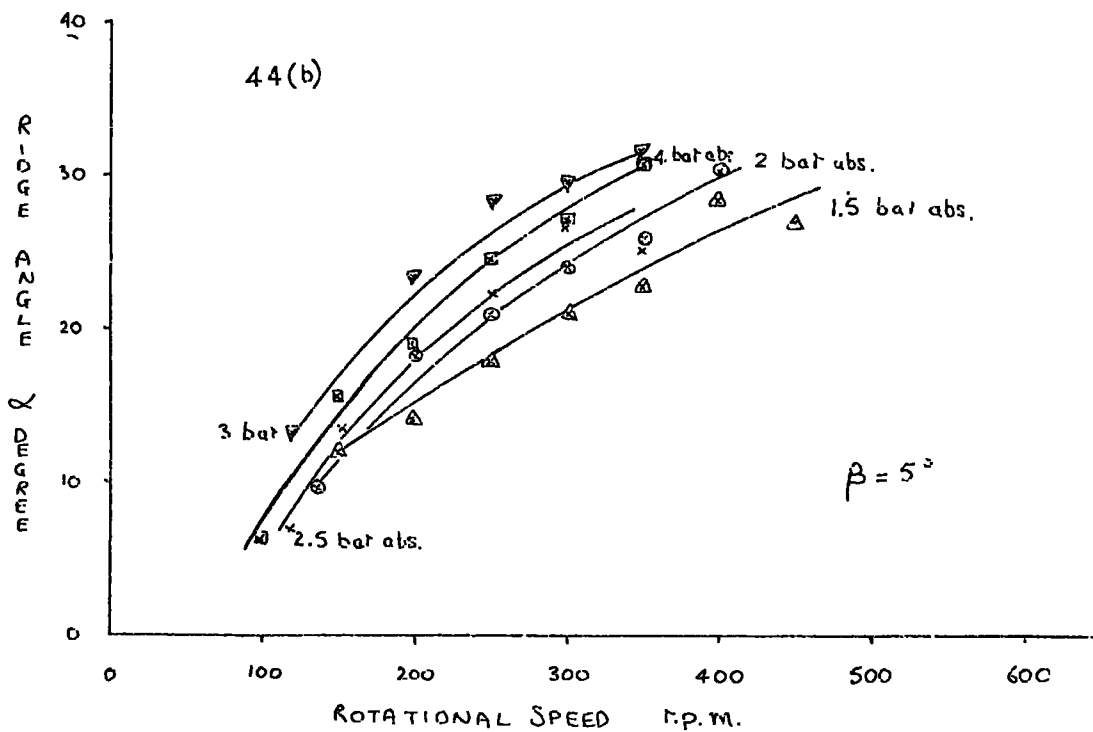


FIGURE 44. VARIATION OF RIDGE ANGLE VERSUS ROTATIONAL SPEED.

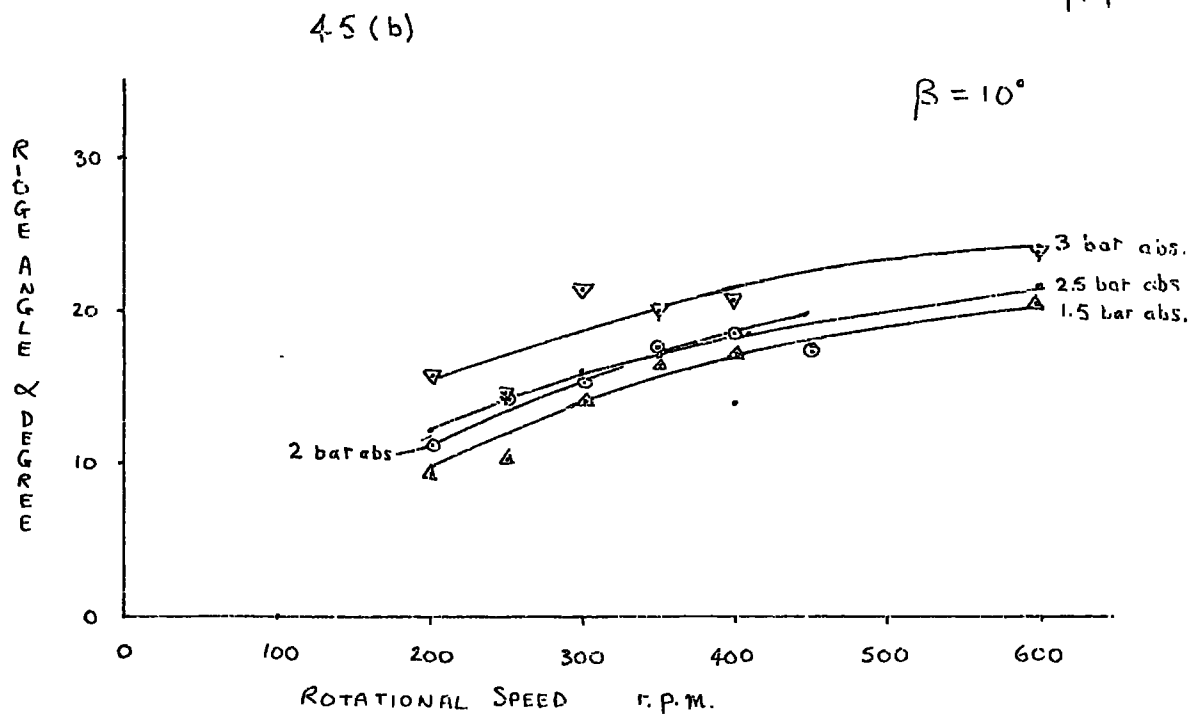
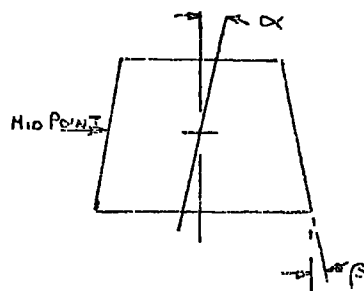
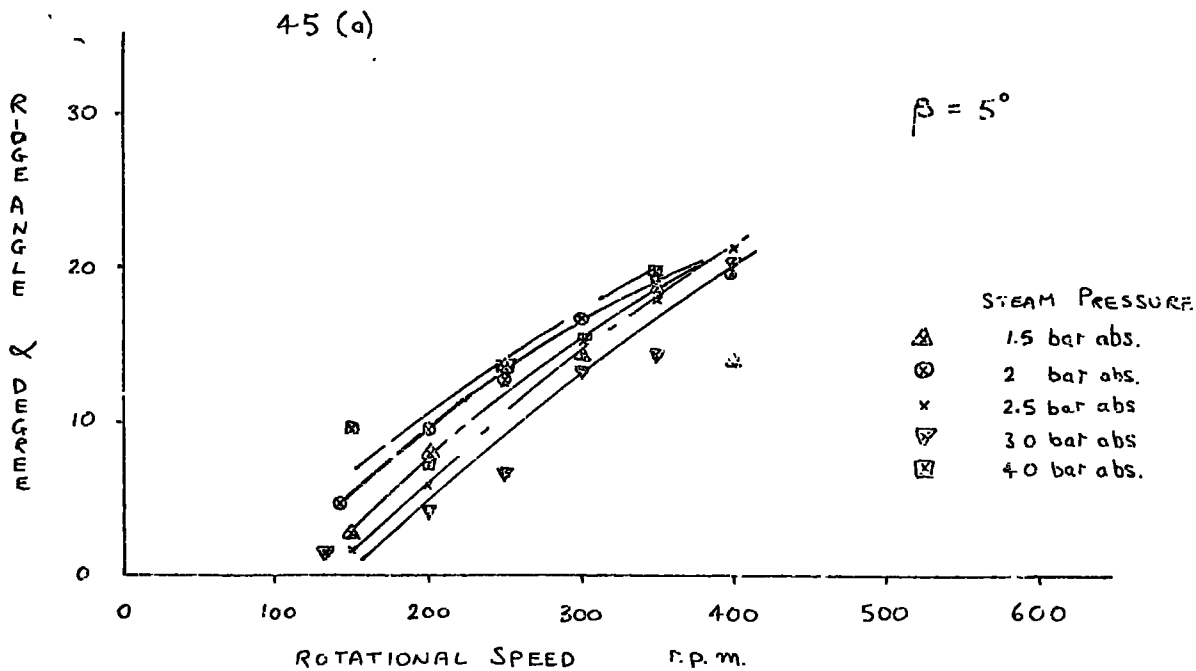


FIGURE 45. THEORETICAL RIDGE ANGLE VERSUS ROTATIONAL SPEED.

for the  $20^\circ$  cone much more clearly. The graphs also show that a peak value of inclination occurs for both cones at a pressure of 3 bar. The mid-point radii, or rather the radius corresponding to a point half way down the cone condensing surface, only are plotted so that a plot of other distances from the starting point of condensation would give a slightly different interpretation. It must also be remembered that a photograph represents only one state of affairs at one instant. A series of photographs taken under apparently identical conditions might show substantial variation in the ridge angle and might necessitate a statistical analysis before conclusions could be formulated. The reason for this change in ridge angle between the two cones could be a combination of two factors, a Coriolis effect and a drag effect. Hoyle and Matthews (56) found that the protrusions which formed on their horizontal cylinders when the radial acceleration reached a value of  $12g$  were distributed evenly over the surface and drifted slowly in a direction opposite to the motion of the rotor, implying that drag was present. In their observations the rotor is cylindrical and no Coriolis components act on the protrusions. For a body where shape implies the presence of Coriolis force, when the rotation is in an anti-clockwise direction flow will be deflected to the right as it progresses along the surface. Thus the two effects act in the same direction. Coriolis forces in our particular case will not be of great magnitude because the change of radius, with apex angles of  $10^\circ$  and  $20^\circ$ , is only small.

One method of testing the effect of the Coriolis terms, which were included in the general equation, was to calculate the circumferential velocity of flow in the ridge and the flow velocity in the X direction. From the circumferential velocity an estimate of the ridge phase velocity was made. Kapitza (9) has already shown, and confirmed by other workers, that the wave velocity is 2.4 times the average fluid velocity. Thus as

means of testing the effect of Coriolis in this case the ridge phase velocity will be taken as 2.4 times the average circumferential velocity as calculated by equation 3.6.21. Then the effect of Coriolis is given by the tangent of the two velocities which must be assumed to act at right angles. The ridge angles so calculated are presented in Figures 45(a) and 45(b). Examination of the curves for  $10^\circ$  and  $20^\circ$  cones reveals that the forms are very similar to the experimental curves of Figures 44(a) and 44(b). The magnitude of the angles are however lower than those measured. As suggested above, it is possible that the observed values are greater than the theoretical predictions because of the enhancement by drag forces from the vapour phase. It can be seen that the  $10^\circ$  cone results exhibit a greater discrepancy than the  $20^\circ$  cone results. This may be explained by the photographs in Figures 17 to 23 which show that the  $10^\circ$  cone condensate surface has a much peakier appearance and thus may create greater drag forces. In general the inclusion of the Coriolis terms in the theoretical solution predict that the greater the cone apex angle the larger the angle which the ridge makes with the cone generator line becomes. This observation is more pronounced at lower rotational speed.

In order to estimate the ridge angle the ridge phase velocity was assumed to be 2.4 times the average film velocity in the circumferential direction. This average film velocity was taken at the point where it reached a maximum. This was accomplished during the computation of the ridge profile by finding this velocity during each step and saving the maximum value. At this point it is worth enquiring about what is happening to the flow within the ridge. The methods of drainage which may be envisaged for the ridge type flow are

- (1) that the troughs of the ridge type flow are drained into the ridge from both sides and that these circumferential velocities

only occur for a small distance into the ridge and the drainage is completed by the component of velocity in the X direction.

- (ii) that the condensate drains from the trough into one side of the ridge preferentially and that the condensate is then drained by the velocity component in the X direction.

For the estimation of the ridge angle (ii) is assumed to be observed in order to neglect the retarding effect of flow into the ridge from the trough occurring on the other side. This is not such a restrictive assumption because if the ridge does receive condensate from both sides our calculated velocity will be that much smaller and so compensate to some extent. The results obtained also lend some credibility to the above assumption. We can see that flow in the ridge is very complex and its action may only be made by hypothesis. Typical velocities in the circumferential direction are .02 m/s at 400 r.p.m and .056 m/s at 600 r.p.m. for  $10^\circ$  and  $20^\circ$  cones respectively. The mean velocities in the X direction for the same rotational speeds are 0.199 m/s and 0.359 m/s for  $10^\circ$  and  $20^\circ$  cones respectively.

Discrepancies in the theory may also be due to the assumption that a semi-parabolic velocity exists at every point in the ridge profile. This assumption cannot be strictly true because of the introduction of the Coriolis component as already mentioned in the theoretical section. The simplifying assumption was necessary to make the equations even approximately soluble. The magnitude of this effect is impossible to predict but the fact that a fair agreement with experimental results throughout this chapter has been possible suggests the theory in outline is correct and should be modified only by factors of minor importance.

The extent to which the coriolis force affects the system depends

on its magnitude relative to the other inertia forces acting in the fluid. A convenient measure of the effect of the Coriolis components is the use of the Rossby number which is the ratio of the magnitude of the two terms  $V_x \nabla V_x$  and  $2\omega V_x$ , which may be written in our notation as

$$Ro = \frac{2\omega V_x}{a_x} \sin \beta. \quad 5.4.1$$

When the Rossby number is much less than 1 the effect of Coriolis forces are negligible and if greater than 1 are dominant. The values of Rossby numbers calculated from 5.4.1 for  $10^\circ$  and  $20^\circ$  cones are plotted in Figure 46. It can be seen that the maximum value of Rossby number is 0.147 and occurs at high speed on the  $20^\circ$  cone. From the definition of the Rossby number it would appear that although not negligible the Coriolis term is by no means dominant. This is to be expected since the rate of change of radius with increase in the X direction is not large with cones of such small apex angle. Examination of the curves reveals that the Coriolis effect increases with increase of speed, pressure and cone angle. It may be concluded then that the effect of Coriolis is of some importance and should be included in the general equation. At some stage however a check must be made to ascertain the effect of Coriolis on the velocity distribution in the X direction. No satisfactory and reasonably tractible way of doing so has yet been found.

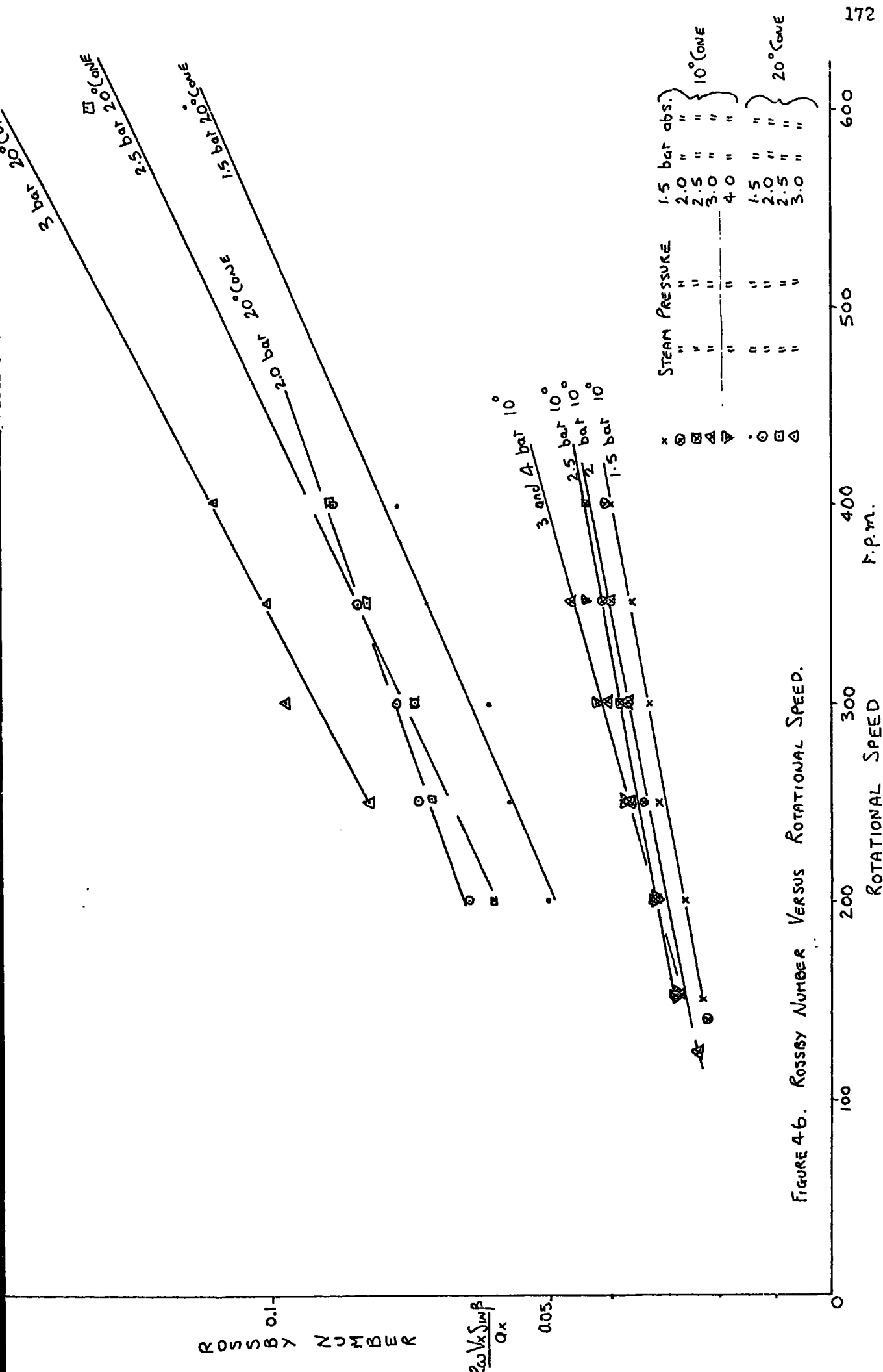


FIGURE 4.6. ROSSBY NUMBER VERSUS ROTATIONAL SPEED.

### 5.5 Energy transfer.

Since the major emphasis of this thesis is concerned with the dynamics of the condensate layer, brief mention will be made of the energy transfer data. Howe (69) has already presented a full account of the heat transfer data and that included here is only for completeness. The temperature profiles of inside and outside wall temperatures plus mean coolant water and steam saturation temperatures are given in Figure 47(a). Figure 47(b) indicates the range of heat flux,  $\phi$ , plotted against the Drex reference temperature.

The Nusselt number is defined as

$$Nu = \frac{h D}{2K}$$

where  $h$  is the heat transfer coefficient for condensing steam. The heat transfer coefficient may be calculated from

$$h = \frac{q}{A_{wo} \Delta T_f}$$

where  $q$ , the energy transferred in watts, is given by Fourier conduction through the cone wall

$$q = \frac{k_w \Delta T_w 2\pi L}{\ln R_2/R_1}$$

with  $L$  the length of the condensing surface,  $R_2$  and  $R_1$  the outer and inner surface radii respectively and  $\Delta T_w$  the cone wall temperature difference. The wall temperature difference is given by the mean outer minus the mean inner wall temperatures over the length of the condensing surface. This heat transfer coefficient must be looked upon as an average one rather than a local value. This will be the value used to calculate the experimental Nusselt number.

The heat transfer coefficient is also given by

$$h = k/\delta$$

Thus heat transfer coefficients may be found for each of the films

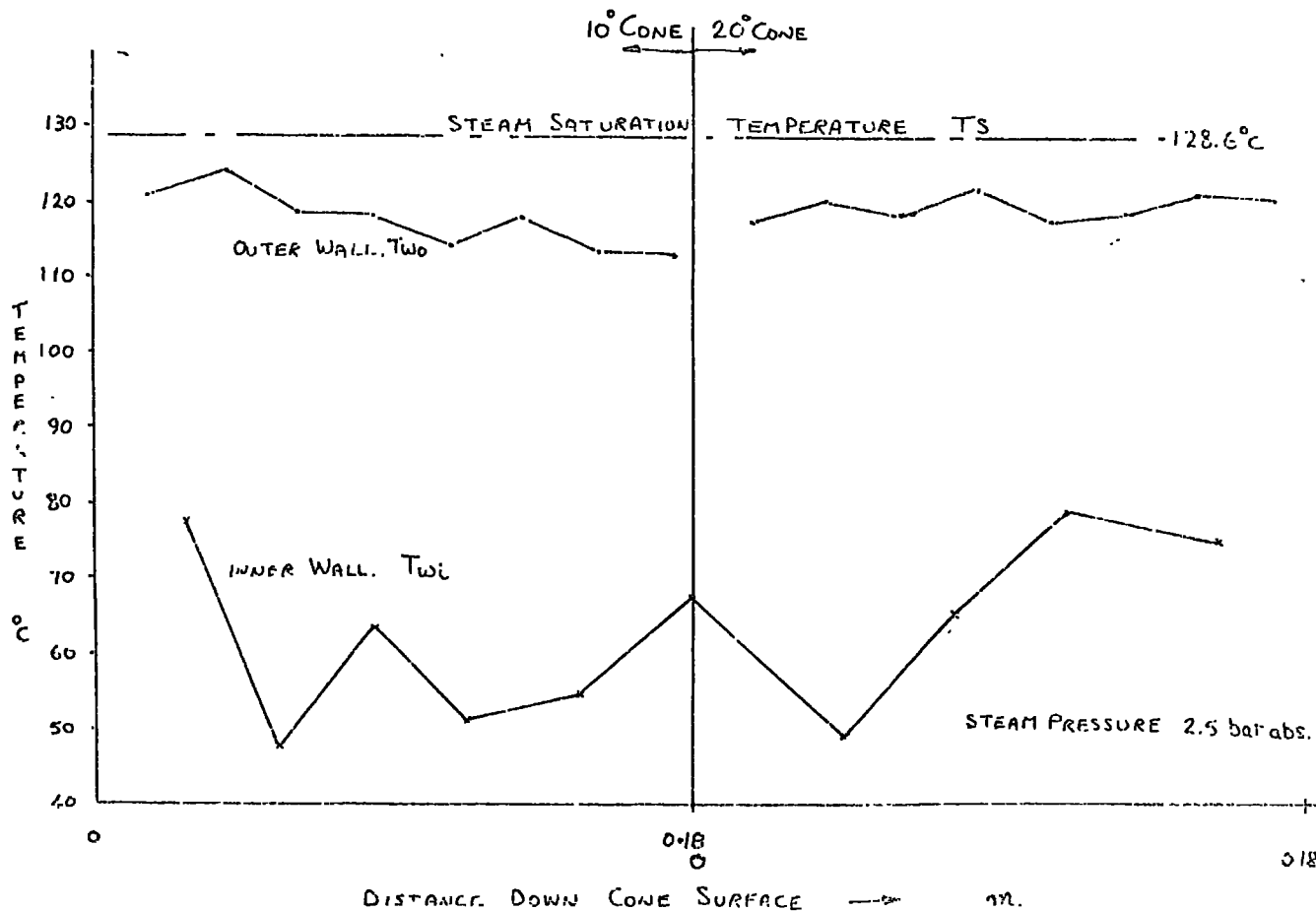


FIGURE 47 (a) TYPICAL CONE SURFACE TEMPERATURE DISTRIBUTION.

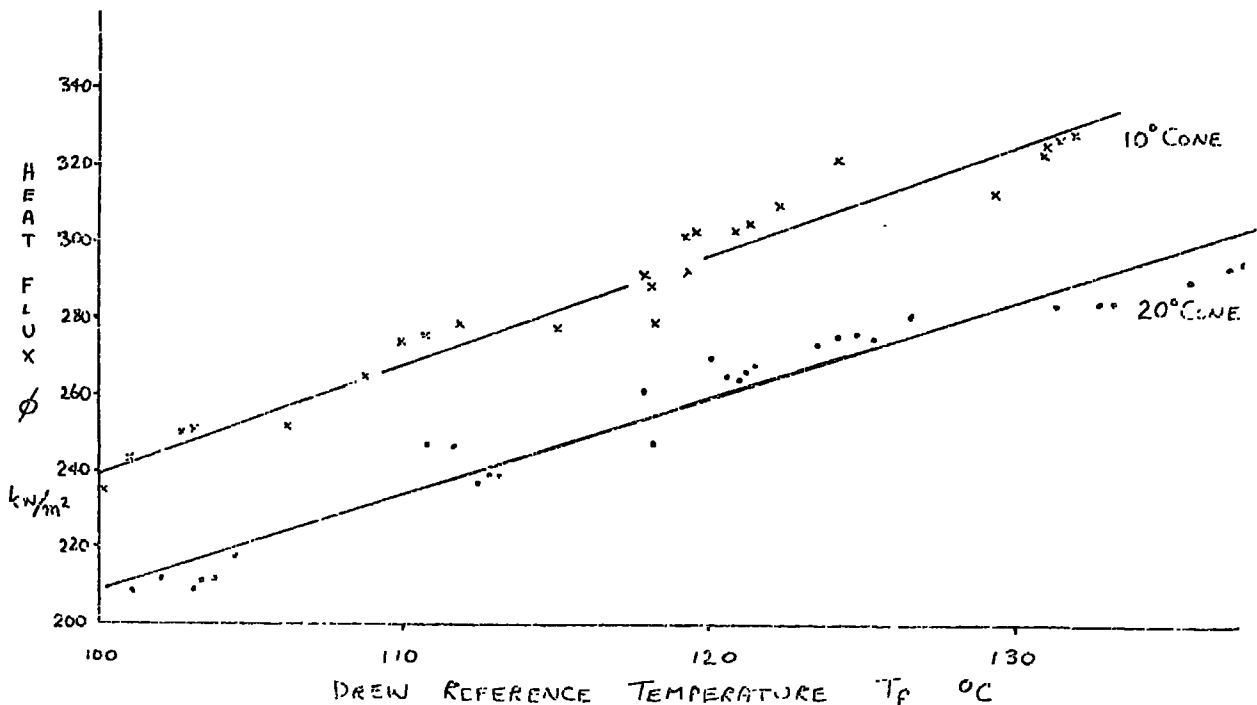


FIGURE 47 (b). HEAT FLUX VERSUS DREW REFERENCE TEMPERATURE

thicknesses plotted in Figures 35 and 36. The comparable one to the experimental value is that calculated from the mean film thickness. Of particular interest are those calculated from the minimum, or trough, film thickness. The values at high speed, 400 r.p.m. and 600 r.p.m. for  $10^\circ$  and  $20^\circ$  cones respectively are 49,000 and 100,000  $w/m^2 \cdot ^\circ K$  at a steam pressure of 1.5 bar absolute. The heat transfer coefficients for the peak film thickness for the above two conditions are both approximately 10,000  $w/m^2 \cdot ^\circ K$  which requires the mean heat transfer coefficients to be 27,390 and 41,000  $w/m^2 \cdot ^\circ K$  respectively. The two laminar film thicknesses, for the above conditions, predict heat transfer coefficients of 13,300 and 19,650  $w/m^2 \cdot ^\circ K$  respectively. The experimental heat transfer coefficients for the same two points are 23,700 and 22,715  $w/m^2 \cdot ^\circ K$  respectively. The  $10^\circ$  cone result for the mean heat transfer coefficient is very close to the experimental result but that of the  $20^\circ$  cone over estimates the coefficient by nearly 80%. This is the highest error in the whole of the theoretically predicted results and is brought about by the form of the solution. The value of  $\Lambda$  was found which allowed the measured peak film thickness divided by the value of  $\delta_{min}$ , calculated from  $\Lambda$ , to be the same as that predicted theoretically from the solution of 3.8.13. However, at the higher rotational speeds especially on the  $20^\circ$  cone the film thickness measurement was very suspect so that the error in calculating heat transfer coefficients is increased accordingly. It can be seen, from Figure 36, that in fact the film thickness has appeared to increase so that this value should be disregarded. The other values of heat transfer coefficients may be observed in Tables 3 and 4 for the theoretical ones and Tables 5 and 6 for the experimental ones for  $10^\circ$  and  $20^\circ$  cones respectively.

One method of comparing the information obtained in this thesis

with other workers is a plot of Nusselt number versus certain non-dimensional terms. The non-dimensional terms most often employed are Reynolds number, Weber number and Rayleigh number. The Weber number has been most frequently used in the past; Nicol and Gacesa (58), Hoyle and Matthews (56) and Singer and Preckshot (53) to name a few. It is possible to rearrange the governing parameter,  $\Lambda$ , to include the Weber number as one of the component terms.

$$\Lambda = \frac{k\Delta T \mu \sigma}{h_{fg}(1 + 0.375cp\Delta T/h_{fg}) \rho^3 a_y \delta_{min}^5}$$

rearranging and regrouping one obtains

$$\Lambda = \frac{3 cp\Delta T}{h_{fg}(1 + 0.375cp\Delta T/h_{fg})} \cdot \frac{1}{Pr We_0} \left(\frac{a_x}{a_y}\right)^2 \quad 5.5.1$$

where

$$We_0 = \frac{Vx^2 \rho}{\sigma} \quad 5.5.2$$

which is a form of the Weber number in terms of the film thickness. It can be seen that  $\Lambda$  is inversely proportional to the Weber number so that as well as an important factor in determining the surface profile it also offers a good correlating factor for the heat transfer results. Figures 48 and 49 present the Weber number versus theoretical and experimental Nusselt numbers respectively. Examination of Figures 48 and 49 reveals that at low Weber numbers the experimental Nusselt numbers are greater than those calculated theoretically. Whereas at higher Weber numbers the experimental Nusselt numbers are lower than the theoretical Nusselt numbers. At low rotational speed it has already been decided that the theoretical results are suspect and this low value is attributable to the much larger wavelengths predicted. In the experimental section mention was made about the difference in the input and output temperatures of the slipping unit causing difficulties at higher rotational speeds. The surface temperatures were found to be reading low, for this reason a larger temperature difference was

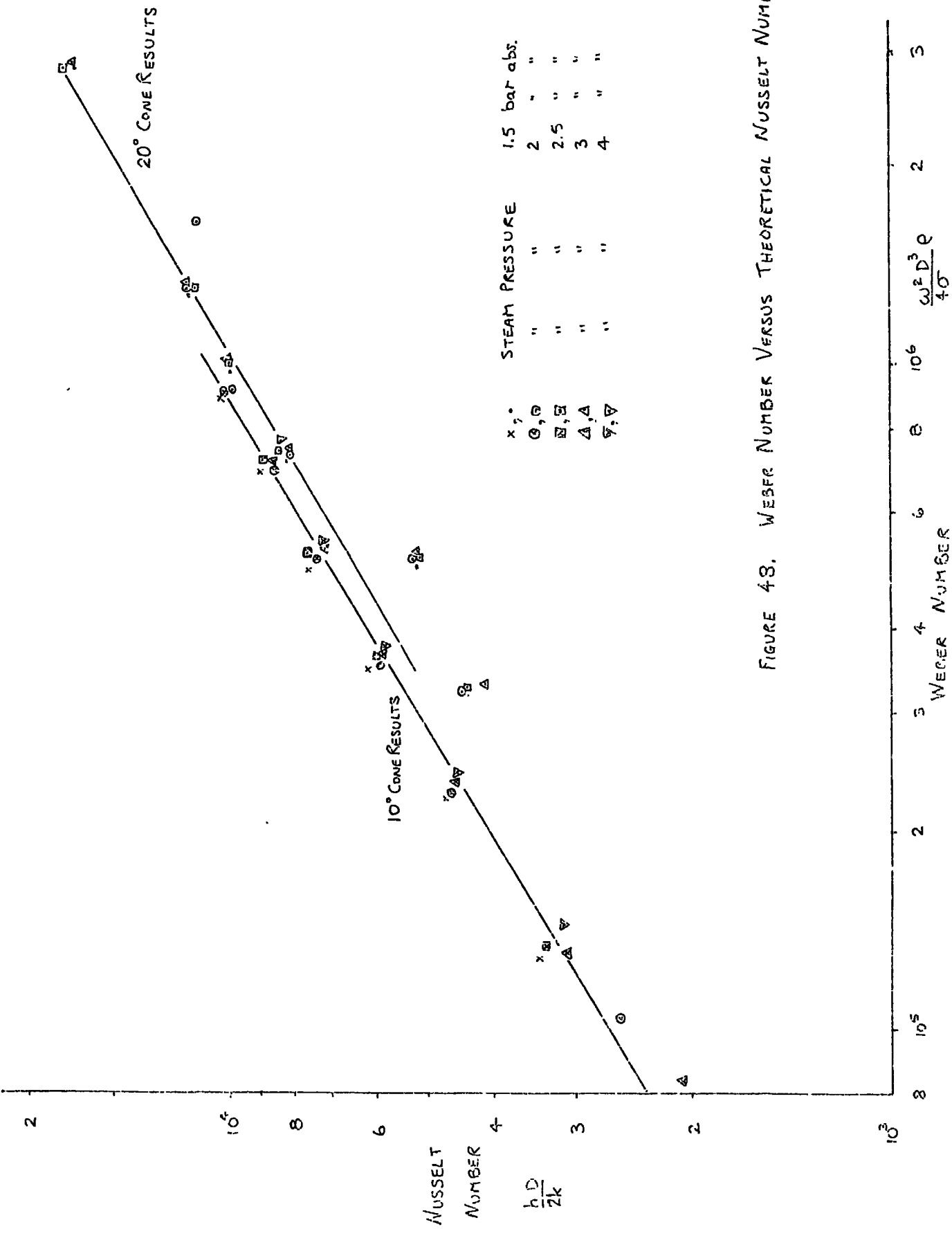


FIGURE 48. WEBER NUMBER VERSUS THEORETICAL NUSSELT NUMBER.

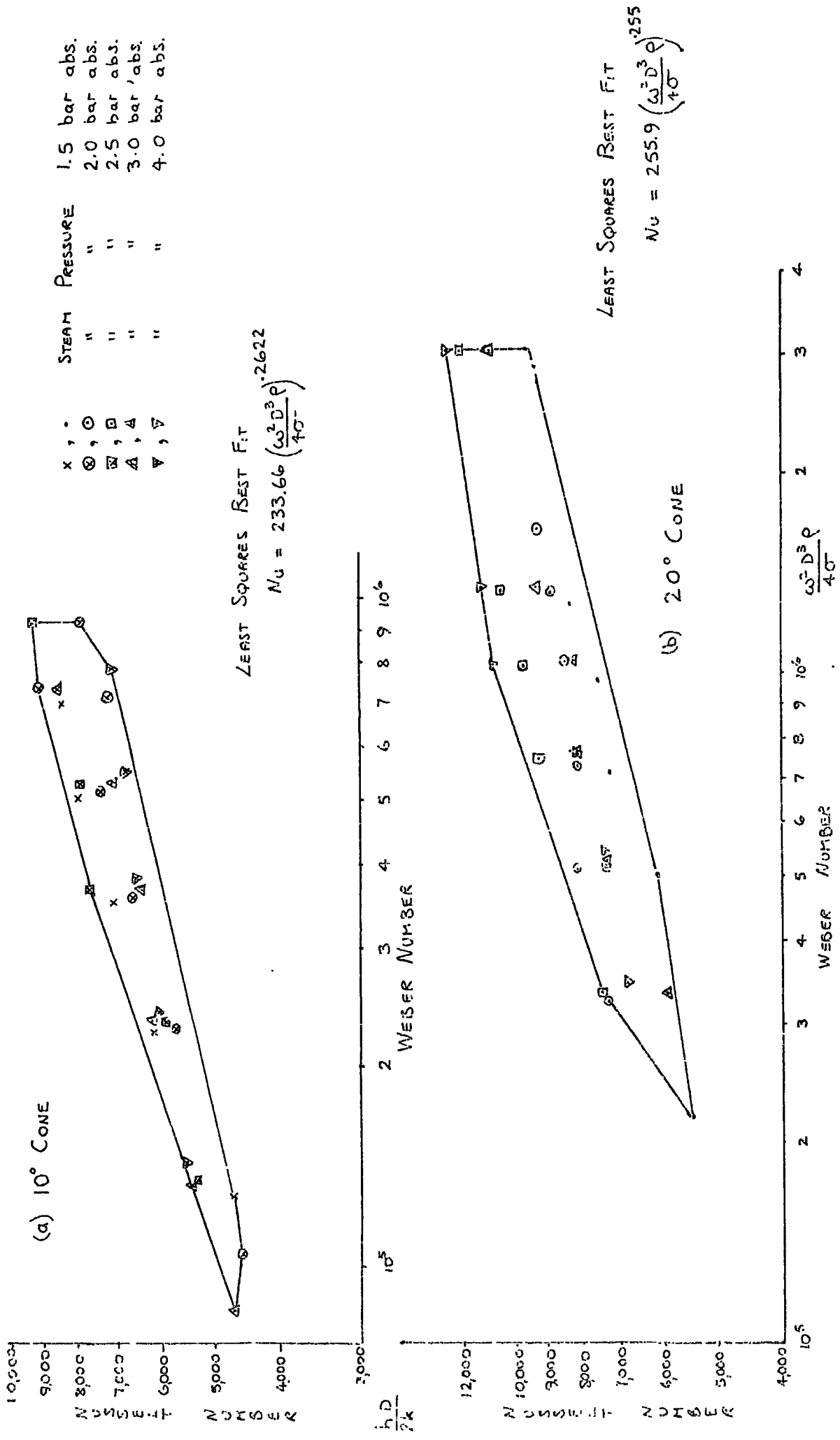


FIGURE 49. WEISER NUMBER VERSUS EXPERIMENTAL NUSSELT NUMBER.

indicated than actually present. This in turn meant lower Nusselt numbers. However the experimental and theoretical results compare favourably within the experimental error of  $\pm 29\%$ . The comparison can be observed more clearly in Figure 50 which also compares the authors contribution to that of other workers. It can be seen that the new data extends the range of the data produced by Hoyle and Matthews (56). Some of the previous workers carried out experimental studies on much smaller test bodies at higher rotational speeds. Two different workers in this category, Yeh (51) and Singer and Preckshot (53), showed that the Nusselt numbers declined after a certain Weber number was reached. Hoyle and Matthews found no such decline and this latter finding has been confirmed in this work. No satisfactory explanation for the decrease in the Nusselt number with increase in Weber number has been suggested. Hoyle and Matthews thought that it might be due to an imperfect seal in their apparatus and Singer and Preckshot attributed it to the retardation of the drops by drag forces resulting in reduced heat transfer.

The experimental data can be correlated by the following equation for both  $10^\circ$  and  $20^\circ$  surfaces to within  $\pm 17\%$  :-

$$\text{Nu} = 250.22 \left( \frac{\omega^2 D^3 \rho}{4 \sigma} \right)^{0.2569} \quad 5.5.3$$

The equation was given by a least squares fit computer programme documented in Appendix E.

It has already been shown that there is a good correlation between Nusselt and Weber numbers. For this particular work, however, it is felt that a more linear relationship exists between the Nusselt and Taylor numbers. The Taylor number can be described as a rotational Reynolds number squared, written in our terms as

$$\text{Ta} = \left( \frac{4 \omega R^2 \rho}{\mu} \right)^2 \quad 5.5.4$$

The experimental values of Nusselt number are plotted against the

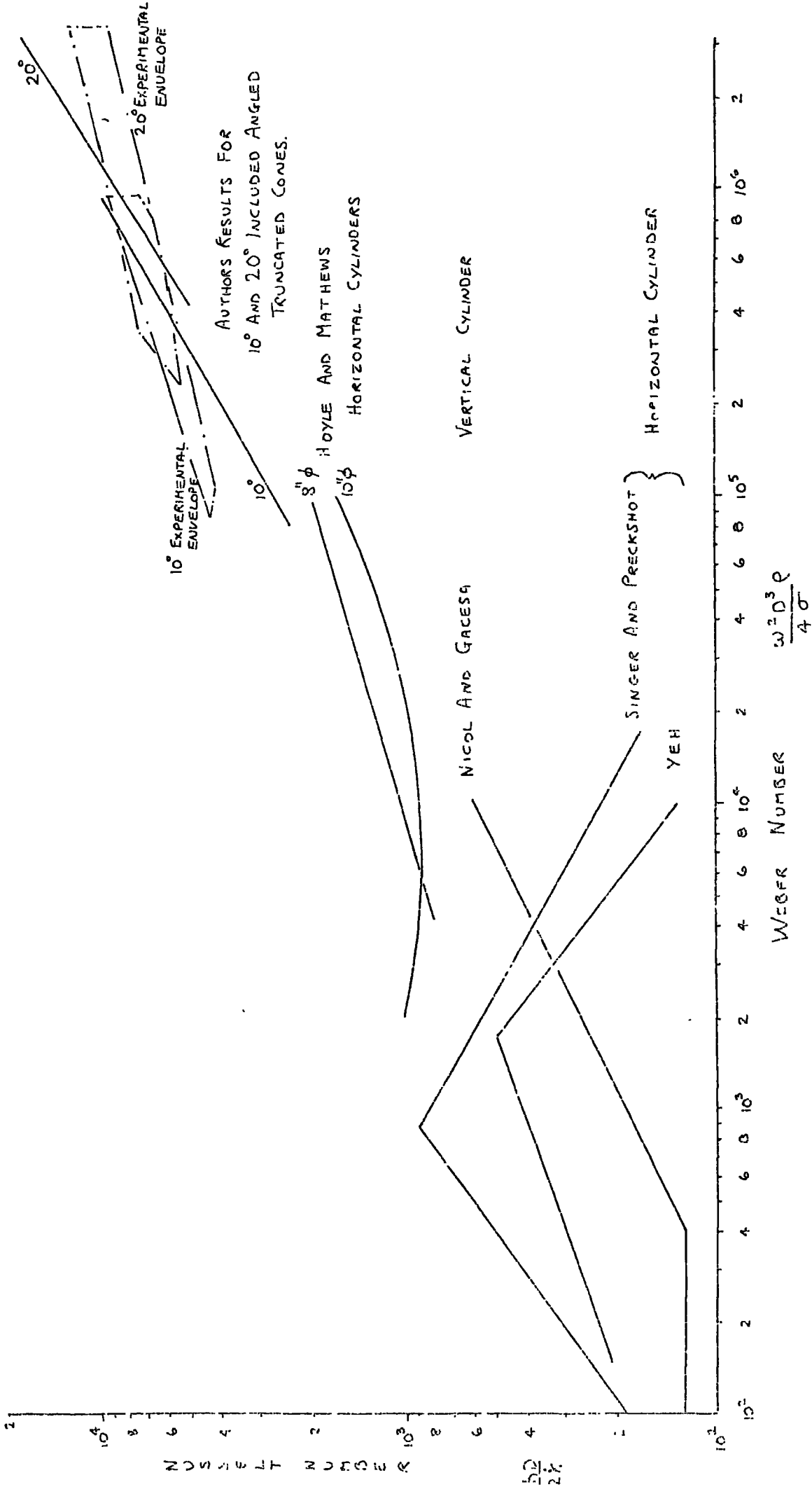
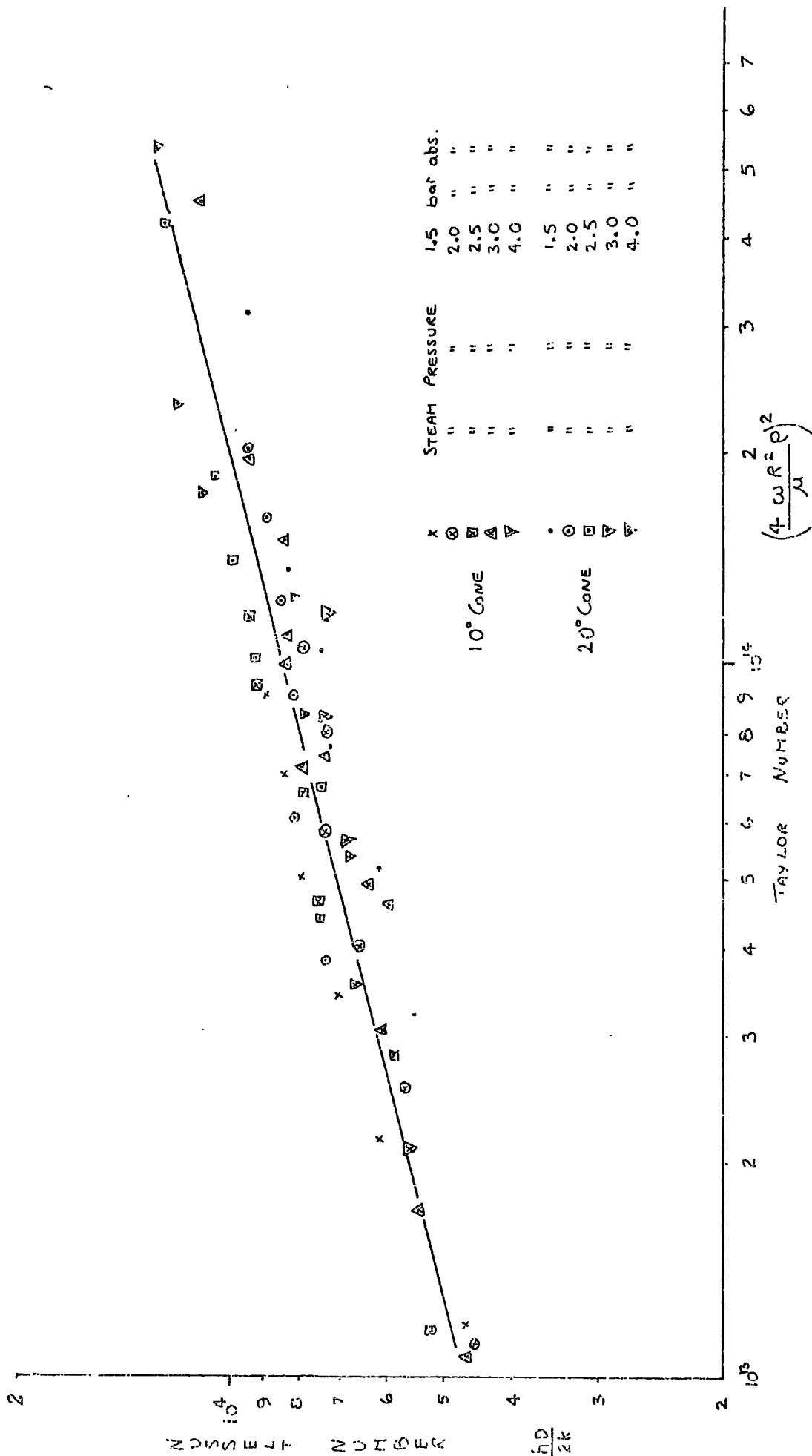


FIGURE 50 COMPARISON OF THE AUTHORS RESULTS TO THOSE OBTAINED BY OTHER WORKERS.



Taylor number in Figure 51. It can be seen that it is possible to draw one line through all the points which allows the Nusselt to be predicted to  $\pm 14\%$  given the Taylor number. The Nusselt number is given by the equation :-

$$\text{Nu} = 1.1132 \text{Ta}^{0.245} \quad 5.5.5$$

To test the validity of the Taylor number as a correlating factor results from other workers have been plotted in Figure 52. Values could only be obtained from graphs in the other authors work so that some error must be allowed in the points presented. Those results taken from Hoyle and Matthews (56) follow a fairly linear increase from the 0.158 m to the 0.394 m diameter cylinders having overlapping points. If the points could have been calculated from original data, and not points from a graph, more importance could be placed on the findings. The results obtained in this thesis do not appear as a continuation as in the Nusselt versus Weber number plot but more as a direct increase in Nusselt number proportional to the increase in test body diameter. This suggests that the Taylor number alone is not sufficient to provide a basis of comparison of all these observations. Only four values of Taylor versus Nusselt number have been plotted for the  $60^\circ$  right cone, taken at different speeds, radii and pressure. All the values were taken in the range where a similar ridge like condensate layer occurred. The Taylor and Nusselt numbers both have numerical values in the same range as the  $10^\circ$  and  $20^\circ$  cones. The slopes of the two lines however are different. The slope of the  $10^\circ$  and  $20^\circ$  line is very close to that of the results of Hoyle and Matthews. Whereas the slope of the  $60^\circ$  cone is greater and may be a more complex function of speed and radius because of the change of regimes of flow which occurs.

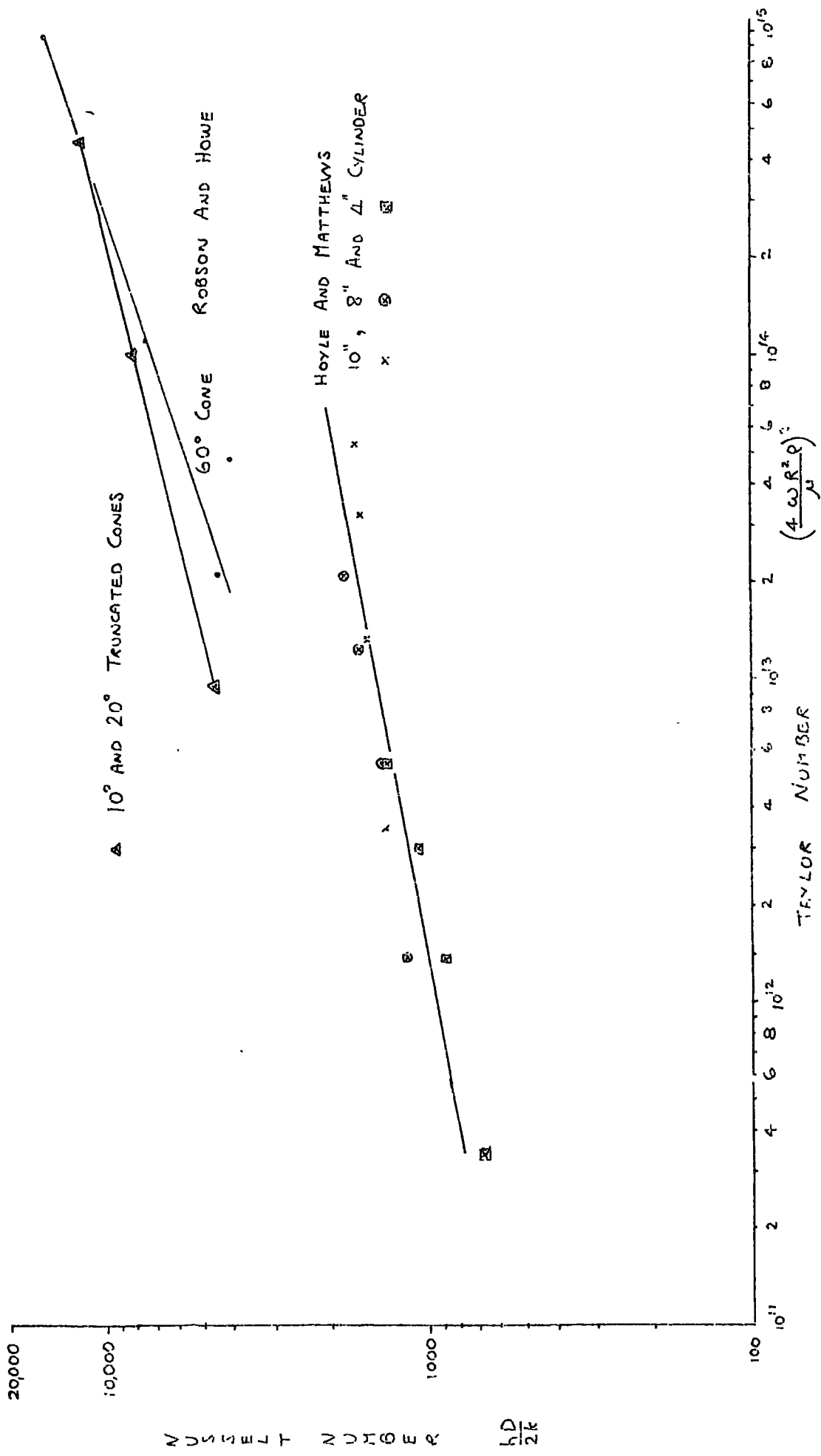


FIGURE 52 NUSSELT NUMBER VERSUS TAYLOR NUMBER FOR DIFFERENT SHAPED BODIES

## 6.0 CONCLUSION

An experimental and theoretical investigation has been carried out on the fluid dynamics of condensate films on the surface of rotating cones. It has been demonstrated that a mathematical model can be constructed of the ridge type flow regime which predicts wavelength and minimum film thickness. The maximum or peak film thickness has been measured but an experimental method, based on conductivity measurement, to obtain a picture of the condensate surface profile failed due to the severity of the operating conditions. The latter technique provided basic information about the drawbacks of using the conductivity measuring equipment with a non-constant temperature fluid.

The theoretical equation derived, even after many assumptions, was of such a nature that it could only be solved in the form of two non-dimensional terms. One,  $\Lambda$ , containing a balance of surface tension and inertial terms and a second,  $\Theta$ , an allowance for Coriolis effects. This is not a particularly satisfactory arrangement because both the terms,  $\Lambda$  and  $\Theta$ , depend on the minimum or trough film thickness. Thus a truly theoretical solution could not be given without prior knowledge of the minimum film thickness. The theoretical solution has been applied inconjunction with experimental data to predict a value of wavelength, minimum film thickness and hence a Nusselt number.

It was hoped that the theory could be used to predict the conditions at which ridges appear and also that at which drops are thrown from the ridge profile. It appears that limitations of the theoretical method employed makes it invalid for the former case since at particular rates of heat flux and rotational speed infinite wavelengths are predicted. Similarly at the instant of drop detachment the theory predicts that the ratio of peak to minimum film thickness attains a value which is in practice impossible. This is caused by the sudden change in heat flux when a drop is detached which cannot be taken into account in the theory.

Data was collected for the  $10^\circ$  cone which shows the effect of increase of condensation rate on the initiation of ridge type flow and drop detachment.

#### Wavelength

The variation of wavelength measured for the range of rotational speeds for which the ridge type drainage occurs is 0.007 to 0.0027 m as the speed increases. The wavelengths of the ridges formed on the  $20^\circ$  cone are greater than those on the  $10^\circ$  cone at the same speed. Theoretically calculated wavelengths demonstrated that at low speeds an anomaly existed which caused the predicted wavelength to be much larger than that observed. It is considered that this discrepancy is due to the fact that certain type waves observed at low speeds will call for a different theoretical approach.

#### Film thickness

It has been possible to measure the peak film thickness of the condensate layer although the accuracy could not be controlled to better than  $\pm 25\%$ . This is an appreciable error but the order of film thickness is correct and is borne out by the heat transfer coefficient calculations. The variation of peak film thickness was found to be in the range 0.086 to 0.066 mm, for increase of speed from 200 to 600 r.p.m., for both  $10^\circ$  and  $20^\circ$  cones. The minimum or trough film thickness was calculated from the theoretical equation and showed that as the speed was increased, at constant steam pressure, its value was reduced at a much greater rate than the peak film thickness. A comparison of the laminar film thickness, as calculated by Howo (69), and a mean film thickness calculated by integrating over one half wavelength showed that the latter was less than the former by a percentage which depended on the speed of rotation. A plot of laminar film thickness divided by minimum film thickness and laminar divided by peak film thickness

against the component of acceleration perpendicular to the cone generator produced a linear relationship on log-log graph paper. These relationships are given as

$$10^\circ \text{ cone} \quad \frac{s_{\text{lam}}}{s_{\text{min}}} = 0.1193 a_y^{0.5606}$$

$$20^\circ \text{ cone} \quad = 0.0611 a_y^{0.6346}$$

and for the peak film thickness,  $s_{\text{max}}$

$$10^\circ \text{ cone} \quad \frac{s_{\text{lam}}}{s_{\text{max}}} = 1.33 a_y^{-0.0875}$$

$$20^\circ \text{ cone} \quad = 2.177 a_y^{-0.2089}$$

Inertia terms

One of the matters to which attention has been given is the effect of Coriolis forces in determining the flow pattern. A measure of the importance of these forces is provided by the Rossby number, a non-dimensional group which is a ratio of the two terms  $V_x \nabla V_x$  and  $2\omega V_x$  and written as  $2\omega V_x S \sin \beta / a_x$ . A maximum Rossby number of 0.147 was obtained for the  $20^\circ$  cone. This is not a value which suggests that Coriolis has a very large effect on the flow process but of enough importance to be included in the governing equations. Calculation of ridge angle,  $\alpha$ , shows that drag may have an important role in the actual drainage angle because the former are all somewhat less than the measured values.

Energy transfer

The experimental data has been correlated by plotting Nusselt number versus Weber number. Comparison with other workers shows that this new data follows the trend of data produced by Hoyle and Matthews (57) on rotating cylinders. A correlation was found by a least squares polynomial fit of the experimental data and given as

$$Nu = 250.22 \left( \frac{\omega^2 \rho^3 R}{4 \sigma} \right)^{0.2569}$$

encompassing all data to within  $\pm 17\%$ .

The heat transfer coefficients predicted from the theoretical ridge model, calculated from the mean film thickness, showed close agreement to the experimental results. The laminar theory always predicted coefficients which were less than the experimental ones. In the ridge model it was found that the heat transfer coefficients were always greater than the laminar ones.

Another non-dimensional term, the Taylor number, was in this particular case shown to be a better correlating factor for the Nusselt number. The Taylor number may be thought of as a rotational Reynolds number squared. A least squares fit of the data resulted in the empirical equation

$$\text{Nu} = 1.1132 \text{Ta}^{0.245}$$

which allows the Nusselt number to be predicted to within  $\pm 14\%$ .

### Further work

The preceding work has shown that it is possible to model, with reasonable accuracy, the ridge type flow occurring on the surface of  $10^\circ$  and  $20^\circ$  rotating truncated cones. However, one point brought out was that a separate analysis must be developed to account for the curtain type wave regime which occurs prior to the development of ridge type waves. This solution must come from a three dimensional treatment and perhaps a change of the coordinate system may simplify matters. The mathematical complexity of such a system would necessarily be enormous.

The failure of the conductivity film thickness measuring technique was caused by line contact around the periphery of the tufnol insulator breaking down. It is therefore necessary to develop some method of achieving this line contact. Possibly this may be obtained by coating the tufnol with a heat resistant resin and heating the test body up to a temperature of about  $250^\circ\text{C}$  and allowing the plug to have a shrink fit.

Some other means of measuring the film thickness may be possible. The use of a radiation technique may be more attractive in the light of the information obtained about the conductivity film thickness measuring device. The problems in this method were that the radiation detector must rotate with the cone and must be very sensitive in order to measure the thin films encountered on the surface of the cones.

It would very useful to develop a high intensity flash light which would allow a more successful study of ridge formation and drop detachment on the  $20^\circ$  cone condensate surface. This would be best situated in the vessel itself. It would be possible then to compare the drop diameters with the ridge wavelength and ascertain the relationship between the two.

The point method was originally developed to check that the conductivity device was giving the correct order of film thickness.

For future development this method could be made more attractive by arranging for the main shaft to run in air bearings. This would then allow a much closer tolerance to be held on the cone movement. The method of measurement in this thesis was accurate but movement in the main bearings was  $\pm 0.0025$  mm which is a large percentage of the measured peak film thickness.

7.0 REFERENCES.

## References

1. Hopf, L.                    Ann. Physik (4) 32, p.777, 1910.
2. Nusselt, N.                Die Oberflachen kondensation des Wasserdampfes,  
Z. Ver. Dent. Ing. Vol. 60, p.541, 1916.
3. Jeffreys, H.              Phil. Mag. (6) 49, p.793, 1925.
4. Chwang, C. T.            M. S. thesis, Mass. Inst. Technol., Cambridge,  
Massachusetts, 1928; data reported by (5).
5. Cooper, C. M.,            The isothermal flow of liquid layers  
Drew, T.B., and            Trans. A.S.M.E. (Chem. Engrs.) Vol.30  
M<sup>c</sup>Adams, W. H.            p.p. 158 - 169, 1934.
6. Kirkbride, C. G.        Heat transfer by condensing vapour on vertical  
tubes, Trans. A.S.M.E. (Chem. Engrs.) Vol.30  
p.p. 170 - 186, 1934.
7. Friedman, S. J.         Liquid films in the viscous flow regime,  
Miller, C. O.              Ind. Eng. Chem. Vol.33, p.p. 885 - 891, 1941.
8. Grimley, H.             Liquid flow conditions in packed towers,  
Trans. Inst. Chem. Engrs., 23, p.228, 1945.
9. Kapitsa, P. L.            Wave flow of thin layers of a viscous fluid (pt.1),  
Collected papers of P.L. Kapitsa p.p. 662 -679,1948.
10. Kapitsa, P. L.         Wave flow in thin films of viscous liquids,(pt.3),  
Kapitsa, S. P.             Collected papers of P.L. Kapitsa, 1949.
11. Taylor, G. I.            The instability of liquid surfaces when accelerated  
in a direction perpendicular to their planes (pt.1),  
Proc. R. Soc. A201, p.p. 192 - 196, 1950.
12. Lewis, D. J.            The instability of liquid surfaces when accelerated  
in a direction perpendicular to their planes (pt.2),  
Proc. R. Soc. A202, p.p.81 - 96, 1950.
13. Dukler, A. E.,         Characteristics of flow in falling liquid films,  
Bergelin, O. P.            Chem. Eng. Prog. Vol.43, No.11, p.p.557 - 563, 1952.
14. Karman, T. Von         Z. Angew., Math., Mech., Vol.1. p.245, 1921.
15. Jackson, M. L.         Liquid films in viscous flow,  
A.I.Ch.E. Journal, Vol.1, No.2, p.p.231 - 240, 1955.
16. Yih, C. S.             Stability of parallel laminar flow with a free  
surface, Proc. 2nd U.S. Congr. Appl. Mech.(A.S.M.E.)  
p.p. 623 -628, 1954.
17. Binnie, A. M.         Experiments on the onset of wave formation on a  
film of water flowing down a vertical plane,  
J. Fluid Mech., Vol.2, p.p.551 - 554, 1957.

18. Brown, R. H. J.      Photographic Jnl. Vol.923, p.130, 1952.
19. Brooke-Benjamin, T. Wave formation in laminar flow down an inclined plane, Jnl. of Fluid Mech., Vol.2, p.p.554, 1957.
20. Belkin, H. H.      Liquid flow down vertical walls,  
Macleod, A. A.      A.I.Ch.E. Journal, Vol.5, No.2, p.p. 245 - 248,  
Monrad, C. C.      June 1959.  
Rothus, R. R.
21. Bushmanov, V. K.      Hydrodynamic stability of a liquid layer on a  
vertical wall, Soviet phys. J.E.T.P Vol.12,  
p.p.873, 1961.
22. Dukler, A. E.      Fluid mechanics and heat transfer in vertical  
falling film systems, Chem. Eng. Prog.,  
Symposium series, Vol.56, No.30, p.p. 1 -10, 1960.
23. Dukler, A. E.      Comparison of theoretical and experimental film  
thickness, Am. Rocket Soc. Jnl. Vol.31,  
p.p. 86 - 87, 1961.
24. Binnie, A. M.      Instability in slightly inclined water channel  
Jnl. Fluid Mech. Vol.5, p.p.561 - 567, 1959.
25. Brooke-Benjamin, T. Development of three dimensional disturbances in  
unstable film of liquid flowing down inclined  
plane, Jnl. Fluid Mech. Vol.10, pp.401-419, 1961.
26. Yih, C. S.      Stability of liquid flow down an inclined plane,  
The Physics Of Fluids, Vol.6, No.3, March 1963.
27. Portalski, S.      Studies of falling liquid film flow,  
Chem. Eng. Sci. Vol.18, p.p.787 - 804, 1963.
28. Portalski, S.      Velocities in film flow of liquids on vertical  
plates, Chem. Eng. Sci. Vol.19, p.p.575-582, 1964.
29. Fulford, G. D.      The flow of liquids in thin films,  
Advances in Chem. Eng<sup>ing</sup>, Vol.5, Academic Press,  
p.p.151 - 236, 1964.
30. Massot, C.      Modified description of wave motion in a falling  
Irani, F. and      film, A.I.Ch.E. Jnl. Vol.12, No.3, p.p.445 - 455,  
Lightfoot, E. N.      May 1966.
31. Ishihara, T.      Open channel flow  
Iwagaki, Y. and      Trans. Am. Soc. Civil Eng. Vol.126, p.p.548 - 563,  
Iwasa, Y.      1961.
32. Yih, C. S.      Instability due to viscosity stratification,  
Jnl. Fluid Mech. Vol.27(pt.2), p.p.357 - 352,  
1967.

33. Anshus, B. E.  
Acrivos, A. Chem. Eng. Sci. Vol.22, p.389, 1967
34. Lee, J. Kapitza's method of film flow description,  
Chem. Eng. Sci. Vol.24, p.p.1309 - 1319, 1969.
35. Gollan, A.  
Sideman, S. On the wave characteristics of falling films,  
A.I.Ch.E. Jnl. Vol.15, No.2, p.p.301 - 303, 1969.
36. Holgate, M. J. The stability of a fluid film on the surface of  
a cone, Ph.D. Thesis, Eng. Sci. Dept., Durham  
University, May 1971.
37. Othmer, D.F. The condensation of steam,  
Ind. and Engng. Chem. Vol.21, No.6, p.p.576 - 583,  
1929.
38. Chow, C. L.  
Hoyle, R. Temperature distribution in the rotor of a steam  
turbine during warm up and hot starts, The Engineer,  
215, p.p.763 - 766, 1963.
39. Hoyle, R.  
Mahabir, H. E. Cold starting temperatures in rotors of marine  
steam turbines, The Engineer, 216, p.p.353 - 356,  
1963.
40. Bromley, L. A. Effect of heat capacity of condensate in condensing,  
Ind. and Engng. Chem. Vol.44, No.12, p.p.1966 - 1969,  
1952
41. Rohsenow, W. M. Heat transfer and temperature distribution in  
laminar film condensation, Trans. A.S.M.E.  
p.p.1645 - 1656, Nov. 1956.
42. Rohsenow, W. H. Effect of vapour velocity on laminar and turbulent  
film condensation, Trans. A.S.M.E. Jnl. Heat Transfer  
Vol. 78, p.p.1637 - 1643, Nov. 1956.
43. Labuntsov, D. A. Heat transfer on film condensation of pure vapours  
on vertical surfaces and horizontal pipes,  
Teploenergetika, Vol.4(1), p.p.72 - 79, 1957.
44. Labuntsov, D. A. Teploenergetika, No.12, p.47, 1956.
45. Sparrow, E. M. A boundary layer treatment of laminar film condensation,  
A.S.M.E. Jnl. Heat Transfer, p.p.13 - 18,  
Feb. 1959.
46. Dukler, A. E. Dynamics of vertical falling film systems,  
Chem. Eng. Prog. Vol.55, No.10, p.p.62 - 67, 1959.
47. Deissler, R. G. N.A.C.A. Tech. notes 2129(1950), 2138(1952), 3145(1959)
48. Lee, J. Turbulent film condensation,  
A.I.Ch.E. Jnl. Vol.10, No.4 p.p.540 - 544, 1964.
49. Gerstman, J.  
Griffith, P. Laminar film condensation on the underside of  
horizontal and inclined surfaces, Int. Jnl. Heat  
and Mass Transfer, Vol.10, p.p.567 - 580, 1967.

50. Kuiken, H. K. On almost inviscid film flows, Int. Jnl. Non-linear Mech. Vol.5, p.p.259 - 267 1970.
51. Yeh, L. The effect of surface speed and steam pressure upon the transfer of heat from steam to a rotating cylinder, Ph.D. Thesis, University of London 1954.
52. Birt, D.C.P. Methods of improving heat transfer from condensing steam and their application to condensers and evaporators, Trans. Inst. Chem. Eng. Vol.37, Brunt, J. J. Sheldon, J. T. Watson, R. p.p.289 - 296, 1959.
53. Singer, R. M. The condensation of vapour on a horizontal Preckshot, G. W. rotating cylinder, Proc. Heat Transfer and Fluid Mech. Inst. No.14, p.205, 1953.
54. Hoyle, R. D. Transient temperature stresses in axially symmetrical systems with special application to a solid rotor of a steam turbine. Proc. I. Mech. Eng. Vol.169, No.31, p.553, 1955.
55. Matthews, D. H. The transfer of heat to cylinders of various diameters rotating in a steam atmosphere, with varying conditions of temperature, pressure and rotational speed, Ph.D. Thesis, Mech. Eng., Imperial College, London. July 1962.
56. Hoyle, R. D. The effect of speed on the condensate layer on a cooled cylinder rotating in a steam atmosphere, Matthews, D. H. Jnl. Fluid Mech. Vol.22, p.105, 1965.
57. Hoyle, R. D. The effect of diameter size and speed of rotation on the heat transfer from steam to cooled cylinders, Matthews, D. H. Int. Jnl. Heat and Mass Transfer, p.1273, 1964.
58. Nicol, A. A. Condensation of steam on a rotating vertical cylinder, Gacesa, M. Trans. A.S.M.E. Jnl. Heat Transfer, p.p.144 - 152, 1970.
59. Sparrow, E. M. A theory of rotating condensation, Gregg, J. L. Trans. A.S.M.E. Jnl. Heat Transfer, Vol.81, p.p.113 - 120, May 1959.
60. Mandapurkar, S.S. Condensation on a horizontal rotating disc, Beatty, K. O. Chem. Engng. Prog. Symposium series, Vol.56, No.30, p.p.129 - 137, 1959.
61. Sparrow, E. M. The effect of vapour drag on rotating condensation, Gregg, J. L. Trans. A.S.M.E. Jnl. Heat Transfer, Vol.82, p.p.71 - 72, Feb. 1960.
62. Espig, H. R. Heat transfer by the condensation of steam on a rotating disc, Ph.D. Thesis, Dept. Mech. Eng., Imperial College, London. 1963.

63. Espig, H. R.  
Hoyle, R. D. The transfer of heat from condensing steam to a cooled rotating disc, Proc. I. Mech. Eng. Vol.182(pt.3H,paper 43), p.p.406 - 412, 1967-68.
64. Espig, H. R.  
Hoyle, R. D. Waves in a thin layer on a rotating disc, Jnl. Fluid Mech. Vol.22(pt.4), p.p.671 -677, 1965.
65. Bromley, L. A. Prediction of performance characteristics of Hickman-Badger centrifugal boiler compression still, Ind. and Eng<sup>NE</sup>. Chem. Vol.50(pt.1), p.p.233 - 236, 1958.
66. Sparrow, E. M.  
Hartnett, J. P. Condensation on a rotating cone, Trans. A.S.M.E. Jnl. Heat Transfer, Vol.83, p.p.101 - 102, Feb. 1961.
67. Howe, M.  
Hoyle, R. D. Heat transfer from condensing steam to a cooled cone rotating about a vertical axis, Proc. I. Mech. Eng. Vol.184(3G), p.p.37 -44, 1970.
68. Robson, B. The formation and drainage of a film of condensate on the surface of a rotating cone, M.Sc. Thesis University of Durham, 1969.
69. Howe, M. Heat transfer of steam onto rotating cones, Ph.D. Thesis, University of Durham, 1972.
70. M<sup>c</sup>Adams, W. H. Heat transmission, 3rd ed., McGraw-Hill Book Company, Inc., New York, 1954.
71. Shield, J. High temperature Adhesives. S.I.R.A. Institute
72. Benedict, R. P. Fundamentals of temperature, pressure and flow measurement, Wiley, 1969
73. Collier, J. G.  
Hewitt, G. F. Film thickness measurement in two-phase flow, Brit. Chem. Eng. Vol.12, p.p.709 - 715, May 1967.
74. Hewitt, G. F.  
King, R. D.  
Lovegrove, P. C. Techniques for liquid film and pressure drop studies in annular two phase flow, A.E.R.E. R3921, 1962.
75. Charvonia, D. A. An experimental investigation of the mean liquid film thickness and the characteristics of the interfacial surface in annular two phase flow, Paper presented at Winter Ann. Meeting of the A.S.M.E. New York, Nov. 26th-Dec 1st,(61-wa-243), 1961.
76. Hewitt, G. F.  
Lovegrove, P. C.  
Nicholls, B. Film thickness measurement in annular two-phase flow using a fluorescence spectrometer technique, A.E.R.E. Chem. Eng. Div. R4478 , 1964  
R4506 , 1969.
77. Black, R. H. Capacitance method of measuring water film thickness, Trans. A.S.C.E. Vol.126, p.p.89 - 94, 1961.

78. Van Rossum, J. J. Experimental investigation of horizontal liquid films, wave formation, atomisation and film thickness, Chem. Eng. Sci., Vol.11, p.p.35 - 62, 1959.
79. National Engineering Laboratory Reports  
 Reports on condensation in the presence of non-condensables, various authors  
 N.E.L. Report No. 219 1966  
 " " Nos. 270, 291, 294 1967  
 " " " 477, 483 1971.
80. Koh, C. Y. Sparrow, E. M. Hartnett, J. P. The two phase boundary layer in laminar film condensation, Int. Jnl. Heat and Mass Transfer, Vol.2, p.p.55 - 66, 1961.
81. Colburn, A. P. Problems in design and research on condensation of vapours and vapour mixtures, Proc. Gen. Discussion on Heat Transfer(I. Mech. E. and A.S.M.E.), p.p.1 - 11, Sept. 1951.
82. Carpenter, E. F. Proc. Gen. Discussion on Heat Transfer(I. Mech. E. and A.S.M.E.), p20, 1951.
83. International Critical Tables
84. Powell, R. W. Correction of metallic thermal and electrical conductivities for both solid and liquid phases, Int. Jnl. Heat and Mass Transfer, Vol.8, p.p.1033 - 1045, 1965.
85. International Business Machines. Continuous Systems Modelling Programme,
86. Lamb, H. Hydrodynamics, p.156, Cambridge Press 1932.

8.0 APPENDICES.

Appendix AFilm thickness measurement

There were several potentially useful means of determining the thickness of a liquid film, these are contained in two basic groups. The first are film averaging methods and the second localised methods. Each of the measuring techniques was critically analysed providing the following information.

(a) Film averaging methods

The hold-up method has been probably the most widely used technique for measuring film thickness. It consists simply of isolating a section of liquid film, allowing it to drain into a container and then determining its volume. This method is unsuitable for use on the present rig. Instantaneous shut off of the steam supply is impossible, although allowance could be made for the amount contained in the vessel, and complicated collection techniques would have to be evolved.

Weighing methods have been used in the past by Collier and Hewitt (73) to measure hold-up in packed columns. The method was similar to the above except that provision was made to measure the weight of hold-up present in the test section during operation. Again this is impossible since the rig was already in situ.

Film conductance methods employ an electrical means to measure the conductance of a length of liquid film. It is necessary however for the film to flow over an insulator and also that an electrolyte be added to increase the conductivity. Both of the latter make this method unsuitable, firstly the cone is metal and secondly no contamination of the condensate was allowable.

(b) Localised methods.

A radio-active emission method was rejected because it meant contaminating the condensate with a radio-active salt. A radiation

detector would have to be situated near the cone surface, so that the amount of radiation detected would depend on the thickness of the radiating layer immediately below the detector. The condensate layer would absorb some of the radiation so that calibration might then present difficulties. The average film thickness could only be found so that for wave profile measurements some other method would have been needed. Jackson (15) employed this method and measured film thicknesses in the order of 1 mm with a precision of 0.1 mm or better.

A radio-active absorption technique was equally difficult to use since a radio-active source must be fixed into the surface and a detector placed such that the film flows between source and detector. Whilst the cone was rotating this would mean that the detector must rotate with the cone to obtain a continuous reading. This was not an insurmountable problem. However, the film thicknesses being dealt with which are in the order of 0.005 to 0.02 mm make the sensitivity of this method very suspect. A point in favour of this method is its comparative ease in setting up and calibrating. For a parallel beam of mono-energetic radiation

$$I = I_0 e^{-\mu \rho x} \quad A1$$

where  $I_0$  is the incident radiation intensity  
 $I$  is the intensity after absorption through liquid layer thickness  $x$   
 $\rho$  is the density of the fluid  
 $\mu$  is the mass absorption coefficient

Needle contact methods have often been used in the past with reasonable accuracy. The method is very simple, a needle is brought up against the film surface until contact is made. An electrical or optical means must be used to ascertain the exact point of contact. Measurement of the point of contact is then possible by micrometer. The surface over

which the fluid flowed acted as a reference and the needle moved forward for a second reading. The difference in the two readings is the film thickness. Wavy flow can be accommodated by using an electrical means. The needle approaching the film makes contact with the wave crests first so that intermittent contact occurs. If on contact an electrical circuit is made then a periodic signal will result. The reading from the micrometer provides the peak film thickness. Further advancement of the needle until continuous contact with the film occurs provides a micrometer reading from which the minimum film thickness can be found. Finally the needle is moved forward for a micrometer reading at the surface over which the liquid is flowing for a reference reading. This method was initially discarded because rotation of the surface against a stationary probe would produce disturbances, limited traverse of the probe could only be envisaged and thirdly measurement can only be made whilst advancing the probe because of the delay in contact breakage during withdrawal caused by surface tension force. Hewitt et al (74) have used this type of set up to observe annular two-phase flow. They report that there was a 'stretching' effect on breaking contact when observing waves.

Light absorption is another method used to measure film thickness. A beam of light was passed through the film from one side and the intensity of light detected on the other side. Charvonia (75) used this method in his work concerned with two-phase flow. It is of course a necessity of any such technique that the test section should be transparent. A recent development employing fibre optic techniques could possibly be adapted for our purpose. In a fibre optic bunch certain fibres are used to transmit light towards the film surface and in the same vicinity have fibres which receive light. When sending and receiving elements are in contact with the surface no light is reflected to the receiving element.

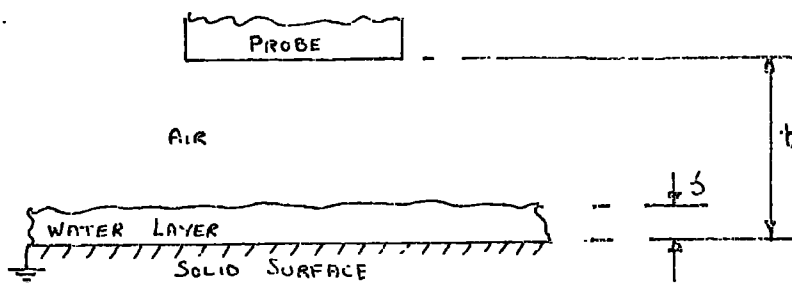
As the distance between the elements and the film surface increases the cone of light from the transmitting element illuminates an increasing area on the film. This area becomes, in effect, the source of a secondary cone of reflected light, which in turn increasingly illuminates the receiving element. This effect was linear for a certain distance depending on, shape of head and the number of fibres used. This type of set up could be perfectly feasible for laminar flow smooth film surfaces. However some detailed research would be necessary in the case of wavy flow. Also for rotating films in a steam environment extra care would be necessary in setting up the equipment. For these reasons this method was not considered practical at the present stage.

Photographic and shadowgraph techniques have been widely used and form a useful means of film thickness measurement in certain cases. Mainly useful in cases of flow on the outside of surfaces, Kapitza (10) employed a shadowgraph technique in his film flow studies. On the face of it this appears a useful method for measurement. However from earlier studies the film thicknesses encountered can not be greater than 0.1  $\mu$ . In the conditions which prevail, a photograph must be taken through a thick glass window, a condensate film on the inner glass surface plus a general blurring of the surface whilst the cone was rotating would make this method very difficult to operate.

A recently developed fluorescent spectrometer method uses a beam of light of a given wavelength which was directed into the liquid film. One drawback to this method was that a fluorescent dyestuff must be added to the liquid under test. The incident light then excited the fluorescent content so that an emission of a new frequency occurred. The quantity of fluorescent light emitted increased with increasing film thickness. The fluorescent light was separated from the reflected incident light by a spectrometer the resultant intensity was measured

with a photo-multiplier, this reading must be calibrated to give film thickness direct. To apply this type of measuring technique some method must be found to cater for the addition of the dyestuff under condensing conditions. Hewitt et al (76) describe the process fully and compare the results obtained with other techniques for two-phase water and air flows.

A further localised technique for film thickness measurement uses the change in capacitance due to dielectric thickness changes between two plates at different potentials. In practice the surface over which the liquid flows acts as one plate and a movable probe held directly above the surface as the other plate. The ability of the system to measure liquid film thickness depends on the very large difference between the relative permittivity of the two dielectrics involved, water and air. The system can be represented simply by the following arrangement,



the capacitance is given by

$$C = \frac{\epsilon_0 A}{\frac{(t-s)}{\epsilon_A} + \frac{s}{\epsilon_w}} \quad A2$$

where

$A$  is the area of the probe

$\epsilon_0$  is the permittivity of free space

$\epsilon_A$  and  $\epsilon_w$  are the relative permittivities of air and water respectively.

The values of  $\epsilon_w$  do not vary much for temperatures between 15 and 20°C, that is between 82.22 and 80.36 respectively. The relative permittivity

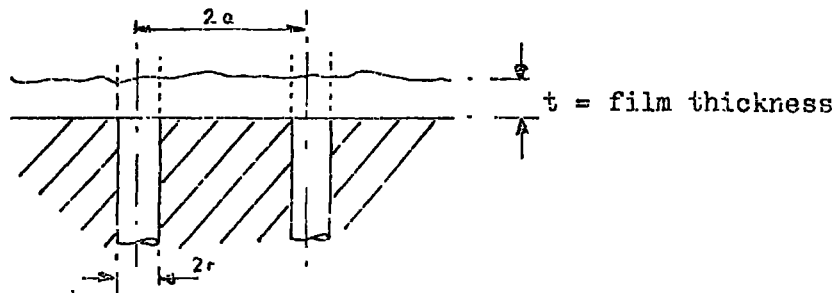
for air does not exceed 1.01. The potential difference across the capacitor varies inversely with capacitance thus the change in water film thickness is directly, and almost linearly, proportional to the potential difference. The probe must be made up in the form of a central area surrounded by a protecting annulus, this arrangement reduces 'fringing', so that the capacitance is as near linear as possible.

Calibration of the unit can be carried out by using slip gauges or an actual liquid film and a point method. This technique was developed further by Black (77) who employed commercially available equipment and was able to resolve wavelength measurements down to 125  $\mu\text{m}$  to an accuracy of  $\pm 0.075 \mu\text{m}$ . For shorter wavelengths a smaller probe would be necessary. The smaller probe would mean a loss in measuring sensitivity because the area of the probe is directly proportional to the capacitance. Holgate (36) employed this technique satisfactorily for his study of fluid flow on the surface of a  $60^\circ$  right cone. He noted that drops falling on the probe surface affected the readings obtained. The method was rejected for our particular application because mean film thickness only would result unless the probe rotated with the cone, an elaborate calibration programme would be necessary to allow for condensate temperature changes and also it would be difficult to prevent drops falling on the probe surface.

Measurement of liquid film thickness has been conveniently carried out using a conductivity device. The procedure was to monitor the change in conductance of a liquid layer flowing over two electrodes. The size of the electrodes and the distance apart determining the sensitivity to film thickness and wavelength measurement. The method employed by Van Rossum (78) was to measure the conductance of the liquid film between two thin platinum electrodes,  $60 \times 10 \text{ mm}$ , glued at a distance of 25 mm apart on the bottom of the channel which formed the apparatus

for studying entrainment, wave formation and atomization of horizontal liquid films. The device was calibrated using a point method for measuring the depth of a stagnant liquid over the electrodes.

Hewitt et al (74) develop a conductivity device having two 1.5 mm diameter stainless steel rods set in a perspex tube section. The device needed calibrating using another more direct measuring technique. Theoretically the system can be assumed to be two parallel infinitely long conductors, shown below, which project into the full thickness of the



film so that the current field can be obtained by using

$$G = \frac{\pi \nu}{\ln \left( \frac{a}{r} + \sqrt{\frac{a^2}{r^2} - 1} \right)} \quad A3$$

where  $G$  (mho/cm) is the conductivity per unit length between two parallel conductors of radius  $r$  and axial spacing  $2a$  in the homogeneous conducting medium of specific conductivity  $\nu$  (mho/cm). Then the conductivity in milli-mhos of a film of thickness  $t$  mm, is given by

$$Cd = \frac{3.1416 \times 10^{-3} t \nu}{\ln \left( \frac{a}{r} + \sqrt{\frac{a^2}{r^2} - 1} \right)} \quad A4$$

$$= \text{Constant} \times t \times \nu \quad A5$$

Since the gauge assumes two parallel conductors extending into the full film thickness, which in practice are flush with the surface, an end effect occurs which cannot be allowed for. Consequently in order to be used as a measuring device calibration is necessary. The conductance measured depends on the specific conductivity of the liquid which varies

with temperature. This must then be catered for in the design of a system. An advantage of this type of measuring technique is that it does not disturb the phenomena occurring naturally. This measuring technique was thought at this point to present the most promising method capable of being developed for our rotating system. The design procedure is given in Appendix B.

## Appendix B

### Film thickness gauge design

The initial design was based on the Hewitt et al (84) conductance measuring device. It consisted of a tufnol background, of 8 mm diameter, in which was located two stainless steel electrodes 2 mm diameter spaced 4 mm apart as shown in Figure 53. Tests showed that there was a consistent and repeatable relationship between the film thickness and the current flowing through the load resistor  $R_x$  shown in Figure 54. The current flowing was not measured, instead a valve voltmeter was used to monitor the potential drop across the load resistor  $R_x$ . This load resistor was chosen such that the maximum film thickness measured produced a full scale deflection of 10 mv.

A preliminary test, using distilled water, with the conductivity device connected to the rig however showed that earthing via the film to the cone surface reduced the sensitivity by half. It was also noted that this loss of sensitivity was dependant on film thickness which created a non-linear relationship between film thickness and current flow through the load resistor.

In the light of these observations a modified design was substituted. A central electrode located in the tufnol background, as shown in Figure 55, eliminated the parallel paths of the former design and used the earth path direct. The relationship between film thickness and potential difference across  $R_x$  is very similar to the former design a comparison is shown in Figure 56.

The final design employed a brand of tufnol which had an absorption rate of 0.2 milligrams per hour and a dielectric constant of 4.5. The diameter chosen was 3.17 mm this being the smallest acceptable machining size. A stainless steel wire 0.914 mm diameter was employed as the central electrode.

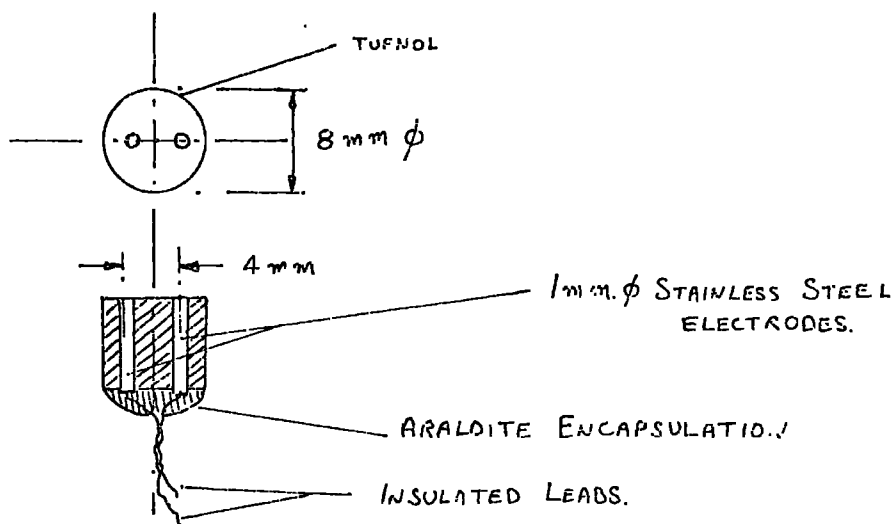


FIGURE 53 INITIAL CONDUCTIVITY FILM THICKNESS MEASURING GAUGE DESIGN.

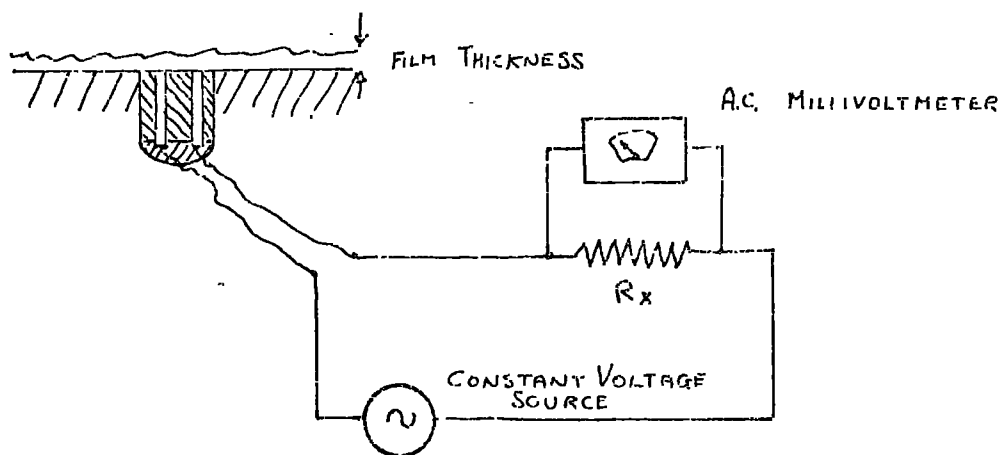


FIGURE 54 MEASURING CIRCUIT DIAGRAM.

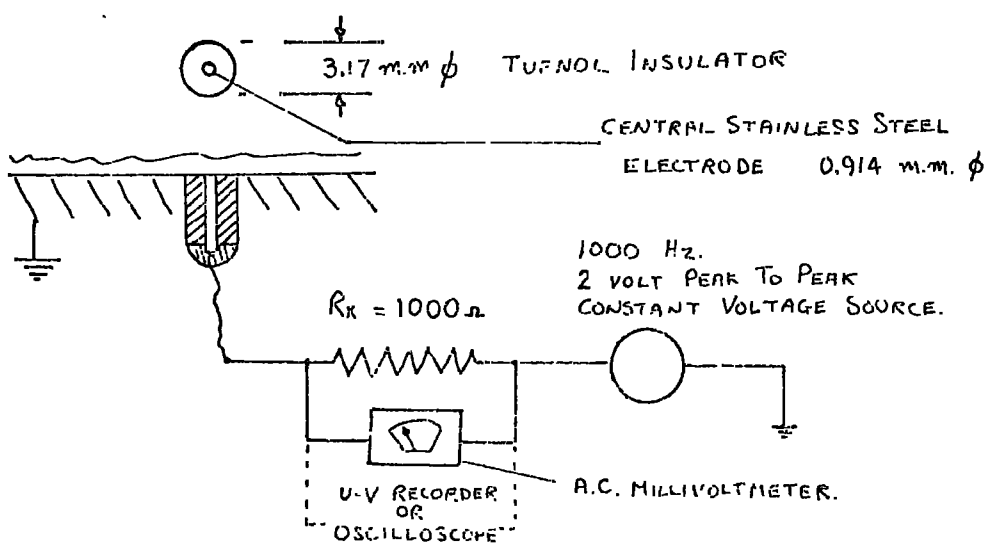


FIGURE 55. FINAL CONDUCTIVITY FILM THICKNESS MEASURING EQUIPMENT

A small test rig was designed and built to calibrate the conductivity device using the steam supply from the main rig. The calibration was necessary to allow for end effects and also the temperature variation of the condensate which occurs with increase of pressure. The small test rig consisted of a vessel having two parts. The steam was condensed in half of the vessel which also acted as a reservoir and the other half held the measuring equipment. The condensate flowed out of the reservoir along a channel and through a weir. The weir was a submerged one in which the condensate was allowed to build up to a predetermined level. The conductivity device was then held in the end of a probe which was immersed in the condensate flowing along the channel. The base of the channel was made of silica glass. The probe was held directly above the glass plate and could be traversed vertically by a micrometer head. The micrometer head is shown in Figure 57. The latter allowed the probe to be controlled distance from the glass plate. This then was a simulation of the actual measuring process, the condensate flows over the conductivity device and the steam surface was simulated by the glass plate.

Calibration was commenced by setting a steam pressure and allowing an initial cleaning through period and a settling down time for the condensate flow along the channel to reach a steady temperature. A test run consisted of measuring the condensate temperature, with a thermocouple situated just upstream of the probe, film thickness and complementary potential difference for a range of film thicknesses. The above procedure was repeated for condensate temperatures ranging from  $100^{\circ}\text{C}$  to  $150^{\circ}\text{C}$ .

The scatter of observations made in this way was other than could well be attributed to chance errors only and on general principles it seemed probable that there was a relationship between pH value and

## TESTS COMPLETED ON TAP WATER

—x—x—x— 1.6 V PEAK TO PEAK, 1000 SOURCE  
 RL = 1000  $\Omega$ , RE-DESIGNED VERSION.  
 —o—o—o— 1.0 V A.C. 50 Hz SOURCE  
 RL = 1000  $\Omega$ , INITIAL DESIGN.

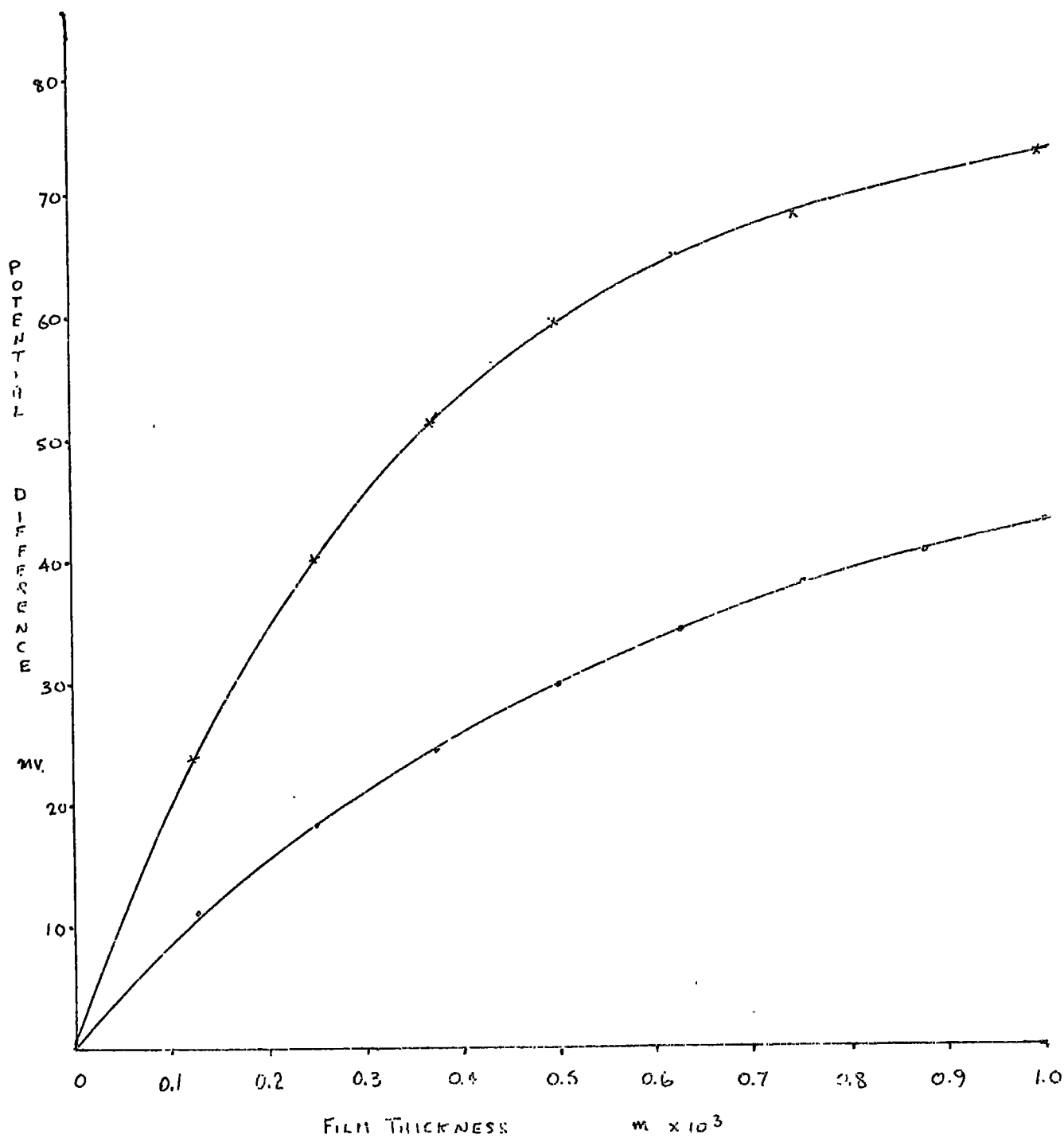
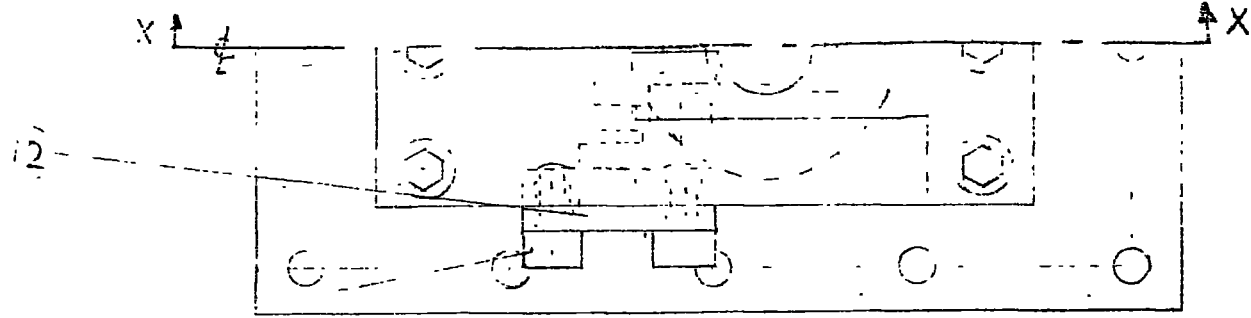
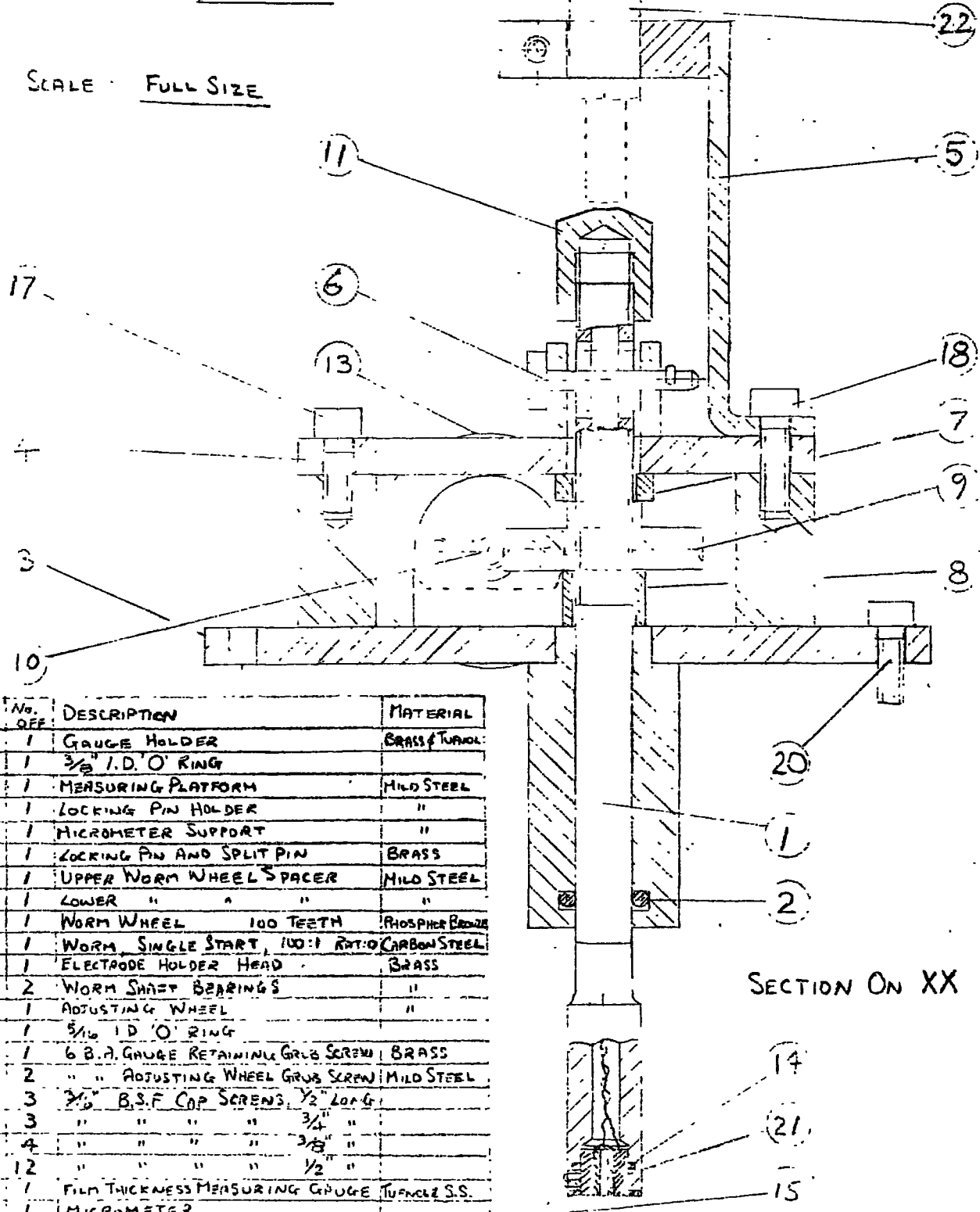


FIGURE 56 RELATIONSHIP BETWEEN FILM THICKNESS AND POTENTIAL DIFFERENCE.



19- HALF-PLAN

SCALE FULL SIZE



PART NO.	NO. OFF.	DESCRIPTION	MATERIAL
1	1	GAUGE HOLDER	BRASS & TURNOL
2	1	3/8" I.D. O' RING	
3	1	MEASURING PLATFORM	MILD STEEL
4	1	LOCKING PIN HOLDER	"
5	1	MICROMETER SUPPORT	"
6	1	LOCKING PIN AND SPLIT PIN	BRASS
7	1	UPPER WORM WHEEL SPACER	MILD STEEL
8	1	LOWER " " "	"
9	1	WORM WHEEL 100 TEETH	PHOSPHOR BRONZE
10	1	WORM, SINGLE START, 100:1 RPT. O	CARBON STEEL
11	1	ELECTRODE HOLDER HEAD	BRASS
12	2	WORM SHAFT BEARINGS	"
13	1	ADJUSTING WHEEL	"
14	1	5/16" I.D. O' RING	
15	1	6 B.A. GAUGE RETAINING GRUB SCREW	BRASS
16	2	" " ADJUSTING WHEEL GRUB SCREW	MILD STEEL
17	3	3/16" B.S.F. COP SCREWS 1/2" LONG	
18	3	" " " " 3/16" "	
19	4	" " " " 3/16" "	
20	12	" " " " 1/2" "	
21	1	FILM THICKNESS MEASURING GAUGE	TURNOLE S.S.
22	1	MICROMETER	

SECTION ON XX

FIGURE 57 TRAVERSING MECHANISM

the conductivity of the fluid under consideration. These relationships are :-

$$\log_{10} K = \log_{10} (\mathcal{A} \times d) - 3 - \frac{1}{2}pw \quad A6$$

where K is the conductance mho/cm

d is the density gm/cc

$\mathcal{A}$  is the equivalent conductance for distilled water

$$\begin{aligned} \mathcal{A} &= \mathcal{A}_{H^+} + \mathcal{A}_{OH^-} \\ &= 315.2 + 174 \end{aligned} \quad A7$$

pw is a variable related to the temperature (83)

The pH value is then given by  $\therefore \frac{1}{2}pw - \log_{10} d \quad A8$

Measured values of pH for the condensate varied from 5.8 to 6.6. Most of measurements were within  $\pm 0.1$  of 6.4. If the condensate were of pure water then at 20°C the pH value would have been 7.0. The difference in pH value indicated that some contamination was present in the condensate.

For film thickness measurement, using the conductivity devices, it would be necessary to take samples of condensate at regular intervals during an experimental run and check the pH value at a reference temperature of 20°C. If the pH value did not fall in the range of  $\pm 0.1$  to 6.4 the entire results would be discarded. The calibration curves were then drawn up for a pH value of 6.4  $\pm 0.1$ , using the mean of three conductivity devices, and are shown in Figure 58.

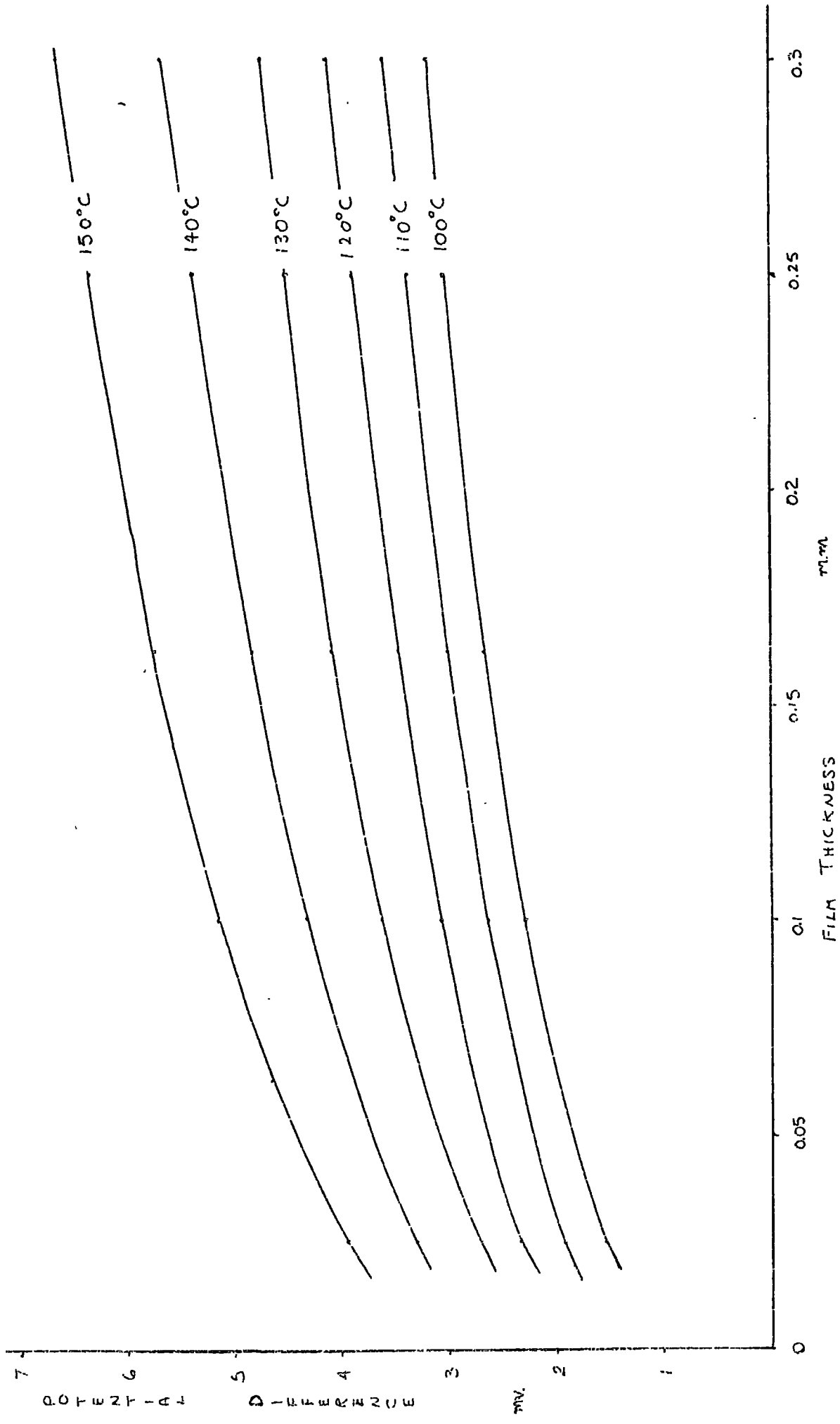


FIGURE 5B CALIBRATION CURVES FOR THE CONDUCTIVITY FILM THICKNESS MEASURING GAUGE

APPENDIX C

Variation of  $\bar{\epsilon}$

Nusselt has shown that the film thickness varies as a function of  $X^{\frac{1}{4}}$ . Thus changes are of small order and may be assumed to obey the following law

$$\bar{\delta} = \text{Constant}(1 + \bar{\epsilon} \bar{X}) \quad A9$$

Differentiating we obtain

$$\frac{\partial \bar{\delta}}{\partial \bar{X}} = \text{Constant} \cdot \bar{\epsilon}$$

If  $\bar{\epsilon}$  is small then the constant becomes  $\bar{\delta}$ , requiring

$$\frac{\partial \bar{\delta}}{\partial \bar{X}} = \bar{\epsilon} \bar{\delta} \quad A10$$

A mass balance over one wavelength requires that

$$\frac{\partial}{\partial X} \int_0^\lambda \int_0^{\bar{\delta}} V_x dY R d\theta dX = \int_0^\lambda \frac{k \Delta T R d\theta dX}{\rho h_{fg} \bar{\delta}} \quad A11$$

Substituting  $\frac{\bar{\delta}^3 \rho a_x}{3\mu}$  for  $\int_0^{\bar{\delta}} V_x dY$  into the above equation one obtains

$$\frac{\partial}{\partial X} \int_0^\lambda \frac{\bar{\delta}^3 \rho a_x R d\theta}{3\mu} = \int_0^\lambda \frac{k \Delta T R d\theta}{\rho h_{fg} \bar{\delta}} \quad A12$$

Operating on the lefthand side of the equation :-

$$\frac{\partial}{\partial X} \int_0^\lambda \frac{\bar{\delta}^3 \rho}{3\mu} (\omega^2 R \sin \beta + g \cos \beta) X \cdot \sin \beta d\theta$$

Performing the differentiation

$$\int_0^\lambda \left[ \frac{\bar{\delta}^3 \rho}{3\mu} (2\omega^2 X \sin^2 \beta + g \cos \beta \sin \beta) + \bar{\delta}^2 \rho a_x R \frac{\partial \bar{\delta}}{\partial X} \right] d\theta$$

Then :-  $\int_0^\lambda \left[ \frac{\bar{\delta}^3 \rho}{3\mu} (2\omega^2 \sin \beta + g \frac{\cos \beta}{X}) + \frac{\bar{\delta}^2 \rho a_x}{\mu} \frac{\partial \bar{\delta}}{\partial X} \right] d\theta = \int_0^\lambda \frac{k \Delta T \cdot d\theta}{\rho h_{fg} \bar{\delta}}$

Putting into non-dimensional form employing equations in 3.8.5

$$\int_0^{\bar{\lambda}} \left[ \frac{\bar{\delta}^3 \bar{\delta}_{MIN} \rho}{3\mu} (2\omega^2 \sin \beta + g \frac{\cos \beta \cdot \sin \beta \cdot \rho \cdot a_x \cdot \bar{\delta}_{MIN}}{\bar{X} \sigma a_x}) + \left( \frac{\bar{\delta}^2 \bar{\delta}_{MIN} \rho}{\mu} \frac{\partial \bar{\delta}}{\partial \bar{X}} \frac{a_x \bar{\delta}_{MIN} \sin \beta}{\sigma a_x} \frac{\rho a_x \bar{\delta}_{MIN}}{\sigma a_x} \right) \right] d\bar{\theta} (\sigma a_x)^{\frac{1}{2}} \frac{1}{R}$$

$$= \int_0^{\bar{\lambda}} \frac{k \Delta T \cdot d\bar{\theta}}{\rho h_{fg} \bar{\delta} \bar{\delta}_{MIN}} (\sigma a_x)^{\frac{1}{2}} \frac{1}{R}$$

Simplifying and replacing the term  $\frac{k \Delta T \sigma \mu}{\rho^2 a_x^2 \bar{\delta}_{MIN}^2 h_{fg}}$  by  $\Lambda$  gives

$$\int_0^{\bar{\lambda}} \left[ \frac{\bar{\delta}^3}{3} \left( \frac{2\omega^2 \sin \beta \sigma}{\rho a_x^2 \bar{\delta}_{MIN}} + g \frac{\cos \beta \sin \beta}{\bar{X} a_x} \right) + \bar{\delta}^2 \frac{\partial \bar{\delta}}{\partial \bar{X}} \right] d\bar{\theta} = \Lambda \int_0^{\bar{\lambda}} \frac{d\bar{\theta}}{\bar{\delta}} \quad A13$$

Substituting A10 into A13

$$\int_0^{\bar{\lambda}} \left[ \frac{\bar{\delta}^3}{3} \left( \frac{2\omega^2 \sin \beta \sigma}{\rho a_x^2 \bar{\delta}_{MIN}} + g \frac{\cos \beta \sin \beta}{\bar{X} a_x} \right) + \bar{\delta}^3 \bar{\epsilon} \right] d\bar{\theta} = \Lambda \int_0^{\bar{\lambda}} \frac{d\bar{\theta}}{\bar{\delta}}$$

Rearranging to obtain  $\bar{\epsilon}$ ,

$$\bar{\epsilon} = \frac{\Lambda \int_0^{\bar{\lambda}} \frac{d\bar{\theta}}{\bar{\delta}} - \frac{1}{\bar{X}} \int_0^{\bar{\lambda}} \frac{\bar{\delta}^3}{3} \left( \frac{2\omega^2 \bar{X} \sin \beta \sigma}{\rho a_x^2 \bar{\delta}_{MIN}} + \frac{g \cos \beta \sin \beta}{a_x} \right) d\bar{\theta}}{\int_0^{\bar{\lambda}} \bar{\delta}^{-3} d\bar{\theta}}$$

Since we have already assumed that changes in the 'X' direction are small and the terms inside the bracket are small compared with the others then the second term in the top line of the equation will be neglected. Thus the term,  $\mathcal{E}$ , becomes

$$\mathcal{E} = \frac{\Lambda \int^{\lambda} \frac{d\bar{\theta}}{\bar{z}}}{\int^{\lambda} \bar{z}^3 d\bar{\theta}} \quad \text{A14}$$

A computer programme was set up to calculate the value of the constant,  $\mathcal{E}$ , to produce a cyclic condition. This procedure consisted of guessing a value of  $\mathcal{E}$  running the Continuous Systems Modelling Programme and then using equation A14 to calculate a new value of  $\mathcal{E}$ . A convergent technique was set up and when the operations produced a final value of  $\bar{z}$  to within  $\pm 0.1\%$  of the starting value of 1.0, was accepted. The above procedure was repeated for a variety of values of  $\Lambda$  to be used in a procedure to correlate the experimental data, described in Appendix D. The values of  $\mathcal{E}$  are given in Table A1.

It is appropriate at this point to note that the constant  $\mathcal{E}$  is not in any way connected with the coriolis term considered in the general equation,  $2 V_x \omega \sin \beta$ . Thus in any subsequent analysis it will be assumed that  $\mathcal{E}$  is not a function of  $\Theta$ .

Table A1

$\Lambda$	$\mathcal{E}$
8.0	0.00917
4.5	0.0112
3.5	0.013
2.72	0.0152
1.65	0.0203
1.00	0.0256
0.6065	0.0321
0.368	0.0389
0.2865	0.042
0.223	0.0445
0.2	0.0452
0.05	0.046
0.02	0.0462

Appendix D

Numerical solution of the governing equation.

The I.B.M. package, the Continuous Systems Modelling Programme (C.S.M.P), was employed to solve the final equation, 3.8.13. This programme is a scientific routine which is capable of solving differential equations numerically using Runge-Kutta, Milne or Simpson step-wise procedures. The solution was obtained using the Runge-Kutta predictor-corrector technique in this particular case. The C.S.M.P. module allowed the complete solution including the mathematical manipulations of the results within itself. The instructions being written in Fortran iv language.

The Runge-Kutta Fourth order process was the numerical method chosen within the C.S.M.P. module. The solution is basically for single first order equations of the form

$$y' = f(x,y) \quad A15$$

or sets of first order equations; hence it may be used for equations of higher order, which can always be represented as a set of first order equations. In advancing one step the function  $f(x,y)$  is computed at a number of intermediate points, the choice of which is to some extent arbitrary. If the point  $x$  has been reached with

$$y(x) = y$$

we calculate in succession the quantities

$$k_0 = h f(x,y)$$

$$k_1 = h f(x + \frac{1}{2}h, y + \frac{1}{2}k_0)$$

$$k_2 = h f(x + \frac{1}{2}h, y + \frac{1}{2}k_1)$$

$$k_3 = h f(x + h, y + k_2)$$

then

$$y(x + h) = y(x) + (k_0 + 2k_1 + 2k_2 + k_3)/6$$

with an error in the order of  $h^5$ . Thus a step length,  $h$ , as small

as possible reduces errors to a minimum. The known starting values must be entered but no special starting procedure is required in the programme.

The C.S.M.P. module is fully described in a technical manual (85), but for solution of our equation it consists of the following :-

- (i) An Initial Section, which allows the governing parameters, physical properties and general algorithms to be set up.
- (ii) The Dynamic Section, in which the governing equation is set out in the form of single order equations. Each of these must be given boundary conditions to act as a starting point.
- (iii) The Terminal Section, which may be used to perform various operations on results obtained from the Dynamic Section. It can also be used to calculate any other relevant quantities and print them out in a convenient form.
- (iv) In order to run the programme the step length, method of solution and duration of run must be given.

The C.S.M.P. module itself is much more comprehensive and that described above is limited to the use made of it in this thesis.

In the text the programme has been employed in two ways. In the theoretical section a parameter variation was examined. Whilst in the discussion an attempt was made to predict theoretically, using some of the experimental data as a check, wavelength, minimum film thickness and heat transfer coefficients. For the former, values of  $\Lambda$  were chosen and in the Initial Section both  $\Theta$  and  $\Omega$  were calculated and then employed directly in the Dynamic Section. The terminal section was not necessary in this case and a direct print out of the surface profile plus the first three derivatives was obtained for the run time. The run time was long enough to cover all the wavelengths produced for the range of  $\Lambda$  chosen. The results are given in Figures 6 and 7.

The second use of the programme was more complex. In the Initial Section all the physical properties required calculating so that all experimental data had to be read into the storage space available in the system. The parameters and algorithms were set up for a special use of the Dynamic and Terminal Sections. The Dynamic Section was the same as the previous one except that the boundary conditions were given variable names. This was to allow the solution over one wavelength to proceed in small steps. In the Terminal Section a procedure was set up to solve the equation in short steps until the maximum value of  $\zeta$  was found which then corresponds to the half wavelength. Because a measurement of film thickness was not available it was decided to use the experimental results in a convergence technique. Two methods were considered

- (i) Employment of the experimental heat flux. A value of  $\Lambda$  was assumed, starting at 0.02, then the other parameters  $\Theta$  and  $\Omega$  were calculated from this value and the experimental data. Equation 3.8.13 was solved as previously until the half wavelength was found. The results were used to calculate a mean heat transfer coefficient and hence the heat flux. The experimental heat flux was calculated and the two compared. If these were within  $\pm 5\%$  of each other the value of  $\Lambda$  assumed was considered to be correct for that particular solution. The large convergence error was tolerated because the experimental error involved is large, up to  $\pm 7\%$ , and also to obtain closer accuracy required more computing time than was available. If the two values were not within  $\pm 5\%$  of each other a convergence factor was applied to the original guess of  $\Lambda$  and the process repeated until the heat fluxes were within the required tolerance.

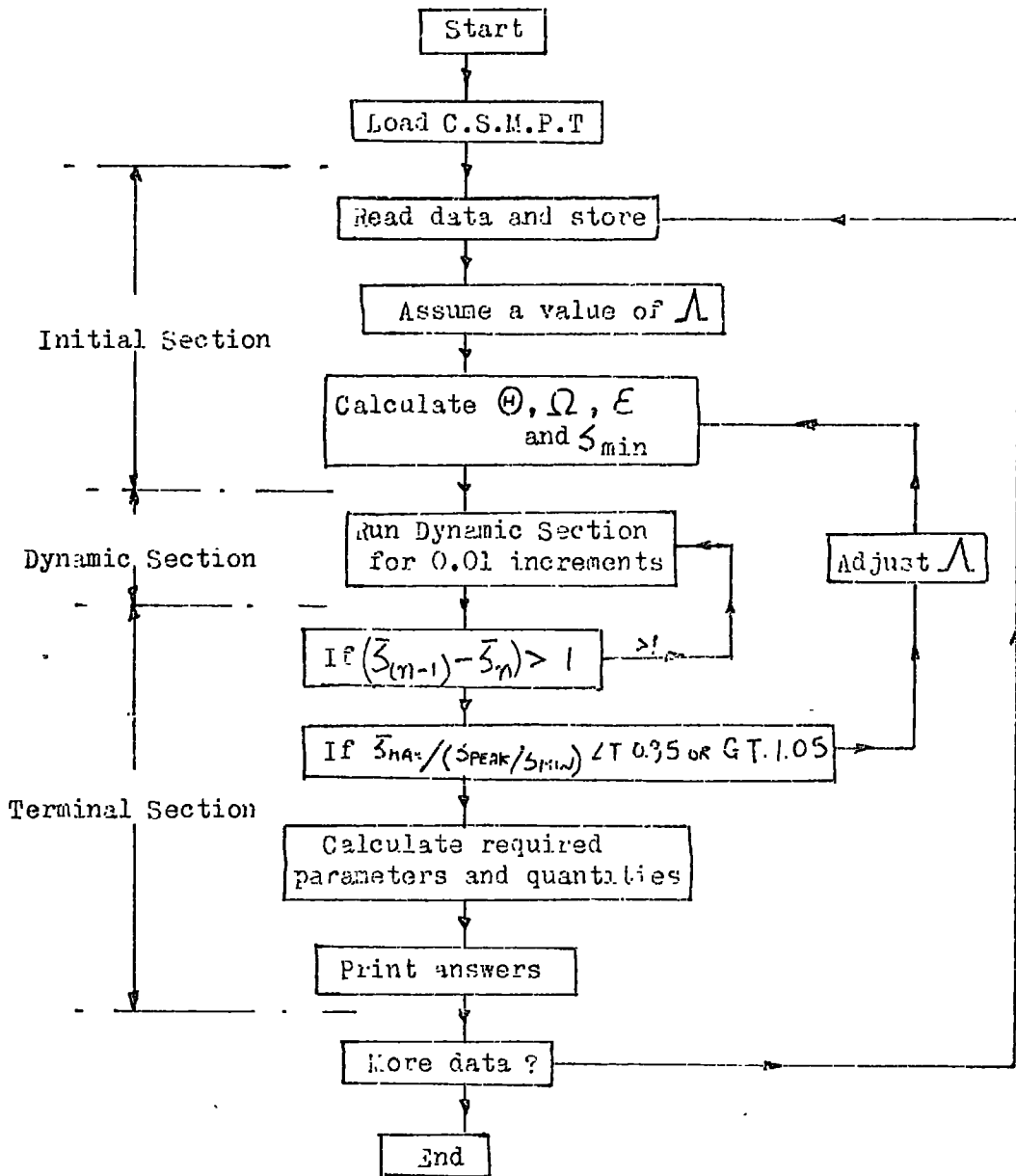
(ii) Employment of the measured peak film thickness. As before a value of  $\Lambda$  was assumed,  $\Theta$  and  $\Omega$  calculated and equation 3.8.13 solved for half a wavelength. The maximum non-dimensional film thickness,  $\bar{\delta}_{\max}$ , was thus obtained directly. A value of minimum film thickness,  $\delta_{\min}$ , was calculated from the assumed value of  $\Lambda$ . The measured peak film thickness was then divided by the calculated value of  $\delta_{\min}$  and the ratio compared with  $\bar{\delta}_{\max}$ . If the two were within  $\pm 5\%$ , for the same reasons as in (i), then the solution was assumed correct for the given value of  $\Lambda$ . Again if the two were not within  $\pm 5\%$  the value of  $\Lambda$  was modified until convergence was obtained.

The two methods were necessary because when employing the heat flux version convergence was very slow and also at low rotational speed would not converge. This was due to the large experimental error in the heat flux which took the convergence factor well outside its range. The programme has a 'switch' built in which allows either mode to be run. The results quoted are for method (ii) which was found to be the most satisfactory.

In the Terminal Section, once a solution to equation 3.8.13 had been obtained, the various non-dimensional groups were calculated, together with, heat transfer coefficients, laminar film thickness by solving equation 2.5.58, and the angle the ridge makes with the cone generator.

The programme and run instructions are given in the following pages :-

Flow diagram for computer programme using film thickness as converging factor.



The programme using heat flux as a convergence factor is very similar except that the second 'If' statement is replaced by:

IF  $\phi_{THEORET} / \phi_{EXP.} < 0.95$  OR  $> 1.05$

W=BEAUTY T=9  
ON WAS: 15:05.50 06-05-73  
SIGNED ON AT 15:11.40 ON 06-05-73  
DAT

SUBROUTINE UPDATE

COMMON ZZ9901(5), IZ9901, ZZ9902, IZ9902, ZZ9903, IZ9903, ZZ9991(54)

COMMON TIME

1, DELT , DELMIN, FINTIM, PDEL , CUTDEL, T3 , T2 , T1 , T  
2, T4 , ZZ0010, ZZ0011, ZZ0012, B3 , B2 , B1 , B0 , AGG  
1, REND , HTC , HAV , HA , X , TI , J , KOUNT , DOG  
1, K , TD , TAV , HFG , C , V , D , B , AL  
1, BB , TDW , TDWA , CC , CF , CFX , CP , AG , LI  
1, L2 , CCN , HMINC , RCT , CCR , ST , CMEGA , TH , I  
1, ZZ0004, AC , ZZ0007, AREA , R2 , R1 , CC , RNL , WAV  
1, WAVE , ERRW , AR , Q , CC , CCG , FTMIN , FTMAX , ERR  
1, HAVC , RE , VPE , RA , RNUC , E , DL , FN , FI

COMMON F2

1, F3 , XL , AML4 , GAM , FE , FLAM , RHH , HMIN , HMEAN  
1, L4 , VX , VXM , C , E1 , E2 , E3 , VO , TAN  
1, WE , WEH , VEL , RRA , RNLX , RNUP , RCS , CTC , FM  
1, HMW , HMY , HMX , HFGL , FR , REVXM , PAK , PAKM , PKM  
1, WN , WL , IZ0001, IZ0002, IZ0003

COMMON AX ( 13 )  
COMMON CX ( 13 )  
COMMON A ( 9 )

COMMON ZZ9992(7841), NALAPM, IZ9992, ZZ9994(437), KEEP, ZZ9995(489)  
\*, IZ0000, ZZ9996(224), IZ9997, IZ9998, ZZ9999( 640)

INTEGER BB

1, DCG , RDNC

DIMENSION XD(2500), HP(100), IHP(100)

107 FORMAT(/, 3X, 'WAVELENGTH', 5X, 'SAT. TEMP', 2X, 'SLR. TEMP', 5X, 'RPN', 5X, 'CONE ANGLE', 5X, 'FMAX', 7X, 'TAV')

96 FORMAT(/, 4X, 'Q(KW)TH', 5X, 'FLUX(TH)', 5X, 'Q(MFAS)', 3X, 'FLUX(MEAS)', 4X, 'HTC(TH)', 5X, 'HTC(MEAS)')

101 FORMAT(/, 5X, 'TD', 10X, 'TAV', 9X, 'TDW', 8X, 'TDWA', 5X, 'M.TH.COND', 5X, 'AREA')

202 FORMAT(/, 2X, 'NUSSLEI NO. (HX/K)', 2X, 'NUSSLEI NO. (TH.)', 5X, 'RAYLEIGH NO.', 5X, 'EST. FLOW VEL')

GO TO(39995, 39996, 39997, 39998), IZ0000

C SYSTEM SEGMENT OF MODEL

39995 CONTINUE

IZ9992= 160  
IZ9997= 4  
IZ9998= 124  
IZ0001= 125  
IZ0002= 138  
IZ0003= 151

READ(5, 39990)(ZZ9999(IZ9999), IZ9999=1, 2)(C)

39990 FORMAT(18A4)

IZ9901= 550019  
IZ9902= 1210056  
IZ9903= 216  
GO TO 39999

C INITIAL SEGMENT OF MODEL

39996 CONTINUE

IF(L1.EQ.2)DCG=3  
IF(KOUNT.EQ.2)GO TO 7  
IF(HAV.GT.HTC.AND.KOUNT.EQ.1)DCG=3  
IF(A(4).LT.220.C.AND.REND.EQ.1)TH=0.000076  
IF(DCG.EQ.3)GO TO 82

```

AC=ACG*(HTC/HAV)*1.2
GC TO 81
82 IF(A(6)/TH.LT.1.2)GC TO 8
AC=ACG*A(6)*1.2/TH
GC TO 81
8 AC=ACG*A(6)*1.05/TH
81 RCNC=RCNC+1
IF(AC.LT.C.C2)AG=0.02
IF(KCUNT.EQ.2.AND.DCG.EQ.1)AG=ACG*HR(BB-2)*1.2
IF(DCG.EQ.3.AND.KCUNT.EQ.2)AG=ACG*THD(K-2)*1.2
IF(DCG.EQ.3.AND.KCUNT.EQ.2.AND.TH(D(K-2).LT.1.2)AG=ACG*THD(K-2)*1.0
IF(RCNC.CT.2)GC TO 6
TD=A(2)-A(3)
TAV=A(3)+0.25*TC
HFG=2557.48-2.7736*A(2)+0.01195*A(2)**2-C.00004312*A(2)**3
C=(554.42+2.2608*TAV-0.011958*TAV**2+C.00001586*TAV**3)*0.000001
V=(924.14-11.0834*TAV+0.05733*TAV**2-C.00010944*TAV**3)*0.000001
ST=(78.777-C.21655*TAV+C.0002688*TAV**2-C.0000010545*TAV**3)*0.001
D=1028.64-0.806482*TAV+0.00218368*TAV**2-C.0000118156*TAV**3
P=A(5)/57.296
AL=A(8)/57.296
TDW=A(3)-A(7)
TDWA=(A(3)+A(7))/2
CC=80.6+0.121*TDWA
OMEGA=2.0*3.14159*A(4)/60
CF=(2*3.14159*A(4)/60)**2*A(9)*COS(B)-9.81*SIN(B)
CFX=(2*3.14159*A(4)/60.0)**2*A(9)*SIN(B)+9.81*CCS(B)
CP=1.4444-0.0003862*TAV+C.0000023805*TAV**2
CP=EXP(CP)
6 IF(TI.CT.0.0)GC TO 7
WRITE(6,333)AO
333 FORMAT(F10.7)
AG=ALOG(AO)
DO 1 I=1,13
IF(AX(I)-AG)1,3,47
1 CONTINUE
2 CCN=CX(I)
GC TO 5
47 CCN=CX(I-1)+(CX(I)-CX(I-1))*(AX(I-1)-AG)/(AX(I-1)-AX(I))
5 HMINC=(C*ST*TD*V/(D**3*CF**2*HFG*AO*(1+0.375*CP*TD/HFG)))*0.2
ROT=((2.0*3.14159*A(4)/60.0)**2*ST*SIN(B)**2)/(HMINC+D*CF**2)
COR=HMINC*6.28318*A(4)*SIN(B)*CFX*(ST*D)**0.5/(V*60.0*CF**1.5)
7 CONTINUE
GC TO 39999
C DYNAMIC SEGMENT OF MODEL
39997 CONTINUE
T4=-3*T1*T3/T-T2-3*T1**2/T+3*AC/T**4-CCN+T*T1*10.0*CCR/3.0-RCT/T
C T3 =INTGRL (B3 ,T4 )
C T2 =INTGRL (B2 ,T3 )
C T1 =INTGRL (B1 ,T2 )
C T =INTGRL (B0 ,T1 )
ZZC010=T3
ZZC011=T2
ZZC012=T1
GO TO 39999
C TERMINAL SEGMENT OF MODEL
39998 CONTINUE
IF(T X)50,61,51
51 B3=T3
B2=T2

```

```

B1=TI
B0=T
TI=TI+0.02
HA=HA+C*C.C4/((T+X)*HMINC)
X=T
IF(KCUNT.GT.1)GC TC 69
GO TO 70
69 XC(J)=TI
XC(J+1)=B0
XC(J+2)=B1
XC(J+3)=B2
XC(J+4)=B3
J=J+5
70 CONTINUE
IF(RCNC.GT.14000)GC TO 66
IF(TI.GT.13.0)GC TC 63
IF(TI.GT.13.0.AND.DCG.FC.3)GC TC 74
CALL RERUN
GC TC 64
61 IF(TI.LT.1.0)GC TC 51
39 IF(DCG.EQ.2)AD=0.02
IF(DCG.EQ.2)DCG=DCG+i
50 IF(DCG.GT.1.AND.TI.LT.13.0)GC TC 38
IF(TI.GT.13.0)GC TC 68
GO TO 59
38 TH=T*HMINC
THD(K)=A(6)/TH
K=K+1
IF(A(6)/TH.GT.1.03)GC TC 62
IF(A(6)/TH.LT.0.95)GC TC 62
GC TC 63
59 HAV=HA*1000/TI
IF(A(5).EQ.5.0)GC TC 42
AREA=3.14159*0.265*(2.0+SIN(P))*0.18
GC TO 42
42 AREA=3.14159*0.2465*(2.0+SIN(B))*0.18
43 IF(A(5).EQ.5.0)GC TC 44
P2=0.265+0.09*SIN(P)
R1=R2-0.0172
GC TO 45
44 R2=0.2465+0.09*SIN(P)
R1=R2-0.0172
45 QC=2*3.14159*CC*TDW*C.18/ALCG(R2/R1)
HTC=CC/(AREA*TC)
HR(BB)=HTC/FAV
BB=BB+1
IF(RCNC.GT.14000)GC TO 66
IF(HAV/HTC.GT.1.01)GC TC 62
IF(HAV/HTC.LT.0.99)GC TC 62
GO TO 63
62 WRITE(6,1002)R2,P2,B1,BC,TI,AC
IF(L2.EQ.3)GC TC 71
IF(A(6)/TH.LT.0.95.AND.KCUNT.EQ.1)GO TO 26
GO TO 68
26 L2=L2+1
WRITE(6,1114)
1114 FORMAT(20HTH GREATER THAN A(6))
GO TO 63
1002 FORMAT(6F13.5)
68 R3=0.0

```

```

B2=0.0
B1=0.0
B0=1.0
T1=0.0
HA=0.0
IF(KCUNT.GT.1)GC TO 67
ACC=AD
IF(ACC.GT.10.0)GC TO 63
67 X=1.0
IF(DCG.EQ.3)WRITE(6,1112)A(6),TH,HMINC,RCNC,ACC
IF(DCG.EQ.2)WRITE(6,1112)HTC,HAV,HMIRC,RCNC,ACC
WRITE(6,1112)CCR,RCT,CCN,ACC
1113 FORMAT(4F10.6)
1112 FORMAT(2F15.8,18,F15.8)
CALL RERUN
GC TO 64
66 WRITE(6,1111)
1111 FORMAT(/,'RANG OUT OF RANGE',/)
IF(RCNC.GT.1400.AND.TH.GT.A(6).AND.KCUNT.EQ.1)GC TO 1191
GC TO 63
1191 KCUNT=KCUNT+1
RCNC=RCNC-2000
XD(2)=1.0
GC TO 1195
63 WRITE(6,1001)TI,X,HAV,HTC,RCNC
IF(RCNC.LT.1400)GC TO 64
IF(T1.LT.13.0)DCG=DCG+1
IF(ACC.GT.10.0)DCG=DCG+1.0
IF(DCG.EQ.2)GC TO 69
1001 FORMAT(4F14.5,18)
WRITE(6,1005)
WRITE(6,1004)AC,CCR,RCT,CCN
1004 FORMAT(4F14.6)
1005 FORMAT(/,6X,'AC',11X,'CCR',11X,'RCT',11X,'CCN')
XD(2)=1.0
IF(KCUNT.GT.1)GC TO 71
KCUNT=KCUNT+1
IF(L2.EQ.2)L2=3
1195 XD(1)=0.0
XD(3)=0.0
XD(4)=0.0
XD(5)=0.0
GC TO 68
74 WRITE(6,1110)
1110 FORMAT(/,'WAVELENGTH OUT OF RANGE')
GC TO 64
71 WRITE(6,1115)
1115 FORMAT(7HRESULTS)
WRITE(6,1005)
WRITE(6,1004)AC,CCR,RCT,CCN
BB=TI/0.02
L1=5*BB
HAV=0
PNL=0
L2=L1-8
WAV=A(1)+0.5/(ST/(C*CF))*0.5
WAVF=BB*0.02
ERPW=(WAVF*WAV)*100.0/WAVF
DO 41 I=2,L2,5
AR=C*2.0*0.02*1000.0/(HMINC*WAVF*(XD(I)+XD(I+5)))

```

```

HAV=HAV+AR
RNU=RNU+2.0*XO(L1-3)*(1/XO(I)+1/XO(I+5))*0.02/WAVF
41 CONTINUE
IF(A(5).EQ.5.0)GC TO 2
AREA=3.14159*C.265*(2.0+SIN(B))*0.18
GO TO 93
2 AREA=3.14159*0.2465*(2.0+SIN(B))*0.18
83 C=HAV*TD*AREA
QQ=Q/AREA
IF(A(5).EQ.5.0)GC TO 4
R2=0.265+C.09*SIN(B)
R1=R2-C.0175
GO TO 85
4 R2=0.2465+C.09*SIN(B)
R1=R2-C.0172
85 QC=2*3.14159*CC*TDW*C.18/ALOG(P2/R1)
QQC=QC/AREA
HTMIN=C*1000.0/HTINC
HTMAX=C*1000.0/A(6)
CFX=(CMEGA)**2*A(9)*SIN(B)+9.81*COS(B)
ERR=(QC-Q)*100.0/QC
HAVC=QQC/TC
PE=3.0*COS(B)*A(6)*HAV*TC*CCS(AL)/(HFG*V*1000.0)
VRE=PE*V/(A(6)*D)
RA=CF/CFX
RNUC=HAV*0.09*0.001/C
WRITE(6,707)
WRITE(6,106)(A(I),I=1,7)
106 FORMAT(7E12.4)
WRITE(6,708)
105 FORMAT(/,6X,'AY',12X,'AX',10X,'AY/AX',9X,'RE',9X,'NCND. H')
WRITE(6,104)CF,CFX,RA,RE,XO(L1-3)
104 FORMAT(5E13.5)
WRITE(6,101)
WRITE(6,95)TD,TAV,TDW,TCWA,CC,AREA
95 FORMAT(6E12.4)
WRITE(6,96)
WRITE(6,93)Q,QQ,CC,QQC,HAV,HAVC
WRITE(6,102)
93 FORMAT(6E12.4)
WRITE(6,97)AC,WAV,ERR,ERRW
97 FORMAT(4F10.4)
102 FORMAT(/,4X,'AC',5X,'NCN-DIM W',3X,'HTC ERR',2X,'N.D.W ERR')
E=9.81*COS(B)/((CMEGA)**2*SIN(B)**2)
DL=C.09/(100.0*E)
IF(A(5).EQ.5.0)GC TO 29
X=0.265/(SIN(B)*E)
GO TO 30
29 X=0.2465/(SIN(B)*E)
30 FN=0
DO 31 I=1,50
F1=X**1.333333*(X+1)**0.333333
F2=(X+DL)**1.333333*(X+DL+1)**0.333333
F3=(X+2*DL)**1.333333*(X+2*DL+1)**0.333333
FN=FN+DL*(F1+F2+4.0+F3)/3.0
X=X+DL*2.0
31 CONTINUE
XL=X**1.333333*(X+1)**0.333333
WRITE(6,122)P,DL,X,XL,E
122 FORMAT(5E12.4)

```

```

AML4=1.333333*FN/XL
GAM=(V/(D*3.14159*2.0*A(4)*SIN(B)/6C))*0.5
CP=1.4444-0.0003862*TAV+0.000033806*TAV**2
CP=EXP(CP)
WRITE(6,123)AML4,GAM,CP,FN
123 FORMAT(4E12.4)
EE=(TD*3.0*C/(V*(HFG+0.275*CP*TD)))*0.25
HLAM=AML4**C.25*GAM*EE
RHH=A(6)/HMINC
HMIN=A(6)/XC(L1-3)
HMINC=(C*ST*TD+V/(C**3*CF**2*HFG*AO*(1+0.375*CP*TD/HFG)))*0.2
HMFAN=0
DO 28 I=2,L2,5
HMEAN=HMEAN+(XC(I)+XC(I+5))*0.02*A(6)/(WAVF*2.0*XC(L1-3))
28 CONTINUE
WRITE(6,112)
WRITE(6,110)HLAM,HMIN,A(6),HMEAN,RHH
WRITE(6,100)
WRITE(6,113)
WRITE(6,111)EE,GAM,E
111 FORMAT(3E13.5)
110 FORMAT(5E13.5)
112 FORMAT(4X,'HLAM',9X,'HMIN',9X,'HPEAK',9X,'HMEAN',8X,7HF/HMIN)
113 FORMAT(/,3X,'NCNC**1/4',5X,'C/SINB*W',5X,'NCNC. E')
L4=L1-2
DO 10 K=143,L4,5
IF(XC(K)-XC(K+5))10,11,11
10 CONTINUE
11 VX=D*CFX*A(6)**2*XC(K-1)**2/(XC(L)-3)**2*3.0*V)
VXI=D*CFX*A(6)**2/(3.0*V)
Q=(ST/(CF*D))*0.5/A(9)
WRITE(6,103)
E1=A(6)**2*D*CF*XC(K)*HMIN/(3.0*V*A(9)*C)
E2=A(6)**2*ST*XC(K+2)*HMIN/(3.0*V*A(9)**3*Q**3)
E3=-A(6)**4*D**2*OMEGA*SIN(B)*CFX/(3*V**2)
VC=E1+E2+E3
TAN=VQ/VX
WE=D*OMEGA**2*A(9)**3/ST*2
WEF=VXM**2*HMEAN*D/ST
VEL=QQC*0.09/(HFG*C*HMEAN*1000)
RRA=CF*C**2*HFG*C**3*A(9)**2/(C*V*TD)
RNUX=HAV*A(9)/(C*1000)
RNUR=HAV*P2*0.001/C
RCS=VXM/(A(9)*2.0*OMEGA)
DTC=2*A(9)*ST*D/V**2
HM=(3.0*TD*V*C/(C**2*HFG*(1+0.375*TD*CP/HFG)))*0.25
HMK=(OMEGA*SIN(B))*1.5/(9.81*CCS(B))
HMY=RNUC*HM*HMK
HMX=0.09*OMEGA**2*SIN(B)**2/(9.81*CCS(B))
HFGI=HFG+0.375*CP*TD
FR=VXM/((9.81*HMEAN)**0.5)
REVXM=VXM*HMEAN*D/V
PAK=V**4*9.81/(C*ST**3)
PAKM=V**4*CFX/(C*ST**3)
PKM=1.0/PAKM
WN=2.0*2.14159*HMEAN/A(1)
WL=WAV/3.14159
WRITE(6,98)VX,VC,Q,TAN
98 FORMAT(3E12.4,16X,F10.5)
WRITE(6,99)E1,E2,E3,RNUX

```

```

99      FORMAT(3F12.4,16X,F12.4)
100     FORMAT(//,4X,'CCRICLIS RESULTS',/)
        WRITE(6,201)
        WRITE(6,200)VPE,VXM
200     FORMAT(10X,2E13.5,/)
201     FORMAT(/,15X,'VRE',12X,'VXM')
103     FORMAT(/,5X,'VX',10X,'VC',6X,'(T/CF.D)1/2*1/R',13X,'TAN ALPHA')
        WRITE(6,117)
        WRITE(6,118)WE,A(8),A(9)
        WRITE(6,198)
        WRITE(6,199)HMINC,HTMIN,HTMAX
198     FORMAT(/,4X,'HMINC',8X,'HTMIN',7X,'HTMAX')
199     FORMAT(3E13.5)
117     FORMAT(/,2X,'WEBER NC',5X,'ALPHA',7X,'RADIUS')
118     FORMAT(3E12.4)
        WRITE(6,202)
        WRITE(6,203)RNUC,RNL,RRA,VEL
203     FORMAT(4X,E13.5,6X,E13.5,5X,E13.5,3X,E13.5,/)
        WRITE(6,197)
197     FORMAT(5X,'HFG',10X,'K',11X,'V',11X,'ST',10X,'C',10X,'D',11X,'CP')
        WRITE(6,190)HFG,C,V,ST,D,B,CP
        WRITE(6,195)
        WRITE(6,194)RGS,OMEGA,DTC
        WRITE(6,192)
        WRITE(6,193)FMX,FMY,FMZ
        WRITE(6,191)
        WRITE(6,190)FR,REVY,PAK,PAKM,FKM
        WRITE(6,188)
        WRITE(6,189)WN,WL
        WRITE(6,187)RNUR,WEH
195     FORMAT(/,2X,'ROSSBY NO.',3X,'OMEGA(RAD/S)',4X,'DTC')
194     FORMAT(3E13.5)
196     FORMAT(7E12.4)
192     FORMAT(/,6X,3HFMX,10X,3HFMY,5X,14PHFG(1+3/8OPTD))
193     FORMAT(3E13.5)
191     FORMAT(/,3X,6HROUOF,7X,7HRE(VXM),7X,6HKAP(C),8X,7HKAP(AY))
190     FORMAT(5E13.5)
188     FORMAT(/,3X,8HWAVE NC.,5X,12HNCON--DIM WLF)
189     FORMAT(2E13.5)
187     FORMAT(2E13.5)
64      CONTINUE
399999 CONTINUE
        RETURN
        END

```

```

N(1,29)
TIME DELT DELMIN FINT IMPR DEL OUTDEL T2 T1 T T4 ZZC010
ZZ0012 ZZ0012 RB B2 B1 B0 ACG RDNC HTC HAV HA X
TI J KCUNT DOG K TD TAV HFG C V D R
AL BR TDW TDWA CC CF CFX CP AG L1 L2 CON
HMINC ROT COR ST OMEGA TH I ZZ0004A0 ZZ0009AREA R2
R1 QC RNU WAV WAVF FRW AR G GC CCC FTMIN HTMAX
ERR HAVC PE VRE RA RNUC E DL FN F1 F2 F3
XL AML4 GAM FE FLAM RHF HMIN HMEAN L4 VX VXM G
E1 E2 E3 VO TAN WE WEF VEL RRA FNUX RNUR RCS
DTD HM HMW HMY HMX HFGL FR REVXM PAK PAKM PKM WN
WL AX CX A BB I J L LC L1 L2 L4
K DOG KCUNT RDNO

```

```

LABEL CONDENSATE FILM MODELING
TABLE AX(1)=-3.91,AX(2)=-2.0,AX(3)=-1.61,AX(4)=-1.5,AX(5)=-1.25,...
AX(6)=-1.0,AX(7)=-0.5,AX(8)=0.0,AX(9)=0.5,AX(10)=1.0,AX(11)...
=1.25,AX(12)=1.5,AX(13)=2.079,CX(1)=0.0462,CX(2)=0.046,...
CX(3)=0.0452,CX(4)=0.0445,CX(5)=0.042,CX(6)=0.0389,...
CX(7)=0.0321,CX(8)=0.0256,CX(9)=0.0203,CX(10)=0.0152,...
CX(11)=0.013,CX(12)=0.0112,CX(13)=0.00817,...
A(1)=0.00186,A(2)=144.6,A(3)=135.0,A(4)=600.0,...
A(5)=10.0,A(6)=0.000691,A(7)=77.5,A(8)=23.30,A(9)=0.281
CONSTANT ACG=0.02,RDNC=1,HTC=1.0,HAV=1.0,HA=0.0,X=1.0,BB=0,...
BO=1.0,TI=0.0,B1=0.0,B2=0.0,J=6,KCUNT=1,DOG=1,K=1,...
TD=0.0,TAV=0.0,HFG=0.0,C=0.0,V=0.0,D=0.0,R=0.0,AL=0.0,RR=1,...
TDW=0.0,TDWA=0.0,CC=0.0,CF=0.0,CFX=0.0,CP=0.0,AG=0.0,L1=1.0,L2=1,...
CON=0.0,HMINC=0.0,ROT=0.0,COR=0.0,ST=0.0,OMEGA=0.0,TH=0.000066
TIMER DELT=0.002,FINTIM=0.02

```

```

END
STOP
E

```

Input data

- |              |  |     |                           |
|--------------|--|-----|---------------------------|
| AX(1) - (13) | ln $\Lambda$                                 | V   | Viscosity                 |
| CX(1) - (13) | $\epsilon$                                   | D   | Density                   |
| A(1)         | Wavelength                                   | ST  | Surface tension           |
| A(2)         | Steam saturation temperature                 | C   | Thermal conductivity      |
| A(3)         | Cone outer wall temperature                  | CC  | Cone thermal conductivity |
| A(4)         | Rotational speed                             | CP  | Specific heat             |
| A(5)         | Beta   | HFG | Enthalpy of vapourisation |
| A(6)         | Peak film thickness                          |     |                           |
| A(7)         | Cone inner wall temperature                  |     |                           |
| A(8)         | Ridge angle(mid-surface)                     |     |                           |
| A(9)         | Radius                                       |     |                           |
| BO,B1,B2,s   | boundary conditions                          |     |                           |
| AO           | $\Lambda$                                    |     |                           |
| ACG          | Initial value of $\Lambda$                   |     |                           |
| CON          | $\epsilon$                                   |     |                           |
| COR          | $\odot$                                      |     |                           |
| ROT          | $\Omega$                                     |     |                           |
| OMEGA        | Angular velocity                             |     |                           |
| TD           | Film temperature difference                  |     |                           |
| TDW          | Cone wall temperature difference             |     |                           |
| TAV          | Drew reference temperature                   |     |                           |
| HT           | Heat transfer coefficients                   |     |                           |
| HAV          | Average heat transfer coefficient            |     |                           |
| CF           | acceleration perpendicular to cone generator |     |                           |
| CFX          | " parallel to cone generator                 |     |                           |

Appendix ELeast squares polynomial curve fitting programme

This programme has been employed to correlate theoretical and experimental data in the form of polynomials. The type of best fits possible are

- (i) a linear relationship between two quantities.
- (ii) a linear- logarithmic relationship.
- (iii) a logarithmic-logarithmic relationship.

The programme can process 200 pairs of results and give a ninth order equation.

G COMPILER

MAIN

06-27-73

18:38.10

```

DOUBLE PRECISION X,Y,A,U,V,ERR,YC
DIMENSION X(200),Y(200),U(10),A(2000),V(250),P(200),G(200)
1 READ(5,5001) L,M,N,Q
WRITE(6,6003)
6003 FORMAT(1H ,25X,'POLYNOMIAL LEAST SQUARES FIT')
READ(5,5000)(X(I),I=1,M)
READ(5,5000)(Y(I),I=1,M)
GO TO(9,10,11,14),L
9 DO 8 I=1,M
8 X(I)=X(I)+A
GO TO 3
10 DO 12 I=1,M
XL=X(I)
12 X(I)=ALOG(XL)
GO TO 3
11 DO 13 I=1,M
XL=X(I)
YL=Y(I)
X(I)=ALOG(XL)
13 Y(I)=ALOG(YL)
GO TO 3
14 DO 15 I=1,M
YL=Y(I)
15 Y(I)=ALOG(YL)
3 CALL PLSQF(X,Y,M,N,U,ERR,A,V)
NI = N+1
WRITE(6,6004)
6004 FORMAT(' CURVE IS OF THE FORM: Y = A0+A1*X+A2*X**2+...+AN*X**N')
WRITE(6,6005)N,M
6006 FORMAT(' ORDER OF CURRENT FIT = ',I2,10X,' NO. OF POINTS GIVEN = ',
1I3/)
DO 2 I=1,NI
II=I-1
2 WRITE(6,6005)II,U(II)
6005 FORMAT(' A',II,' = ',E14.6)
DO 20 I=1,M
G(I)=Y(I)-A(I)
IF(Y(I).EQ.0.0) GO TO 20
P(I)=A(I)*100.0/Y(I)
20 CONTINUE
WRITE(6,6002)
6002 FORMAT(///8X,'X',12X,'Y',11X,'ERROR',10X,'YCALC',10X,'% ERROR')
WRITE(6,6000) (X(I),Y(I),A(I),G(I),P(I), I=1,M)
5000 FORMAT(8F10.0)
WRITE(5,6007)
6007 FORMAT('C %ERROR% IS THE ALGEBRAIC DIFF. BETWEEN THE VALUE')
WRITE(6,6060)
6060 FORMAT(1H , 'GIVEN FOR Y AND THAT FOUND FROM THE FITTED CURVE')
READ(1,5001)N
IF(N)4,1,3
5001 FORMAT(12,2I5,2X,F10.0)
6000 FORMAT(1H ,4E14.6,F14.6)
4 STCP
END

```

```

SUBROUTINE DSIMQ(A,B,N,KS)
DOUBLE PRECISION A,B,BIGA
DIMENSION A(1),B(1)
C     FORWARD SOLUTION
TOL=0.0
KS=0
JJ=-N
DO 65 J=1,N
JY=J+1
JJ=JJ+N+1
BIGA=0
IT=JJ-J
DO 30 I=J,N
C     SEARCH FOR MAXIMUM COEFFICIENT IN COLUMN
IJ=IT+I
IF(DABS(BIGA)-DABS(A(IJ))) 20,30,30
20 BIGA=A(IJ)
IMAX=I
30 CONTINUE
C     TEST FOR PIVOT LESS THAN TOLERANCE %SINGULAR MATRIX<
IF(DABS(BIGA)-TOL) 35,35,40
35 KS=1
RETURN
C     INTERCHANGE ROWS IF NECESSARY
40 I1=J+N*(J-2)
IT=IMAX-J
DO 50 K=J,N
I1=I1+N
I2=I1+IT
SAVE=A(I1)
A(I1)=A(I2)
A(I2)=SAVE
C     DIVIDE EQUATION BY LEADING COEFFICIENT
50 A(I1)=A(I1)/BIGA
SAVE=B(IMAX)
B(IMAX)=B(J)
B(J)=SAVE/BIGA
C     ELIMINATE NEXT VARIABLE
IF(J=N) 55,70,55
55 IQS=N*(J-1)
DO 65 IX=JY,N
IXJ=IQS+IX
IT=J-IX
DO 60 JX=JY,N
IXJX=N*(JX-1)+IX
JXJ=IXJX+IT
60 A(IXJX)=A(IXJX)-(A(IXJ)*A(JXJ))
65 B(IX)=B(IX)-(B(J)*A(IXJ))
C     BACK SOLUTION
70 NY=N-1
IT=N*N
DO 80 J=1,NY
IA=IT-J
IB=N-J
IC=N
DO 80 K=1,J
B( IB)=B( IB)-A( IA)*B( IC)
IA=IA-N
80 IC=IC-1
RETURN
END

```

```

SUBROUTINE PLSQF (X,Y,M,N,U,ERR,A,V)
DOUBLE PRECISION X,Y,A,U,V,ERR,YC
DIMENSION X(1),Y(1),A(1),U(1),V(1)
DO 3 I=1,M
A(I)=1.0
DO 3 J=1,N
JJ=J*M+I
J1=JJ-M
3 A(JJ)=A(J1)*X(I)
CALL DGTPE (A,Y,U,M,N+1,1)
CALL DGTPRD (A,A,V,M,N+1,N+1)
CALL DSIMQ (V,U,N+1,NERR)
ERR=0
J1=N+1
DO 2 I=1,M
YC=0.0
DO 1 J=1,J1
JJ=M*(J-1)+I
1 YC=A(JJ)*U(J)+YC
A(I) = Y(I)-YC
2 ERR=A(I)*A(I)+ERR
RETURN
END

```

```

SUBROUTINE DGTPRD(A,B,R,N,M,L)
DOUBLE PRECISION A,B,R
DIMENSION A(1),B(1),R(1)
IR=0
IK=-N
DO 10 K=1,L
IJ=0
IK=IK+N
DO 10 J=1,M
IB=IK
IR=IR+1
R(IR)=0
DO 10 I=1,N
IJ=IJ+1
IB=IB+1
10 R(IR)=R(IR)+A(IJ)*B(IB)
RETURN
END

```

APPENDIX F

Equation 3.8.9 shows that the non-dimensional term qualifying  $\bar{z}^3$  is  $2\Omega + \frac{g \cos \beta}{\bar{x} a_x}$ . When this thesis was first submitted the equation 3.8.9 was obtained but the non-dimensional term qualifying  $\bar{z}^3$  was simply  $\Omega$ . This occurred because a simplifying assumption was introduced at too early a stage in the analysis. This assumption, although justifiable in this analysis, was not in terms of a general equation. The assumption made was that since the included angle of the cone was small an incremental change in the 'X' direction would cause a very small change in the radius so that the radius may be assumed constant. Thus the cone would be built up of small slices of cylinders. This assumption is necessary at a later stage in order to reduce the problem to a 2-dimensional one so that a numerical solution was possible.

It is not possible, due to lack of time, to re-compute the whole of the theoretical values using the new non-dimensional term  $2\Omega + \frac{g \cos \beta}{\bar{x} a_x}$ . It is possible to show the effect of assuming  $\Omega$  instead of  $2\Omega + \frac{g \cos \beta}{\bar{x} a_x}$  for this analysis is small and causes no major change in the form of the solution. This was demonstrated by performing the integration of equation 3.8.9 using the two values of non-dimensional parameter. The equation to be solved is the same but the term 'ROT' in the dynamic modelling section of the C.S.M.P. package is modified to :-

$$\begin{aligned} XN &= A(9) * D * C F ** 2 * HMIN / (ST * CEX * SIN(B)) \\ ROT &= ((2 * 3.14159 * A(4) / 60) ** 2 * ST * SIN(B) ** 2 / HMINC * C * C F ** 2) \\ ROT &= 2 * ROT + 9.81 * COS(B) / (XN * CEX) \end{aligned}$$

A number of computer runs were performed. The one included here is a typical result. In the thesis the value for  $\Omega$  used is 0.000391. The new value,  $2\Omega + \frac{g \cos \beta}{\bar{x} a_x}$ , is 0.000932. The curves are so close that a graphical comparison is not applicable. The results obtained show that the non-dimensional half wavelength and the peak value of non-dimensional

film thickness are :-

$$(1) \text{ For 'ROT' = } 0.000391, \quad \lambda/2 = 5.94, \quad \bar{z}_{\max} = 1.9055$$

$$(2) \text{ For 'ROT' = } 0.000932, \quad \lambda/2 = 5.92, \quad \bar{z}_{\max} = 1.8988$$

The error, in assuming  $\Omega \bar{z}^3$  instead of  $(2\Omega + \frac{9\cos^2\beta}{\bar{x}^2 a_x}) \bar{z}^3$ , was calculated to be less than 0.35% in the non-dimensional peak film thickness and 0.17% in the non-dimensional wavelength.

9.0 TABLES

Table 1

Results for 10<sup>0</sup> conc.

Wavelength m	Ts °C	T <sub>wo</sub> °C	T <sub>wi</sub> °C	N rpm	$\beta$	Film thickness m
Pressure 1.5 bar absolute.						
0.00557	111.1	93.4	48.9	152	5	0.0000850
0.0052	111.2	96.8	49.3	200	5	0.0000787
0.00449	111.3	98.3	49.4	250	5	0.0000762
0.0042	111.7	99.8	49.6	300	5	0.0000711
0.00345	111.7	100.4	49.6	352	5	0.0000685
0.00304	111.0	100.4	49.9	400	5	0.0000685
Pressure 2.0 bar absolute.						
0.00631	122.0	101.0	50.3	135	5	0.0000838
0.00581	122.0	104.5	51.3	200	5	0.0000850
0.00467	121.8	106.3	51.4	250	5	0.0000762
0.00365	121.1	107.1	51.8	300	5	0.0000724
0.00309	121.6	107.3	52.2	350	5	0.0000711
0.00279	121.6	108.3	52.5	400	5	0.000066
Pressure 2.5 bar absolute.						
0.0068	129.0	109.8	56.0	152	5	0.0000787
0.00492	128.6	111.1	56.1	200	5	0.0000736
0.00454	128.5	114.0	56.1	250	5	0.0000711
0.00406	128.2	114.3	56.3	300	5	0.0000711
0.00344	128.5	116.1	56.2	350	5	0.000066
0.00342	128.5	116.4	56.3	400	5	0.000066
Pressure 3.0 bar absolute.						
0.00691	134.6	112.5	57.0	120	5	0.0000864
0.00587	134.8	114.7	56.5	150	5	0.0000838
0.00506	134.8	116.5	56.5	200	5	0.0000762
0.00421	134.8	117.1	56.8	250	5	0.0000749
0.00403	134.8	118.3	57.0	300	5	0.0000724
0.00345	135.0	120.3	57.0	350	5	-
Pressure 4.0 bar absolute.						
0.00582	145.2	124.1	62.6	154	5	0.0000813
0.00526	146.0	126.0	62.7	200	5	0.0000749
0.0049	144.8	126.4	62.7	250	5	0.0000724
0.00462	144.8	126.8	62.7	300	5	0.0000711
0.00417	144.8	127.4	63.0	350	5	-

Table 2

Results for 20° cone.

Wavelength m	T <sub>s</sub> °C	T <sub>wo</sub> °C	T <sub>wi</sub> °C	N rpm	$\beta$	Film thickness m
Pressure 1.5 bar absolute.						
0.0056	113.0	97.1	54.5	200	10	0.0000762
0.00439	113.0	98.8	55.7	250	10	0.0000737
0.00461	112.2	100.3	58.0	300	10	0.0000685
0.00389	112.3	100.6	58.1	350	10	0.0000685
0.00327	111.9	101.3	58.4	400	10	0.000066
0.00256	111.6	102.0	58.0	600	10	0.0000685
Pressure 2.0 bar absolute.						
0.00573	121.0	107.0	57.1	200	10	0.0000333
0.00508	121.0	108.4	58.8	250	10	0.0000787
0.00409	121.5	109.4	61.8	300	10	0.0000737
0.00388	121.4	109.8	62.0	350	10	0.0000711
0.00322	120.9	110.0	62.3	400	10	0.0000685
0.00281	120.9	110.3	62.5	450	10	0.0000608
Pressure 2.5 bar absolute.						
0.00542	128.5	114.1	62.0	200	10	0.0000737
0.00512	128.0	114.3	65.0	250	10	0.0000762
0.00465	129.1	117.0	63.2	300	10	0.0000711
0.00383	128.8	117.8	65.1	350	10	0.0000685
0.0033	129.0	118.5	65.6	400	10	0.000066
0.00281	128.2	119.1	66.0	600	10	0.000066
Pressure 3.0 bar absolute.						
0.00554	134.8	116.5	63.5	200	10	0.0000313
0.00512	135.2	119.9	65.7	250	10	0.0000799
0.00462	134.6	120.8	66.1	300	10	0.0000787
0.0042	135.1	121.6	67.5	350	10	0.0000737
0.0032	134.4	122.3	68.0	400	10	0.0000723
0.0022	134.5	124.0	63.4	600	10	0.0000585
Pressure 4.0 bar absolute.						
0.00457	144.2	127.1	71.2	200	10	-
0.00424	143.9	129.1	73.3	250	10	-
0.00357	143.9	129.7	74.0	300	10	-
0.00284	143.9	133.0	76.0	350	10	-
0.00219	144.6	134.5	77.3	400	10	-
0.00186	144.6	135.0	77.5	600	10	-

Table 3

Theoretical results for 10° cone

Wavelength m	Film thickness			Nusselt no.	Heat trans. coeff.	
	Laminar mm	Mean mm	$\delta_{\text{mir}}$ mm		$h_{\text{mean}}$ k#/m <sup>2</sup> K	$h_{\text{min}}$ K
Pressure 1.5 bar absolute.						
0.0164	0.07843	0.0718	0.06593	3395.3	9.075	10.311
0.0092	0.06987	0.05796	0.04445	4664.5	12.49	15.313
0.00619	0.06388	0.0471	0.02937	6149.1	16.47	23.193
0.00481	0.05375	0.04073	0.02221	7545.0	21.23	30.696
0.00391	0.05469	0.03707	0.01749	8398.2	23.86	39.004
0.00329	0.05122	0.03518	0.01394	10214.0	27.39	43.924
Pressure 2.0 bar absolute.						
0.02833	0.08233	0.05857	0.07261	2576.4	6.92	9.403
0.00983	0.07232	0.05973	0.04345	4596.7	12.36	15.743
0.00626	0.0658	0.04826	0.03097	5959.1	16.04	22.101
0.00478	0.0604	0.04154	0.02266	7392.2	19.90	30.214
0.00391	0.0574	0.03856	0.01818	8547.0	23.01	37.655
0.00334	0.05345	0.03499	0.01544	9782.1	26.34	44.362
Pressure 2.5 bar absolute.						
0.0135	0.07784	0.06599	0.0646	3323.5	8.972	10.613
0.00991	0.07158	0.0589	0.04944	4519.5	12.19	14.158
0.00634	0.06397	0.04674	0.03163	6023.7	16.04	21.696
0.00475	0.05963	0.04094	0.02245	7479.8	20.18	30.567
0.00386	0.05451	0.03621	0.01768	8945.8	24.15	38.834
0.00333	0.05135	0.03474	0.01433	10025.0	27.06	46.295
Pressure 3.0 bar absolute.						
0.03205	0.08327	0.08113	0.07959	2076.7	5.604	8.733
0.02203	0.07834	0.06874	0.0645	3127.3	8.443	10.645
0.00954	0.0718	0.05851	0.04691	4534.9	12.25	14.642
0.00631	0.06688	0.04861	0.03226	5849.9	15.80	21.295
0.0048	0.06234	0.04247	0.02389	7169.3	19.37	28.753
-	0.0577	-	-	-	-	-
Pressure 4.0 bar absolute.						
0.02026	0.07791	0.06728	0.0645	3253.3	8.443	10.645
0.00981	0.07247	0.05932	0.04333	4492.7	12.15	14.235
0.00555	0.0667	0.04787	0.03278	5942.0	15.80	20.984
0.00478	0.06248	0.04207	0.02416	7160.4	19.37	28.476
-	0.05794	-	-	-	-	-

Table 4

Theoretical results for 20° cone.

Wavelength m	Film thickness			Nusselt no.	Heat trans. coeff.	
	Laminar mm	Mean mm	$\delta_{\min}$ mm		$h_{\text{mean}}$ kW/m <sup>2</sup>	$h_{\min}$ K
Pressure 1.5 bar absolute.						
0.0186	0.06336	0.05351	0.04941	4.345	10.550	9.940
0.0146	0.05661	0.05560	0.03631	5.158	12.530	9.250
0.00509	0.05024	0.04101	0.02305	8.154	19.820	9.958
0.00392	0.04682	0.03759	0.01743	9.75	23.700	9.959
0.0033	0.04302	0.03472	0.01396	11.347	27.590	10.339
0.00195	0.03473	0.03261	0.00700	16.869	41.030	9.964
Pressure 2.0 bar absolute.						
0.0184	0.06041	0.04973	0.04643	4.314	10.520	9.168
0.0146	0.05411	0.05434	0.03410	5.212	12.720	9.702
0.00532	0.04969	0.04651	0.02452	8.038	19.600	9.295
0.00385	0.04602	0.03807	0.01622	10.002	24.420	9.636
0.00324	0.04270	0.03555	0.01333	11.500	28.080	10.002
0.00419	0.04013	0.05052	0.02259	11.016	26.900	11.269
Pressure 2.5 bar absolute.						
0.01815	0.06017	0.04670	0.04669	4.391	10.740	9.720
0.0145	0.05474	0.05094	0.03496	5.169	12.640	9.006
0.00487	0.04913	0.04104	0.02105	8.459	20.700	9.658
0.00413	0.04488	0.04010	0.01971	9.849	24.100	10.026
0.00425	0.04178	0.04741	0.02166	10.324	25.270	10.407
0.00193	0.03337	0.03133	0.00673	17.574	43.020	10.208
Pressure 3.0 bar absolute .						
0.018	0.06359	0.06111	0.04839	4.055	9.925	9.449
0.0144	0.05530	0.05525	0.03685	5.217	12.780	8.601
0.00506	0.05043	0.04719	0.02290	8.111	19.870	8.733
0.00382	0.04696	0.04010	0.01614	9.368	24.170	9.327
0.00314	0.04304	0.04741	0.01261	11.549	28.290	9.503
0.0019	0.03337	0.03133	0.00679	17.133	41.980	10.039

Table 5

Experimental parameters for 10° cone.

Nusselt no.	Taylor no. $\times 10^{-13}$	Weber no.	Centrifugal acc.		Heat trans. coeff. k#/m <sup>2</sup> K
			X dir. m/s <sup>2</sup>	Y dir. m/s <sup>2</sup>	
Pressure 1.5 bar absolute.					
4653.6	1.198	128,380	15.293	62.245	12.452
6117.9	2.180	223,300	19.330	108.390	16.379
6979.2	3.483	350,600	24.706	169.840	18.698
7860.1	5.133	506,400	31.277	244.945	21.074
8346.0	7.127	698,000	39.378	337.541	22.382
8847.3	9.173	901,000	48.003	436.124	23.724
Pressure 2.0 bar absolute.					
4478.8	1.109	103,500	14.127	43.920	12.030
5649.7	2.553	223,300	19.330	108.390	15.184
6537.2	4.084	353,600	24.706	169.840	17.725
7350.7	5.925	517,000	31.277	244.945	19.794
7172.5	8.104	704,200	39.043	333.707	19.306
7814.2	10.725	921,600	48.003	436.124	21.040
Pressure 2.5 bar absolute.					
5230.6	1.631	134,140	15.293	62.245	14.099
5870.5	2.866	232,800	19.330	108.390	15.829
7469.1	4.642	356,300	24.706	169.840	20.150
7806.2	6.701	527,000	31.277	244.945	21.063
9043.9	9.499	732,600	39.547	339.467	24.412
9300.9	11.937	917,800	47.053	425.267	25.197
Pressure 3.0 bar absolute.					
4694.4	1.077	84,580	13.213	38.473	12.667
5416.2	1.730	132,400	15.149	60.595	14.622
6138.2	3.143	236,400	19.350	108.390	16.577
6381.2	4.947	369,800	24.706	169.840	17.234
6963.9	7.226	533,400	31.277	244.945	18.313
8452.7	10.137	728,200	39.043	333.707	22.788
Pressure 4.0 bar absolute.					
5499.0	2.117	143,400	15.439	63.916	14.870
5973.3	3.657	243,200	19.330	108.390	16.169
6540.9	5.714	380,000	24.706	169.840	17.690
6729.9	8.264	547,600	31.277	244.945	18.202
6993.5	11.977	739,400	40.739	353.098	18.929

Table 6

Experimental parameters for 20° cone.

Nusselt no.	Taylor no. $\times 10^{-13}$	Weber no.	Centrifugal acc.		Heat trans. coeff. $\text{kW/m}^2 \text{ K}$
			X dir. $\text{m/s}^2$	Y dir. $\text{m/s}^2$	
Pressure 1.5 bar absolute.					
5439.1	3.273	215,200	31.065	119.684	13.204
6169.2	5.240	499,000	43.104	137.964	14.937
7239.6	7.679	120,200	57.819	271.413	17.597
7399.1	10.502	990,800	75.210	370.045	17.937
8247.4	13.826	1292,600	95.276	433.346	20.054
9339.6	31.372	2893,000	202.295	1090.733	22.715
Pressure 2.0 bar absolute.					
7261.8	3.896	326,200	31.065	119.684	17.715
8033.3	6.201	511,000	43.104	137.964	19.603
8046.7	9.067	737,600	57.819	271.413	19.643
8421.2	12.400	1004,800	75.210	370.045	20.584
8956.8	16.203	1312,400	95.276	433.346	21.367
9231.9	20.588	1662,000	113.013	612.320	22.540
Pressure 2.5 bar absolute.					
7411.6	4.408	332,600	31.065	119.684	18.125
7387.2	6.891	519,600	43.104	137.964	19.065
9127.2	10.304	753,000	57.819	271.413	22.334
9350.9	14.145	1026,600	75.210	370.045	24.103
10336.0	13.647	1343,000	95.276	433.346	25.372
12013.0	42.224	3024,000	202.295	1090.733	29.405
Pressure 3.0 bar absolute.					
5942.9	4.653	335,000	31.065	119.684	14.546
7292.0	7.590	523,400	43.104	137.964	17.853
8165.4	11.020	763,000	57.819	271.413	19.999
8266.2	15.168	1033,200	75.210	370.045	20.243
9263.4	19.918	1353,300	95.276	433.346	22.692
10943.0	45.715	3063,000	202.295	1090.733	26.815
Pressure 4.0 bar absolute.					
6773.3	5.449	345,600	31.065	119.684	16.617
7333.6	8.639	542,400	43.104	137.964	19.216
8161.9	12.593	782,000	57.819	271.413	20.009
10913.2	17.742	1072,200	75.210	370.045	26.763
11846.0	23.590	1405,800	95.276	433.346	29.042
12534.1	53.347	3166,000	202.295	1090.733	30.729

Table 7

Ridge angle and Rossby number.

10° Cone.

 $\beta = 5^\circ$ 

Ridge angle $\alpha$			Vx m/s	V $\theta$ m/s	Rossby number	Theoretical ridge angle $\frac{1}{2}$
Experimental $\frac{1}{4}$	$\frac{1}{2}$	values $\frac{3}{4}$				
Pressure 1.5 bar absolute.						
11°30'	12°00'	13°48'	0.124	0.0019	0.0226	2°48'
13 00	13 48	15 24	0.1375	0.00506	0.026	7 48
17 24	18 00	20 18	0.167	0.00873	0.0309	13 30
20 54	21 06	23 00	0.1858	0.00784	0.0324	14 24
21 36	22 54	23 12	0.218	0.0169	0.0355	18 42
27 30	28 48	28 48	0.260	0.0200	0.0396	13 36
Pressure 2.0 bar absolute.						
-	9 54	12 06	0.1204	0.00149	0.021	4 48
17 36	18 36	19 12	0.1736	0.0074	0.0326	9 30
20 24	21 00	23 06	0.1804	0.00626	0.0333	12 42
22 48	24 06	24 54	0.207	0.0126	0.0363	16 42
25 30	26 03	27 54	0.249	0.0152	0.0403	18 54
29 00	30 24	30 18	0.266	0.0164	0.0405	19 30
Pressure 2.5 bar absolute.						
12 06	13 30	16 50	0.1238	0.00146	0.0225	1 36
18 00	18 12	20 00	0.138	0.00427	0.0261	5 54
22 00	22 24	23 48	0.167	0.00876	0.0309	12 30
26 48	26 54	30 12	0.212	0.00996	0.0371	15 18
23 30	25 08	26 00	0.234	0.0139	0.0382	18 00
30 48	31 00	32 00	0.279	0.0258	0.0428	21 48
Pressure 3.0 bar absolute.						
12 54	13 12	14 30	0.1372	0.0143	0.0228	1 30
14 48	15 00	15 36	0.145	0.00264	0.0262	4 00
23 06	23 48	24 30	0.154	0.00526	0.0291	6 42
27 06	28 18	29 06	0.192	0.00302	0.0355	13 48
28 30	29 42	30 00	0.228	0.0155	0.0399	14 06
31 24	32 18	32 36	0.278	0.0222	0.0457	20 18
Pressure 4.0 bar absolute.						
15 06	15 48	17 12	0.150	0.00286	0.0273	9 48
17 54	18 54	20 42	0.1613	0.00582	0.0304	7 06
24 36	24 57	27 30	0.193	0.00706	0.0357	13 48
25 00	27 00	28 06	0.236	0.0165	0.0413	15 12
29 06	30 54	31 06	0.265	0.0177	0.0428	19 18

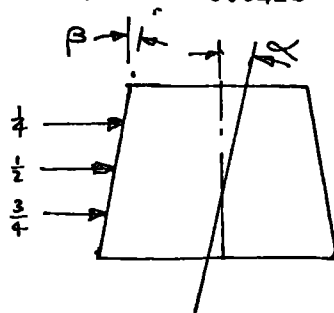


Table 8

Ridge angle and Rossby number.			20° Cone.		$\beta = 10^\circ$	
Ridge angle $\alpha$			$V_x$ m/s	$V_\theta$ m/s	Rossby number	Theoretical ridge angle $\frac{1}{2}$
Experimental $\frac{1}{4}$	$\frac{1}{2}$	values $\frac{1}{4}$				
Pressure 1.5 bar absolute.						
14°00'	14°00'	15°00'	0.2085	0.00374	0.0488	9°06'
14 30	16 00	18 00	0.274	0.00948	0.0578	10 18
15 00	16 03	17 30	0.3203	0.0161	0.0604	14 18
15 30	17 54	18 30	0.417	0.02166	0.0705	16 36
17 00	18 09	19 48	0.4931	0.0246	0.0753	17 12
18 36	19 36	22 24	1.132	0.0557	0.1221	20 30
Pressure 2.0 bar absolute.						
12 42	13 39	15 24	0.2752	0.0053	0.0644	11 06
13 18	14 30	15 06	0.3399	0.0119	0.0717	14 24
14 00	15 00	17 12	0.4029	0.023	0.076	15 06
14 12	15 24	16 06	0.4889	0.02625	0.0827	17 54
16 54	17 15	19 00	0.575	0.03018	0.0873	18 24
17 18	18 54	19 48	0.562	0.0282	0.0779	17 18
Pressure 2.5 bar absolute.						
11 00	11 09	13 30	0.258	0.0045	0.0604	12 06
14 18	14 24	16 21	0.3359	0.01085	0.0708	14 30
13 18	15 00	16 30	0.399	0.0215	0.0753	16 18
16 36	17 27	19 30	0.4847	0.0238	0.082	17 00
21 36	23 24	24 30	0.5727	0.0369	0.0874	14 00
21 24	21 42	22 36	1.218	0.06275	0.1309	21 30
Pressure 3.0 bar absolute.						
16 12	16 24	18 24	0.282	0.00478	0.066	15 36
18 00	18 27	21 30	0.3876	0.0127	0.0817	14 09
20 18	21 17	22 48	0.5065	0.0339	0.0955	21 18
20 00	22 09	22 36	0.5811	0.0338	0.0983	20 00
23 21	24 36	25 42	0.7103	0.0404	0.1084	20 36
22 30	25 42	26 12	1.367	0.0759	0.1469	23 36
Pressure 4.0 bar absolute.						
19 00	19 48	21 00	-	-	-	-
19 06	19 18	21 18	-	-	-	-
20 18	20 36	21 30	-	-	-	-
21 36	21 18	24 12	-	-	-	-
21 48	22 36	25 13	-	-	-	-
21 54	23 18	25 30	-	-	-	-

